Cellular stress characterisation in *S. cerevisiae* budding yeast using optical microscopy

Sarah Lecinski

PhD

University of York

Physics

April 2022

Abstract

The term "cellular stress" covers various environmental and metabolic events that threaten cell survival. In response, eukaryotic cells can adapt their metabolism to acute changes in their surrounding environment to maintain cellular homeostasis and ensure survival. The cell is an enclosed system with macromolecules and functional compartments diffusing in a liquid-like environment, the cytoplasm. The position in time and space of these elements influences every aspect of cell biology, from molecular interactions and enzymatic activities to the process of cell division itself.
Cellular stress episodes can interfere with the timing of these physiological processes: perturbations modify the cytoplasm volume and composition (e.g., accumulation of damaged proteins), including changes of intracellular physical properties such as macromolecular crowding influencing diffusion and spatio-temporal dynamics of the whole system. Consequently, cellular stress dynamics have been of strong interest to physicists and biologists.

In continuity with previous research in the field, this project aimed to explore these aspects of cellular physiology and gain new insight into cellular stress responses and crowding dynamics in the budding yeast *Saccharomyces cerevisiae*, a eukaryotic model sensitive to environmental stresses. This thesis sets out to investigate the influence of hyperosmotic shock, glucose availability, and cell growth on macromolecular crowding. I present a methodology developed to identify local regions of crowding in yeast cells using a previously generated Förster Resonance Energy Transfer Technology (FRET) crowding biosensor called CrGE. I describe experimental and analysis procedures to quantify crowding at subcellular levels and have developed new strains controlling the expression of fluorescently tagged cytoplasmic aggregates. To identify fluorescent clusters on cellular models, single molecule characterisations for stoichiometry and diffusion tracks *in vivo* were performed using bespoke Slimfield microscopy. Cellular sub-compartments were visualised and tracked over time using confocal microscopy, giving insight into polarised inheritance events in the budding yeast.

List publications

Articles

Shepherd JW*, **Lecinski S***, Shashkova S, MacDonald C, Leake MC (2020) Molecular crowding in yeast: dependence on ionic strength, glucose conditions, and sensor copy number. Methods 193, 54-61. *Joint first author contribution

Lecinski S*, Shepherd JW*, Frame L, Hayton I, MacDonald C, Leake MC (2021) Investigating molecular crowding during cell division in budding yeast with FRET. Topics in Membranes, 88, 75-118. *Joint first author contribution

Reith P, Braam S, Welkenhuysen N, **Lecinski S**, Shepherd JW, MacDonald C, Shashkova S, Leake MC, Hohmann S, Cvijovic M. The effect of lithium on the budding yeast *Saccharomyces cerevisiae* to stress adaptation. Microorganisms 2022, 10(3), 590. (Syncrop collaboration)

Lecinski S, Shepherd JW, Syeda A, MacDonald C, Leake MC. Protein aggregates dynamic and localisation in budding yeast cells. Paper in preparation.

Posters

Lecinski S, Shashkova S, MacDonald C, Leake MC. Aging, and inheritance of aggregates in *Saccharomyces cerevisiae* yeast cells: Characterization with multi-dimensional optical microscopy. Presented at the North of England Cell Biology Forum, Aug 2018, Huddersfield (UK).

Lecinski S, MacDonald C, Leake MC. Survival mechanisms during asymmetric cell division: High resolution microscopy for characterisation and single molecule detection. Presented at the EMBO Cell polarity meeting, May 2019, Sant Feliu (SP).

Lecinski S, MacDonald C, Leake MC. Gene circuits and multi-dimensional optical microscopy: Characterisation of cellular stress. Presented at the RMS Microscience Microscopy Congress series, Jul 2019, Manchester, (UK) – Award: RMS national Travel grant and presented at the IOP physics meets biology annual meeting, Sept 2019, Oxford (UK).

Lecinski S, MacDonald C, Leake MC. Survival mechanisms and response to cellular stress: Characterisation with multi-dimensional optical microscopy. Presented at the Neubias conference, Feb 2020, Bordeaux (FR).

Lecinski S, Shepherd JW, MacDonald C, Leake MC Crowding and cellular stress responses in *S. cerevisiae*: Characterisation with multi-dimensional optical microscopy. Presented at the IOP Physics meets biology, Jul 2021, Online. – Award: Poster prize.

Acknowledgements

I greatly thank my supervisors, Professor Mark Leake and Doctor Chris MacDonald, for all the support, comments, and encouragement. I feel incredibly lucky to have had the opportunity to work with them and have grown so much as a scientist as a result.

I would like to thank Dr Jack Shepherd for his valuable contribution to the published work presented in this thesis and our great science discussions.

Thank you to Dr Sviatlana Shashkova, Dr Kamilla Laidlaw, Dr Aisha Syeda, Dr Jamieson Howard, Maria Chechik, David Sherlock, Dr Adam Wollman, and Dr Ji-Eun Lee, who have fully contributed to my learning experience since I first joined the lab. I am extending my thanks to all members of the Leake and MacDonald labs, with whom I had amazing moments, and to my Thesis Advisory Panel members, Christian Diget and Laurence Wilson, who fully contributed to developing my critical thinking.

To the University of York, the department of Physics and the department of Biology, thank you for the amazing work environment. I thank the Bioscience Technology Facility for their assistance with confocal imaging.

Thank you to my family and friends for their support. Specifically, thank you to my parents for their continuous love, encouragement, and support; my gratitude is beyond any words can express.

Thank you to my funding body, the Marie Sklodowska-Curie Actions (Syncrop doctoral network), for supporting this project. Finally, I would like to express once again all my gratitude for the great experience it was to conduct research within the University of York and to everyone who has been involved, far or close, in this project.

Declaration

I declare that this thesis is a presentation of original work and I am the sole author. This work has not previously been presented for an award at this, or any other, University. All sources are acknowledged as references.

- Dr Jack Shepherd's contribution to the development and implementation of various Python analysis utilities and in performing single molecule analysis of the CrGE sensor.
- Dr Adam Wolman for his developed MATLAB single molecule analysis software.

SIGNED: Sarah Lecinski DATE: 04/05/2023

Table of contents

Abbreviations

BF	Brightfield
Bp	Base pair
ConA	ConcanavalinA
CPY	Carboxypeptidase Y
CrGE	mCerulean3-mCitrine crowding FRET sensor
CrGE2.3	mGFP-mScarlet-I crowding FRET sensor
$CuSo_4$	Copper sulfate
DIC	differential interference contrast
DMSO	Dimethylsulfoxide
E. coli	Escherichia coli
Em λ	Emission wavelength
EPI	Epifluorescence illumination (microscopy)
ER	Endoplasmic reticulum
Ex λ	Excitation wavelength
FRAP	Fluorescence Recovery After Photobleaching
FRET	Förster resonance energy transfer
GUI	Graphic user interface
HILO	highly inclined and laminated optical (microscopy)
HIS	Histidine
HOG	High-osmolarity glycerol
I.R	Infra-Red
IC	Internal conversion
ISC	Inter System Crossing
LEU	Leucine
LiCl	Lithium Chloride

MET	Methionine
MW	Molecular weight
NaCl	Sodium Chloride
NMR	Nuclear Magnetic Resonance
PALM	Photoactivated Localization Microscopy
PBS	Phosphate Buffered Saline
PEG	polyethylene glycol
QY	Quantum yield
Ratiometric FRET	RatioFRET
ROI	Region of interest
ROS	Reactive oxygen species
Rpm	Rotation per min
SSIM	Saturated structured illumination microscopy
STORM	Stochastic Optical Reconstruction Microscopy
TIRF	Total Internal Reflection Fluorescence (microscopy)
U.V	Ultraviolet
URA	Uracil
YNB	Yeast Nitrogen Base
YPD	Yeast extract peptone dextrose media

List of tables

List of figures

Thesis structure

This thesis contains seven chapters.

Chapter 1: Introduces relevant background information and contextualises the research. This includes an initial focus on fluorescence and fluorescence microscopy, followed by definitions of cellular stress in eukaryotic cells, including the budding yeast model used in this work.

Chapter 2: Presents detailed methods used and developed to address each aspect of the research project.

Chapter 3: Presents results related to macromolecular crowding quantified during osmotic stress using a FRET crowding sensor expressed in yeast.

Chapter 4: Presents results for localised subcellular crowding in yeast at the single cell and single molecule resolution.

Chapter 5: Presents results from an investigation of cellular stress using an optimised aggregation reporter in the budding yeast.

Chapter 6: Presents extra work and experiment trials relevant to my PhD journey and not included in previous chapters.

Chapter 7: Discuss my work in the broader context of the field, with reflections and perspective on the project, and mention of possible future directions.

Appendix: Includes extra information and figures, such as code used and bibliography referencing all cited work in the thesis.

Chapter 1. Introduction and literature review

1. Fluorescence and microscopy

1.1. Fluorescence for biological research

1.1.1. Brief history and definition

In 1845, Sir Frederik William Herschel discovered fluorescence by observing a transparent quinine solution exposed to the sunlight and noticing its consequent bright blue colour reflection (Herschel, 1845). Later, in 1852, the British scientist George Gabriel Stokes further described this phenomenon in his article called *"On the change of refrangibility of light"* (Stokes, 1852). He reported his simple experiment performed with a tube containing a solution of quinine. The tube exposed to the different visible parts of the light spectrum emits a blue light when specifically exposed to UV light rays (Lakowicz, 2006; Stokes, 1852) Figure 1-1.

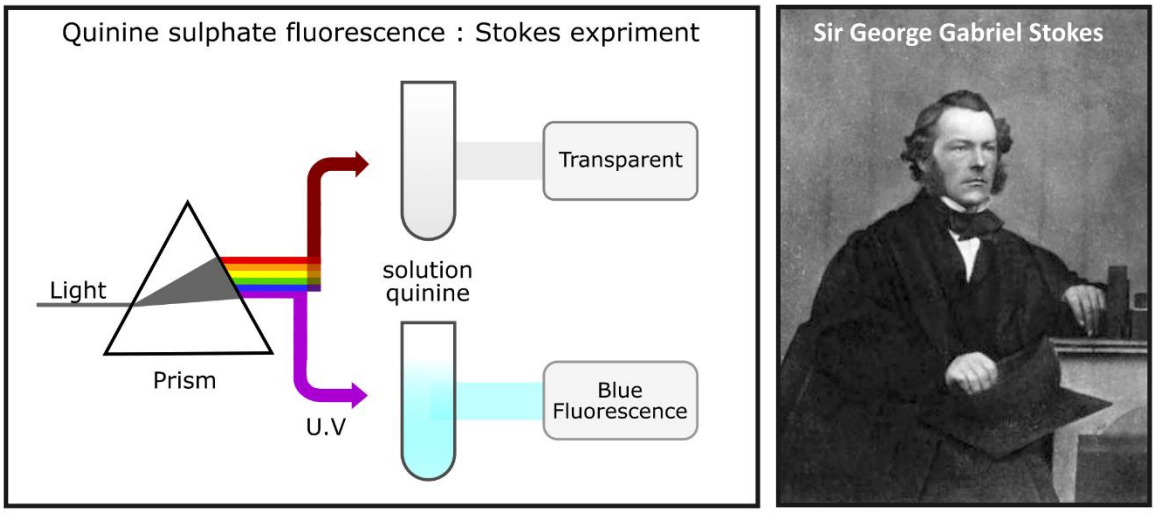

Figure 1-1: Fluorescence discovery, Stokes experiment

Left: Schematic representation of the Stokes experiment demonstrating blue fluorescence for a solution of quinine after UV light excitation. Right: Portrait of George Gabriel Stokes (Altenbach, 2020).

Since then, the term "fluorescence" has defined the ability of a specific molecule or fluorophore to emit light upon excitation by a specific range of light rays, or wavelengths, from the visible spectrum (Malley, 1994). Fluorescence is commonly described as a “fast” photoluminescence process (Demas & Demas, 2003) with an emission rate of around 10^{-8} seconds (Lakowicz, 2006) as opposed to phosphorescence with an average longer emission rate of about 10^{-6} to 100 seconds, certain phosphorescent material can display an afterglow for hours (Atkins & De Paula, 2014; Dreier, 2017).

This “near-instant” emission after excitation for fluorescence has naturally led to the selection of fluorescent probes and proteins as tools to observe real-time events and dynamics in the field of biology, and by using fluorescence microscopes (Jennison & Morgan, 1950).

1.1.2. Fluorophores and electronic states

The French physicist Francis Perrin in 1929 established fluorescence emission occurs after direct relaxation from the excited state to the ground state (Perrin, 1929), a distinct process from phosphorescence occurring after transition through an intermediate state (Perrin, 1929; Siraj et al., 2016; Valeur & Berberan-Santos, 2011).

In 1933, the Perrin-Jabloński or Jabloński diagram named after the Polish physicist Aleksander Jabloński (Jabloński, 1933) regrouped in a simplified and schematic way the different electronic paths of emission and relaxation for an excited molecule. It describes at a molecular and atomistic level the fluorescence path and alternative paths such as non-radiative relaxation like quenching and vibrational relaxation (Figure 1-2).

Upon energy absorption or excitation (black arrows in Figure 1-2), the molecule's electronic state transforms very rapidly from the ground state (S_0) into an excited state (S_n) and at specific vibrational levels (v=n) depending on the absorbed photon energy level. Electronically excited states are intrinsically unstable, to allow a return to the stable S_0 ground state, electrons go through the relaxation process to dissipate the excess energy. This step can follow several paths, either radiative such as fluorescence or non-radiative like for quenching.

Fluorescence (Figure 1-2: green arrows) occurs when radiation is emitted from the first excited singlet state S_1, intrinsically unstable to dissipate the exceeding energy and allow the molecule to return to the ground state (S_0), the sable state observed prior excitation (Albrecht, 2008; Masters, 2008).

In contrast, phosphorescence defines radiation emitted from the triplet state T_1 reached beforehand via intersystem crossing from S_1 (Siraj et al., 2016). As shown in Figure 1-2, there is therefore an extra step compared to fluorescence, this step involves a change in spin multiplicity between triplet (T) and singlet state (S), the two processes are therefore different by the electronic configuration of their excited state (Andrews & Lipson, 2021; Siraj et al., 2016; Valeur, 2011).

Finally, non-radiative relaxation occurs following an $S_1 – S_0$ transition similarly to the one observed for fluorescence, only without light emission. Quenching is also a non-radiative process and occurs from the triplet state T_1 following a necessary first step transition from a single state to a triple state also called the intersystem crossing (Valeur, 2001). See Figure 1-2.

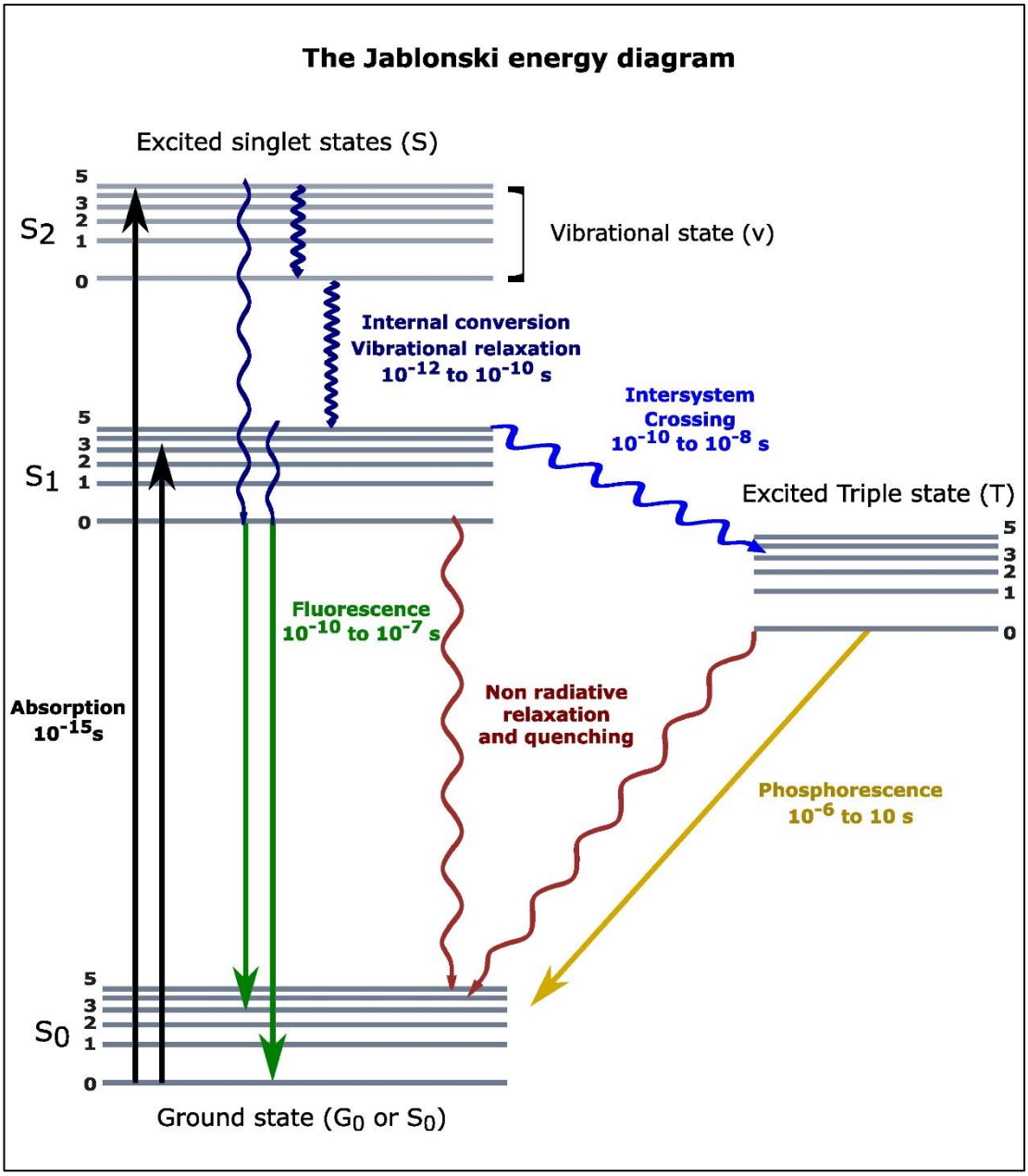

Figure 1-2: The Jabloński diagram

Simplified schematic representation of the electronic states of a molecule and the transitional path available following energy absorption event. Timescales of transition between states are indicated in seconds.

1.1.3. The spectrum of light and Stokes shift

When fluorescence occurs, the energy level of photons absorbed by the fluorophore is of higher energy than the ones emitted as the molecule returns to the ground state S_0. On the visible spectrum of light (Figure 1-3.A), a shift is typically observed between excitation spectra of lower wavelength and emission spectra with a maximum at a higher wavelength (Jennison & Morgan, 1950) (Figure 1-3.B).

The Stokes shift, named after G.G Stokes who first observed it, is a critical notion behind the development of modern fluorescence microscopy. Indeed, techniques were developed to detect and filter signals between the emitted light and the excitation beam establishing fluorescence efficiency (Jennison & Morgan, 1950; Renz, 2013; Rusk, 2009). Fluorescence efficiency measured by the quantum yield Ø representing the ratio between the numbers of emitted and absorbed photons, $\emptyset = \frac{Photon\ emitted}{Photon\ absorbed}$. As the fluorophore's nature defines its absorption profile on the electromagnetic spectrum of light, this value helps also define an optimal pic of excitation to maximise signal emission, away from potential spectral overlap for example.

The relation between wavelength and energy follows Einstein's light quantum theory and the wave-particle duality of light (Einstein & Infeld, 1938). The energy of a photon is directly proportional to the photon's electromagnetic frequency and by extent inversely proportional to the wavelength, also represented by the Stokes-Einstein equation (Einstein, 1905) $E = hf = \frac{hc}{\lambda}$ where E is energy (J), h is Planck's constant, f is frequency (Hz), c is the speed of light and λ is the photon's wavelength (in metres).

Consequently, the flow of photons absorbed is of higher energy therefore of lower wavelength and the ones emitted are of lower energy thus higher wavelength (Figure 1-3.C).

A.

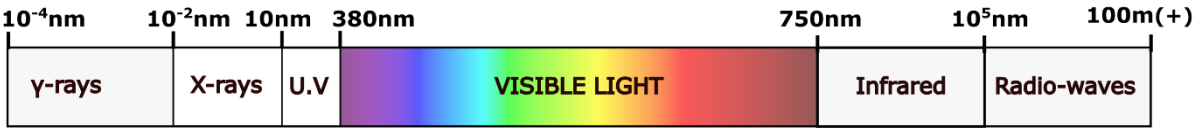

B.

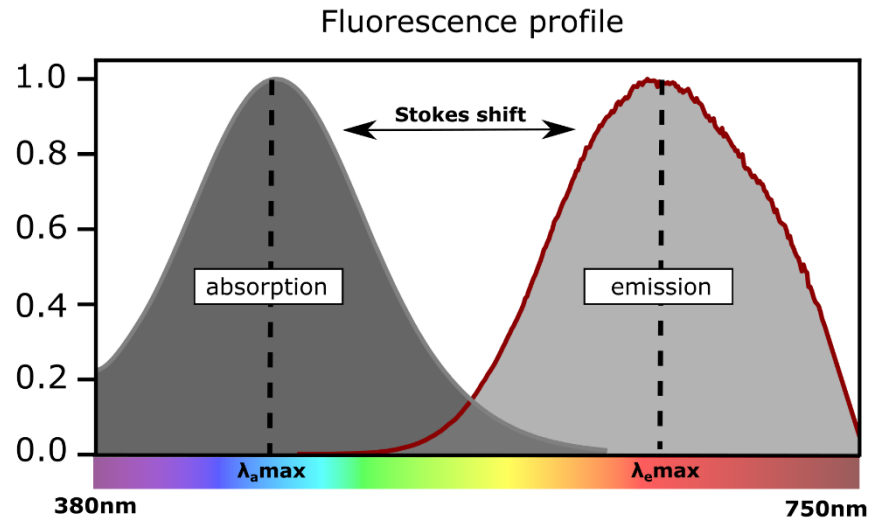

C.

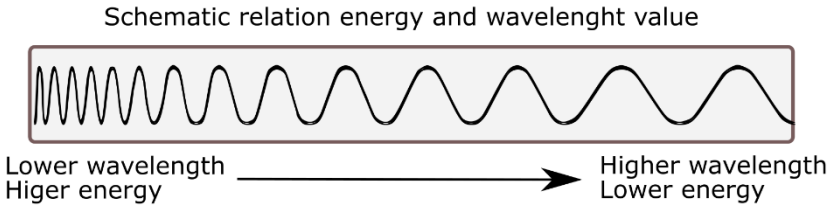

Figure 1-3: The electromagnetic spectrum of light and Stokes shift

A: Schematic representation of the spectrum of light, the visible light is defined between 380 nm and 750 nm, below that range is found UV (10-380 nm), X-rays (<10 nm) and gamma rays (< 10^{-2} nm) and above is infrared up to 10^5 nm and radio-wave (> 10^5 nm).

B: Schematic presenting Stokes shift between spectral excitation and absorption of a fluorescence molecule with typically the maximum of excitation/absorption lambda max of lower wavelength than the emission one. C: Schematic representation of the anti-proportional relation between energy and wavelength. The higher the wavelength, the lower the photon's energy.

1.2. Fluorescence microscopy *in vivo*

1.2.1. Improving image contrast

Cellular systems are challenging to study with regular brightfield microscopy, they appear transparent with very low details on subcellular structures (Thorn, 2016). Most cells display a low refractive index close to the one of water due to their high water content, around 70% of the total mass, the most abundant molecule in a cell (Cooper & Hausman, 2000; Mentré, 2012). This low refractive index can additionally generate scatter interferences with the incident light affecting the level of details and resolution observed in the resulting image (Wollman et al., 2015). Optical contrast improvements were achieved through progress on both microscopic techniques and sample preparations.

Differential interference contrast microscopy (DIC) is an example of such a technological improvement to observe cells by microscopy and is widely used in biology as it provides stronger contrast to define cellular boundaries, even of intracellular features including certain organelles (Frohlich, 2008). For DIC only polarised light illuminates the sample via a two-prism system called the Nomarski prism, through the first prism two beams orthogonally polarized are generated, separated by a sub-wavelength distance also called the shear distance (Wang & Fang, 2012). This configuration generates two brightfield images behind the objective, these intermediates images are shifted back by the second prism and overlayed to generate the final DIC image with a characteristic dark-light emphasis on edges (Wang & Fang, 2012).

Secondly, on sample preparation, fluorescence dyes and biocompatible proteins greatly increase contrast and pushed down to the subcellular level detail for observation of the structure and even molecules. Indeed, biocompatible dyes were found or developed to target specific cellular structures such as DAPI binding specifically the DNA in the nucleus in eukaryotic cells (Kapuscinski, 1995), others bind the membrane (Lichius & Zeilinger, 2019), the vacuole (Vida & Emr, 1995), mitochondria (Wang et al., 2019) and other various living compartments (Wang et al., 2019). Commonly used fluorescent dyes offer the strong advantage to identify structure but protocols for sample preparation required

multiples steps including incubation times or washing steps, increasing the margin for experimental errors; they also need to be carefully chosen for bio-experiment compatibility with particular attention on the lifetime but also cytotoxicity and interference with cellular physiology.

Advances in genetic manipulation (e.g., the CRISPR-Cas9) and the discovery of fluorescent proteins have allowed the development of new technologies applied to biological systems. Cloning techniques allow the expression in cells of fluorescent proteins, fully biocompatible and generally tagged to endogenous proteins to constitute molecular probes, emitting a trackable and quantifiable signal. Indeed, synthetic fluorescent sensors were developed to access more quantitative information with dynamic characterisation for a new range of physical parameters, such as pH (Chen et al., 2020), crowding (Liu et al., 2018; Miyagi et al., 2021), macromolecular co-localisation and interaction (Wang et al., 2012), intracellular glucose level (Otten et al., 2019; Veetil et al., 2010).

The fluorescent protein GFP first extracted from the jellyfish *Aequorea Victoria* is historically the first isolated fluorescent protein (Shimomura, 1979) and is still extensively used. The protein forms a cylinder barrel-like structure composed of eleven β-strands and three amino acids held in its centre (Serine, dehydro-Tyrosine and Glycine) forming the chromophore responsible for its fluorescence. (See Figure 1-4). GFP can emit photons in the green spectrum when excited at around 400 nm (maximum pick of excitation ~488 nm) (Ormö et al., 1996; Shashkova & Leake, 2017). Since its discovery many versions of the protein were developed, to either create new fluorescent colours or to enhance physical properties for better detection (see Table 1-1). For example, the Cherry protein was isolated in the *Discosoma*, a type of Sea anemone and found emitting naturally in the red (Bevis & Glick, 2002), but also NeonGreen derived from a cephalochordate *Branchiostoma lanceolatum* (Shaner et al., 2013) and the synthetic Scarlet (Bindels et al., 2017) with both quantum yields higher than classical fluorophores such as GFP and mCherry (Bindels et al., 2017; Shaner et al., 2013). Monomeric versions of these proteins have also been developed to increase tracking reliability and reduce the small tendency for dimerization of these proteins when in close proximity. In

consequence, enhanced and monomeric versions are preceded by an indicative “e” or “m” in nomenclatures and are progressively becoming the new standard probes used in the field.

However, using fluorescent proteins *in vivo* still represents a challenge mainly due to their weak physical properties. Their photo-physics is generally poor with quick irreversible photobleaching after emission (around 10^6 photons) (Plank et al., 2009). Techniques of illumination and acquisition are critical and so are limiting yet in constant development for improvement to mitigate photo-physical limitations (Plank et al., 2009).

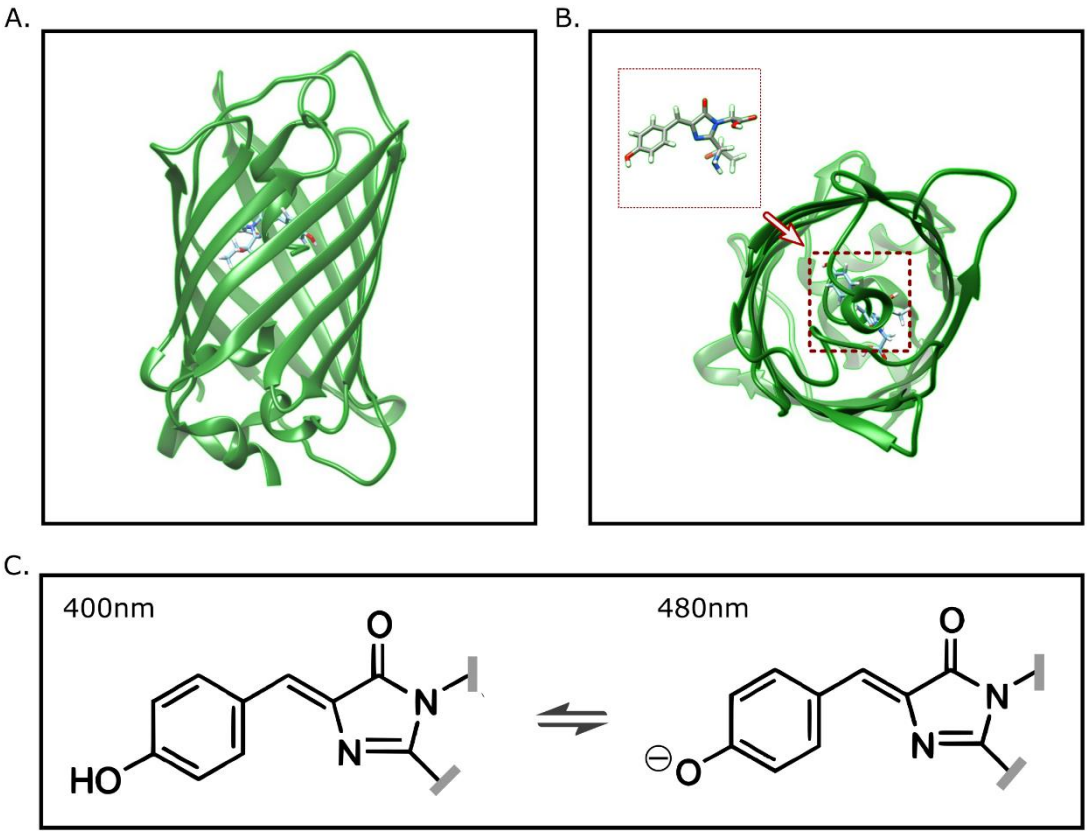

Figure 1-4: 3D structure of a GFP molecule

Three-dimensional structure of GFP fluorescent protein isolated from the jellyfish *Aequorea victoria*. A: typical barrel structure (beta-sheet) with chromophore visible in the middle of the structure. B: Top-down display of the GFP, highlighting the barrel shape of the protein and the presence of the chromophore at its centre (red box). Images were obtained using UCSF Chimera 3D visualisation software (Pettersen et al., 2004) and the X-ray crystallography resolved structure from the pdb data bank PDBcode:

2AWK (Wood et al., 2005). C: Chemical representation of GFP mature chromophore responsible for green fluorescence. This chromophore can exist in two states, neutral absorbing at 400 nm or ionic form (anionic) absorbing at 480 nm (Jung et al., 2005).

Name	Ex λ	Elm λ	QY	MW	Colour	Origin
sfGFP (Pédelacq et al., 2006)	485	510	0.65	26.8	Green	*Aequorea Victoria*
EGFP (Cormack et al., 1996)	488	507	0.6	26.9	Green	*Aequorea Victoria*
mNeonGreen (Shaner et al., 2013)	506	517	0.08	26.6	Green	*B.lanceolatum*
mCherry (Shaner et al., 2004)	587	610	0.22	26.7	Red	*Discosoma sp.*
mScarlet-I (Bindels et al., 2017)	569	593	0.54	26.4	Red	Synthetic construct
EYFP (Ormö et al., 1996)	513	527	0.67	27.0	Yellow	*Aequorea Victoria*
mCitrine (Zacharias et al., 2002)	516	529	0.74	27.1	Yellow	*Aequorea Victoria*
CFP (Heim et al., 1994)	434	477	0.4	26.9	Cyan	*Aequorea Victoria*
mCerulean3 (Markwardt et al., 2011)	433	475	0.87	26.7	Cyan	*Aequorea Victoria*

Table 1-1: Key fluorophores and optical properties

Information extracted from the fluorophores from the online accessible fpbase (fpbase.org): In order, Exλ and Emλ in nanometres, respectively the wavelength for the maximum of excitation and the one for emission. QY is the quantum yield, the ratio between photons emitted and photons absorbed. The molecular weight in kDa for each protein, the emitting fluorescent colour and source (organism of origin).

Newly synthesised polypeptides including fluorophores, go through a maturation process to acquire their functional 3D structure. Typically, GFP maturation time is 13 minutes (25 minutes for EGFP and under 10 minutes for super-folder GFP). As proteins mature, their optical properties, such as the quantum yield, can be altered (Khmelinskii

et al., 2012; Shashkova et al., 2018). The pH of the environment can also alter the optical properties of fluorescent proteins. EGFP and mEGFP have a pKa of 6 and display relatively stable fluorescence in environments with a pH between 6 and 10. However, the fluorescence measured decreases in an environment with a pH below 6 and increases at a pH above 10-12 (Edwards et al., 1981; Patterson et al., 1997). Acidic environments can therefore quench GFP fluorescence. This is due to the protonation of the molecule in a pH condition below its pKa.

Using different GFP variants with different pH, GFP pH-sensitive biosensors have been developed to quantify pH changes and identify alkaline or acidic environments (Han & Burgess, 2010; Kneen et al., 1998; Llopis et al., 1998).

For example, pHluorin derived from the *Aequorea victoria* GFP has become very popular as an enhanced ratiometric pH sensor (Mahon, 2011; Miesenböck et al., 1998). The sensor excitation spectrum is bimodal, with two peaks at 395 and 475 nm. Upon acidification, the excitation peak at 395 nm decreases while the other one at 475 nm increases (Miesenböck et al., 1998). This ratiometric pH-sensitivity facilitates the monitoring of any cellular pathways between compartments with different pH (from neutral to acidic), such as vesicular trafficking (Chen et al., 2012; Opazo et al., 2010) and endocytose pathways (Prosser et al., 2010; Prosser et al., 2016; Sankaranarayanan et al., 2000). More generally, various mutants were developed exploiting fluorophores' pH sensitivity with pKa ranging from 3.8 such as the acid-resistant Gamillus (Shinoda et al., 2018) to higher pKa such as the YFP-H148G/T203Y with a pKa of 8 (Elsliger et al., 1999).

1.2.2. Fluorescence microscopy *in vivo*

Concomitant with the development of fluorescence tools, fluorescence microscopy techniques greatly progressed, and nowadays they offer a range of imaging set-ups designed to observe and measure biological dynamics. This technology was developed in the twentieth century by German physicists Otto Heimstädt and Heinrich Lehmann (Lakowicz, 2006; Schermelleh et al., 2019), and in 1967, dichroic mirrors were introduced to the microscopic set-up, greatly improving the noise ratio contrast. Dichroic mirrors can indeed discriminate between wavelengths of light; a select wavelength will pass through the mirror, while another will be blocked and reflected. Since fluorescence microscopes were built using this same standard design (Sanderson, 2000; Wollman et al., 2015) (see

Figure 1-5). Several illumination modes were developed each offering distinct advantages. (Figure 1-6).

In epifluorescence microscopy (Verdaasdonk et al., 2014a; Webb & Brown, 2012) the light collected is from most of the sample, including the out-of-focus region, with the signal from the whole cell collected (Figure 1-6.A).

In contrast, Total Internal Reflection Fluorescence (TIRF) microscopy (Fish, 2009) illuminates the sample with a small evanescent wave (~ 100 nm in depth) generated by the angle of incidence (critical angle) for total reflection on the microscope coverslip. Generally, only the surface of biological material is illuminated, with the rest of the sample out of the focus region (not excited), reducing signal contamination from the rest of the sample and therefore greatly improving the details observed in the narrow volume at the contact of the coverslip (Figure 1-6.B).

Highly Inclined and Laminated Optical sheet (HILO) microscopy (Tokunaga et al., 2008) occurs when the angle of incidence gives an inclined illumination covering only partially the sample at a sharp angle. The signal-to-noise ratio is slightly lower than observed with TIRF microscopy, still conferring increased image contrast with lower background noise compared to epifluorescence (Figure 1-6.C).

Confocal microscopy (Elliott, 2020; Minsky, 1961) allows precise sectioning of the sample, excluding the out-of-focused region from the light collected. The microscope is equipped with two pinholes, one is positioned right after the light source reducing the illumination to only a small portion of the sample, and a second pinhole is placed just before the detector to only collect in-focus light (Figure 1-6.D). The set-up drastically reduces noise in the image acquired, allowing for in-depth imaging of the sample with multiple sectioning through its volume, allowing for three-dimensional reconstruction for example. This technique is used extensively in cell biology to resolve the cell structure of bacteria (Tran et al., 2014), fungi (Hansen et al., 2000), and mammalian cell lines (Milczarek et al., 2017). It was also reportedly used for clinical and medical purposes where confocal laser scanning microscopy is used as a routine diagnostic (Liu & Xu, 2019), for example, to examine breast tissues and pathological tissues such as carcinomas (Liu et al., 1997).

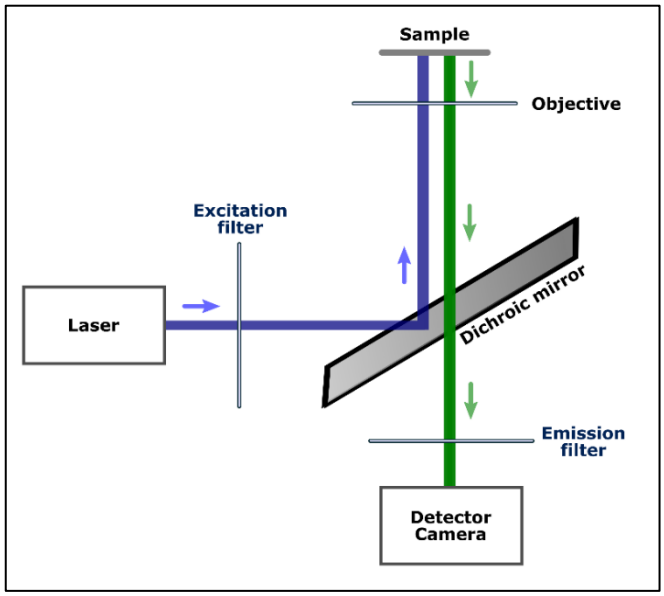

Figure 1-5: Classic wide-field fluorescence microscope

Schematic representing the classic wide-field/epifluorescence microscope configuration: The excitation light, after going through the excitation filter, is reflected by the dichroic mirror, and the light is directed through the objective before reaching the sample. In return, the emitted light is first collected by the objective lens before selectively passing through the dichroic mirror to finally reach the emission filter and the camera behind it for detection.

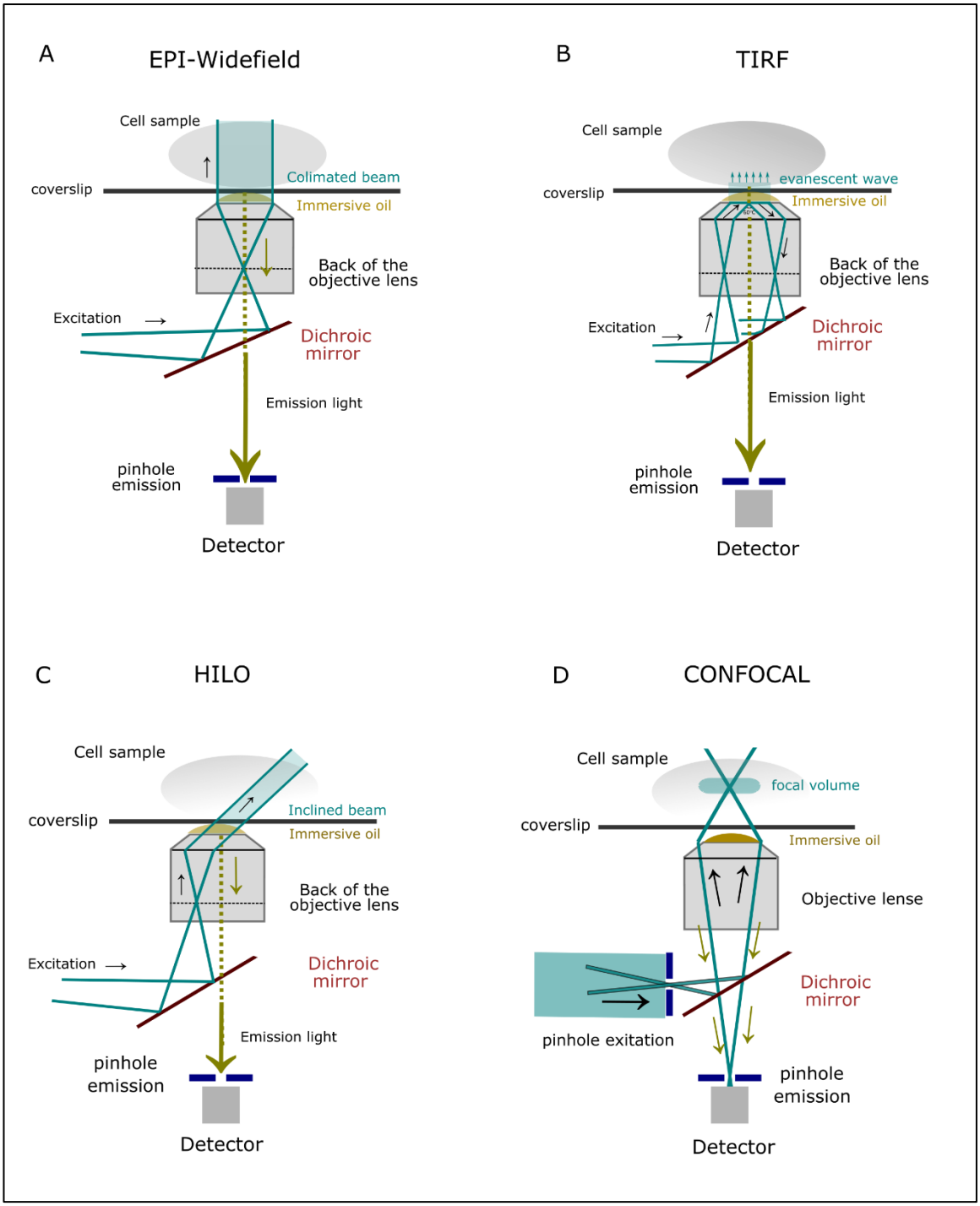

Figure 1-6: Different modes of illumination

Schematic representation for different types of microscopy. A: epifluorescence microscopy (Webb & Brown, 2012), B: Total Internal Reflections Microscopy (TIRF) (Fish, 2009), C: Confocal microscopy (Elliott, 2020; Minsky, 1961) and D: Highly Inclined and Laminated Optical sheet (HILO) microscopy (Tokunaga et al., 2008).

1.2.3. Breaking the diffraction barrier, super-resolution microscopy

As presented above, optical wide-field microscopy offers limited localisation precision. The diffraction limit of light or the Abbe Limit (Abbe, 1873), thresholds the distance resolution down to approximately 150 nm. This is roughly half the wavelength of the visible light. The Abbe limit considers for the NA (Numerical Aperture) the refractive index and was defined for microscopy; however, the diffraction limit was also defined in a wider context by the Rayleigh criterion (Rayleigh, 1879). Under the Rayleigh criterion, the resolution limit is defined by $\Delta x = \frac{0.61\lambda}{NA}$ whilst the abbe limit is defined by $\Delta x = \frac{0.5\lambda}{NA}$ (Δx is the distance between two identified objects (from their respective intensity localisation peak), λ the wavelength for the flow of photons emitted, and NA is the system numerical aperture.

At a subcellular level, biological molecules and fluorescent proteins are only a few nanometres in effective length scale, much smaller than this fixed limit for resolution. In consequence, attempts to image objects distanced below the diffraction limit result in a blurred image with a lost position signal for both molecules (see Figure 1-7.A). In detail, the light wave focused through the microscope objective forms a defined focal spot. The intensity profile of this spot defines the point spread function (PSF), which generally has a similar width to that of the focal spot. As a result, if the distance between two identical emitting objects is less than the PSF width, they will appear as a single object and therefore be unresolvable from each other, resulting in a blurred image (Hell & Wichmann, 1994; Wollman et al., 2015).

Nevertheless, new techniques were recently developed to reach resolutions beyond the diffraction limit. These recent techniques precisely exploit fluorescent probes' physical properties to isolate their signal. Imaging set-up for temporal/sequential excitation of selected fluorophores allows the detection of single molecules at distances beyond those resolved by the diffraction limit (Gustafsson, 2000; Leake, 2013; Schermelleh et al., 2019).

These super-resolution approaches are currently classified under two groups, the first regroup techniques for super-resolution reach via patterned Illumination where the mode of illumination and acquisition help to spatially modulate probes emission and

limit simultaneous emission. The methods help generate a heterogeneous activation of isolated single molecules. This includes techniques such as STimulated Emission Depletion (STED) (Blom & Widengren, 2017), Structural Similarity Index Measure (SSIM) (Heintzmann & Huser, 2017) or Slimfield microscopy (Plank et al., 2009) which specifically relies on the temporal separation of fluorophores in the "ON" state only (Plank et al., 2009; Shepherd & Leake, 2022). The second category involves imaging using photo-activatable fluorophores; the emission pattern is generally stochastic, and it includes photo-switching probes with the ability to enter ON/OFF states (transition to dark-state). Similarly, a sequential detection of single molecules allows an increased spatial localisation for molecules within the diffraction-limited region (Chozinski et al., 2014). This includes techniques such as STORM (Stochastic Optical Reconstruction Microscopy) (Rust et al., 2006a) or PALM microscopy (Photoactivated Localization Microscopy) (Betzig et al., 2006).

All super-resolution techniques follow therefore a core concept, the technique must enable a sequential and stochastic activation of fluorescent single molecules to isolate the signal from single molecules and via reconstruction to generate an image of higher resolution bypassing the diffraction limit. Indeed, images are post-processed, and every single molecule identified with its local precision position is obtained via intensity Gaussian fit before reconstitution of the super-resolution image. See Figure 1-7.B.

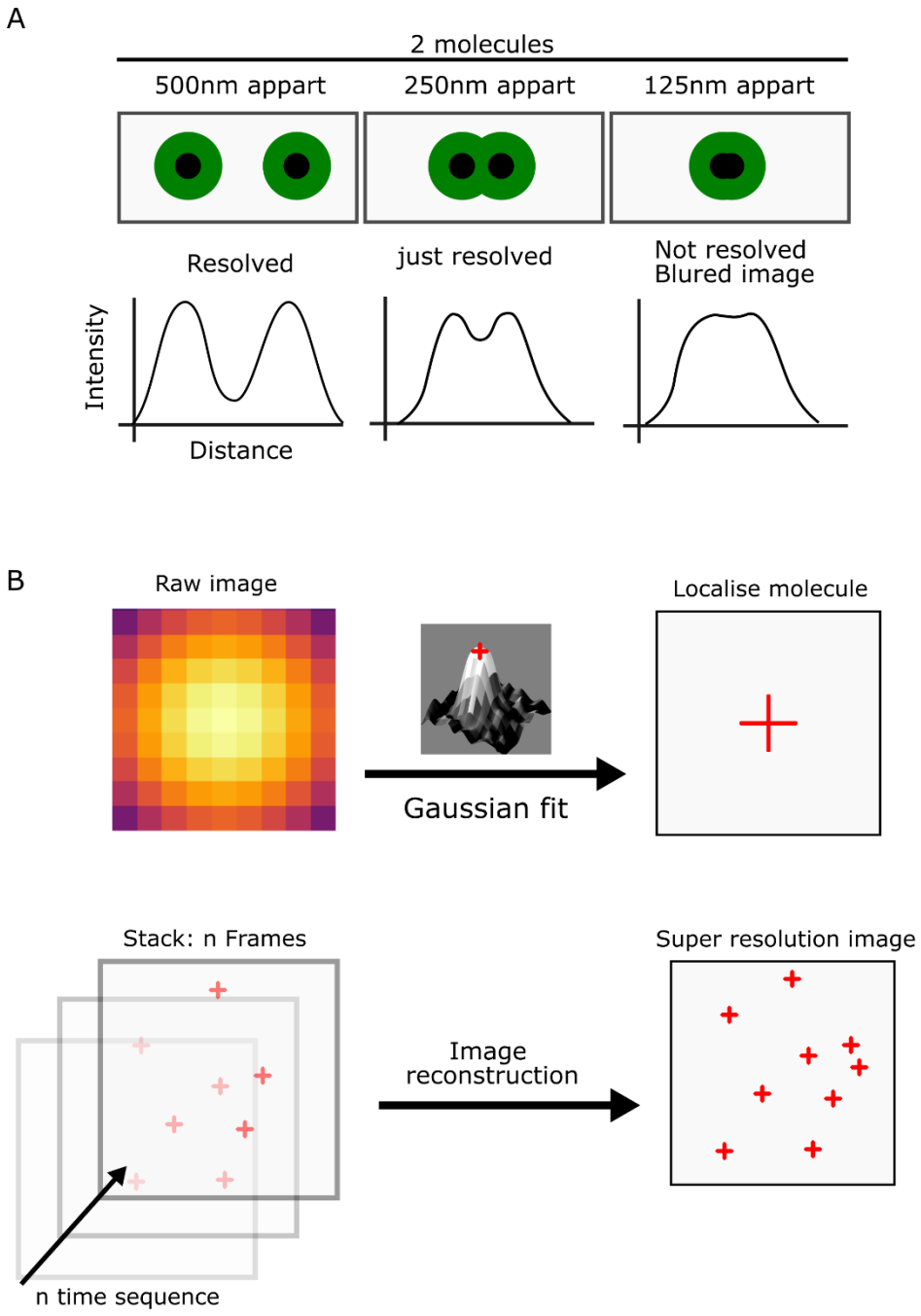

Figure 1-7: Diffraction barrier and single molecule

A: Diffraction limit and spatial resolution between two objects. B: Core principle for single-molecule localisation in super-resolution microscopy, spatial localisation via Gaussian fit and image reconstruction from an acquired stack of sequentially activated fluorophores.

Technique	Short Description	Spatial Resolution
Wide-field (EPI)	The classic fluorescence microscopy, the entire object is exposed to light (Verdaasdonk et al., 2014b).	Diffraction limited ~ 200 nm. Applies also to the other illumination type, TIRF & HILO
Confocal	Confined volume excited, via two pinholes optical set-up (Elliott, 2020; Minsky, 1961).	Diffraction limited ~ 200 nm
STORM	Image reconstructed from stochastic switch bright state to dark state and vice versa of the illuminated pool of spatially distinct fluorophores (usually organic dyes) (Rust et al., 2006b).	~9 nm
PALM	Stochastic activation for a pool of fluorophores with usually photo-switchable and convertible fluorescent proteins followed by localization detection for the reconstruction of the image (Betzig et al., 2006).	20 nm
SLIMFIELD	Optics similar to epi-fluorescence set-up, imaging on a small focal plan with high laser power excitation, allowing to reveal single molecules via stack acquisition for detection and tracking of single molecules (Plank et al., 2009).	20 to 30 nm

Table 1-2: Different types of microscopy

Table detailing a brief description of key microscopy techniques.

2. Cellular stress in eukaryotes

2.1. Adaptation to cellular stress and homeostasis

2.1.1. Highly conserved stress responses

Cellular stress responses define the set of defence mechanisms to maintain cell integrity facing environmental or intracellular stress stimuli. These processes are essential for survival and therefore highly conserved throughout evolution (Fulda et al., 2010). Various types of stresses exist and accordingly, various stress responses can be triggered, depending on the nature (e.g., temperature, nutrient availability, mechanical stress), the intensity or the exposure of the stress endured (Fulda et al., 2010). Thermal stress, or heat shock, specifically destabilises protein folding activities and protein structures. In general, the cell reacts by producing heat shock proteins promoting protein folding, such as the HSP70 (Park et al., 2007; Vabulas et al., 2010). Another example is the photolyase, produced in response to DNA damage resulting from UV light exposure, this enzyme can recognise and repair UV light-specific DNA damages such as cyclobutane pyrimidine dimers compromising DNA and RNA polymerases activities (Cadet et al., 2005; Jackson & Bartek, 2009). The enzyme, conserved, has orthologues found in bacteria (Aravind et al., 1999), fungi (Suter et al., 2000), and complex eukaryotes such as plants (Singh et al., 2020) and mammalian cells (Vechtomova et al., 2021). Moreover, defence mechanisms counter-balance the harmful effects of stress and trigger various metabolic changes, generally for cell size (Kiehl et al., 2011), shape (Nestor-Bergmann et al., 2019) and related intracytoplasmic organisation including protein and organelle localisation (Marini et al., 2020). These morphological changes can influence molecular interactions, diffusion, gene expression, affecting the whole physiology and metabolism of cells.

2.1.2. Cellular fate, monitoring homeostasis.

Cellular survival is characterised by cellular growth powered by cell division. During a stress event, energetic resources are directed to palliated stress detrimental effects at the expense of cell division and growth until full recovery. If recovery metabolic strategies cannot reach a new metabolic equilibrium or homeostasis and assure a return to cellular growth activities, then generally cell death programs are activated (e.g., apoptosis or necrosis) (Spear & Ng, 2003). Cellular survival is therefore dependent on homeostasis and the establishment of viable conditions for cell division. Monitoring homeostasis is therefore key to the cell fate and growth/death "decision-making" following a stress event. See Figure 1-8.

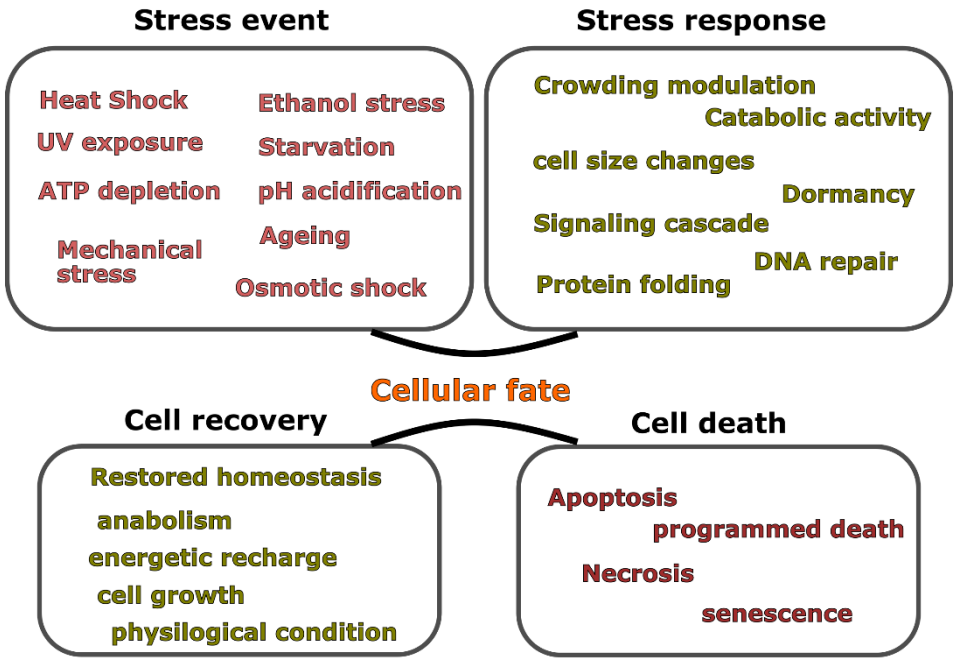

Figure 1-8: Cellular stress and cellular fate

Schematic representing various metabolic activities related to cellular stress and cellular fate consequences.

Cellular homeostasis is a complex metabolic state, dynamic and multi-factor regulated (Asarian et al., 2012). This equilibrium is dynamic and influenced by environmental changes, but also internal changes associated with key metabolic activity (e.g., growth or ageing). Interestingly ageing can be approached as a source of cellular

stress, indeed, as the cell ages metabolic by-products accumulate, which are often cytotoxic if not eliminated. Such as the accumulation of reactive oxygen species (ROS) (Liochev, 2013; Perrone et al., 2008) or of extrachromosomal rDNA circles (ERCs) (Lumpkin et al., 1985; Sinclair & Guarente, 1997).

Stress episodes induce a drastic shift from this ideal equilibrium, and recovery relies on feedback loops to buffer the effect and restore the state of balance. Classically a stimulus gets sensed by molecular captors or sensors inducing a specific response via subsequent signalling cascades. The HOG (High Osmolarity Glycerol) pathway for adaptation to hyperosmotic shock is for example a MAP-kinase (Mitogen-activated protein kinases) signalling system initiated by sensors localised at the plasma membrane (Hohmann, 2009; Mager & Siderius, 2002).

Homeostasis includes temperature control and glucose regulation critical for survival across living cells and organisms. pH is another important parameter strongly regulated to assure protein enzymatic activities in the cytoplasm or organelles (Takahashi & Schachtele, 1990), proteins interactions (Dumetz et al., 2008) and even structures (O'Brien et al., 2012). Precise control of the level of protons relies on the coordination between primary proton pumps at the plasma membrane and various endoplasmic proton exchangers, furthermore, metabolites in the cells also contribute and act as a buffer to maintain intracellular pH stability (Orij et al., 2012; Pittman, 2012) (Figure 1-9).

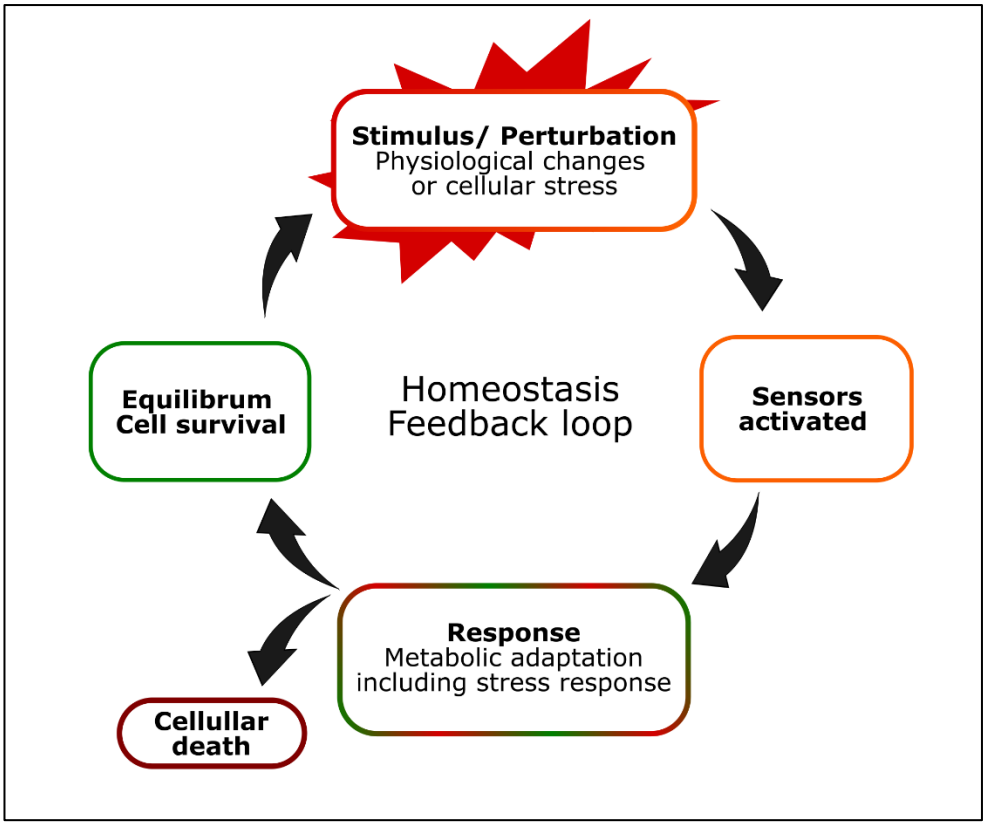

Figure 1-9: Homeostasis feedback loop

Simplified schematic showing the feedback loop principle, applied to monitor and maintain cellular homeostasis.

2.2. Macromolecular crowding

2.2.1. Crowding definition

The section defining molecular crowding was extracted and adapted from published work:

Lecinski, S., Shepherd, J. W., Frame, L., Hayton, I., MacDonald, C., & Leake, M. C. (2021). Investigating molecular crowding during cell division and hyperosmotic stress in budding yeast with FRET. In Current Topics in Membranes (Vol. 88, pp. 75–118). Academic Press.

The term “molecular crowding” describes the range of molecular confinement-induced effects (e.g., mobility, soft attractions, and repulsion forces) observed in a closed system

of concentrated molecules. Cells are highly crowded membrane-bound environments containing a range of biomolecular species including proteins, polysaccharides and nucleic acids. Typically, these molecules occupy a huge volume of the cell (up to 40%), equivalent to a concentration of up to 400 mg/ml (Fulton, 1982; Zimmerman & Trach, 1991). Two terms can be encountered in the literature: "macromolecular crowding" referring to the dynamic effects of volume exclusion encountered between two molecules and "macromolecular confinement" referring to the same effect caused by the static shape and size of the system (Sanfelice et al., 2013; Zhang et al., 2019; Zhou et al., 2008). Both describe a typical free-space limitation occurring in a highly concentrated environment of molecules which leads to non-specific interactions between macromolecules in close proximity (Sarkar et al., 2013). Excluded volume theory is a key concept to understanding macromolecular crowding and what macromolecular crowding can do to proteins (Garner & Burg, 1994; Kuznetsova et al., 2014). By their presence, molecules exclude access to the solvent/surface of other molecules. This imposed volume restriction where exclusion is dependent on the molecule's size and shape (Figure 1-10). As a result, if each molecule excludes a certain volume from every other, and the mobility of each is also reduced – a molecule can only diffuse into an available volume, which effectively slows the time scale of the overall diffusive process. Note also that the overall effect of the multiple biomolecular species *in vivo* is referred to exclusively as crowding with the term "concentration" used generally for individual protein species, which may be at a low concentration in an overall high crowding environment or *vice versa* (Ellis, 2007; Minton, 2006). Interestingly, in theory, the excluded volume of two monomers do not overlap, but if molecules can biochemically interact to form a stable new entity, this new molecule will now have its own excluded volume changing the solvent availability for other proteins (André & Spruijt, 2020; Minton, 2001; Poland, 1992) - see Figure 1-10). These dynamic effects have raised new interest in the context of protein aggregation (Jing et al., 2020), intracellular organisation (Löwe et al., 2020), and membrane-less compartments in the cytoplasm, for example, the formation of liquid-liquid phase separation in the cytoplasm (Franzmann et al., 2018; Jin et al., 2021; Park et al., 2020).

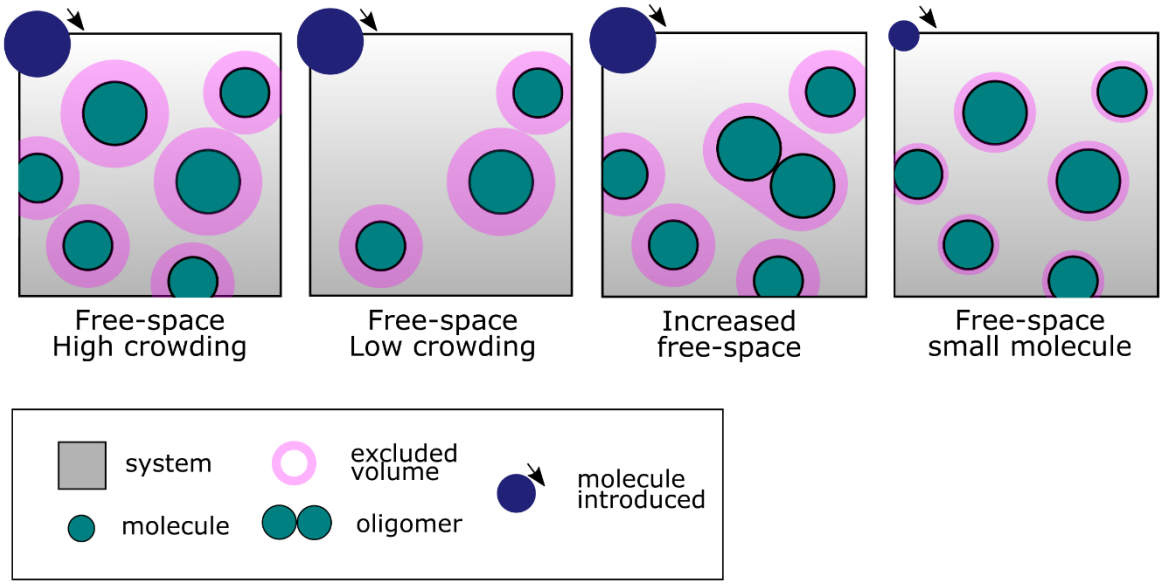

Figure 1-10: Excluded volume effect

"Illustration of the concept of excluded volume, solvent availability, and molecular crowding for molecules in a confined environment. In pink the excluded volume for each molecule in the system, therefore, limiting mobility and solvent accessibility for the molecules introduced (dark blue molecules on top). The third panel shows how protein oligomerization may modify solvent availability for another molecule and the last panel shows the different excluded volume observed in the system for a molecule introduced of a smaller size, excluded volume is dependent on its shape and size." (Lecinski et al., 2021).

2.2.2. The influence of macromolecular crowding on proteins

Macromolecular crowding can influence the diffusion of molecules and proteins. The diffusion of a molecule is dependent on the molecule's intrinsic parameters, such as its size (Sharp, 2015), and the hydrodynamic radius of the particle (Skóra et al., 2021), but also on parameters related to its surrounding environment, like the temperature (Sidell & Hazel, 1987) and viscosity (Luby-Phelps, 2013). This is described in the Stoke-Einstein equation (Einstein, 1905), $D = \frac{K_b T}{6\pi\eta r}$ where, k_B is the Boltzmann constant, T is the temperature, η is the dynamic viscosity and r is the radius of the particle. By influencing

these factors macromolecular crowding directly affects the mobility of molecules (Dix & Verkman, 2008). These effects have a direct impact on the thermodynamic and kinetic aspects of molecular processes and biochemical reactions occurring in the cell (Hu et al., 2007; Zhou, 2013; Zimmerman & Trach, 1991).

Notably, crowding has been shown to promote oligomerization (Zhou, 2013) and aggregation, with the formation of insoluble structures. It also influences protein folding (Jing et al., 2020; Phillip & Schreiber, 2013) and the kinetics of physical protein-protein and protein-nuclei interactions (Nguemaha et al., 2019; Phillip & Schreiber, 2013; Stagg et al., 2007). Macromolecular crowding plays a role in diverse biological processes including protein conformational changes (Dong et al., 2010), signalling cascades (Rohwer et al., 1998) and intracellular transport (Nettesheim et al., 2020). Recent NMR (Nuclear Magnetic Resonance) studies have for example highlighted the bovine serum albumin as a crowder can form weak interactions with the histidine carrier (HPr) protein at their binding site decreases the EIN(phosphotransferase Enzyme I)-HPr complex binding affinity and/or accelerating its dissociation (Dong et al., 2022).

In vitro and *in silico* studies brought further insight into atomic scale dynamics regarding interaction and forces at play between crowders and molecules. Studies using ficoll as an inert crowder have established size dependency: as crowding increases in the environment, small and large molecules diffusion decreases (Sharp, 2015) however smaller crowders generally tend to increase protein stability (Sharp, 2015; Zhou, 2013). The pool of molecules accumulated in the intracellular environment has a variety of shapes and sizes and chemical properties resulting in attractive and repulsive forces between molecules. *In vivo,* crowders are therefore more complex entities with intrinsic properties which may affect surrounded molecules (Fiorini et al., 2015; Rivas & Minton, 2016). The composition of the cytoplasm, the nature of crowders and the nature of proteins all play a role in the crowding effect observed, impacting macromolecules behaviour and rearrangement (Rivas et al., 2004).

These include weak intersections (nonspecific chemical interactions and steric repulsion), which are therefore also involved in the crowding dynamic and contribute to the decrease of diffusion typically observe in a crowded environment (König et al., 2021; Rivas & Minton, 2016). These features have been described as a characteristic

consequence of crowding (Garner & Burg, 1994). Soft interactions are induced by the chemical properties of the molecule and affect the enthalpy and the entropy with non-covalent interactions (Černý & Hobza, 2007), including electrostatic forces or inter-molecule hydrogen bonds and weak interactions such as van der Waals and hydrophobic interactions (Černý & Hobza, 2007; Cheung & Thirumalai, 2007; Takahashi, 1997).

These interactions can either promote or counteract the effect of excluded volume (Miklos et al., 2010; Rusinga & Weis, 2017; Sarkar et al., 2013). There are therefore two major components of crowding, first the occurrence of hard interactions or excluded volume effects and second the chemical effects or soft/weak interactions (Sarkar et al., 2013).

2.2.3. Osmotic stress and crowding

Section adapted from published work:

Lecinski, S., Shepherd, J. W., Frame, L., Hayton, I., MacDonald, C., & Leake, M. C. (2021). Investigating molecular crowding during cell division and hyperosmotic stress in budding yeast with FRET. In Current Topics in Membranes (Vol. 88, pp. 75–118). Academic Press.

Upon osmotic stress, when cells are exposed to a high ionic strength environment, the cell volume suddenly reduces because of the osmotic pressure generated, which triggers a diffusion-driven water exchange from the cell cytosol to the external environment. This drastic volume reduction spatially confines the pool of macromolecules inside the cells and directly increases molecular crowding. In response, cells activate biochemical pathways such as that involving the protein Hog1 to produce a gain in volume via internal pressure generation (Tamás et al., 2000). This occurs notably via the production of glycerol (Hohmann, 2002) and the regulation of transporters at the plasma membrane such as aquaporins to control the glycerol/water ratio (Hohmann, 2015a; Saito & Posas, 2012). In eukaryotic cells, osmostress and osmoregulation have been extensively studied using yeast as a model (Babazadeh et al., 2017; Gibson et al., 2007; Hsu et al., 2015; Özcan & Johnston, 1999) a unicellular organism particularly susceptible to osmotic shock (Figure 1-11). Physical changes and responses induced by osmotic stress are,

therefore, directly connected to crowding dynamics and are key to maintain cell integrity.

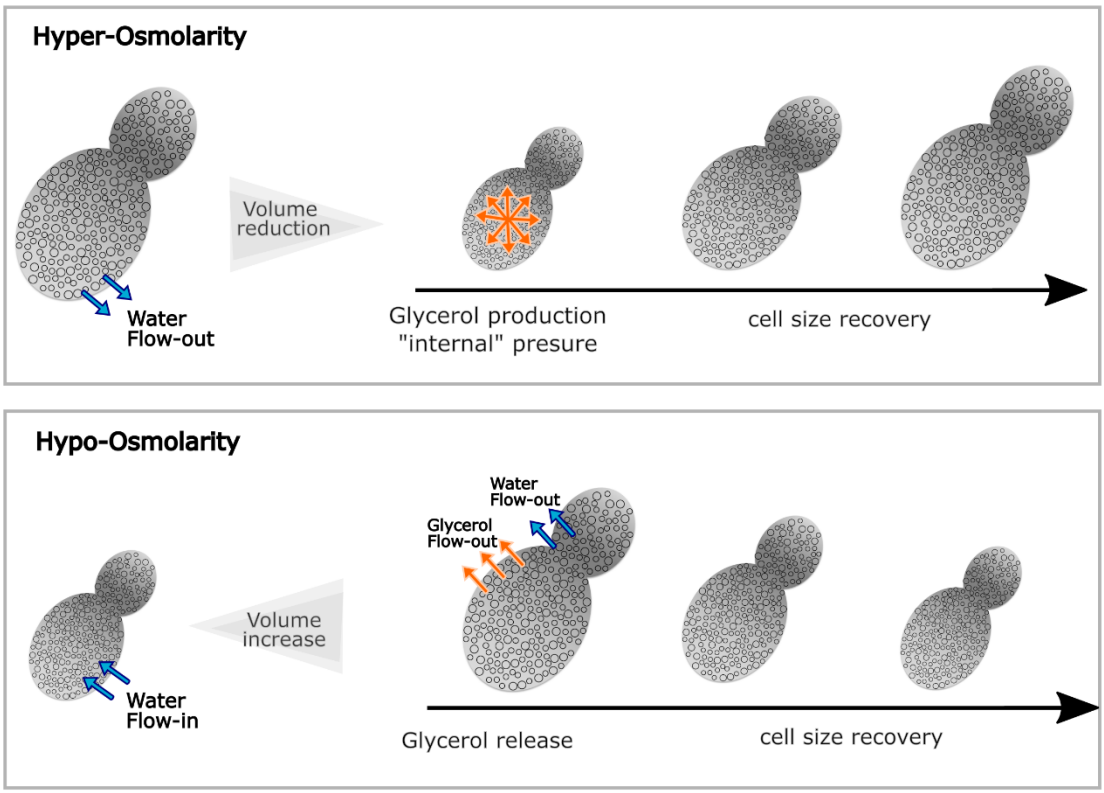

Figure 1-11: Osmotic shock in yeast

“Schematic osmotic shock response in yeast. Under hyperosmotic stress, cell size drastically reduces as water flows out of the cells, resulting in an increased crowding effect in the cytoplasm and the activating osmoregulation Hog1 pathways, the subsequent production of glycerol in the cytoplasm pressure back the cell to recover its initial size. On the contrary during hypo-tonic osmotic stress water flows in and the cell volume increases, less glycerol is produced and transporters such as aquaporin are upregulated to allow water to flow in and help the cell recover its original size.” (Lecinski et al., 2021).

2.3. *Saccharomyces cerevisiae* for cellular stress and ageing research

2.3.1. Budding yeast as a eukaryotic cellular model

Saccharomyces cerevisiae yeast is a unicellular eukaryote organism from the fungi family subgroup (Parapouli et al., 2020). Eukaryotes are defined by their distinct intracellular compartmentalisation (Vellai & Vida, 1999) (Figure 1-12). Inside the cell, different structures called organelles exist and support distinct cellular functions. Among others, the nucleus holds the genetic information (Hancock, 2014), the endoplasmic reticulum (ER) ensures the biosynthesis of molecules (Ghaemmaghami et al., 2003), the Golgi apparatus orchestrates post-transcriptional modifications of proteins, the vacuole drives protein degradation (Thumm, 2000), and the mitochondria is required for energy production via oxidative phosphorylation (Friedman & Nunnari, 2014).

This intracellular organisation is shared across the eukaryotic kingdom (animals, plants and fungi) with many metabolic pathways conserved across these organisms (Dahiya et al., 2020). This includes essential mechanisms such as DNA replication, and recombination, but also transcription, translation and trafficking, even mitochondrial respiration, and lipid metabolism (Dahiya et al., 2020; Nielsen, 2013; Petranovic et al., 2010). As mentioned in the sections above stress responses are also strongly associated with conserved and essential cellular metabolic functions (López-Otín et al., 2013; Petranovic et al., 2010).

Yeast is a eukaryotic organism with a simple organisation compared to eukaryotic mammalian cells such as human cells. Yeast is indeed a unicellular organism, one cell is the whole organism, in contrast to humans when the organism is composed of billions of cells, organized in organs assuring critical functions and involving additional metabolic cooperation between cells (Asarian et al., 2012).

All these criteria make *S. cerevisiae* an excellent candidate to understand dynamics in eukaryotic cells (Perocchi et al., 2008; Zimmermann et al., 2018). And is indeed commonly employed for biological and biomedical research. This model exhibits various other advantages, their small size (diameter *ca.* 5 to 8 µm) and fast cell doubling time (~ 90 min) makes them ideal to study ageing or cellular stress processes, in comparison,

mammalian doubling time is around 24h (Zámborszky et al., 2007). The yeast genome has been extensively studied, it is the first organism whose genome was entirely sequenced (Goffeau et al., 1996), an historical context that has favours diverse scientific investigations using yeast cells and genetic manipulations for insight into its cellular biochemistry and fundamental bio-mechanism (Dujon, 1996; Engel et al., 2014).

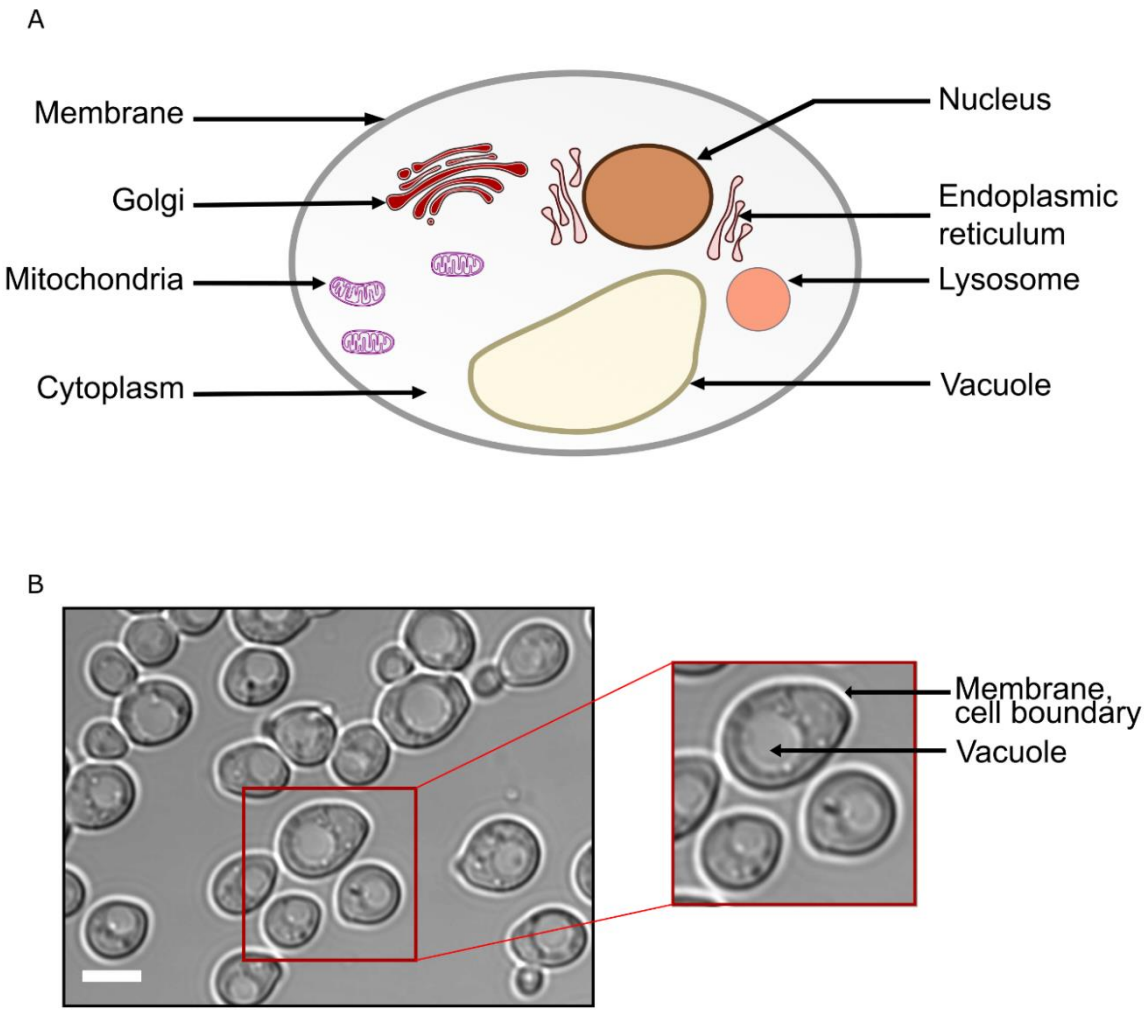

Figure 1-12: Unicellular eukaryote *S. cerevisiae* yeast cells

A: Schematic representation of a yeast cell, cellular compartments present in the cytoplasm, and the fluid/ semi-liquid material enclosed by the plasma membrane.

B: Brightfield image showing budding yeast and identifiable structure (5 µm scale bar).

Although yeast cells are a great model to study conserved fundamental metabolic mechanisms in eukaryotes in the context of biomedical research, the model has several

limitations (Duina et al., 2014; Dujon, 1996; Gershon & Gershon, 2000). Yeast cells are independent unicellular organisms and therefore cannot capture the complexity of multicellular and inter-tissue interactions found in mammalian cells. Tissue differentiation and tissue-specific regulation is often a key element to understanding human disorders at the cellular level. As yeasts lack this level of cellular organisation, aspects of their physiology do not necessarily translate to mammalian cells (Mohammadi et al., 2015). Yeast cells are classified in the kingdom of fungi (Gilliland, 1971), as such, they possess an organelle specific to fungi, the vacuole (Thumm, 2000). The vacuole performs catalytic functions and ensures correct cellular pH, (Eskes et al., 2018) and osmotic and ion homeostasis (Li & Kane, 2009; Veses et al., 2008). The presence of the vacuole in yeast was also described as a storage compartment of ions for the cell such as zinc (Devirgiliis et al., 2004; Li & Kane, 2009; Simm et al., 2007). Additionally, the vacuole is involved in various vesicle-mediated protein transport pathways including endocytic traffic to and from the plasma membrane (Bryant & Stevens, 1998; Jones et al., 1997) or ubiquitinated cargo directed to the vacuole in yeast for degradation (MacDonald et al., 2012; Shields & Piper, 2011). The lysosome fulfils the catalytic role in mammalian cells, and although different, some studies have labelled the vacuole as the “yeast-lysosome” (Li & Kane, 2009; Mechler et al., 1988; Zhang et al., 2021).

Yeast cells also possess a cell wall, an extracellular component surrounding the plasma membrane and composed mainly of glucans, chitin, and glycoproteins (Garcia-Rubio et al., 2020; Northcote & Horne, 1952; Smits et al., 1999). Cell walls are typical of fungi and plant cells, but are not present in human cells (Bowman & Free, 2006). It contributes to the cell shape and integrity of the organism during growth and cell division (Bowman & Free, 2006; Lesage & Bussey, 2006). The size and shape of cells are different between human and yeast cells, which will influence molecular crowding and the spatio-temporal distribution of sub-cellular components. Yeast cells hold therefore very distinct physiology, including metabolic response to cellular stress not shared with human cells (Ohtsuka et al., 2022; Piekarska et al., 2010). These are key examples of how yeast cells differ from other eukaryotic cells, and such differences should always be considered when interpreting data or making an analogy from one cellular model to another.

2.3.2. Cell polarity, asymmetrical cell division

Section adapted from (Lecinski et al., 2021).

Lecinski, S., Shepherd, J. W., Frame, L., Hayton, I., MacDonald, C., & Leake, M. C. (2021). Investigating molecular crowding during cell division and hyperosmotic stress in budding yeast with FRET. In Current Topics in Membranes (Vol. 88, pp. 75–118). Academic Press.

In *Saccharomyces cerevisiae* cells (also called budding yeast), mitosis and cytokinesis take place via a budding process, where a bud emerges and grows from the mother cell (Chen et al., 2011; Juanes & Piatti, 2016). This process requires the establishment of a cell polarity between the mother cell and daughter cell (Bi & Park, 2012) and therefore close regulation of the cytoplasmic content and spatial organisation (Nasmyth, 1996), including changes in membrane morphology. Cell division is therefore a highly asymmetrical process (Higuchi-Sanabria et al., 2014) associated with a range of biochemical processes involving protein-protein interactions (Chen et al., 2011) and significant materials and compartments transport (Champion et al., 2017; Yeong, 2005). All these processes rely on biomolecular rearrangements and volume changes, and as such may impact local macromolecular crowding conditions. The budding process in *S. cerevisiae* is specifically characterised by the formation of a septin ring on the cell membrane early in the replication cycle (Byers & Goetsch, 1976; Chen et al., 2011). This septin ring acts as a junction between the mother cell and the daughter cell (Vrabioiu & Mitchison, 2006) and defines the mother cell/daughter cell polarity (Juanes & Piatti, 2016) (Figure 1-13). During this process, the role of the plasma-associated GTPase protein Cdc42 is key to initiating the polarization process (Okada et al., 2013) and triggering the recruitment of proteins to form the septin ring at the interface between mother and daughter cell in a region generally known as the bud neck (Faty et al., 2002; McMurray et al., 2011). Several septins are recruited to make this hetero-oligomeric structure, with key proteins Shs1, Cdc3, Cdc10, Cdc11, and Cdc12 forming a characteristic double-ring shape (McMurray et al., 2011; Vrabioiu & Mitchison, 2006). Meanwhile, the cytoskeleton network is restructured such that it is polarized along the axis of the bud neck between the mother and daughter cell (Moseley & Goode, 2006),

to facilitate the active transport of complexes and organelles (Juanes & Piatti, 2016; Warren & Wickner, 1996) to the daughter cell, mainly accomplished by myosin transport along actin cables (Knoblach & Rachubinski, 2015; Macara & Mili, 2008). These changes yet related to the controlled and functional polarity leading to the formation of daughters at local points on the cell surfaces (Chiou et al., 2017). The newly formed cell is also generally of smaller size than the mother however as the cell ages this asymmetry tends to fade and aged cells reaching the limit of replicative life span produce daughter cells of higher volume (Sinclair et al., 1998; Sinclair & Guarente, 1997). Furthermore, as the cell divides new cells will generally emerge in proximity to the previous bud scar (Chant & Pringle, 1995; Mortimer & Johnston, 1959).

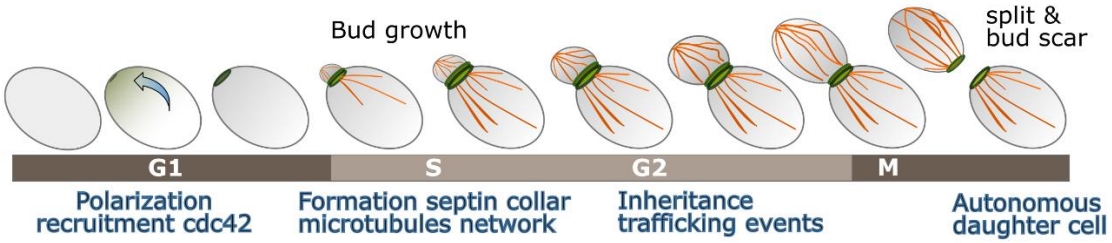

Figure 1-13: Asymmetric cell division

Simple representation of a single yeast cell dividing, polarization to form the bud neck and the septin rings (green) and cytoskeleton polarised through the bud neck in (orange).

2.3.3. Cell polarity and molecular marker of stress

Age or stress-damaged molecules such as extrachromosomal rDNA circles (Lumpkin et al., 1985; Sinclair & Guarente, 1997) and damaged proteins (Chiti & Dobson, 2017) are retained inside the mother cell volume (Figure 1-14) (Higuchi-Sanabria et al., 2014; López-Otín et al., 2013; Zhou et al., 2014). The bud-neck region has been described as a "diffusion barrier" influencing trafficking events and the relative cytosolic volume between the mother cell and daughter cell (Clay, Caudron, Denoth-Lippuner, Boettcher, Frei, et al., 2014; Gladfelter et al., 2001; Shcheprova et al., 2008; Sugiyama & Tanaka, 2019; Valdez-Taubas & Pelham, 2003). Although given the active super-diffusive transport which dominates trafficking, the existence of a meaningful physical diffusion barrier is still an open debate (Nyström & Liu, 2014; Zhou et al., 2011). The influence of macromolecular crowding at the highly localised region between the mother and daughter cell interface remains unknown as well.

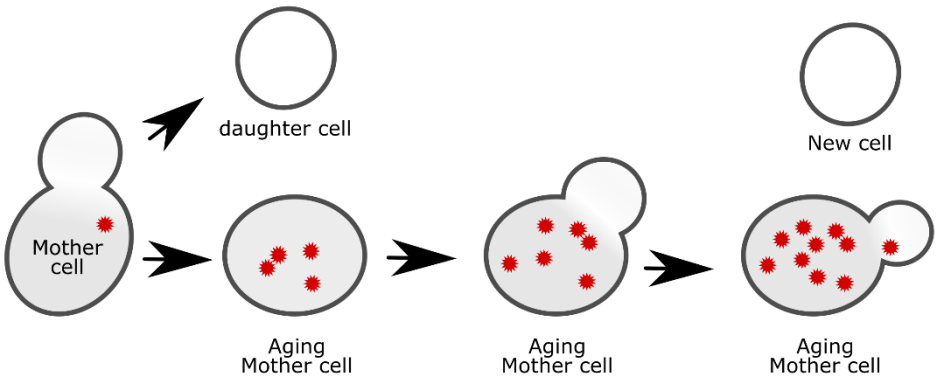

Figure 1-14: Aggregates inheritance and intracellular localisation

Schematic representing yeast cell ageing and reported segregation of proteo-toxics in the mother cell during cell division.

Secondly, the existence of aggregate local deposits was reported mainly centralised in the proximity of key organelles, such as IPOD (Insoluble-Protein-Deposit) reported close to the vacuole in yeast cells or JUNQ deposits (Juxta Nuclear Quality control), adjacent to the nucleus (Burri & Lithgow, 2004; Spokoini et al., 2012). The formation of such

aggresomes as a compact body was reported as a factor-dependent process, requiring for example calmodulin, the cytoskeleton actin cables but also protein such as the heat shock protein Hsp104 (Song et al., 2014).

The spatial dynamics of proteotoxics in the cell are more likely influenced by multiple factors, involving directed metabolic active signalling cellular response, also dependant on cell homeostasis regulation, phase of the cell cycle, environmental stress experienced and any physiological changes influencing key physical parameters, such as macromolecular crowding.

These mechanics might similarly influence the localisation of molecules, and crowders in the cells. In eukaryotic cells, the occurrence of trafficking events and the execution of metabolic pathways requires the recruitment of various macromolecules at local sites in the cell. These events generally set in motion a complete restructuration of the intracellular environment, from its content to the spatial localisation of compartments and molecules. The composition of the cells is therefore not homogenous across its volume which is suspected to generate local crowding differences such as a gradient of crowders in the cell.

Quantifying crowding dynamics or other physicochemical properties in living cells is however challenging, but recent improvements in optical microscope technology and the development of synthetic fluorescent protein sensors have enabled whole-cell measurements of crowding during ageing and under osmotic stress (Mouton et al., 2020). In essence, these sensors consist of a (Förster resonance energy transfer) FRET-pair of fluorescent proteins on an alpha-helical “spring” (Boersma et al., 2015). In crowded conditions, the proteins are pushed closer together, generating a distinct signal from less crowded conditions. By imaging with dual-colour fluorescence microscopy, the FRET efficiency can be quantified and used as a signature for molecular crowding (Liu et al., 2017; Mouton et al., 2020) - see the next section below for FRET general principle description.

2.3.4. FRET fluorescence for molecular bio-sensing

Förster resonance energy transfer or FRET technique (Förster, 1948) lies in the capability two molecules have to exchange energy from one molecule, the donor to the other, the acceptor. For FRET to occur, two specific conditions are required. The emission spectrum of the donor molecule needs to overlap with the absorption spectra of the acceptor. Then, the physical distance (r) between the two probes is critical, they both need to be in close proximity generally in a range between 1 to 10 nm (Figure 1-15). The FRET efficiency ($Efret$) can be related to the donor-acceptor distance.

$$Efret = \frac{1}{1 + \left(\frac{r}{Ro}\right)^6} = \frac{Ro^6}{Ro^6 + r^6}$$

The FRET signal is therefore linked to the nanometre scale distance information. Where R_0 is the Förster distance, the distance at which energy transfer is efficient at 50% (Figure 1-15).

The FRET signal is therefore an indirect read out of the distance between two capable molecules, a quantifiable read out. Therefore numerous sensors were designed to typically oscillate between strictly an “open” conformation (FRET negative) or “closed” conformation (FRET positive) useful to confirm protein-protein interaction (Margineanu et al., 2016). Dynamic FRET sensors were developed with the ability to oscillate between a range of distances and are more generally used for relative comparison of behaviour between conditions, such as the CrGE crowding sensor used in this study (Boersma et al., 2015).

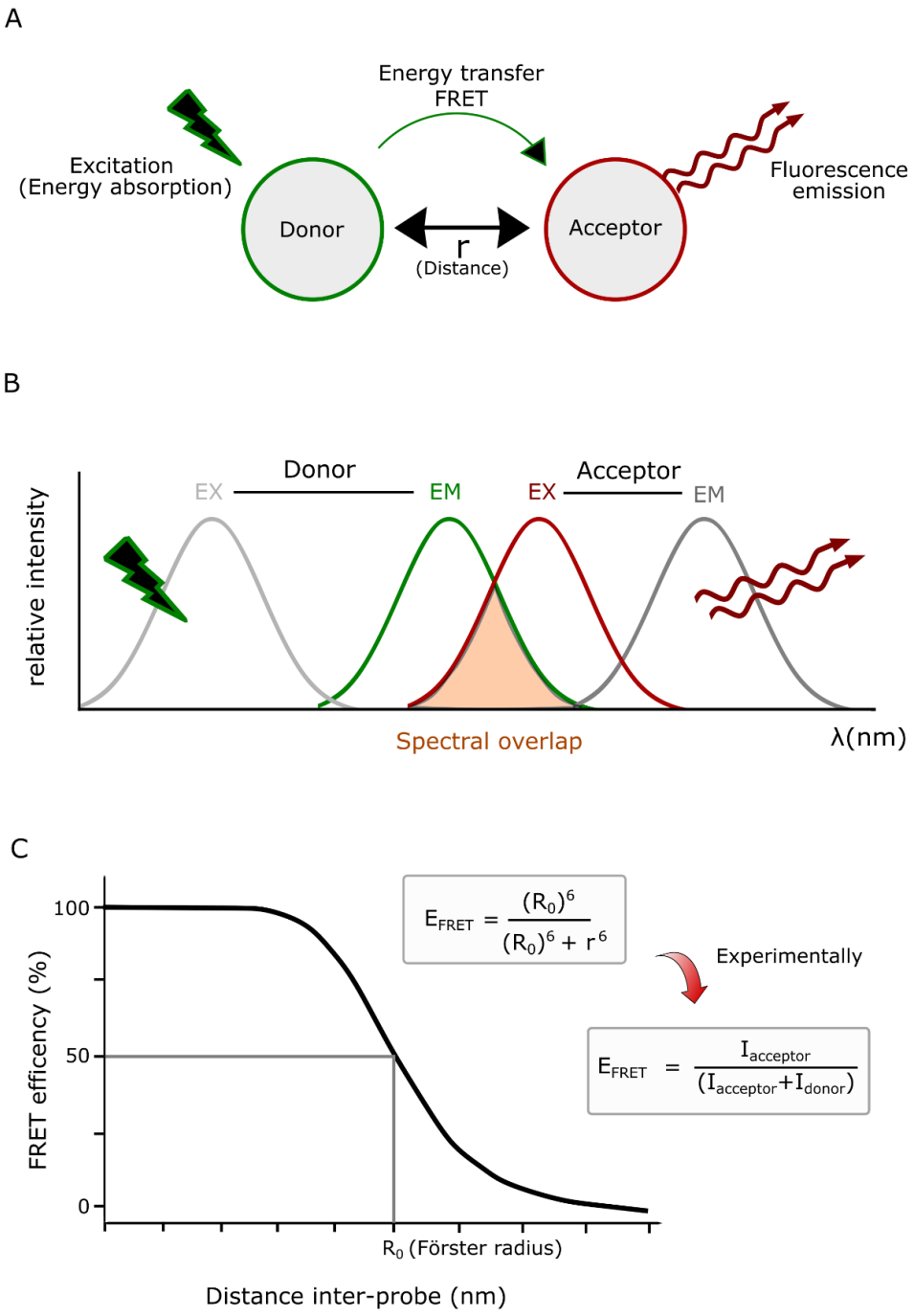

Figure 1-15: Förster Resonance Energy transfer (FRET) principles

A: Schematic representation of FRET energy transfer between two fluorescent probes in proximity (the distance r < 8 to 10 nm) the donor excited is represented in green and the acceptor in red. B: Schematic explaining the spectrum overlap required between the donor (emission spectrum highlighted in green) and the acceptor (excitation spectrum highlighted in red). C: Relation between FRET efficiency and probes inter distance.

Chapter 2. Methods and experimental procedures

1. Cellular culture

1.1. Strains used in the project

Code	Strain name	Genotype
YSL01	WT-BY4742	MATα *his3Δ1 leu2Δ0 lys2Δ0 ura3Δ0* (Baker Brachmann et al., 1998; Winston et al., 1995)
YSL02	WT-BY4741	MATa *his3Δ1 leu2Δ0 met15Δ0 ura3Δ0* (Baker Brachmann et al., 1998; Winston et al., 1995)
YSL03	PRC1-Agg-GFP	BY4742 MATα *his3Δ1 leu2Δ0 lys2Δ0 ura3Δ0* pRS316 *PRC1*-ΔssCPY*-GFP (Donation Hohmann & Cvijovic Lab)
YSL04	Agg-GFP	BY4742 MATα *his3Δ1 leu2Δ0 lys2Δ0 ura3Δ0* pRS316-*CUP1*-ΔssCPY*-GFP
YSL05	Agg-mGFP	BY4742 MATα *his3Δ1 leu2Δ0 lys2Δ0 ura3Δ0* pRS316-*CUP1*-ΔsCPY*-mGFP
YSL06	Agg-mNeonGreen	BY4742 MATα *his3Δ1 leu2Δ0 lys2Δ0 ura3Δ0* pRS316-*CUP1*-ΔssCPY*-mNeonGreen
YSL07	Agg- mScarlet-I	BY4742 MATα *his3Δ1 leu2Δ0 lys2Δ0 ura3Δ0* pRS316-*CUP1*-ΔssCPY*-mScarlet-I
YSL08	Agg- mGFP-LeuConv	BY4742 MATα *his3Δ1 leu2Δ0 lys2Δ0 ura3Δ0* pRS315-*CUP1*-ΔssCPY*-mGFP
YSL09	Agg- mScarlet-I-LeuConv	BY4742 MATα *his3Δ1 leu2Δ0 lys2Δ0 ura3Δ0* pRS315-*CUP1*-ΔssCPY*-mScarlet-I
YSL10	Agg-mNeonGreen-LeuConv	BY4742 MATa *his3Δ1 leu2Δ0 met15Δ0 ura3Δ0* pRS316 *CUP1*-ΔssCPY*-mNeonGreen
YSL11	CrGE FRET sensor	BY4741 MATa *his3Δ1 leu2Δ0 met15Δ0 ura3Δ0* CrGE::HIS3 (Liu et al., 2018) (Donation Boersma and Poolman Lab)
YSL12	CrGE2.3 FRET sensor	BY4741 MATa *his3Δ1 leu2Δ0 met15Δ0 ura3Δ0* CrGE2.3::HIS3 (Mouton et al., 2020) (Donation Boersma and Poolman Lab)
YSL13	EGFP- Hof1	BY4741 MATa *his3Δ1 leu2Δ0 met15Δ0 ura3Δ0* EGFP-Hof1::URA3 (Weill et al., 2018) (Donation Schrodinger Lab SWAp-Tag library)
YSL14	EGFP -Cdc11	BY4741 MATa *his3Δ1 leu2Δ0 met15Δ0 ura3Δ0* EGFP-Cdc11::URA3

YSL15	EGFP-Cdc12	BY4741 MATa *his3Δ1 leu2Δ0 met15Δ0 ura3Δ0* EGFP-Cdc12::URA3 (SWAp-Tag library)
YSL16	EGFP -Myo1	BY4741 MATa *his3Δ1 leu2Δ0 met15Δ0 ura3Δ0* EGFP -Myo1::URA3 (SWAp-Tag library)
YSL17	Agg-mScI-Hof1-EGFP	BY4742 MATα *his3Δ1 leu2Δ0 lys2Δ0 ura3Δ0* EGFP-HOF1::URA3|pRS315-*CUP1*-ΔssCPY*-mScarlet-I

Table 2-1: Yeast strain library used in this project

1.2. Relevant background on yeast genetics

Lab yeast strains were developed to simplify genetic manipulation and the construction of mutant strains to exhibit new phenotypes. This study used two wild type (WT) haploid background strains: BY4741 (MATa *his3Δ1 leu2Δ0 met15Δ0 ura3Δ0*) and BY4742 (MATα *his3Δ1 leu2Δ0 lys2Δ0 ura3Δ0*). MATα and MATa refer to the mating type of each strain. Cells produce accordingly α-factor or a-factor. However, if MATα haploid cells find factor-a produced by the opposite mating type in their environment, instead of dividing by mitosis, the cells will form a characteristic protrusion becoming a shmoo, the pre-step before two shmoo fusion or mate to form diploid cells (Chen & Davis, 2000).

The following genotype "MATα *his3Δ1 leu2Δ0 lys2Δ0 ura3Δ0*" in the wild type BY4742 for example, indicated key genes permanently deleted and allowing heterotrophic selection for the retention of an exogenous piece of DNA introduced in the cell. In short, cells cannot survive without producing essential amino acids or bases such as leucine, methionine, uracil and histidine (Baker Brachmann et al., 1998; Satyanarayana et al., 1968). Specific genes deleted in this wild-type strain (*HIS3*, *LEU2*, *MET15* and *URA3*) all encode biosynthetic enzymes that are required for the cells to synthesise histidine, leucine, methionine and uracil, respectively (Cost & Boeke, 1996; Vidal & Gaber, 1994). Therefore, these cells can only survive in a media or environment supplemented by these essential components (Tomlin et al., 2001). However, returning these genes (e.g., through homologous recombination to regions of the genome or through a transformation with a plasmid) allows for selection in media lacking the respective

component (Tomlin et al., 2001). One useful application of this simple selection method allows fluorescently tagged proteins of interest to be expressed simultaneously with very high efficiency in strains of choice (e.g., wild-type or mutants).

In yeast, the high copy number pRS plasmid series (Sikorski & Hieter, 1989) was specifically used to optimise the amino acid heterotrophic selection, with high copy expression plasmids and cassettes for efficient cloning with homology to the deleted marker region, favouring genomic recombination and stable integration.

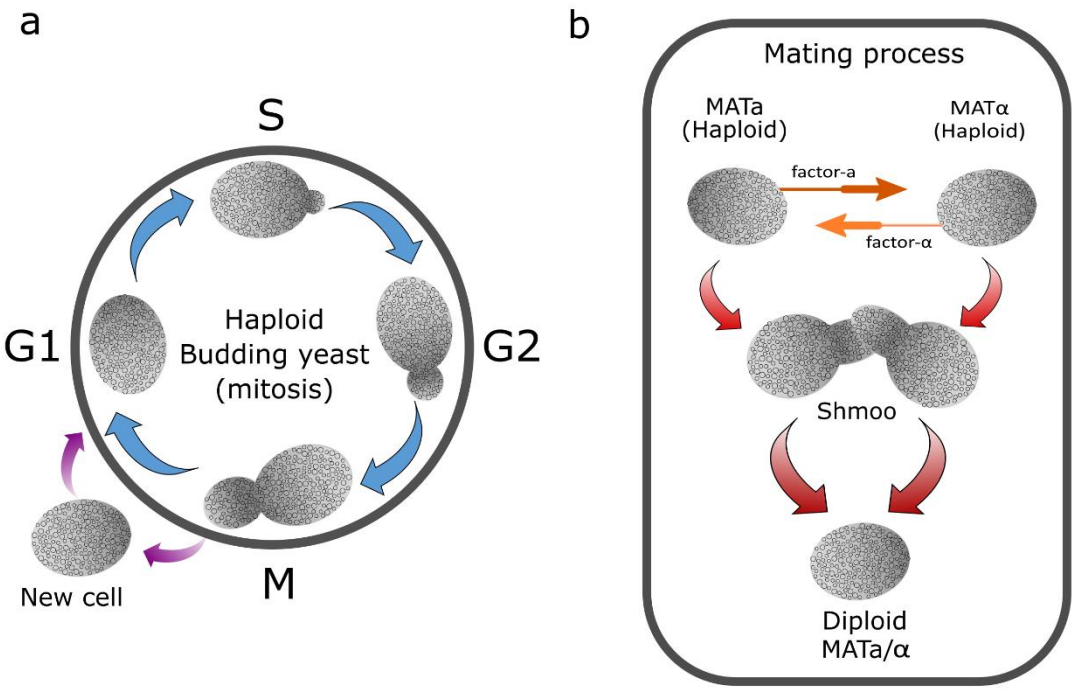

Figure 2-1: Budding and mating in yeast

(a) Schematic representation of haploid yeast cells dividing by budding (asexual reproduction) (b) Schematic representation of two cells of opposite mating type mating to produce a diploid cell (sexual reproduction).

1.3. Growth condition

- All percentages expressed are w/v.
- All media were autoclaved before use, and stock solutions such as glycerol and glucose were filter sterilized with a 0.2 µm filter (Starlab).
- Yeast and bacterial cells were stored with 8% DMSO at -80^{o}C.

1.3.1. Yeast growth

Yeast cultures were first left to grow on a plate at 30^{o}C optimal growth temperature and in either rich media YPD (2% glucose, 2% peptone, 1% yeast extract) or YNB (2% glucose, 1x yeast nitrogen base; relevant amino acids for auxotrophic based selection).

Tube specification and growth condition optimisation: 5 ml of culture in 15 ml polystyrene or glass culture tube with loose polystyrene cap (Starlab) to maintain oxygenation during growth, tubes where additionally inclined in the incubator rack to avoid yeast sedimentation otherwise observed especially during overnight culture even with strong shaking. The inclination angle helps to maximise steer potential in the tube within a reasonable rotation speed set on the incubator. Agar plates for cellular culture were made from the same media composition supplemented by 2% agar, poured into plates after autoclaving and left to solidify into sterile laminar flow cupboards.

1.3.2. Bacterial growth

Bacterial cultures were grown in standard 15 ml Falcon tubes (5 to 10 ml culture) at 37^{o}C in LB broth (Bertani, 1951) or 2YT (6% tryptone, 1% yeast extract, 0.5% NaCl). Plates for solid culture were made from the same media composition supplemented by 2% agar, poured into plates after autoclaving and left to solidify into sterile laminar flow cupboards. Media was generally supplemented before incubation with 100 mg/ml ampicillin X1000 stock solution (ampicillin in water stored at -20^{o}C), for antibiotic selection when required.

1.3.3. Measuring optical density

The optical density was measured using a commercial spectrometer set to read absorbance at 600 nm. 1 ml final volume was loaded per cuvette measured. The sterile growth media was used as the control at a 1/10 dilution of the culture of interest as the proportional relation between absorbance and concentration only applies at low cell concentration sample, following the Beer-Lambert law described by the following equation $A = \varepsilon CL$ where A is the read absorbance, ε is the molar extinction coefficient, C is the concentration and L is the light path length. As cells grow, they occupy the media, which generates scattered light influencing the absorbance read-out of the media by the spectrometer, therefore the technique measures a scatter light effect and not the effective absorbance. However, the Beer-Lambert equation was shown to still be valid for low-density cellular solutions.

1.3.4. Yeast Growth assay

Growth assay was performed on synthetic drop-out agar plates made on the day and left to dry under a serial laminar flow cabinet. A 10-fold serially diluted plate from a culture grown was prepared and 5 µl of each dilution was loaded using a paper template to keep an equal distance between each drop. Plates were left to dry for 5 to 10 minutes and incubated at 30^{o}C, ready to be photographed first after 24 hours of incubation, and a second time after 48 hours.

1.3.5. Yeast cell synchronization

MATa BY4741 yeast cells grown to their mid-log phase were incubated for 120 minutes with 10 µM α-factor, pheromone from of the opposite mating type (Zymo-Research Corp) to effectively arrest cell division at the G1 stage while they acquire the shmoo phenotype (Chen & Davis, 2000). Following incubation, cells were centrifuged for 3 minutes at 3000xg and washed two times with growth media (synthetic drop out or YPD) to remove α-factor excess and allow a homogenous return to cell division. Cells were grown for 8 hours at 30^{o}C for recovery to the budding phenotype (no shmoo cells remaining in culture).

1.4. Yeast cell transformation

1.4.1. Yeast competent cells

From frozen stock, a scrip of yeast strain of interest spread onto a YPD, or minimal media plate was allowed to grow overnight at 30^{o}C under shaking conditions. A scrip from a clonal colony on the plate was re-suspended into 5 ml liquid culture with appropriate media (YPD or minimal) and grown overnight at 30^{o}C in 180 rpm shaking. 3 ml of this overnight culture was added to 47 ml YPD in a sterile 50 ml flask and incubated in a 30°C shaker until cell growth reached an optical density at 600 nm (OD600) of 1. The culture was centrifuged at 3000 rpm for 2 minutes, the supernatant discarded and the pellet re-suspended in 5 ml of filtered sterilised LiTE sorbitol (100 mM lithium acetate, 10 mM Tris HCl pH 7.5, 1.2 M sorbitol, 1 mM EDTA, 200 µM calcium chloride). Cells were again centrifuged at the same speed and the pellet was resuspended in 1 ml LiTe Sorbitol before incubation for 1 hour at 30°C with shaking. After incubation, competent cells were left to rest for 30 minutes on ice, ready for transformation. Competent cells were stored at -80^{o}C in yeast freezing buffer (40% glycerol and 0.05% NaCl) at a 1:2 ratio volume.

1.4.2. Yeast transformation

Yeast cells from frozen stock were thawed, and each transformation was made using 100 µl of competent cells with 500 ng of plasmid DNA with the addition of 5 µl of salmon sperm DNA at 10 mg/ml (Thermofisher, UK). And 70% (w/v) of polyethylene glycol 3350 or polyethylene glycol 4000 in solution (PEG). After incubation for 45 minutes at 30^{o}C, competent cells were heat-shocked at 42^{o}C for 20 minutes. Following, cells were centrifuged at 3,000xg for 3 minutes, the supernatant was removed and the pellet was re-suspended in 200 µl sterile water. Cells were plated on selective agar plates made of minimal media YNB lacking relevant amino acids and left to grow at 30^{o}C, typically for two days until visible colonies grew on the plate.

1.4.3. *E. coli* competent cells

From frozen stock, WT *E. coli* was grown overnight at 37°C on an LB plate (without antibiotic -ampicillin). A single colony was used to inoculate 10 ml of LB media and grown overnight at 37°C with 180 rpm shaking. This overnight culture was diluted to 50 ml in fresh LB and cultured to an optical density of 600 nm of 0.6 to 0.8, corresponding to log phase. Cells were then harvested by centrifugation at 8000 rpm, washed twice with 1 mL 0.1 M calcium chloride and incubated on ice for 10 minutes and washed a final time in 0.1 M of calcium chloride and stored on ice for 30 minutes before transformation.

1.4.4. *E. coli* transformation

10 µl of competent *E. coli* bacterial cells were thawed per transformation and mixed with 1 to 10 µg plasmid DNA. Cells were incubated on ice for 10 minutes, heat shocked at 42°C for 30 seconds, and then returned to the ice for at least 2 minutes before 200 µl of LB media was added. Cells were left to recover for 20 minutes at 37°C with 180 rpm shaking before spreading on an LB agar plate, generally containing ampicillin at a concentration of 100 mg/ml as standard practice for plasmid selection.

2. Strain engineering

2.1. Molecular cloning techniques

2.1.1. Gibson assembly reaction

Gibson assembly is a cloning technique that exploits recombination by homology properties of eukaryotic cells. It allows a DNA sequence coding for a protein of interest to be inserted into an available plasmid vector. The reaction was performed using NEB products and following supplier recommendations for optimised cloning efficiency. 20 µl reaction solution was prepared, containing, the Gibson assembly master mix with the exonuclease, DNA polymerase and ligase in isothermal buffer (2x NEB Gibson assembly master mix), 50 to 100 ng of designed linearised vector and 2 to 3-fold the amount of PCR clean insert. This mix was left for 60 minutes at 50°C and transferred onto the ice to cool down before transformation.

2.1.2. Ligation

Ligation was performed using NEB Quick Ligation Kit. 20 µl reaction containing 10 µl of Quick Ligase Reaction Buffer (2X), approximately 50 ng of linearised double digest vector DNA (~4k) and a molar ratio of 1:3 vector to double digest insert DNA recommended, topped by nuclease-free water. The reaction was left to incubate for 5 min at room temperature (~ 25°C) and ready for transformation.

2.1.3. Site-directed mutagenesis.

Single nucleotide mutagenesis was performed using NEB Q5® Site-Directed Mutagenesis Kit and associated protocol. First step PCR (Polymerase Chain Reaction) primer amplification: 25 µl reaction mix was prepared using 1x Q5 Hot Start High-Fidelity, 10 µM forward Primer and 10 µM reverse Primer, 1 to 25 ng/µl of template DNA topped by nuclease-free water. The mix was amplified with the following cycling condition set on the PCR thermocycler.

Step	Temperature	Cycle
Initial denaturation	98°C for 30S	X1
Denaturation Annealing Extension	98 °C for 10s 55 °C for 10s 72 °C for 30s	X25
Final extension	72 °C for 2min	X1

Table 2-2: Standard conditions set for PCR on the PCR thermocycler

Second step, the ligase enzymatic reaction: 10 µl total reaction was made using 1 µl of PCR Product, 1X KLD Enzyme (Kinase, Ligase, *DpnI*), 1X KLD Reaction Buffer topped by nuclease-free water. The mixture was incubated for 5 min at room temperature before transformation.

2.1.4. Polymerase Chain Reaction (PCR)

Polymerase Chain Reaction amplification of designed primers (forward and reverse) was performed from a prepared PCR reactions mix containing:

- Plasmid DNA template at very low concentration (typically 1 µg/µl).

- dNTPs (a mixture of the four bases necessary for elongation - dATP dTTP, dCTP, dGTP).
- A high-fidelity DNA polymerase like the Phusion (NEB Ltd.).
- A stock buffer containing $MgCl_2$ (15 µM).
- A total volume of reaction mix was made up to 50 µl with the following standard concentration.

Standard reaction:

Component	Concentration
Template DNA	1 µg/µl
pHusion polymerase	0.02U/µl
Forward primers	0.5 µM
reverse primers	0.5 µM
4 dNTPs mix	200 µM
Phusion HF Buffer	1x // including 1.5 µM $MgCl_2$

Table 2-3: Standard reagents concentrations for PCR

Standard thermocycler condition:

Step	Temperature	Cycle
Initial denaturation	98°C for 2min	X1
Denaturation Annealing Extension	98 °C for 10s 55 °C for 20s 72 °C for 20s	X30
Final extension	72 °C for 10s	X1

Table 2-4: Setting for PCR on a Thermocycler

2.1.5. PCR purification

PCR purification was done using a commercial kit, "QIAquick PCR Purification Kit" (QIAGEN, Ltd.) and following the recommended protocol. The PCR product was loaded to a designed 1.5 ml spin column holding a silica membrane to absorb and bind DNA (1:5 ratio sample & PB buffer for optimal binding). Flow through was discarded after 1 min centrifugation at full speed, 17,900xg or 13000 rpm. The column was washed with 750 µl of PB Buffer and centrifuged again for 1 minute. The column was placed in a clean 1.5 ml Eppendorf tube to elute DNA, 50 µl nuclease-free water or EB buffer (10 mM Tris·Cl, pH 8.5) was added to the column, left to rest at room temperature for 2 min before full speed centrifugation to recover a "clean" PRC product. The procedure

effectively removes extra components used during the PCR reaction, such as primers and other impurities that could alter the efficiency of later cloning manipulation such as salts, nucleotides or enzymes (polymerases).

2.1.6. Agarose gel electrophoresis

Gels were prepared at 1 or 0.8% agarose (w/v) in TAE buffer (40 mM Tris Acetate, 1 mM EDTA, pH 8.0). The solution was then microwaved until complete dissolution of the agarose powder (~1 min microwaving total). 5 µl of SYBR Safe (ThermoFisher- alternative to Ethidium-Bromide) for a 50 ml solution was poured into a hermetic gel cassette with a gel comb and left to cool down until complete polymerisation. The gel formed was transferred into the electrophoresis tank filed with TAE buffer.

As standard, 5 µl DNA samples were mixed with gel loading dye (6x stock- 10 mM Tris-HCl, pH 7.6) 0.03 % bromophenol blue, 0.03 % xylene cyanol FF, 60 % glycerol 60 mM EDTA. - ThermoFisher). At least one well was allocated to load the DNA marker (1 kb marker, New England Biolabs Ltd). Finally, the gel was run at 100 volts for 25 min before the visualisation of DNA fragments separated by size, with either an ultraviolet or a blue light trans-illuminator.

2.1.7. Gel DNA extraction

Gel DNA extraction was performed using a commercial kit, the “QIAquick Gel extraction kit” using a silica-membrane-based spin column for DNA fragments from 70 bp to 10 kb (part number: 28706X4, QIAGEN, Ltd.). The supplier protocol was followed for the extraction. In short, after agarose gel electrophoresis (see section above) identified DNA bands of interest were cut out of the gel with a clean scalpel and transferred into a sterile 1.5 ml tube.

Gel was dissolved with commercial QG buffer (3:1 volume proportion) and incubated at 50°C for 10 min. The sample was loaded onto an appropriate 1.5 ml silica-membrane-based spin-column and centrifuged at full speed (13000rpm). The resulting supernatant was discarded and column rinsed one time with 100% isopropanol and washed with PB buffer containing ethanol before elution with generally 50 µl of either EB buffer (10 mM Tris.Cl, pH 8.5) or sterile nuclease-free water.

2.1.8. Restriction endonuclease digestion

Commercial enzymes were supplied by New England Biolabs (NEB, Ltd.), from their High-Fidelity (HF) restriction enzyme product range. This selection of enzymes has the advantage of being cross-compatible and optimally active under the same reaction mix, the NEB cut-smart buffer, an essential requirement to perform double digestion (two different enzymes to cut the same plasmid).

For single reaction digestion used in general to linearize genomic plasmids, the reaction was set in an Eppendorf tube following supplier recommendation. Reaction prepared using one endonuclease enzyme including controls. Reactions were set-up in an Eppendorf tube. The standard reaction volume of 50 µl was then incubated for 15 min at 37^{o}C and verified by gel electrophoresis (see section 2.1.6).

Double digests reactions were performed using simultaneously two enzymes in the reaction tube, usually to cut out fragments from the plasmid backbone or verify the plasmid construct. Similarly, reactions were prepared (including controls) following supplier recommendation. Reactions were set-up in an Eppendorf tube. The standard reaction volume of 50 µl was then incubated for 15 min at 37^{o}C and verified by gel electrophoresis (see section 2.1.6).

2.1.9. Mini-prep

5 ml bacterial culture in LB was grown at 37^{o}C with the appropriate antibiotic (see section 1.3.2) Plasmid DNA was extracted from the culture using the QIAprep Miniprep kit (QIAGEN, Ltd.) and following the supplier's recommendations. DNA was eluted with 100 µl nuclease-free water or EB buffer (10 mM Tris·Cl, pH 8.5), DNA concentration was measured using a nano-drop spectrophotometer and the eluted volume in an Eppendorf tube was stored on a bench or at -20^{o}C for long term conservation.

2.1.10. Measuring DNA absorbance

DNA concentration was estimated using a nano-drop spectrophotometer (NanoDrop™ 2000/2000c, ThermoFisher) and following manufacturer instructions for absorbance reading at 260 nm. 1.5 µL sample or blank (Water or EB buffer) was loaded.

2.1.11. Ethanol precipitation for genomic integration

In an Eppendorf tube, 500 µl of PCR product were supplemented with 10 µl salmon sperm, 15 µl of 3 M sodium acetate at pH 5.5 and 1 ml of 100% ethanol and frozen down at -80^{o}C for 30 min. The solution was centrifuged at full speed (13000 rpm) for 10 min and the supernatant was removed. The characteristic white pellet was washed three times with 1 ml of 70% EtOH and left to dry for 3 min at 42^{o}C before adding 30 µl of TE. The solution was left overnight on a bench until the pellet completely dissolve in the 30 µl of TE and was ready for transformation.

2.1.12. DNA Sequencing

Sequencing of DNA was provided by Eurofin genomic TubSeq service, the service was used routinely as a verification step after DNA cloning on new material was generated. Samples were prepared following the manufacturer's recommendation. Typically, 15 µl pre-mixed reaction sample in Eppendorf tubes, containing ~50 ng/µl a plasmid DNA and one primer of interest at 10 µM.

2.1.13. Primer's synthesis

Designed DNA Oligos (see methods in section 2.1.14) were manufactured by either Integrated DNA Technologies (IDT, UK) or a custom oligo service provided by Sigma-Aldrich, Ltd. New primers received were dissolved in indicated nuclease-free volume to generate a 100 µM stock solution.

2.1.14. Map design and visualisation

Plasmid maps and primers (reverse and forward) were designed using the DNASTAR Lasergene bioinformatics software. The software was used to visualise sequencing results and perform sequence alignment checks. Occasionally alternative software were used including the genome compiler software or the open-source Serial cloner software.

2.2. Plasmid construction

Name	**Source**
P695: *CUP1*-GFP in pRS316	Chris MacDonald Lab
Prs316 (URA3 marker – yeast expression plasmid)	Chris MacDonald Lab
Prs315 (LEU2 marker – yeast expression plasmid)	Chris MacDonald Lab
PeT14-B (T7 promotor – bacterial expression plasmid)	Mark Leake lab

Table 2-5: List of backbone plasmids used in this study

2.2.1. CrGE Genomic integration in BY4742

The CrGE FRET sensor (Boersma et al., 2015; Mouton et al., 2020) regulated under the *TEF1* promoter was sub-cloned into the pRS303 cassette, a yeast integration vector which was linearized by single digest with NsiI restriction endonuclease before transformation into wild-type BY4742 yeast cells for stable integration at the HIS3 locus by *in vivo* homologous recombination. Agar plates made of 2% glucose synthetic drop-out media lacking Histidine (SD –His, Formedium Ltd.) were used to isolate successful integrations. After 24h to 48h incubation at 30°C, an isolated single clone was suspended into 5 to 8 ml of the appropriate media and incubated overnight at 30°C with shaking on (180 rpm). 1 ml from a mid-log phase culture (OD600 = 0.4 - 0.6) were harvested and resuspended immediately in 1 ml of imaging buffer, ready for sample preparation and imaging.

2.2.2. Cloning cytoplasmic fluorescent protein aggregates.

Note: To simplify referencing and labelling, plasmid codes were attributed to mirror the strain name (e.g., YSL04 yeast strain contains the pSL04 plasmid). *CUP1*-ΔssCPY*-mGFP was generated via two intermediate steps from PRC1-ΔssCPY*-GFP donated plasmid (pSL03 – see Table 2-1). First ΔssCPY* sequence was transferred into a new plasmid backbone (*CUP1*-GFP in pRS316) to generate the intermediate strain *CUP1*-ΔssCPY*-GFP using the Gibson assembly technique (see section 2.1.1). Primers cm193 and cm194 were required (see Table 2-6). Secondly, the GFP sequence was mutated by directed mutagenesis (A206K) performed on PRC1- ΔssCPY*-GFP to generate additional PRC1-ΔssCPY*-mGFP and the newly cloned mGFP sequence was extracted by PCR and added by Gibson assembly to form the *CUP1*- ΔssCPY*-GFP constructed sequence. Using HindIII and XhoI restriction enzymes to linearise plasmid and take out the GFP sequence.

Oligo Name	Sequence (5'-3')	Description
cm193	GATATTAAGAAAAACAAACT GTAACGAATTCATGATCTCAT TGCAAAGACCG	*CUP1*- ΔssCPY* - Forward primer - used to extract ΔssCPY* sequence for Gibson Assembly in p695
cm194	CCACGGTGGTTTCTCCTTACT CGAGATGTCTAAAGGTGAAG	ΔssCPY*-GFP – reverse primer - used to extract ΔssCPY* sequence for Gibson Assembly in p695
S1	CACACAATCTAAACTTTCGAA AGATCC	GFP - Forward primer – used to induce single nucleotide mutagenesis (GFP to mGFP)
S2	CAGACAACCATTACCTGTC	GFP – Reverse primer – used to induce single nucleotide mutagenesis (GFP to mGFP)
s8	GGTGGTTTCTCCTTACTCGA GATGAGTAAAGGAGAAGAA CTTTTCACTGG	Forward primer - Xho1 site Gibson assembly for mGFP
S9	CCAGATATTCTATGGCAAAG CTTTTATTTGTATAGTTCATC CATGCC	Reverse primer- HindIII site Gibson assembly for mGFP
s5	GGTGTTTCCAACACTGTCGC CGCTGGTAAGG	ORF ΔssCPY* - Forward sequencing primer
cm195	GGTGATGCTACTTACGGTAA ATTGACC	GFP ORF Forward sequencing primer
S3	GGCAGACAAACAAAAGAAT GG	mGFP - Forward sequencing primer- used to verify mGFP site-directed mutagenesis.

Table 2-6: Primers used to construct fluorescent aggregate reporter

2.2.3. Inducing cytoplasmic fluorescent protein aggregates

The inducible *CUP1* promotor (Fogel & Welch, 1982) was activated using 100 µM copper sulphate. The stock solution of 100 mM copper sulphate in water was prepared and filtered sterilised (0.22 µm cut-off filters) and stored at room temperature.

2.3. Recombinant fluorophore production *in vitro*

Protein expression was achieved by inducing expression in *E. coli* of the recombinant protein of interest. Importantly for this protocol expression, the plasmid must contain a T7 promotor, the protein ORF including a His-tag either in the N or C-terminal of the protein and an antibiotic resistance marker, ampicillin for this study.

2.3.1. IPTG expression

Appropriate expression plasmid was transformed into BL21(DE3) or BL21(DE3) plysS*,* *E. coli* strains and left to grow on a plate with antibiotic selection. A single colony was grown overnight in 30 ml LB with appropriate antibiotic (ampicillin) at 37^{o}C with shaking at 180 rpm. 2 ml of this overnight culture was transferred into 500 ml LB with ampicillin and left to grow until log phase (OD tolerance: working window between 0.6 to 0.8), IPTG was then added at a concentration of 100 µg/ml (when OD between 0.6 to 0.8), and cell culture incubated for 24h at 18^{o}C, 180rpm.

2.3.2. Cell lysis

After 24 hours of incubation, the culture was centrifuged at 4000 rpm for 20 min, the supernatant discarded and the pellet of cells resuspended in 30 ml of lysis buffer (10 mM sodium phosphate (NaPi), 100 mM NaCl, 0.1 mM 4-(2-aminoethyl)-benzenesulfonyl fluoride hydrochloride (AEBSF), pH 7.4) and left to freeze at -80^{o}C. Cells were then thawed before sonication on ice (100% power burst, 20-sec pulse followed by a 20-sec pause - repeated six times). The sonicated mixture was centrifuged for 40 min at 12000 to 15000xg. Cell lysate supernatant was kept on ice and the pellet of cellular debris was

discarded. Lysate was then filtered with a 0.45 µm filter, one aliquot was kept aside for verifying SDS-page after the first step of purification.

2.3.3. SDS-PAGE: Denaturant protein gel electrophoresis

SDS PAGE of either 4%,12% acrylamide or 10% plain. Using a standard protocol where 20 µl total were prepared with 15 µl of sample in 5 µl of 4x SDS-page buffer. Samples were left at 95^{o}C for 5 min, then loaded into pre-cast gels with 2 to 5 µl of protein ladder (precision plus protein ladder, Biorad inc). Gels were run at 150 or 200 volts for approximatively 45 min and incubated for a minimum of 30 min in Coomassie stain or run-blue SDS stain (Expedeon, Ltd.). The gel was rinsed twice with water to improve gel contrast. Photographs were then taken for record.

2.3.4. HIS tag purification

HIS-tag purification was performed using a gravity nickel column (HIS-Gravitrap, healthcare) and following the manufacturer's recommendations.

The column was equilibrated with 20 ml low imidazole loading buffer (20 mM imidazole, 50 mM NaPi, 300 mM NaCl, pH 8.0) before loading filtered lysate to the column. Elution was performed with 20 ml of a high imidazole loading buffer (250 mM imidazole, 50 mM NaPi, 300 mM NaCl, pH 8.0) and manually collected in 0.5 ml faction in Eppendorf tubes.

2.3.5. Dialysis

Dialysis was performed by loading the sample in a 12.6 kDa cut-off hydrated membrane, incubated overnight at 4^{o}C in 2 litres of dialysis buffer (50 mM NaPi, 300 mM NaCl, pH 8.0) with gentle magnetic stirring.

2.3.6. Gel filtration – chromatography size column exclusion

Performed using the AKTA pure, a protein purification instrument and loaded with a HiLoad 16/60 Superdex 200 gel filtration column (Sigma-Aldrich, UK). The dialysed sample was injected using a 10 ml syringe. Elution was performed with standard phosphate buffer (10 mM NaPi, pH 7.4) with 4 ml fractions collected. UV profile was

monitored by the instrument allowing the identification of fractions containing the protein eluted, aliquots were collected for SDS-page verification.

2.3.7. Storing *in vitro* protein

The final solution of protein was flash frozen in 10 µl aliquots with liquid nitrogen and stored immediately at -80°C. Note that for long-term conservation 50% glycerol can be added as cryo- protectant. Protein concentration was measured on a Nanodrop 2000 Spectrometer (ThermoFisher) set to read out absorbance at 280 nm wavelength. Extinction coefficients were obtained from the sensor amino-acid sequence via the Expasy-ProtParam tool using the Edelhoch method via the extinction coefficients for Tryptophan and Tyrosine determined by the Pace methods (Edelhoch, 1967; Mach et al., 1992; Pace et al., 1995; Walker, 2005). Giving 56395 M^{-1} cm^{-1} for the CrGE2.3 sensor and 48040 M^{-1} cm^{-1} for the CrGE sensor.

2.3.8. mNeonGreen and mScarlet-I *in vitro* purification

mNeonGreen and mScarlet-I were cloned in pET-14b by ligation (see Chapter 2.2.1.2) and using NdeI and BamHI for plasmid digestion and ligation procedures. The pET-14b vector (Cat. No. 69660-3) carries an N-terminal His-Tag plus a trombone cleavage site in its N-terminal region.

Primers used are given in Table 2-7 below:

Oligo Name	Sequence (5'-3')	Description
S10	GGCAGCCATATGGTGAG CAAGGGCGAG	Forward-NdeI-mNeonGreen to integrate mNeonGreen into pET-14b plasmid
S11	CATGGACGAGCTGTACAA GTAGGGATCCGGCTGCT	Reverse-BamHI-mNeonGren to integrate mNeonGreen into pET-14b plasmid
S12	GGCAGCCATATGGTCTCC AAAGGAGAG	Forward-NdeI-mScarlet-I to integrate mScarlet-I into pET-14bplasmid
S13	GTATGGATGAGCTGTATA AATAAGGATCCGGCTGCT	Reverse-BamHI-mScarlet-I to integrate mScarlet-I into pET-14b plasmid

Table 2-7: Primers for mNeonGreen and mScarlet-I in pET-14b bacterial vector

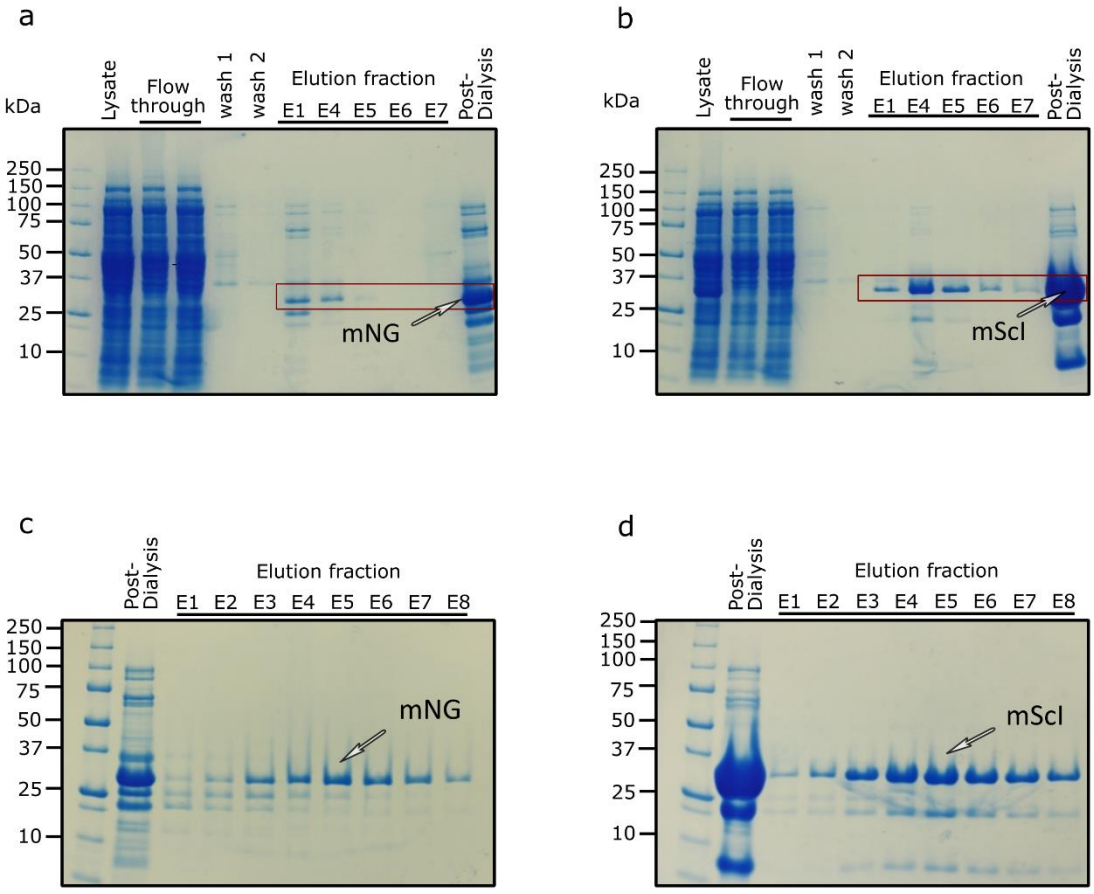

Figure 2-2: mScarlet-I and mNeonGreen purification

(a) and (b) 4–12% SDS-PAGE for his-tag purification of respectively mNeonGreen and mScarlet-I performed using gravity nickel column. The gel shows from left to right the molecular marker, cell lysate, sample of the initial flow-through, the two washes prior to elution, and the elution fraction selected to verify the presence of the protein. The last column shows the sample after concentration via dialysis. (c) and (d) 4–12% SDS-PAGE gel for the size column exclusion or gel filtration performed to purify respectively mNeonGreen and mScarlet-I. Showing from left to right, the molecular marker, the sample before running gel filtration (post His-tag purification and dialysis). White arrows indicate the expected band size for both proteins purified (mNG: 28.79 kDa and mScI: 28.43 kDa).

We note the presence of extra bands visible in the gel after the two-step purification process described above. This is often observed after purification, especially for overexpressed fluorescent proteins. It most likely represents unmatured protein purified alongside the mature protein. Cleaved proteins during the process could be suspected too, however, the use of a lysis inhibitor acts to strongly reduce and prevent their presence. Even if minimal, the presence of unmatured proteins in the mix can influence the optical property of the protein such as its brightness, this is a technical limitation and something to be aware of for analysis methodology (e.g., data normalisation).

1.1.1 CrGE2.3 *in vitro* purification

The CrGE2.3 sequence was expressed following the protein purification protocol described above in section Chapter 2.2.3. These were incorporated in PRSET-A by ligation using NdeI and HindIII. The sequence was cloned with its 6xHIS tag sequence attached to the N-terminal of the protein for purification.

Primers used are given in Table 2-8 below.

Oligo Name	Sequence (5'-3')	Description
S32	TTAAGAAGGAGATATACATATGAG CCATCACCATCACCACCATAAG	pRSET-A ligation CrGE2.3_Forward (NdeI site)
S33	TATGGATGAGCTGTACAAATAAAA GCTTGATCCGGCTGCTAACAAAG	pRSET-A HindIII_CrGE23_ reverse
S34	TCTTGCTCATTAGAAAGAAAGCAT AGCAATCTAATCTAAGAAGCT	Forward pRS303 CrGE before mCerulean3
S35	GCTGCAAAGGCAGGTAGTGGTGG TTCAGGTGGTTCCGGTGGTTCTGG	Forward pRS303 CrGE before mCitrine

Table 2-8: Primers for CrGE2.3 in PRSET-A bacterial expression vector

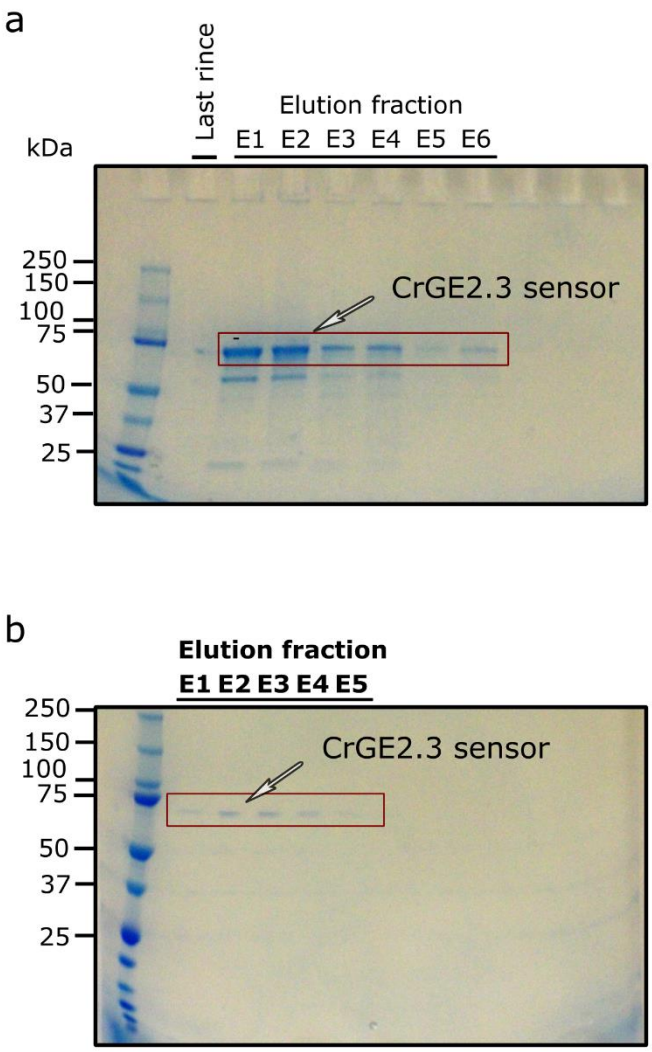

Figure 2-3: CrGE2.3 purification

(a) SDS-PAGE for His-tag purification of CrGE2.3 following the same protocol of purification as described above in section Chapter 2.2.3, here only showing the elution fraction checked. (b) SDS-PAGE representing the CrGE2.3 elution by gel filtration. White arrows indicate the expected CrGE2.3 band size (63.47 kDa). See also the elution profile plot in Appendix ap.0-1.

3. Microscopy and imaging methods

3.1. Plasma clean coverslips

On the day of the experiment, coverslips were individually placed on a coverslip holder rack and were plasma cleaned for 1 min prior using commercial table-top plasma cleaner (Harrick Plasma Cleaners Inc).

3.2. Tunnel slides

Tunnel slides were made using plasma clean square coverslips (22x22 mm No. 1.5 BK7 Menzel-Glazer glass coverslips, Germany) and standard microscopy glass slides (Syeda et al., 2019). On the microscope slide two strips of double-sided tape were attached parallel to each other and apart from approximately 5 mm to create a tunnel or flow channel, capable to hold 5 to 10 µL after closing up from the top of the tunnel with the coverslip attached to the tape (Leake et al., 2006).

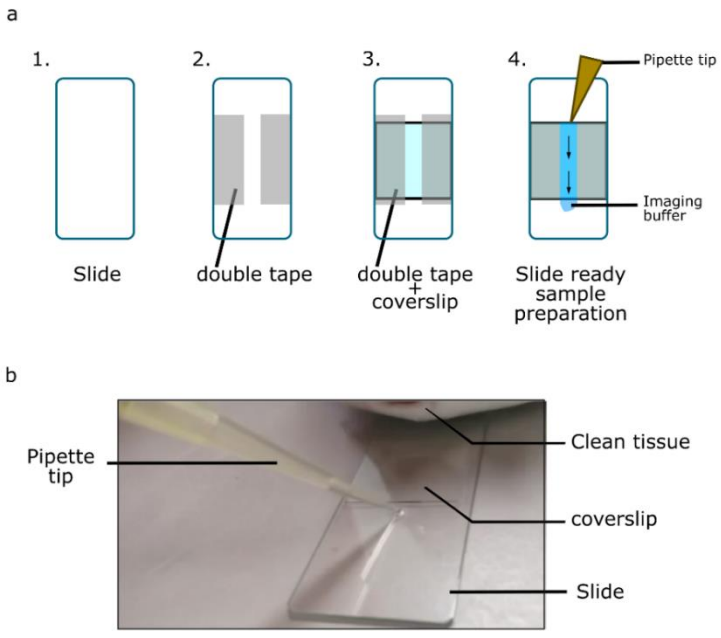

Figure 2-4: Tunnel slide

(a) Schematic representation for tunnel making slide protocol, four steps. The tunnel slide is made by two parallel strips of double-face tape on a glass slide (steps 1 and 2).

A fresh plasma clean coverslip on top of it allows the tunnel formation (step 3), exceeding of tape is removed and finally, the buffer can be added on one side of the tunnel (step 4). (b) photograph of a tunnel slide being loaded with sample/imaging buffer, representing the schematic step 4. The buffer surplus is removed by capillarity flow with clean white tissue and the sample ready to image is sealed with transparent nail polish.

3.3. Imaging *in vitro* assay

In vitro molecules were prepared on a tunnel slide (see
Figure 2-4), the coverslip was functionalised with 20 µl of 1 to 2 µg/ml of specific anti-bodies to stain the fluorescent protein (e.g., Anti-GFP). The slide with antibodies was left up-side-down in a humidity chamber for 5 min to allow antibodies to non-specifically bind to the glass coverslip and was washed out with 200 µl imaging buffer, generally PBS (Phosphate-buffered saline) or NaPi (Sodium Phosphate buffer) at pH 7.4. Following, 20 µl of 1 mg/ml of bovine serum albumin (BSA) was added to the tunnel and incubated again for 5 min in a humidity chamber (up-side down). After 5 min the channel was rinsed with 200 µl of imaging buffer. 20 µl of fluorescent protein was added, with an ideal concentration of 1 µg/ml and incubate for 5 min at room temperature. After 5 min the channel was rinsed with 200 µl imaging buffer the tunnel slide was finally sealed with nail polish and ready to image under the microscope (see Chapter 2.3.7).

3.4. Imaging *in vivo*

3.4.1. Vacuole labelling

Cells grown to log phase were incubated in YPD containing 0.8 µM FM4-64 for 1 h at 30^{o}C, then washed two times in minimal media before a 1 h chase period in minimal media to label only vacuoles, before sample preparation and imaging.

3.4.2. Yeast cells coverslip staining

On either side of a tunnel slide. Typically, 20 µL of imaging buffer (10 mM NaPi at pH 7.4) was first introduced to wash the tunnels followed by 20 µL of 1 mg/ml Concanavalin A (ConA) to functionalised the coverslip for cell attachment, the ConA introduced was allowed to incubate with slide up-side down for 5 minutes, preferably in a humidified chamber to minimise evaporation. Finally, the ConA was washed with 200 µL of imaging buffer before adding 20 µL of cells. After 5 minutes of incubation in the same condition, inverted in a humidity chamber to promote adhesion to the coverslip. A final channel wash was performed with 200 µL of imaging buffer, the tunnel slide was then sealed on both ends with nail varnish (Cosgrove et al., 2020).

On 35 mm glass dishes (Ibidi GmbH, Germany) (Section Chapter 2.3.5.1, below) 300 µl of 1 mg/ml ConA solution was added to the glass region of the dishes and incubated for 5 min with the lid on. The ConA solution was then gently removed with a pipette and the dish was rinsed 3 times with approximatively 5 ml of sterile water. And finally, left without the lid to dry under a laminar flow sterile cabinet for 30 minutes ready to use. Generally, 300 µl of cells were added incubated for 5 min and rinsed three times with 5 ml of imaging buffer.

3.5. Confocal microscopy

3.5.1. Flowcell system

A time-lapse experiment with media exchanges was performed using a bespoke flowcell device, built to be compatible with inverted microscopes. Two 50 ml syringes were tipped with 25 mm needles and connected to a tight-fitting silicone tube, all sealed together with parafilm. One syringe is to push the media into a 35 mm glass-bottom dish (Ibidi GmbH, Germany). The other syringe serves to remove it.

The plastic cap of 35 mm glass dishes (Ibidi GmbH, Germany) was pierced using a heated syringe needle to create a hole the size of the silicone tube used, for both the tube entry and the exit point for media exchange. The tube used to flow media in was positioned

to not touch the stagnant media in the dish. The exiting tube was placed further down, in close proximity to the bottom of the ibidi dish, to maximise the volume absorbed. The process takes all together ~ 1 min to 2 min to complete. (Figure 2-5). An imaging interval of 5 minutes was typically used.

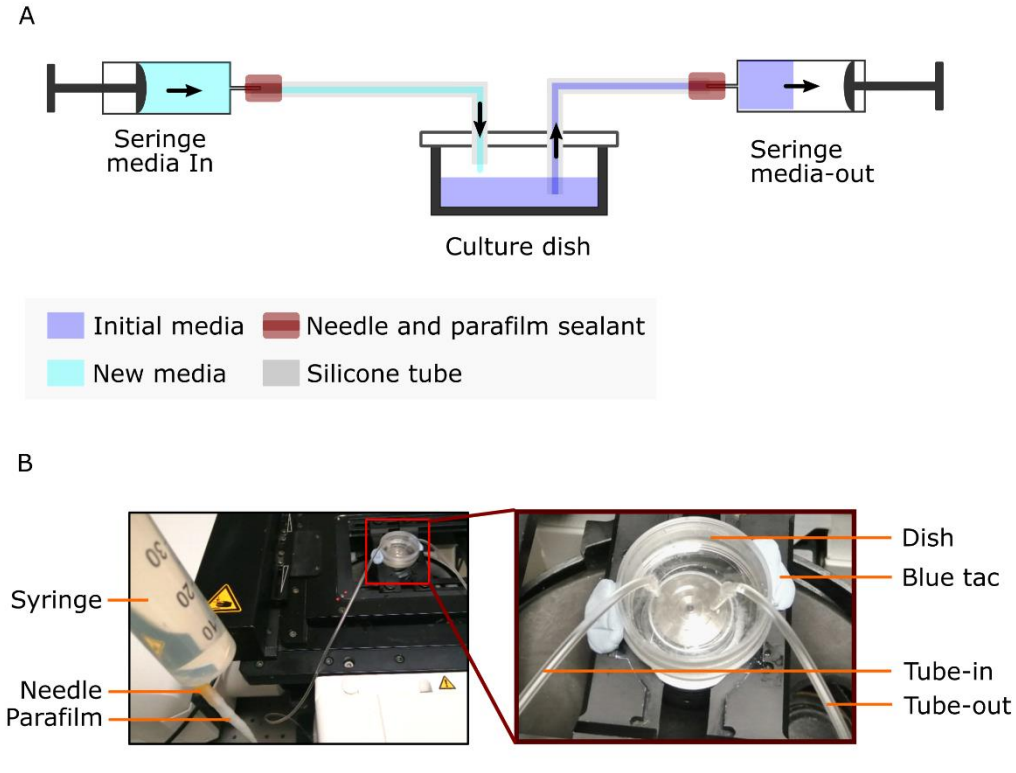

Figure 2-5: Flowcell system

A: Schematic representation exchange media with previously developed flowcell system (Laidlaw et al., 2021) B: Photograph system installed on confocal microscopy Zeiss 880.

3.5.2. Confocal setting CrGE mCerulean-mCitrine FRET readout.

The CrGE sensor is built with mCerulean fluorophore (Ex 420 nm and Em 475 nm) at the N-terminus and mCitrine fluorophore (Ex 515 nm; Em 525 nm) at the C-terminus forming the FRET pair.

On either the confocal microscope LMS 710 or the inverted 880 Zeiss both equipped with a 63x NA 1.4 oil-immersion objective lens (Plan-Apochromat). The following excitation lasers and imaging wavelength ranges were applied: mCerulean3 with 458

nm and 454/515 nm, mCitrine with 514 nm and 524/601 nm and FRET with 458 nm and 458/601 nm. Lasers set respectively to 0.7% (or 0.23 µW) and 2.1% (or 0.23 µW) of maximum power, on the LMS 710.

On the inverted 880 microscope, the imaging set-up was as follows; mCerulean3 458 nm (argon laser) for 463/500 nm emission filter and 1.5% laser power (or 1.42 µW) and FRET 458 nm for 525/606 nm emission filter.

The triple-colour experiment was performed through sequential acquisition for each imaged colour. First, the acquisition of the CrGE FRET signal (following the imaging condition above) seconded by the acquisition of FM4-64 vacuole dye fluorescence using a 561 nm wavelength laser (Argon) at 5% of maximum power (or 20.9uW) and the following emission filter: 578/731 nm. See also in (Lecinski et al., 2021; Shepherd, Lecinski, et al., 2021).

3.5.3. Confocal settings, imaging fluorescence aggregates

Aggregates were imaged using the LSM 880 Zeiss microscopes (see section above), with 488 and 561 or 633 nm wavelength lasers. Intensity and gain were optimised and kept for each experiment (including replicates). Detector digital gain was set to 1 and a scanning time of 1.23 seconds per frame. 2% (2.09 µW) laser power was used to image green fluorescence (mGFP) and 1% (4.1 µW) when imaging red fluorescence to minimise bleaching of sensitive mCherry and mScarlet-I.

3.5.4. Acquiring z stack

Z stacks images were acquired notably to observe aggregates in 3D were done with 0.33 µm sections across the sample usually around 5 to 6 µm thickness. Imaging was performed on the inverted 880, Zeiss microscope, as described above.

3.5.5. Airyscan for bud neck 3D structure

Airyscan imaging is a confocal setting that was mainly used in this project to resolve the structure of the bud neck in yeast a region between mother cell and daughter cells in the budding yeast. Imaging was performed on the inverted LSM 880, Zeiss microscope, equipped with an Airyscan module (Huff, 2015). LSM 880 using Plan-Apochromat 63×/1.4 objective lenses with 488 nm Argos laser set at 2% laser power (~ 2.09 µW) with emission range between 495 and 550 nm to collect GFP green fluorescence signal. Detector digital gain was set to 1.4 and the scanning time to 1.56 seconds.

3.6. Flow Cytometry

A flow cytometry experiment was performed to assess the influence of copper on GFP fluorescence (Figure 5-3.a). Cell samples at log phase were diluted on a 96-well square plate and readout was performed with the assistance of the York bio-imaging facility on a Beckman Coulter MoFlo Astrios cytometer and using a 488 nm laser.

3.7. Single-molecule detection using Slimfield microscopy

3.7.1. A bespoke microscope

The Slimfield microscopy technique uses a standard epifluorescence illumination set-up however designed on a bespoke microscope to specifically generate a greatly reduced excitation field. The Gaussian intensity profile generated by the laser beam is indeed greatly reduced typically of a width lesser than 10 microns over the sample. Compared to classic epifluorescence is approximatively smaller by a factor of 10, as a result, the excitation intensity is strongly increased, up to ~ 100 times compared to wide-field image intensities (Plank et al., 2009; Wollman & Leake, 2016). This feature strongly reduces the background noise and enables single-molecule detection precision. Typically, the field of view is 30 square microns, enough to contain small eukaryotic cells such as yeast cells, an ideal configuration for single-cell imaging. Coupled with the fast acquisition (millisecond time scale), cellular dynamics can be observed by fluorescence at a molecular scale, and meaningful molecular and cellular parameters can be

extracted, such as copy number, diffusion coefficient, the stoichiometry of molecular complexes, and the dynamics of fluorescent proteins in the cytoplasm (Plank et al., 2009; Shashkova et al., 2018). Dual-colour imaging can be performed with this type of device opening perspective of colocalisation experiments (Figure 2-6).

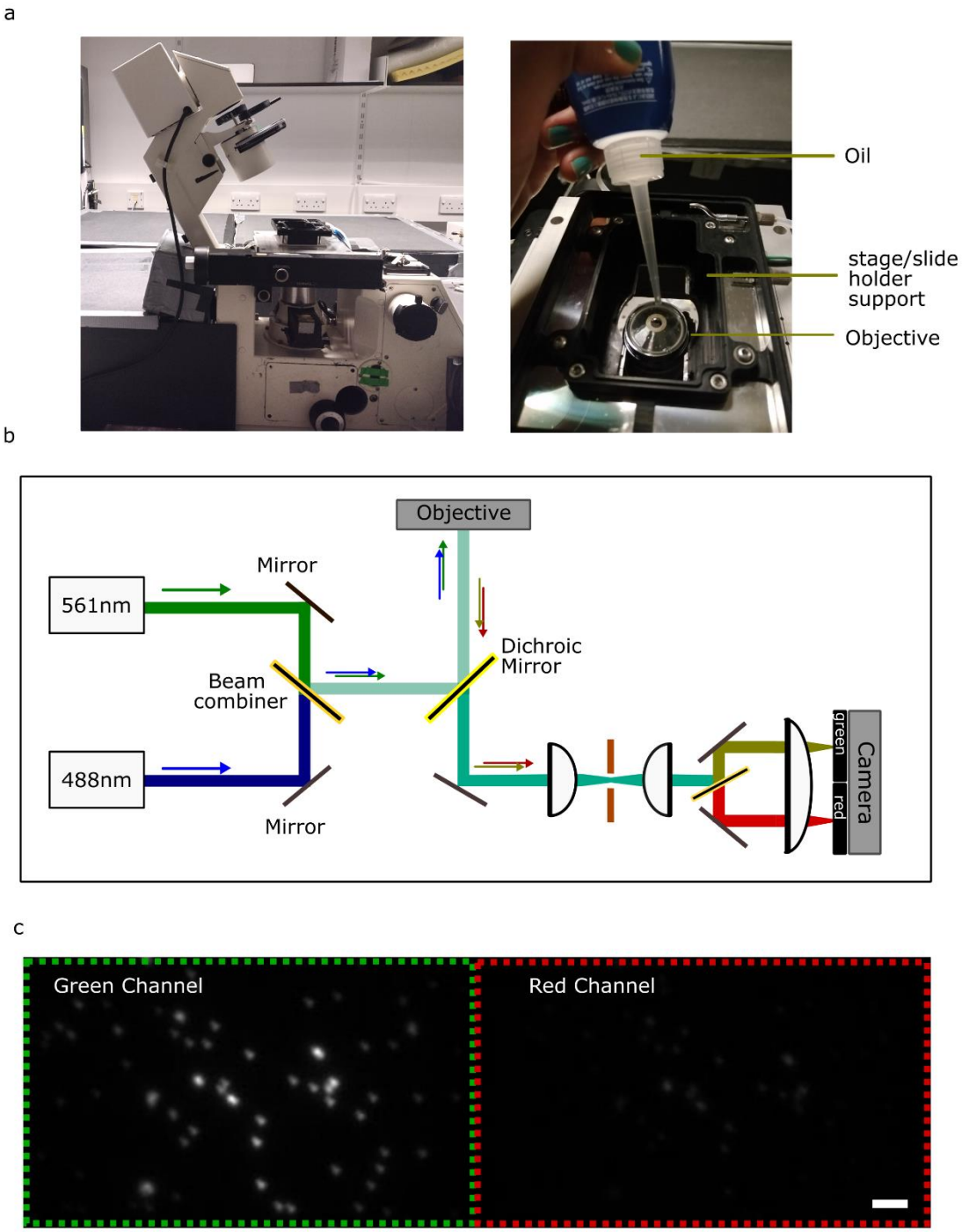

Figure 2-6: Slimfield microscopy

(a) Photograph single molecule Slimfield microscopy, on the left, the microscope body and, on the right, the objective and sample area (b) schematic optical path of the Slimfield microscope. (c) Green and red channels on the microscope field of view, respectively on the left and right of the image. Dotted frames and labels highlight the position of each channel. Green beads are visible on the green channel. 1 µm scale bar.

3.7.2. Microscope preparation

Control beads and field of view illumination using diluted at 1/1000 in PBS, supplied by ThermoFisher, with the following characteristics: Fluosphere carboxylates, modified microspheres, 0.2 µm orange fluorescent (540/560), 2% solids, in distilled water with 2 mM azide. And Fluosphere carboxylates, modified microsphere, 0.2 µm orange fluorescent (505/515), 2% solids. Laser alignment set to epi-illumination with micrometre set at 5 mm in the current set-up.

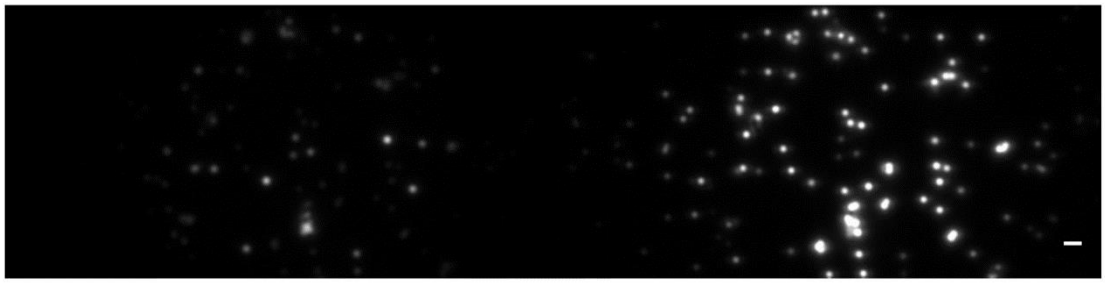

Figure 2-7: Mixed fluorescent beads used to optimise microscopy

The capture of Slimfield field of view for a sample of mixed fluorescent orange and green beads. 1 µm Scale bar.

3.7.3. Acquiring data

For CrGE *in vivo*: On the Slimfield microscope equipped with a 100X oil-immersion Nikon Plan Apo 1.49 NA objective lens, a CFP/YFP dichroic mirror (part number ZT442/514rpc, Chroma Technology Corporation) adapted to utilise 445 nm and 514 nm laser (Coherent Inc) with respectively 475 nm emission filter, 50 mm Diameter, 50 nm Bandwidth, OD 6 (Part-number 86-364, Edmund Optics Inc) and 543 nm emission filter, 25 mm Diameter, 22 nm Bandwidth, OD 6 (Part-number 67-032, Edmund Optics Inc).

The imaging was performed using the 445 nm at 13.5 mW laser power and the 514 nm laser at 14 mW, set on “continuous wave” for both. The microscope possesses a 300 mm tube lens for 53 nm/pixel resolution. Exposure time was set to 10 ms. Using the 445 nm laser, 100 frames were first acquired, and the shutter was triggered manually and programmed to stay open for 7 acquisition frames equivalents at 70 ms. In the acceptor channel, 1000 frames were acquired again and with the same manually triggered shutter system.

The donor/FRET channels were excited first followed by the acceptor channel. The image collected by an sCMOS camera (BSI Prime 95B) was split into two channels for blue and yellow channels side-by-side imaging. To avoid photobleaching effects, Slimfield data analysis was achieved using the first frames holding a strong and bright initial signal.

For CrGE2.3 *in vivo:* The CrGE2.3 (mGFP-mScarlet-I) FRET sensor expressed in BY4741 wild-type yeast was imaged as followed with a bespoke Slimfield single-molecule microscope set for epifluorescence (Wollman & Leake, 2015): 488 nm (Obis LS laser) and 561 nm (LX series laser), laser power were both set to 20 mW at the sample. The set-up held an EGFP/mCherry dichroic mirror (part number ZET488/561m, Chroma Technology Corporation) with the following emission filters: A 525/50 nm single-band bandpass filter (part number FF03-525/50, laser 2000 photonics, Ltd.) and a 604 nm laser bandpass filter (part number ZT594rdc, Chroma Technology Corporation).

The sample was quickly photobleached and 5000 frames were taken at 10 ms exposure (first 1000 to 2000 frames analysed).

Imaging aggregates: aggregate strains were imaged with a similar set-up on the bespoke Slimfield single-molecule microscope set for epifluorescence (Wollman & Leake, 2015): 488 nm (Obis LS laser) set to 20 mW at the sample. 1000 to 1500 frames were taken at 5 ms exposure.

3.8. Image and data visualisation

Confocal data images were analysed using Fiji (version: ImageJ2.3.0_Java 1.8.0_172). The Cell Magic wand plugin (Walker, 2016) was used to segment cells on DIC or brightfield channel and generate regions of interest (ROIs) for measurement.

An inbuilt plugin and a bespoke macro were developed to measure and calculate the average ratiometric FRET or *NFRET* parameter within each cell. Cell areas were also extracted using the bespoke macro.

The main analysis workflow was developed with Dr Jack Shepherd. The programme is coded in Python 3.0 and utilises the deep learning software YeastSpotter. (Lu et al., 2019) for cell segmentation and generates ratiometric maps from the raw data. Plots were generated using Python matplotlib (Hunter, 2007) and seaborn library (Waskom, 2021).

A MATLAB-based single-molecule analysis tool developed by Dr Adam Wolman was used to perform single-molecule analyses from data acquired using Slimfield microscopy.

3.8.1. Ratiometric FRET calculation measurement

Methods extracted from (Shepherd, Lecinski, et al., 2021) to define ratiometric FRET, and NFRET and to present the initial exploration to determine the advantages and inconvenient of both methods.

The intensities were corrected for autofluorescence by subtraction of the mean autofluorescence values found by imaging BY4742 wild-type cells in experimental conditions. As in previous work (Boersma et al., 2015) we defined the ratiometric FRET as I_F/I_D where where I_F is the intensity in the FRET channel under donor excitation and I_D is the intensity in the donor channel under donor excitation. Using this approach, bleed-through corrections are not required since they are manifest as a constant offset in the ratiometric FRET distribution, while in line with previous work with this FRET

sensor (Boersma et al., 2015) cross-excitation can be neglected as it is a minimal contribution (around 4% of the excitation peak).

We also analysed our data with another common approach using normalised ratiometric FRET (Mouton et al., 2020; Xia & Liu, 2001), defined as $NFRET = I_F/\sqrt{I_D I_A}$ where I_F and I_D are defined as above and I_A is the intensity in the acceptor channel under acceptor excitation. In general, for *NFRET* analysis to be valid, intensities must be corrected for background, bleed-through, and cross-excitation of the acceptor under donor excitation. Here, we estimated bleed-through to be <7% in our confocal microscopy given the filter sets used. Comparing the uncorrected *NFRET* with the ratiometric FRET still indicated qualitative agreement without bleed-through correction. In all cases, we corrected for background noise which was accounted for by subtraction of the mean background of a region of interest in each confocal microscopy image, and autofluorescence which was taken to be the mean of a wild type of dataset imaged under experimental conditions.

NFRET normalises the FRET efficiency signal to overcome variations in copy number between the acceptor and the donor. As both entities are synthesised together, this disparity can be due to maturation differences between the two fluorophores, quenching of molecules in particular conditions (pH), or due to degradation pathways in the cell. Therefore, using NFRET allows us to report with higher precision a corrected FRET efficiency. CrGE2.3 sensor has similar pH sensitivity and maturation kinetics between the two fluorescent proteins (the mScarlet-I and mGFP FRET pair) more favourable than the difference observed for mCerulean3 and mCitrine fluorescent proteins of the CrGE sensor. Therefore, we compared the result between ratiometric FRET and the normalised FRET ratio (NFRET) to correct for the unequal number of effective donors and acceptors in the pool of sensors expressed in the cells. Indeed, various parameters can influence the number of optically operational fluorescent proteins (e.g., maturation/degradation dynamics). Determining the NFRET eliminates differences between treated conditions affecting the components while retaining readouts from crowding.

3.8.2. CrGE Pixel maps and CrGE2.3 *in vivo* analysis

This section presents the analysis code developed in Python by Dr Jack Shepherd and used to explore data acquired subcellular ratiometric and FRET efficiency characterisation. Extracted from (Lecinski et al., 2021) and (Shepherd, Lecinski, et al., 2021).

Bespoke simulation software was written in Python 3 using SciPy (Virtanen et al., 2020), NumPy (Oliphant, 2006) and Matplotlib (Hunter, 2007). First, a canonical point spread function was found using the freely available Python library (Gohlke, 2020), and was down-sampled to create a point spread function (PSF) cuboid unit of (xyz) 50x50x100 nm voxels. A randomly sized ellipsoidal cell (Wollman & Leake, 2016) was placed in a 3D pixel grid where each pixel also had a side length of 50 nm, and within this was placed a spherical excluded volume to act as a vacuole. A point in this volume was selected and if found to be inside the cell but outside the excluded volume the locus was accepted. The canonical PSF intensity was then multiplied by a random factor between 0.9 and 1.1 to simulate variation in fluorophore brightness and a given fraction of the intensity was placed in the donor volume at the selected point, while the remaining intensity was given to the FRET volume. Finally, the canonical PSF intensity was multiplied by the ratio of the accepter to donor brightness, and again the brightness was scaled in the region 0.9-1.1. This process was performed until 105 fluorophores had been accepted. Finally, every voxel was given a background noise value taken from a Gaussian distribution with parameters found experimentally, and within the cell the voxels were additionally given an autofluorescence value, again the Gaussian distribution of which was found from the confocal imaging data of wild type yeast in experimental conditions. To simulate the excluded membrane volume, the autofluorescence region was extended beyond the volume in which fluorophores were placed.

CrGE2.3 tracks and FRET read-out were obtained using PySTACHIO (Shepherd, Higgins, et al., 2021) with snr_min_threshold=0.5 and struct_disk_radius=9 in Alternating Laser Excitation (ALEX) mode. We relaxed our usual constraints on trajectory length because ALEX mode with 10 ms exposure allows considerable diffusion between successive

captures in one channel and thus trajectory linking is compromised in this single-molecule regime. Following PySTACHIO analysis, we began by finding the translation-only registration transformation between channels using brightfield images and the pystackreg library (Thévenaz, 2021). We then applied the registration transformation to the trajectories identified by PySTACHIO as well as to the fluorescence stacks. We performed colocalisation using PySTACHIO with the distance cut-off set to 2 pixels and the overlap integral set to 0.75 – this is the "true" colocalisation metric, with the distance cut-off used to decrease computational cost by not calculating overlap integrals for foci which will fall beneath the overlap integral threshold. If spots in the donor and acceptor channel were accepted as being one FRET sensor, we then estimated the FRET position using the mean position of the donor and acceptor and found the summed intensity with local background correction as in PySTACHIO. Finally, we measured the normalized FRET parameter NFRET:

$$\mathrm{NFRET} = \frac{I_{FRET}}{\sqrt{I_D I_A}}$$

which has been reported as a crowding proxy previously (Mouton et al., 2020). These values were plotted using matplotlib (Hunter, 2007). Data analysis here was performed using a bespoke Python routine which made use of scikit-image (Van der Walt et al., 2014), Pillow (Clark, 2015), NumPy (Oliphant, 2006), and openCV (Bradski, 2000) for image data handling.

To generate heat maps, the ratiometric FRET values in the stacks of images were calculated for each pixel rather than an average fluorescence intensity. Relative molecular stoichiometry of the dye was estimated either with conservation of energy considerations or by normalising it to the highest intensity pixel in the acceptor channel. For conservation of energy stoichiometry estimation, the conserved energy quantity was taken to be

$$E_{conserved} = hc\left(\frac{I_D}{\lambda_D} + \frac{I_F}{\lambda_A} + \frac{I_A}{\lambda_A}\right),$$

where h is Planck's constant, c is the speed of light, I_D, I_A, and I_F are the intensities in the donor, acceptor, and FRET channels respectively, and λ_D and λ_A are the peak emission wavelengths of mCerulean3 and mCitrine respectively. The E value was calculated for each pixel in the region of interest, and the resulting heatmap was normalised to the highest value to give an approximation of the relative copy number.

Chapter 3. Sensing crowding in yeast

1. Introduction

In this study, I used a FRET-based macromolecular crowding sensor, called CrGE (Liu et al., 2018) to sense hyper-osmotic shock mainly induced by sodium chloride salt (NaCl). This type of stress induces a rapid change in extracellular ionic strength with a consequent effect on molecular crowding within cells. The high ionic strength medium overwhelms ions import and export and leads to a sudden decrease in cell volume with a concomitant increase in crowding (Hohmann, 2015a).

This chapter aims to present the crowding sensor used in this study and report new insights on budding yeast physiology and the influence of glucose availability on crowding, and during cellular growth.

I also present the development of ImageJ-based tools (macro) to semi-automate measurement of ratiometric FRET and cell area in bio-imaging images. This initial work led the direction of my research toward assessing subcellular dynamics and the development of methods of investigation and analysis to observe them (see Chapter 4).

The narrative of this chapter was constructed using parts of the data and writing sections from two published papers associated with my thesis work:

Shepherd, J. W., Lecinski, S., Wragg, J., Shashkova, S., MacDonald, C., & Leake, M. C. (2021). Molecular crowding in single eukaryotic cells: Using cell environment biosensing and single-molecule optical microscopy to probe dependence on extracellular ionic strength, local glucose conditions, and sensor copy number. Methods, 193, 54–61.

Lecinski, S., Shepherd, J. W., Frame, L., Hayton, I., MacDonald, C., & Leake, M. C. (2021). Investigating molecular crowding during cell division and hyperosmotic stress in budding yeast with FRET. In Current Topics in Membranes (Vol. 88, pp. 75–118). Academic Press.

2. Crowding and osmotic shock

2.1. The CrGE sensor

Expressed in *S. cerevisiae* the cytoplasmic CrGE crowding FRET based sensor (Boersma et al., 2015) uses fluorescent cyan protein mCerulean3 (Markwardt et al., 2011) as a donor and the yellow mCitrine (Zacharias et al., 2002) as the acceptor. See Figure 3-1. In low crowding, the donor and acceptor are separated such that non-radiative energy transfer is low, energy is emitted by the donor fluorophore, and low FRET efficiency is observed. A crowded environment will bring the two dyes closer to each other promoting non-radiative energy transfer and emission by the acceptor fluorophore, hence a higher FRET efficiency.

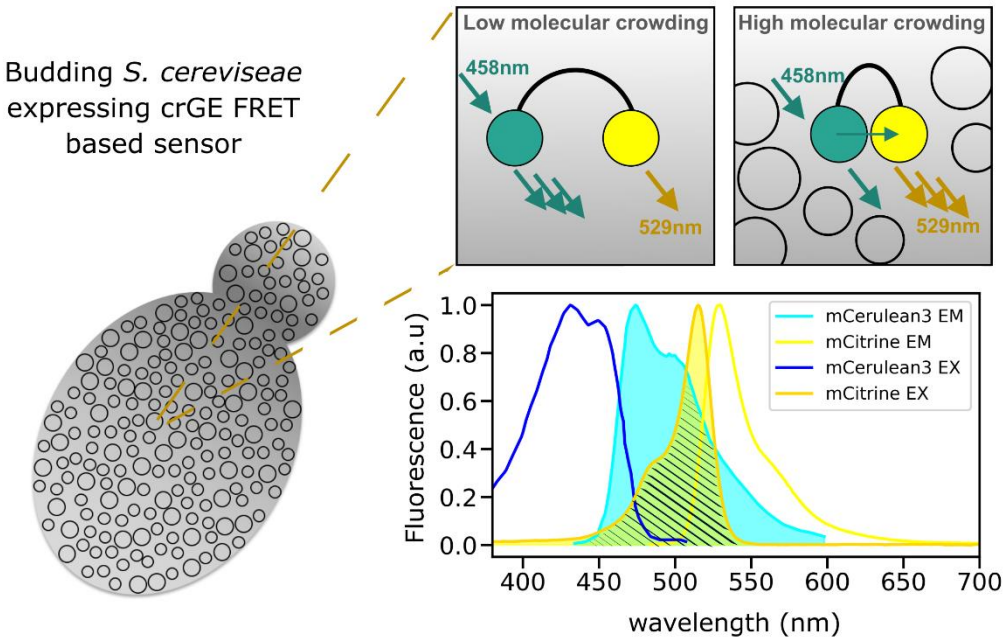

Figure 3-1: Presentation crowding sensor.

Schematic representation of the CrGE FRET-based sensor and the spectrum of excitation/emission for both probes constituting the CrGE sensor, mCerulean3 (Markwardt et al., 2011) the donor, and mCitrine (Zacharias et al., 2002) the acceptor.

2.2. NaCl induced hyperosmotic shock

Hyper-osmotic stress is commonly used in biological research to investigate cellular stress response and cell survival strategy. In detail, higher osmolarity in the environment than in the intracellular milieu generates a physico-mechanical pressure forcing immediately the water to flow out of the cell through the semi-permeable plasma membrane (Alfieri & Petronini, 2007; Hohmann, 2002; Morris et al., 1986). This is a common cellular response observed both in bacteria such as *E. coli* or eukaryotic cells such as yeast or mammalian cells (Ho, 2006; Hohmann, 2015b; Record Jr et al., 1998). Three different stages built the stress response and cellular defence mechanism: first, the immediate cellular changes resulting from the immediate cell volume and water content reduction or shrinkage of the cell (Hohmann & Mager, 2007), with high osmolarity in the surrounding environment cells rapidly lose intracellular water inducing a loss of turgor and the shrinkage of cells, instantaneously leading to the raise of macromolecular crowding in the intracellular environment with consequences in molecule mobilities and metabolic actions. In eukaryotic cells, the cytoskeleton can collapse with the depolarisation of actin patches observed and the reorganisation of the filaments (Chowdhury et al., 1992). Secondly, the repair and recovery process is set in motion via the activation of specific MAP-kinase (Mitogen-Activated Protein kinase) cascade pathways, while the cell division is arrested. The arrest has been reported to occur at either the G1 or G2/M stage with the down regulation or inhibition of key regulating kinase such as Cln3p or Cln2p (Bellí et al., 2001). The glycerol channel Fps1p closes to avoid its export out of the cell and maximise its intracellular accumulation to regain turgor (Hohmann, 2002). Hyperosmotic stress in eukaryotic cells and especially in mammalian cells causes cell shrinkage due to the osmotic efflux of water leading to increases in intracellular ionic strength (Alfieri & Petronini, 2007). The cell volume recovery is also mediated by the ion transport systems (Lang et al., 1998; McManus et al., 1995). Potassium homeostasis for example plays an important role to ensure survival. It helps regulate the intracellular pH, cell volume and plasma-membrane potential (Bubnová et al., 2014). A high concentration of potassium is required for cell division and accordingly efficient uptake of potassium occurs after osmotic stress to

promote cellular growth (Bubnová et al., 2014). In yeast cells the high-osmolarity glycerol (HOG) MAP-kinase pathway is triggered to initiate glycerol synthesis, this pathway also leads to the activation of ENA1, a gene coding for a sodium pump (Proft & Serrano, 1999), and also regulates transcription of the GPD1 coding for a dehydrogenase (glycerol 3-phosphate dehydrogenase) (Albertyn et al., 1994) allowing the *de novo* biosynthesis of glycerol and contributing as well as the efflux restriction to rapidly increase the concentration of glycerol in the media (Albertyn et al., 1994). These metabolic modulations finally allow the cell to progressively regain resources, to reach a new equilibrium into a viable physiology and a metabolism capable of sustaining cellular growth (Brewster & Gustin, 1994).

With yeast strain expressing the CrGE sensor, I first verified its capability to sense macromolecular crowding under salt induced hyper osmotic stress. Initially by quantifying the FRET efficiency (using the ratiometric FRET method – see Chapter 2.3.8) and area changes in cells experiencing osmotic stress (Figure 3-2).

At 0 M NaCl, cells are in a low-stress condition, under exposure to 1 M NaCl crowding increases, evidenced by the ratiometric FRET increasing by 13.7% (Figure 3-2.a and b) while measurable cell area is reduced by around 21% (Figure 3-2.c), consistent with previously found values (Hohmann, 2015a), and due to water being mechanically forced from the cell by osmotic pressure (Hohmann, 2002).

As I first used the FRET sensor, I also worked to optimise post-acquisition cell segmentation methods and measurements. Using ImageJ-based macro I coded a small program that semi-optimised segmentation and intensity measurements from fluorescence channels of interest: here the donor and FRET channel one, to calculate the ratiometric FRET (ratioFRET), or including the acceptor channel if calculating the NFRET (see Chapter 2.3.8). The macro workflow developed to automate this process, the ratioFRET is presented in Figure 3-3. See also the full code in Appendix ap.0-4.

Cells were initially segmented using the cell magic wand tool plugin (Walker, 2016) that detects cell edges, or manually with ImageJ in-built selection tool. Stored outlines were utilised by a bespoke macro measuring intensities and areas.

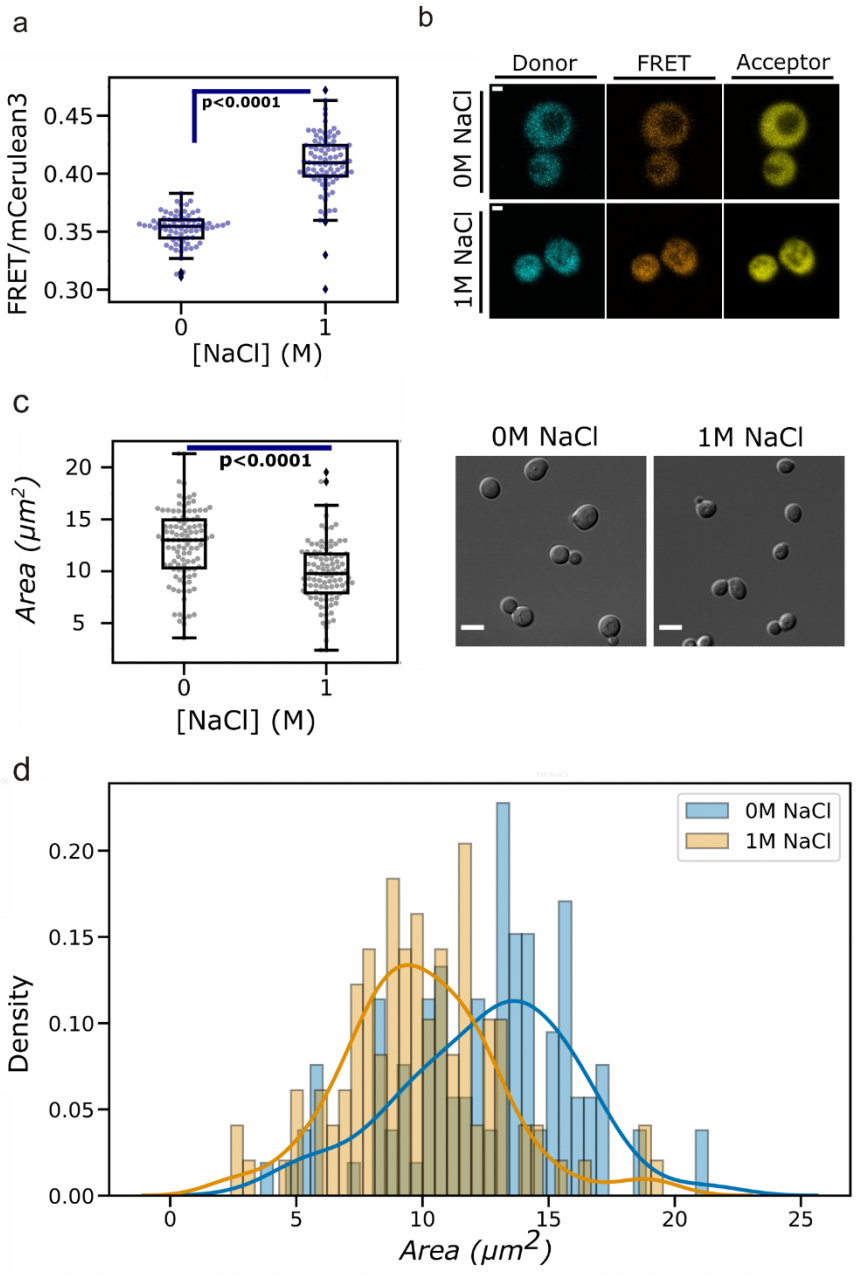

Figure 3-2: CrGE dynamic FRET sensor

(a) Left: jitter plot of FRET/mCerulean3 values for yeast grown in 2% glucose and measured in the absence (0 M) and presence (1 M) of NaCl, including box plot and significance testing. (b) Fluorescence micrographs of CrGE in both 0 M and 1 M NaCl, displaying from left to right the donor, FRET, and acceptor channel. Scale bar: 1 µm. (c) On the left: jitter plot of the same data with box plotting and significance testing as in panel b. On the right: DIC images of the cells in low (0 M) and high (1 M) ionic strength

buffer. Scale bars: 5 µm. (d) Histogram with the fit of cell area imaged in 0 M NaCl (blue) and 1 M NaCl (orange) conditions and grown in 2% glucose. Representation of the data presented in panel c to highlight the cell size reduction typically observed under hyperosmotic stress, the histogram allowing the visualisation of the size distribution observed for each condition. Areas are given in µm^2, with data fit by Kernel Density Estimation (KDE) (Leake, 2014) using the seaborn library function distplot (Waskom, 2021). KDE bandwidth is set using the rule-of-thumb Scott's (Jones et al., 1996; Scott & Terrell, 1987).

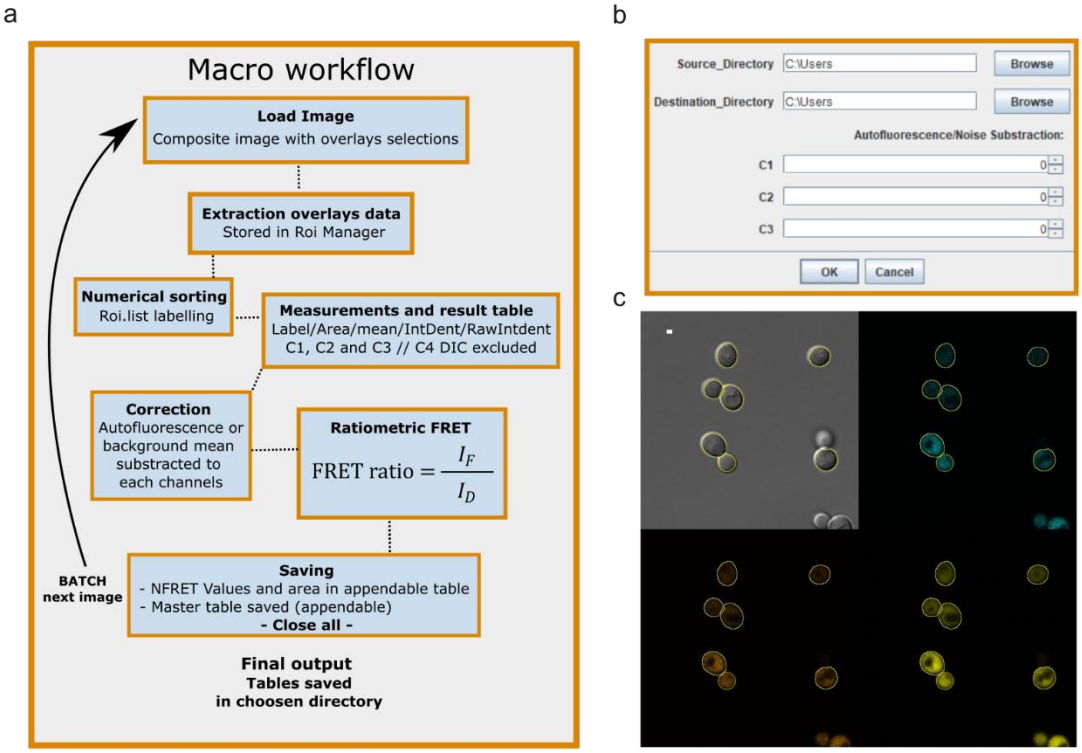

Figure 3-3: ImageJ macro for ratiometric FRET

(a) Workflow description of the ImageJ macro used to analyse data from the confocal microscope. (b) GUI of the ImageJ macro used to analyse data from the confocal microscope. (c) Visualisation composite image acquired, cells outline generated either with the selection tool or the cell magic wand tool plugin (Walker, 2016) and saved as metadata in the form of overlays (inactive selections), the image is composed of four channels, C1 (blue): mCerulean3 excitation, the donor; C2 (orange): the FRET channel; C3 (yellow): mCitrine, the acceptor, C4 (grey): DIC visual. Macro code in Appendix ap.0-4.

The strong cell size reduction observed during hyper-osmotic stress is occurring instantaneously in presence of NaCl (with 1 M tested here). Thus, this morphological change forces the cell content to a smaller volume, automatically inducing confinement effects such as crowding. This result confirms the CrGE sensor is efficiently capable to detect crowding upshift. In the next session, I looked for other elements influencing macromolecular crowding and quantified the impact of glucose availability during cellular growth on macromolecular crowding.

3. Cell growth and crowding

3.1. Glucose and basal molecular crowding

Glucose is a nutrient for eukaryotic cells, including yeast, and is used to produce energy, molecules of ATP, essential to ensure all "active" metabolic activities (Gonçalves & Planta, 1998; Teusink et al., 2000). In the literature, recent studies showed that sugar starvation influences the diffusivity of molecules (Joyner et al., 2016). This work tracked two large molecules, called mRNPs and chromatin, in yeast cells starved of sugars. During starvation, both molecules were shown to be less able to move around in their respective localisation in the cell: chromatin is the complex of DNA and proteins forming the chromosomes in the nucleus of eukaryotic cells (Comings, 1972), while mRNPs, standing for messenger ribonucleoproteins, are found in the cytoplasm (Hieronymus & Silver, 2004; Minich & Ovchinnikov, 1992). This observation appears to be due to water loss and cell size reduction reported in cells starved for glucose, therefore also inducing macromolecular crowding shift (Albers et al., 2007; Pluskal et al., 2011; Turner et al., 2012). The cells become smaller, leading to a more crowded intracellular environment. This phenomenon was described in various eukaryotic cells such as yeast or mammalian cells (Guo et al., 2017; Mourão et al., 2014; Winderickx et al., 2003) but also for bacteria cells (Parry et al., 2014; Shi et al., 2021). Few studies have suggested the physical changes triggered by starvation are not only a consequence of the stress but also a

critical response to ensure cell survival (Agozzino et al., 2020; Franzmann & Alberti, 2019; Janapala et al., 2019).

Stressed cells can also enter a quiescent state, a reversible state where the cell cycle is arrested and metabolic function is reduced to ensure survival, generally, cells re-enter a proliferation state once they meet more favourable conditions to sustain cellular growth (De Virgilio, 2012). The cytoplasm of quiescent cells was shown to become more acidic (Munder et al., 2016; Musgrove et al., 1987), which causes many proteins to bind to each other and form large clumps, altering the nature of the intracellular environment (Broach, 2012; Munder et al., 2016; Rabouille & Alberti, 2017). Munder and collaborators' work revealed that the interior of cells undergoes a transition from a fluid-like state to a solid-like state in restricted environments (Munder et al., 2016). In yeast and other eukaryotes, the overall intracellular acidification induced by energy starvation was also shown to trigger the agglomeration and compaction of several enzymes (Munder et al., 2016; Petrovska et al., 2014; Rabouille & Alberti, 2017).

Other effects were also reported in correlation to the cellular stress response and tight survival behaviours, such as the reversible formation of membrane-less compartments in eukaryotic cells (van Leeuwen & Rabouille, 2019), the lipid droplets modulation in size and number (Kurat et al., 2006), and the reported enhancement of plasma membrane invaginations leading to a wrinkled structure of the membrane, especially during hyperosmotic stress or starvation (Morris et al., 1986; Simonin et al., 2007; Slaninová et al., 2000). Furthermore, the vacuole in yeast has been reported to increase in size in cells depleted of energy (Desfougères et al., 2016; Joyner et al., 2016).

These stress changes are associated with cell morphology, size changes and intracellular spatial reorganisation. All can be associated with crowding dynamics. Therefore, methods monitoring these changes have been developed as reporters to quantify crowding. The reorganisation of ribosome distribution was observed in starved cells for example (Marini et al., 2020). For example, in starved cells ribosomes are excluded from cell areas and stress-induced membrane-less compartments, which increases ribosome density locally in the cytoplasm (Marini et al., 2020). Measuring the local density of

ribosome become therefore informative to identify crowding state changes. Using this method crowding was identified as one of the factors responsible for promoting the assembly of eIF2B filaments (Marini et al., 2020). Generally, the formation of large protein assemblies was suggested as a survival strategy to protect proteins from extended damage (Franzmann & Alberti, 2019; Nüske et al., 2020), to generate a reserve and save resources in the long term (Franzmann & Alberti, 2019; Nüske et al., 2020; Petrovska et al., 2014), such as the formation of a pool of actin reserves (Sagot et al., 2006). These assemblies during nutrient stress can downregulate protein activity to equally preserve resources (Bleoanca & Bahrim, 2013; Miura & Yanagita, 1972; Riback et al., 2017). Glucose-related metabolic activities are therefore associated with a range of molecular rearrangements influencing the spatio-temporal organisation in cells.

These can influence the readout of the ratiometric FRET sensor presented. These changes can impact the global crowding dynamics of the cells. The time scale of these dynamics, the maturation of fluorophores, the acidification of the environment or degradation pathways can influence the optical properties of the sensor and thus the FRET read-out. The normalisation of the results becomes often necessary to validate the significance of the changes observed (see results below and in Appendix ap.0-2). Alternative methods to assess crowding dynamics *in vivo* and with fluorescent reporters exist. Mainly, diffusive properties have been assessed as an indicator of environmental crowding (Bulthuis et al., 2023). Accordingly, the CrGE sensor and any fluorescent proteins can be tracked in the cytoplasm to access diffusive information. Other techniques could be considered to access the diffusion information, such as FRAP (Fluorescence Recovery After Photobleaching) (Jacobson et al., 1976). Diffusion accessed this way can indeed give information on the local crowding and confinement state experienced by molecules in the area tested (Cai et al., 2022; Dey et al., 2021; Lippincott-Schwartz et al., 2018). But other methods can also indicate changes in the microenvironment such as measuring the effective dry mass in a cell population (Löwe et al., 2020; Michel et al., 2019; Rana et al., 2020).

In essence, cellular stress and glucose availability can induce a whole range of morphological and physico-chemical changes (e.g., pH, dry mass, ions strength), which

can impact the performance of the sensor. The combination methods to access crowding such as the ones mentioned above can help us decouple these effects, to isolate the crowding information.

To first investigate whether glucose availability during growth affects the molecular crowding at low osmotic stress, cells were grown at 1%, 2% or 4% glucose and imaged in 50 mM NaPi as described in previous work with the sensor (Mouton et al., 2020). Cells grown in 1% glucose showed the highest ratiometric FRET, with a small shift of -2.7% between 1% and 2% glucose growth conditions (Figure 3-4). When analysing the same data with *NFRET* we find that the shift is approximately 0.3% if the comparison is based on the mean *NFRET* value or 0.6% if the median is used as the reference (Appendix ap.0-2). The difference between 1% and 4% glucose conditions is more dramatic, with the ratiometric FRET reduced by 11.6% and the NFRET value reduced by 4.3% (Appendix ap.0-2). Therefore, across conditions, we find a reduction in molecular crowding with increasing local glucose concentration. Although in the main text, we include data from one set of experiments, we have taken multiple datasets and note that they all demonstrate a statistically significant difference in crowding between yeast grown in 1% and 4% glucose. The difference between 1% and 2% is more variable and would require further investigation (Figure 3-5.a).

Perturbation of the cells with 1 M NaCl also leads to different ratiometric FRET values. Specifically, the cells grown at 4% glucose undergo a higher relative shift in ratiometric FRET than those grown at 1% or 2% glucose, but the FRET ratio overall remains below that in the lower two glucose cases (Figure 3-4 and Figure 3-5.a). It appears that while the osmotic shock produces an increase in ratiometric FRET of 10-15% in each case, the underlying metabolic state of the yeast remains important in determining the final crowding state.

To cope with changes in external osmolarity, the High-Osmolarity Glycerol (HOG) pathway mediates the regulation of glycerol production and water release, changing the properties of the cytoplasm and potentially impacting crowding (Saito & Posas, 2012). Hyperosmotic conditions cause glycerol accumulation within the cell to maintain cell size and water homeostasis (Petelenz-Kurdziel et al., 2013). The mechanical pressure

that appeared within the cell leads to an increase in macromolecular crowding. However, the glucose conditions we used do not seem to influence the cell volume (Figure 3-4.b and Figure 3-5.b).

We hypothesize that the overnight growth under lower glucose conditions (1% and 2%), leads to lower water content within the cell compared to that in cells grown with 4% glucose. As 4% glucose would mean higher external osmolarity than 1% and 2%, therefore, the changes in crowding may be caused not only by glycerol/water ratio shift but also trehalose and other osmolytes concentrations as has been suggested for respiring cells (Babazadeh et al., 2017). This is supported by the relative behaviour of the different samples upon application of 1 M NaCl (Figure 3-4.d). The FRET/mCerulean3 values increase by approximately the same proportion but remain lower in the 4% glucose case, indicating that there is a fundamental water-osmolyte ratio difference between the samples.

Finally, Figure 3-4.c displays a heatmap with Pearson test correlation performed for each glucose availability condition to assess if a correlation exists between FRETratio and area. For each condition, there is no clear correlation with correlation coefficient values all approaching 0.

As a side note, some Kernel Density Estimation (KDE) fits of these data (Figure 3-4.a and b) look a little bimodal, possibly as a result of bet-hedging behaviour as seen in budding yeast previously (Bagamery et al., 2020), where authors note that bet-hedging across the population is non-mutational and bimodal. In high-glucose conditions, bimodal differences may help to guard the population against glucose deprivation. However, the extent to which subcellular crowding is heterogeneous is unclear, and it is unknown how or if crowding is clustered around subcellular features that use molecular machines or ion pumps to regulate local conditions. Previous work has mostly used analysis techniques which rely on ensemble average fluorescence signal values over a cell or region of interest to calculate a ratiometric FRET value (Boersma et al., 2015; Mouton et al., 2020). However, rapid super-resolving single-molecule optical microscopy called Slimfield (Plank et al., 2009) has been extensively used in single and dual-colour imaging experiments (Badrinarayanan et al., 2012; Reyes-Lamothe et al., 2010; Shashkova et al., 2021; Wollman et al., 2017) to perform tracking of individual

molecules, find their localisation and estimate total copy numbers on a cell-by-cell basis (Shashkova & Leake, 2017).

The osmolarity of glucose is dependent on the number of molecules in a solution (Stigter, 1960). 1 M solution of glucose is a 1 osmolar (1 osmol) solution whereas 1 M solution of NaCl decomposed in Na+ and Cl- ions is 2 osmolar (2 osmols) and 1 M sorbitol classically used to induce osmotic stress is a 1 osmolar (1 osmol). The osmolarity of 4% glucose is 0.22 osmole/litre, 2% glucose is 0.11 osmole/litre and 1% is 0.055 osmole/litre. The concentration of NaCl and sorbitol typically used to induce osmotic crowding upshift is 1.5 osmolar to 2 osmolar equivalent, while the osmolarity at 4% glucose is 0.22. This is considerably smaller, almost 7 times smaller and representing only 14.66% of 1.5 M sorbitol osmolarity (1.5 osmols) and 11% of 1 M NaCl osmolarity (2 osmols). Compared to 1% or 2% glucose, the osmolarity of 4% glucose is insufficient to induce a significant cell size shift generally associated with the crowding upshift under osmotic pressure as shown in Figure 3-4-b. This suggests that the effect observed at 4% cannot only be explained by the effect of the osmolarity of glucose but also by the metabolic consequence of glucose availability.

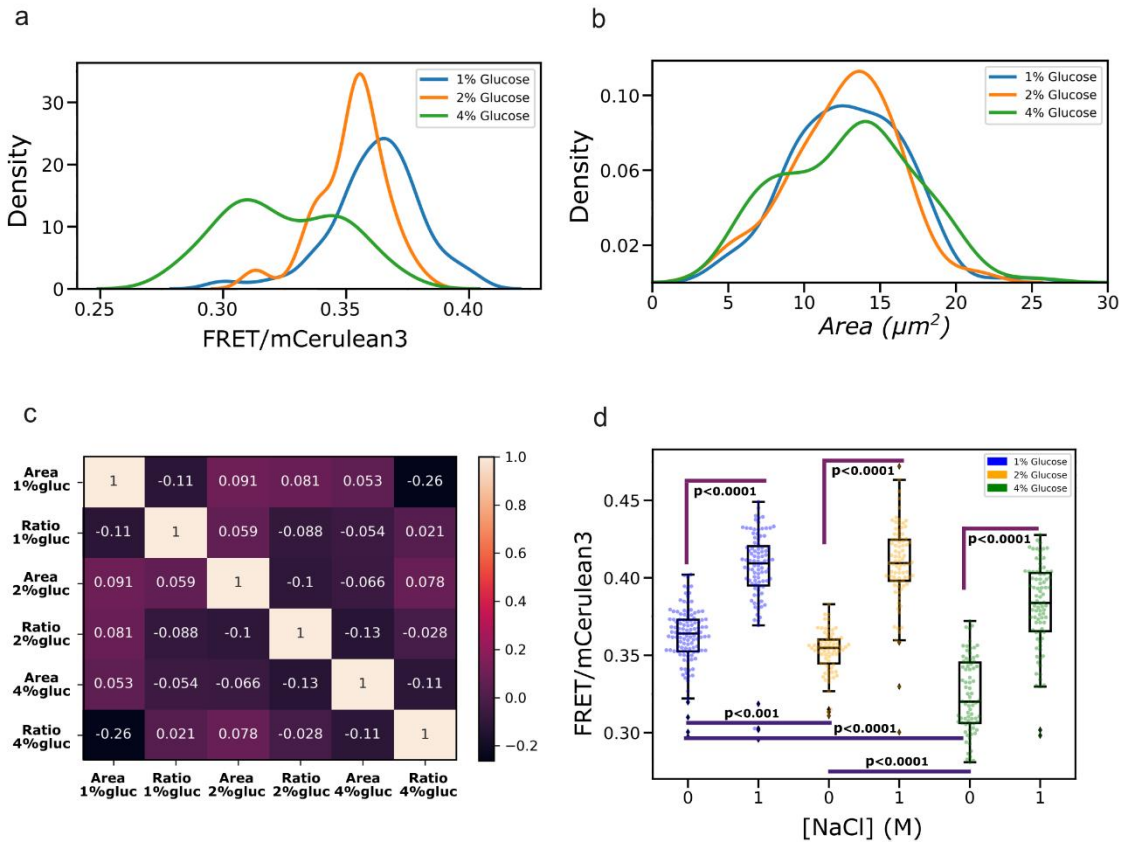

Figure 3-4: Glucose availability and crowding

(a) Kernel density estimates (KDEs) of the ratiometric FRET distribution for cells grown in 1%, 2%, and 4% glucose conditions and imaged at 0 M NaCl. For all conditions N>100. For histograms and the raw data associated see Appendix ap.0-3 (b) KDE of the cell size distribution, with area in μm^2, for cells grown in 1%, 2%, and 4% glucose and imaged at 0 M NaCl. Lines are given by a KDE fit. See Appendix ap.0-3 for histograms and the raw data associated (c) Correlation heatmap between area and ratioFRET measured in each glucose condition, pairwise Pearson correlation coefficient between all datasets using the seaborn library (Waskom, 2021) and displaying within each square Pearson standard correlation coefficient (d) Jitter plot showing FRET/mCerulean3 at high (1 M) and low (0 M) salt concentration for cells grown at 1%, 2%, and 4% glucose and imaged in 50 mM NaPi. Here as we perform 6 *t*-tests we corrected the accepted p value via the Bonferroni method (Dunn, 1961), thus here p=0.0083. Boxes represent the interquartile range (IQR), with bars extending 1.5*IQR from the upper and lower quartile. Diamonds indicate data outside this range.

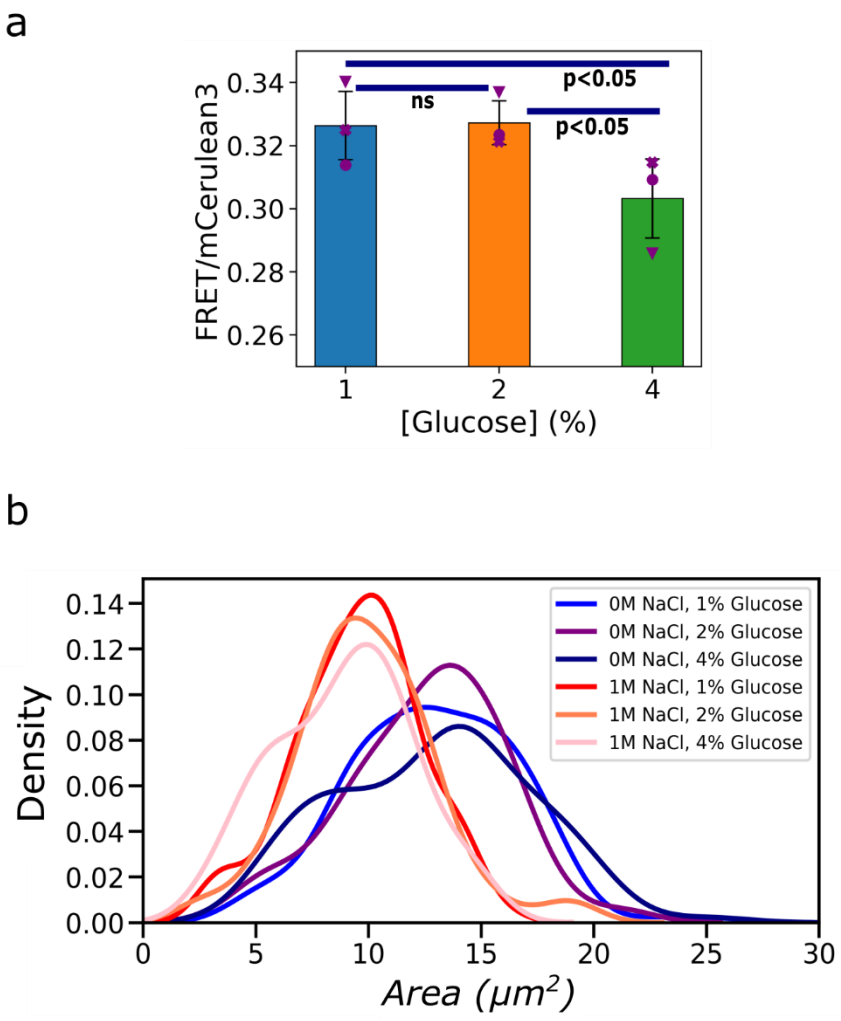

Figure 3-5: Osmotic stress and crowding

(a) Experiment repeats. Circles, triangles and crosses indicate the experiment was performed on the same day with the same overnight liquid culture. (b) Area measurements at 0 M and 1 M NaCl for all glucose conditions (1%, 2% and 4%). Lines are KDE fits.

3.2. Crowding on budding yeast: mother cell vs daughter cells

To try to understand if there is a crowing dynamic associated with cellular growth, I compared mother cells and daughter cells during budding, when both cells were still attached and connected. Budding is a known asymmetric process therefore this

comparison aims to assess if the observed polarisation and asymmetry between dividing *S. cerevisiae* influence the crowding environment. We expressed the CrGE crowding sensor and grew cells to mid-log phase (OD_{600} = 0.4 - 0.6) in synthetic complete media containing relevant glucose concentration and performed confocal microscopy. Figure 3-6 shows the average ratiometric FRET characterised between mother cells and daughter cells/growing buds. This analysis showed a similar FRET readout for mother cells and daughter cells with a mean ratioFRET of 0.347 and 0.344 respectively. Interestingly the cell size distribution shows daughter cells to be 35.4% smaller than mother cells with respectively a cell mean area of 14.453 μm^2 against 5.124 μm^2 (Figure 3-6.a and b). We found that for exponentially dividing cells, the individual cellular area was not correlated with FRET (Figure 3-6.c and d), consistent with the essential role of crowding stability in cellular integrity and survival (Mouton et al., 2020; Van Den Berg et al., 2017). However, there was a greater range of ratiometric FRET values found for smaller cells, which includes the growing daughter cells and buds (Figure 3-6.c). This extended variability for cells size at the lowest range can notably be the consequence of technical issues, small bud tends to grow out of focus in the imaging field of view, on a different plan than the mother cell and potentially resulting in less accurate read-out from increased noise in smaller volumes. Any biological interpretation remains therefore hypothetical. Under this context, one hypothesis is that, if true, the variability could be due to a lower cell volume, leading to smaller cells having a greater sensitivity to their immediate environment during initial growth. Moreover, in growing cells, the stage in the replication cycle may be correlated with crowding and the transport of large materials from one cell to another such as inherited organelles and may lead to relatively short-term crowding variability.

Figure 3-6.d shows two sub-populations of budding yeast plotted against the bud area. This analysis is split into two groups, the first group displayed higher ratiometric FRET in the mother cell than in the daughter cell and the second group where lower ratiometric FRET was measured in the mother cell than in the daughter cell. For those two categories, we see that cell areas between the two conditions are statistically equivalent with no statistical differences as measured by both Student's *t*-test (Kalpic et al., 2011) and the non-parametric Brunner-Munzel (Brunner & Munzel, 2000) test between the

two populations. We, therefore, conclude that the cell size during normal growth is not a predictive factor for subcellular crowding and confirm a relative stability of crowding during cellular growth, for cells budding. This is coherent with the crowding stability previously observed between young and old cells (Mouton et al., 2020).

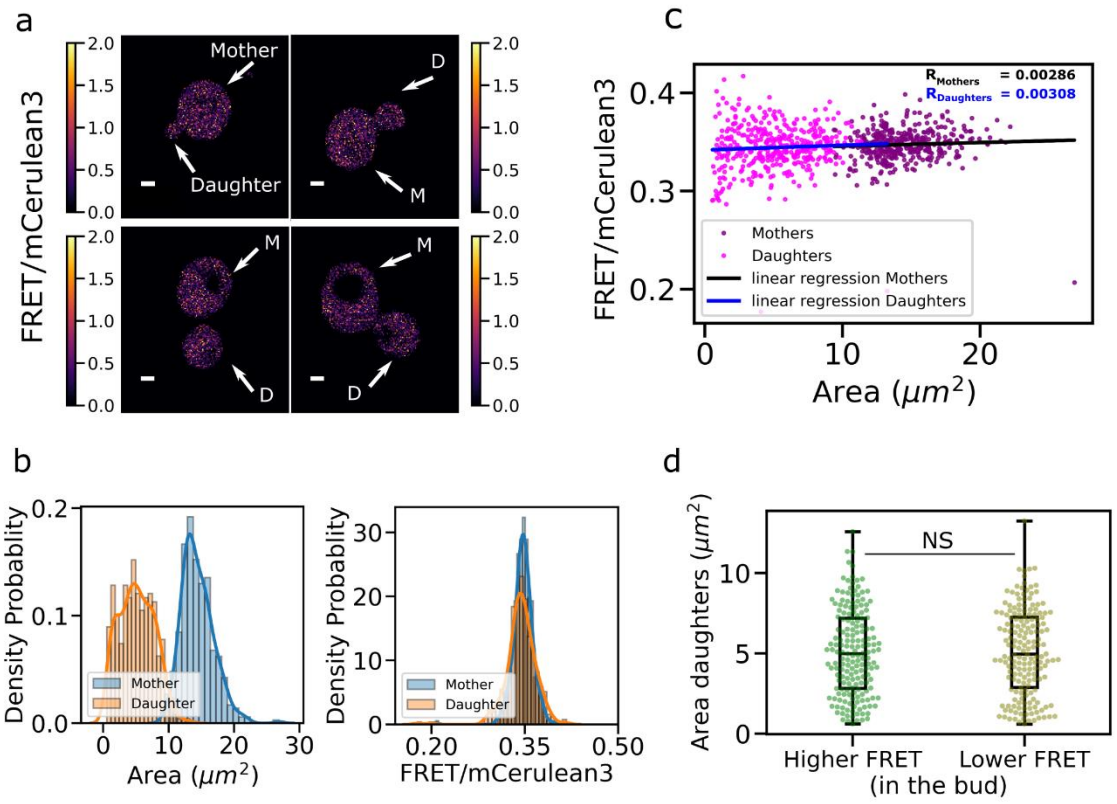

Figure 3-6: Mother and daughter crowding stability

(a) Micrograph of the CrGE ratiometric FRET (FRET/mCerulean3) maps of the budding yeasts analysed, with white arrows to show the mother cell and the daughter cell of each budding yeast. (b) Scatter plot of mother and daughter cell ratiometric FRET against cell area. (c) From left to right, histograms comparing the cell area between mother cells and daughter cells and comparison of the FRET efficiency between mother cells and daughter cells, R-squared values from respective linear regression indicated on the top-right of the figure. (d) Crowding and cell size dependence, comparison between mother cells and daughter cells. Two populations of cells were measured, one with buds displaying a higher FRET efficiency than their mother cells, and the other with buds displaying a lower FRET efficiency than their mother cells.

4. Analysing plasma membrane region

The sensor does not localise to the lumen of the vacuole; therefore, the vacuoles represent an excluded volume with no fluorescence signal. I performed a control analysis to assess the influence of the vacuole as an excluded volume. I measured fluorescence intensity in the cell for each image (see imaging conditions in Chapter 2 section 3.5.2) including or excluding the vacuole from the segmentation mask. I then calculated and compared the average ratiometric FRET of cells including or not the vacuole in the volume measured (See Figure 3-7.a). This analysis showed no significant difference between the conditions for the same dataset.

To identify sub-cellular regions cluster of crowding in the cytoplasm, I focused first on measuring crowding in proximity to the plasma membrane. I have developed a macro able to generate ring shape outlines of customised width around the identified cell edges (see Figure 3-7.b and code in Appendix ap.0-5). Using this macro, I targeted the region in contact with the plasma membrane, a region potentially interesting as key to various trafficking events (e.g., endocytosis, signal pathway, protein sorting at the plasma membrane) all of which could influence crowding at a subcellular level.

This analysis showed however no significant difference in ratioFRET measured between the near plasma membrane region, the remaining volume in the cytoplasm or the whole cell volume (Figure 3-7.b). This analysis did not show the expected result however it has allowed the development of an interesting macro which can generate customisable ring-shaped segmentation masks around identified cells in the image.

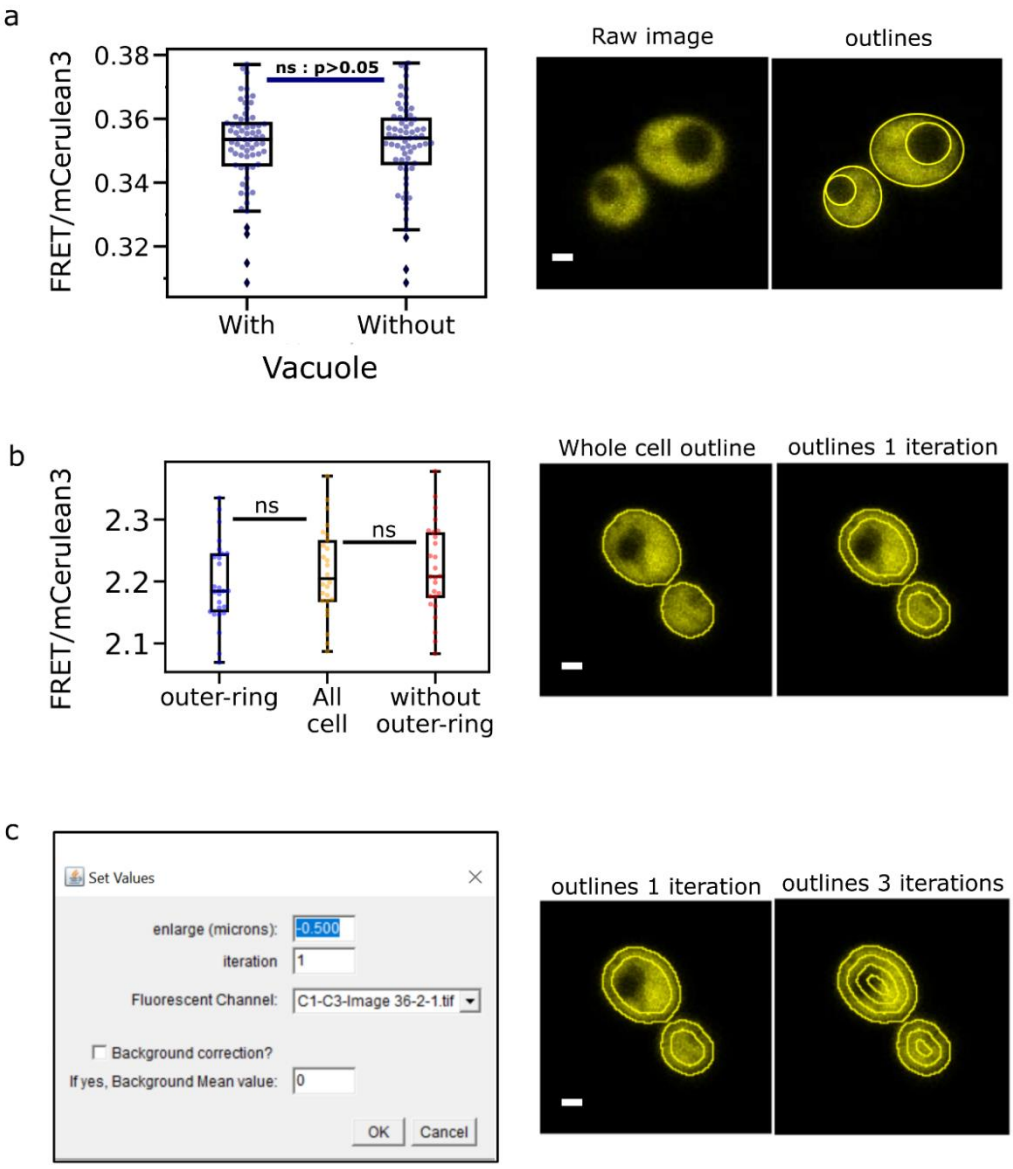

Figure 3-7: Cell volume segmentation outlines

(a) Jitter plot of ratiometric FRET values for *S. cerevisiae* grown in 2% glucose and imaged with 0 M NaCl, with and without including the vacuole in the analysis. Boxes represent the interquartile range (IQR), with bars extending 1.5*IQR from the upper and lower quartile. Diamonds indicate data outside this range. Student's t-test shown with p=0.05. on the left, images with segmentation outlines in yellow, using a composite selection tool in Fiji to opt out the vacuole from the selection (b) Average ratiometric FRET in the area underneath the plasma membrane. 200 nm ring at the cytoplasmic periphery of the cell drawn and intensities were measured by ImageJ/Fiji macro on a scaled image

within the segmentation outlines (in yellow). Intensity values were measured in both channels to calculate FRET/mCerulean3 ratio. Results were plotted for the outer ring, the whole cell, and the cell without the outer ring regions. NS indicate a non-significant correlation between the data with a non-parametric Brunner-Munzel test (Brunner & Munzel, 2000) p-value greater than 0.05. (c) Visual macro GUI when the macro run illustrates the ability to generate sequentially ring selections from the initial selected ROI. See code Appendix ap.0-5.

5. Conclusion

This chapter presents the FRET-based CrGE crowding sensor expressed in the cell cytoplasm and demonstrates its capability to quantify crowding changes, as previously documented (Boersma et al., 2015; Mouton et al., 2020). The sensor was used here to assess molecular crowding changes against osmotic stress and glucose concentration to sustain cellular growth. It was also used to investigate the mother-daughter cell crowding polarity. Analysis was performed using developed and implemented semi-automatic whole-cell measurement methods. The results show the expected cellular response to osmotic stress for yeast cells exposed to 1 M NaCl and experiencing a hyperosmotic shock. An increase in crowding was measured, as reflected by ratioFRET increasing by 13.7% for cells exposed to 1 M NaCl compared to unstressed cells in media containing 0 M NaCl (Figure 3-2.a and b). This increase in crowding is correlated with a measurable cell area reduction of 21% due to osmotic pressure and following water loss from the cytoplasm to the extracellular environment (Figure 3-2.c).

Secondly, FRET ratios were measured in basal conditions and also under osmotic stress conditions for cells grown under 4%, 2%, or 1% glucose to determine whether glucose availability during cellular growth influences crowding. This experiment showed molecular crowding decreasing as basal glucose concentration increased with no associated difference in the cell area, indicating the presence of a metabolic crowding response to glucose availability. Indeed, for all conditions tested, cell area measurements show no statistical differences, yet crowding for cells grown at 1%

glucose was higher than for the two other conditions (Figure 3-4). Between 1% and 2% glucose, a small shift is also measured with a significant reduction of 2.7% or (0.6% with the mean normalised NFRET) (Figure 3-4). Between 1% and 4% glucose, the ratiometric FRET reduces by 11.6% (or 4.3% with the mean normalised NFRET). Interestingly, under osmotic stress, cells grown with 4% glucose display a greater shift in ratiometric FRET than those grown at 1% or 2% glucose (Figure 3-4). These results highlight the presence of a high-glucose metabolic state that fundamentally alters physical conditions inside the cell (Figure 3-4 and Figure 3-5). Finally, experiments comparing mother cells and daughter cells revealed a relative stability of crowding between the two types of cells, with no significant FRET readout difference (Figure 3-6.a and b), confirming that cell size is not correlated to the ratioFRET read out, with daughter cells being on average 35.4% larger than mother cells (Figure 3-6).

6. Discussion

This chapter highlights key methodologies adopted for the rest of this project, such as the comparison between NFRET and ratiometric FRET to select the more appropriate methods to monitor crowding changes in cells. NFRET, normalise the FRET efficiency signal and is therefore a more robust method, however, the ratioFRET method was selected compared to NFRET values for its advantage of preserving acceptor bleaching from the acquisition; indeed, the ratioFRET does not require direct excitation of the acceptor for its intensity and therefore preserves the sensor from bleaching bias. This will make it useful to perform time-lapse measurements and assess crowding dynamics at various time-scales.

A possible bet-hedging behaviour is observed in Figure 3-4 for cells experiencing 4% glucose availability, a phenomenon that has been previously reported for budding yeast (Bagamery et al., 2020). Suggestions of bimodal behaviour in cells lead to questions about crowding regulation over time; the dynamic could be cell cycle or age related. Our experiment comparing the mother cell and daughter cell confirmed the relative stability of crowding in the entire volume even during cell division. confirmed by previously

published work in the community, notably between old and young cells (relative to replicative span life) (Mouton et al., 2020). Finally, the work presented was performed by extracting the average fluorescence signal (pixel values) over a pre-defined region of interest for each channel of interest (donor, FRET, acceptor) and in the area delimiting the cell. Values were then used to calculate ratioFRET values (Boersma et al., 2015; Mouton et al., 2020). This methodology quantifies crowding changes for a population of cells. It efficiently highlights crowding levels and gives a global phenotype to the group of cells studied. Therefore, it does not consider the metabolic individuality and inter-variability for each cell within this population, or, at a smaller scale, the potential crowding disparities within the cytoplasmic volume. Indeed, cells in the same population can be at different stages of their cell cycle and have different ages and sizes, and all this variability within the same group could cause slightly different responses to the identical stress condition they are exposed to. This could explain the bet-hedging effect observed. Trying to break down the signal to a local region, as well as to perform cell by cell analysis might lead to new insight on crowding micro-management in the cell.

As a first attempt to access local crowding information, I analysed the region boarding the plasma membrane to evaluate the presence of any significant local differences. It has allowed the development of a new macro that generates personalised ring-shaped masks to segment the plasma membrane, an analysis tool complementary to the initial macro coded to automate intensity measurements (Appendix ap.0-5).

The next chapter will report on my work pushed further to investigate crowding in localised regions and access subcellular-level information.

Chapter 4. Subcellular crowding dynamic and stress recovery

1. Introduction

This chapter presents the latest development of this project to push further the FRET read-out analysis to access new layers of information for yeast cells expressing the sensor. Results show how using microscopy techniques such as confocal or Slimfield allowed us to calculate approximate sensor copy numbers and to demonstrate crowding within the cell is not dependent on local sensor concentration. It also showed crowding dynamics with subcellular details, using realistic simulations of single-cell FRET heatmaps. Finally, a section of this chapter is dedicated to results from tracking individual FRET sensor molecules diffusing through a crowded cytosolic landscape.

Similarly, to the previous chapter, this chapter report results from data and sections extracted and adapted from the two first papers listed below:

Shepherd, J. W., Lecinski, S., Wragg, J., Shashkova, S., MacDonald, C., & Leake, M. C. (2021). Molecular crowding in single eukaryotic cells: Using cell environment biosensing and single-molecule optical microscopy to probe dependence on extracellular ionic strength, local glucose conditions, and sensor copy number. Methods, 193, 54–61.

Lecinski, S., Shepherd, J. W., Frame, L., Hayton, I., MacDonald, C., & Leake, M. C. (2021). Investigating molecular crowding during cell division and hyperosmotic stress in budding yeast with FRET. In Current Topics in Membranes (Vol. 88, pp. 75–118). Academic Press.

2. Local crowding readout

2.1. Local crowding gradient at the bud-neck

To further investigate local crowding dynamics during cell division, I focussed on the bud neck, as the narrow region connecting the mother cell and daughter cell during mitosis, key to establishing polarity and molecular traffic between the two cells (Faty et al., 2002; Perez & Thorner, 2019). First, we selected several markers of the bud neck (Myo1, Cdc1, Cdc12 and Hof1) tagged with super-folder GFP (sfGFP) from an extended strain library (Weill et al., 2018) available at the MacDonald lab (see Table 2-1). We verified their localisation to this region by confocal microscopy and confirmed the tag did not perturb growth (Appendix ap.0-6). I then observed the typical ring formation along bud emergence and the splitting event at the end of division for cells expressing sfGFP-Hof1 (Figure 4-1.a).

I resolved the 3D bud neck structure via time-lapse Airyscan microscopy (Huff, 2015) on the fluorescent reporter sfGFP-Hof1 (Figure 4-1.b). The 3D structure showed the characteristic bud neck structure which consists of two parallel doughnut-like septin rings. The measured average dimensions of bud necks were 0.57 µm in thickness along the mother-daughter axis and 0.89 µm in apparent diameter consistent with previously reported measurements (Li et al., 2021). These are the bud neck dimensions that we used to set spatial parameters in subsequent analysis (Figure 4-1.c).

Measurement of local crowding from either side of the bud neck was performed using a bespoke Python-based semi-automatic analysis workflow which automatically generated regions of set width around a user-specified bud neck (Figure 4-2). Three regions were defined – one for the bud neck itself and one each for the adjacent regions in the mother and daughter cells. A width of 0.5 µm was specified for the bud neck area as indicated by our length and width quantification. In the mother and daughter cells we analysed only the 200 nm region immediately adjacent to the bud neck in each cell (Figure 4-2.b). We additionally separated cells into three categories, one grouping small

buds at the beginning of the division process which we defined as buds with an area below 3 μm^2. Large buds, with cell volume comparable to the mother cell and which are close to a scission event, were defined as buds with an area above 7 μm^2. All remaining bud sizes were defined as medium size (Figure 4-2.b). For all three categories, the daughter cell maintains a higher ratiometric FRET readout through the cell cycle at the immediate region next to the bud neck while there is a significantly lower FRET at the equivalent region in the mother cell. We measured a mean FRET efficiency of 0.263 ± 0.08 (± SD) for the daughter cell and 0.188 ± 0.05 for the mother cell for the small bud, a 28% difference. For medium bud sizes, the buds have a mean ratiometric FRET of 0.285 ± 0.07 compared to 0.190 ± 0.04 for the mother cells a 68% FRET efficiency jump between the mother cell and the daughter cell. For large buds, we find a mean ratiometric FRET of 0.294 ± 0.07 for the daughter and 0.195 ± 0.05 for the daughter equivalent to a 66% jump.

Therefore, using our automatic workflow for analysis (Figure 4-2.a), all conditions show a significant difference on either side of the bud neck, highlighting a polarised crowding trend during replication. As opposed to regions near the membrane, yet known to be highly trafficked regions but appearing to experience equivalent level crowding to the rest of the cytoplasmic space (as previously shown in chapter 3, Figure 3-7). However, these dynamics happen on a millisecond timescale and from these data, it appears that only highly constrained environments such as the bud neck can sustain a measurable difference in crowding with the method of analysis employed.

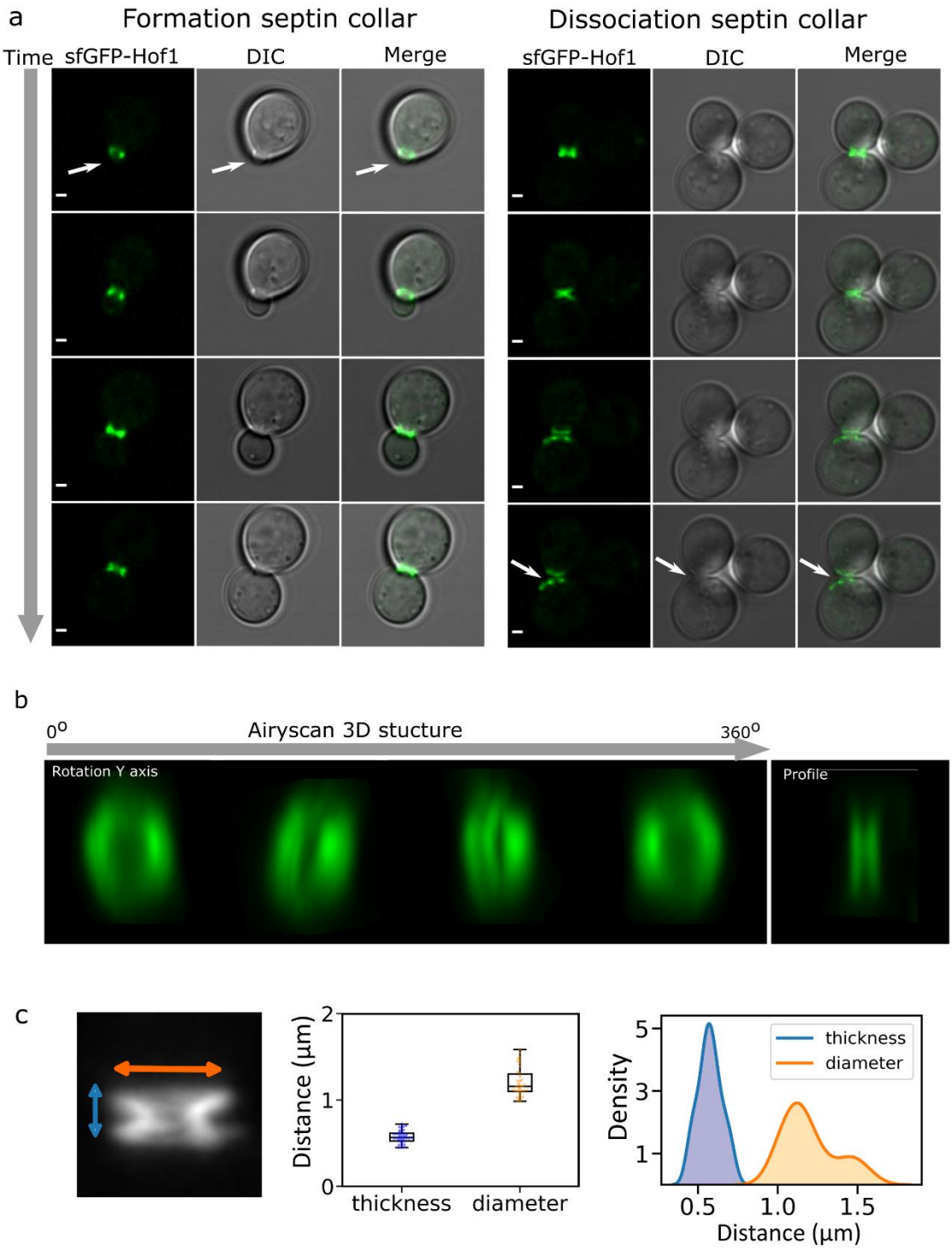

Figure 4-1: Bud neck 3D structure

(a) Confocal image of sfGFP-Hof1 expressed in budding yeast. Showing the fluorescence channel with sfGFP-Hof1, the DIC grey channel and the merge between the two channels. Scale bar: 1 µm. Right: visualisation formation of the bud neck. Left: Visualisation cytokinesis event with dissociation of the septin rings- Both indicated with

white arrows. (b) The 3D structure of the bud neck was resolved using Airyscan confocal microscopy, 24 slices of 0.18 µm spacing allowing the full capture of the bud neck's volume. The micrograph shows the 3D volume at a different angle of rotation along the y-axis, revealing the doughnut-like structure and the profile picture shows the width of the two visible septin contractile rings. (c) Bud neck dimensions. Showing visual of a z-projected image of 3D bud neck Airyscan stack image (left) with Jitter (centre) and KDE plot distribution (right) of the bud neck measured thickness and diameter.

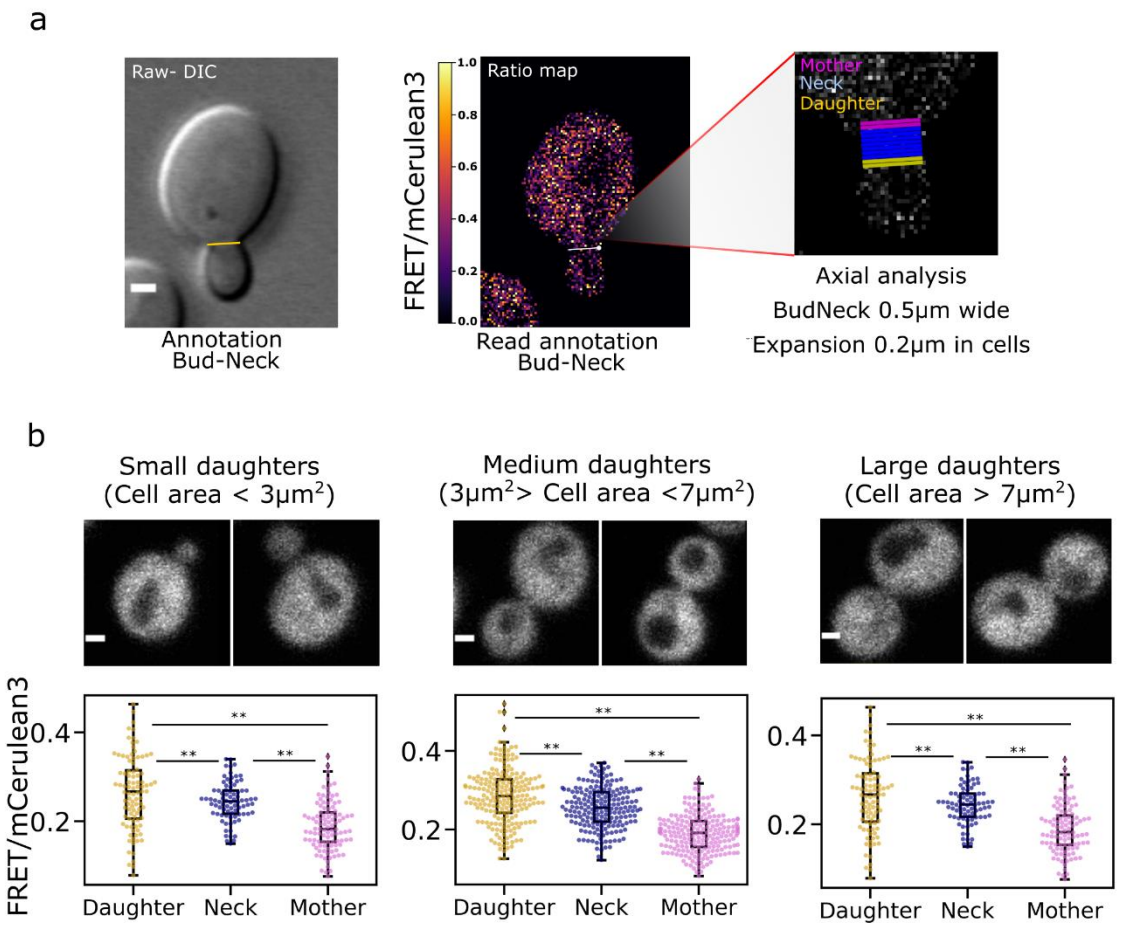

Figure 4-2: Crowding quantification at the bud neck

(a) Bud neck annotation, from left to right showing the raw image (DIC channel) with a manually drawn line between the mother cell and daughter cell to define the region of interest (yellow line), Scale bar: 1 µm. The raw annotated image is read by our bespoke

Python utility, visible in the centre showing a ratiometric map with the bud neck line in white, white dot as the indicator of the line orientation, to determine mother and daughter cell position. In the left output visual of the area measured using our Python-based analysis code, in pink and yellow the area of 200 nm, respectively entering the mother cell and the daughter cell, from the defined region of the bud neck in blue. (b) Crowding readout at the bud neck. The figure shows an example of each cell category, the small bud with a bud size inferior to 3 μm^2, large buds with an area above 7 μm^2 and medium category with all the intermediated daughter cells measured. Below each category, the respective Jitter plots representative of the FRET efficiency measured at the bud neck extremity of the mother cells, the defined bud region, and the daughter cell. A double asterisk indicates a non-parametric Brunner-Munzel test (Brunner & Munzel, 2000) less than 0.005. Scale bar: 1 µm.

2.2. Heterogeneous read-out on pixel-by-pixel ratiometric maps

Often metabolic responses to stress are short-lived reactions typically occurring in the millisecond timescale (Kirschner et al., 1975; Zhao & Craig, 2003). This includes nutrient-dependent responses (Bermejo et al., 2011; Shashkova et al., 2021), ageing (Jeon et al., 2011; Vevea et al., 2013), environmental adaptation (Li et al., 2015; Shashkova et al., 2021) and various metabolic changes required to biological functions in the cell.

Crowding influences parameters involved in these processes, from transient interactions to mediate signalling pathways and protein expression (Nussinov et al., 2021; ten Wolde & Mugler, 2014), to the diffusivity and localisation of proteins (Ando & Skolnick, 2010; Trovato & Tozzini, 2014), including their kinetic (Tabaka et al., 2014) folding and conformational changes (Christiansen et al., 2013; Jing et al., 2020). Other spatio-temporal parameters involving organelles, metabolites and proteins can contribute to confinement effects within a cell, such as the formation of the cytoskeleton during cellular growth (Gilson & Zhou, 2007; Janmey & Kinnunen, 2006; Lindahl & Sansom, 2008; Wollman & Leake, 2015) or cell polarity typically observed in yeast cells (Chenevert, 1993; Hettema & Laan, 2023; Jacobs & Lew, 2022; Lecinski et al., 2021; Xie

& Lipke, 2010). Observing local changes as they occur in small intracellular areas is a real challenge we attempted to address.

To investigate further local crowding, with the help of Dr Jack Shepherd we developed a workflow to map crowding and visualized in time and space ratiometric FRET values. First generated ratiometric maps were performed to assess thresholding methods and minimized abnormal FRET values observed specifically at the plasma membrane. We noticed a ring of apparent high FRET/mCerulean3 values and thus an apparent high crowding region around the cell boundary, similar to that seen in the vacuole (Figure 4-3.a), suggesting that the membrane is a similar excluded volume. To discern whether this was an effect due to autofluorescence and noise or due instead to a genuinely high crowding environment in the cell membrane, we simulated a yeast cell undergoing FRET as described in Methods Chapter 2.3.8.2.

With a straightforward simulation in the absence of an excluded volume in the membrane, we see no anomalous values as expected (Figure 4-3.b). Upon addition of a simulated plasma membrane which emits fluorescence due to autofluorescence only, we recreated perfectly the confocal images, with a higher-FRET state apparently existing (Figure 4-3.c). To remove this source of potential error in later tracking, we determined the ideal thresholding from autofluorescence data taken by fluorescence microscopy of wild-type yeast. We have set the threshold for the experimental data according to the donor channel fluorescence value ID, comparing it to a test value ID, T where this value is taken to be the mean autofluorescence in the donor channel, plus a certain number of standard deviations. We note that for a Gaussian distribution 99.5% of the population is contained in the region $[\mu - 3\sigma, \mu + 3\sigma]$ and therefore does not go above mean plus or minus three standard deviations.

In Figure 4-3.a, as the threshold increases the anomalous FRET/mCerulean3 values reduce until at mean plus three standard deviations they are effectively totally removed. This is clear evidence that the FRET probe has not penetrated the membrane and the higher values seen are coming from autofluorescence noise. Cross-checking this approach with simulated data (Figure 4-3.b) we see almost identical behaviour, and

therefore determine that the membrane is indeed an excluded volume which should be rejected from single-molecule tracking analysis. Hereafter therefore all heatmaps are generated with the mean plus three sigma test, and pixels that fail to meet the criteria are set to 0.

Having accounted for the autofluorescence, the FRET/mCerulean3 values within each cell are relatively flat, though some apparent high values around the vacuolar region and the cell membrane were observed for some of the cells in Figure 4-3, indicating that in the majority of the cytosol the yeast cells have assumed the physical equilibrium configuration of equally dispersed crowding but there may be some perturbations to this around membranes. A line profile of a single cell appears in Figure 4-3.b and shows a distribution around a mean though with some noise in the regions of the vacuole and membranes and importantly giving an indication of heterogeneous pixel distribution of ratio value Figure 4-3.d.

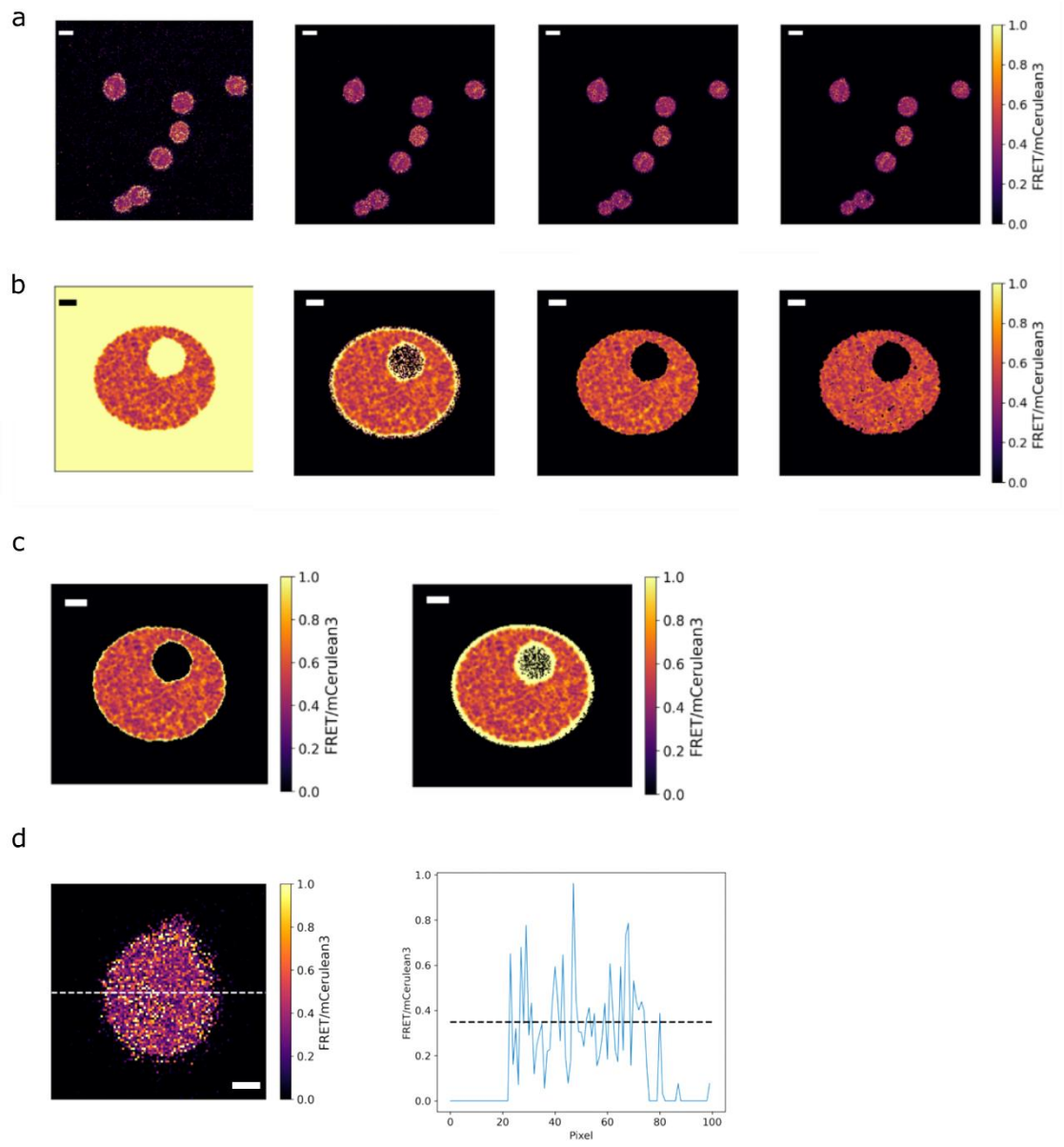

Figure 4-3: Ratiometric maps initial visual and test thresholding methods

(a) Confocal data of CrGE in 0 M NaCl and analysed pixel-by-pixel shows a high-FRET ring at the cell edge. This may be segmented out by only including pixels where $I_D > I_{D,T}$ where $I_{D,T}$ are the mean donor autofluorescence values plus a number of standard deviations in the pixel autofluorescence values. Going left to right, these are thresholding with the mean only, thresholding with the means plus one standard deviation, thresholding with means plus two standard deviations, and thresholding with means plus three standard deviations. We see that thresholding in the final case removes >99.5% of autofluorescence-only pixels and effectively removes the anomalous ring. Scale bars: 5 µm. (b) Results of thresholding simulated data. In the final panel with

mean plus three standard deviations the simulated cell shows some over-thresholding with genuine pixel excluded, while the mean plus two standard deviations show almost identical characteristics to the cell simulated without an excluded membrane volume in panel d. Scale bars: 1 µm. (c) Simulating a yeast cell without and with an outer membrane acting as an excluded volume (upper and lower panels respectively). The addition of the excluded volumes leads to a characteristic high-FRET ring, an anomaly caused by different autofluorescence values in each channel. Scale bars: 1 µm.

(d) The map on the right side of the panel represents the FRET/mCerulean3 heatmap of a single cell isolated. The dashed white line indicates the position of the line profile taken for measurement. Scale bar: 1 µm. The graph on the left side of the figure panel represents the corresponding ratiometric FRET line profile.

To investigate how crowding progresses through the whole replicative cycle I performed confocal imaging with cells immobilised with Concanavalin A (ConA) on a bespoke flowcell system (Laidlaw et al., 2021) and a time-lapse experiment on growing cells. Analysis and visualisation were further developed and performed using a bespoke Python 3 utility I run on newly acquired data to generate FRET/mCerulean3 ratiometric heat maps showing local regions of high FRET intensity coupled with prior segmentation using the YeastSpotter deep learning model a performant method of segmentation ultimately selected for this type of analysis (Lu et al., 2019). The whole cell ratiometric FRET values were individually tracked using a simple centroid tracking method to plot cell crowding through time.

Figure 4-4.a shows ratiometric heat maps of cells that have undergone 1 M NaCl osmotic shock after 20 min in media lacking salt (Figure 4-4.a - left panel) and ratiometric maps of a cell budding in standard growth conditions (Figure 4-4.a- right panel). In both conditions, we see a heterogeneous distribution of values across the cytoplasmic volume and an overall increase of crowding values when 1 M NaCl shock is introduced. We also qualitatively observe low and high localised regions of crowding (ratioFRET values) in budding cells in the absence of osmotic stress (Figure 4-4- white arrows highlighting hot-spot regions). The heatmaps generated were thresholded against the background noise in the imaging frame. Doing so improves the signal-to-noise ratio of

the ratiometric signal inside the cells, calculated from the raw fluorescence signal of the sensor. The SNR of the hot spot compared to the rest of the cell's FRET signal is generally high, with the majority of spots having SNR > 0.4, a threshold commonly used for tracking single molecules *in vivo* (Shepherd, Higgins, et al., 2021), giving confidence that the hot spots are a distinct region of higher crowding and not due to noise. The imaging set-up and the time-lapse nature of the experiment introduce additional limitations to this type of experiment and analysis, such as the typical drift focus on the field of view as cells grow. Other issues like the maturation state of fluorophores, can affect the readout and may contribute to the apparition of non-significant hot spots. Furthermore, the time scale of biological events is in the order of milliseconds, and various intracellular displacement events of proteins and compartments can compromise the identification, in real-time, of delimited local hotspots. However, generally, this data strongly supports a working methodology for intracellular insights into living cells with reported techniques for imaging and segmenting cells and tracking and mapping quantifiable FRET fluorescence signals.

Figure 4-4.b shows our cell-by-cell tracking analysis, where the mean FRET efficiency for each cell is plotted against time. The resulting figures reveal that in the osmotically shocked population crowding rises sharply shortly after the stress media is introduced. Over time the cells recover and the ratiometric FRET reduces beyond its initial value (Figure 4-4.b – graphic on the left). Meanwhile, ratiometric FRET increases slowly in non-stress media which we hypothesize is associated with the replicative cycle of *S. cerevisiae* (Figure 4-4.b- graphic on the right).

These results lead to many interesting open questions regarding the relationship between cell division and local crowding. Cell division is a cyclic event (Johnston et al., 1977; Li et al., 2004) and the contribution of this dynamic to crowding modulation can be investigated with similar time-lapse methods. Indeed further experiments will help strengthen and further support our hypothesis for local crowding hotspots associated with cell division. Measurement across several generations and ideally in synchronised cells (homogenised cell cycle stage) will help to confirm the result presented and will bring valuable insight into cellular polarity and ageing dynamics. This could potentially

help identify repeating local crowding shift patterns or reoccurring during cell division. This hypothesis is concordant with organelle inheritance synchronicity (e.g., vacuole, mitochondria or nucleus inheritance). Other mechanisms can also influence the sensor readout. These mechanisms include the ones in response to cellular stress such as osmotic stress. Indeed, water content changes (e.g., aquaporins) (Ahmadpour et al., 2014), glycerol (via the HOG pathway for osmoregulation) (Hohmann et al., 2007), and solute fluxes (potassium pumps) (Sáez et al., 2009) can directly influence the sensor readout and efficiency. Ageing or starvation was also shown to change the physical nature of the cytoplasm from a liquid to a solid-like state (Joyner et al., 2016; Munder et al., 2016) impacting directly the diffusivity of molecules (Joyner et al., 2016). More generally, changes in the composition of the intracellular content and its properties can have the potential to influence crowding at the subcellular level and thus the FRET readout; this includes metabolic changes for environmental adaptation and processes related to cellular growth.

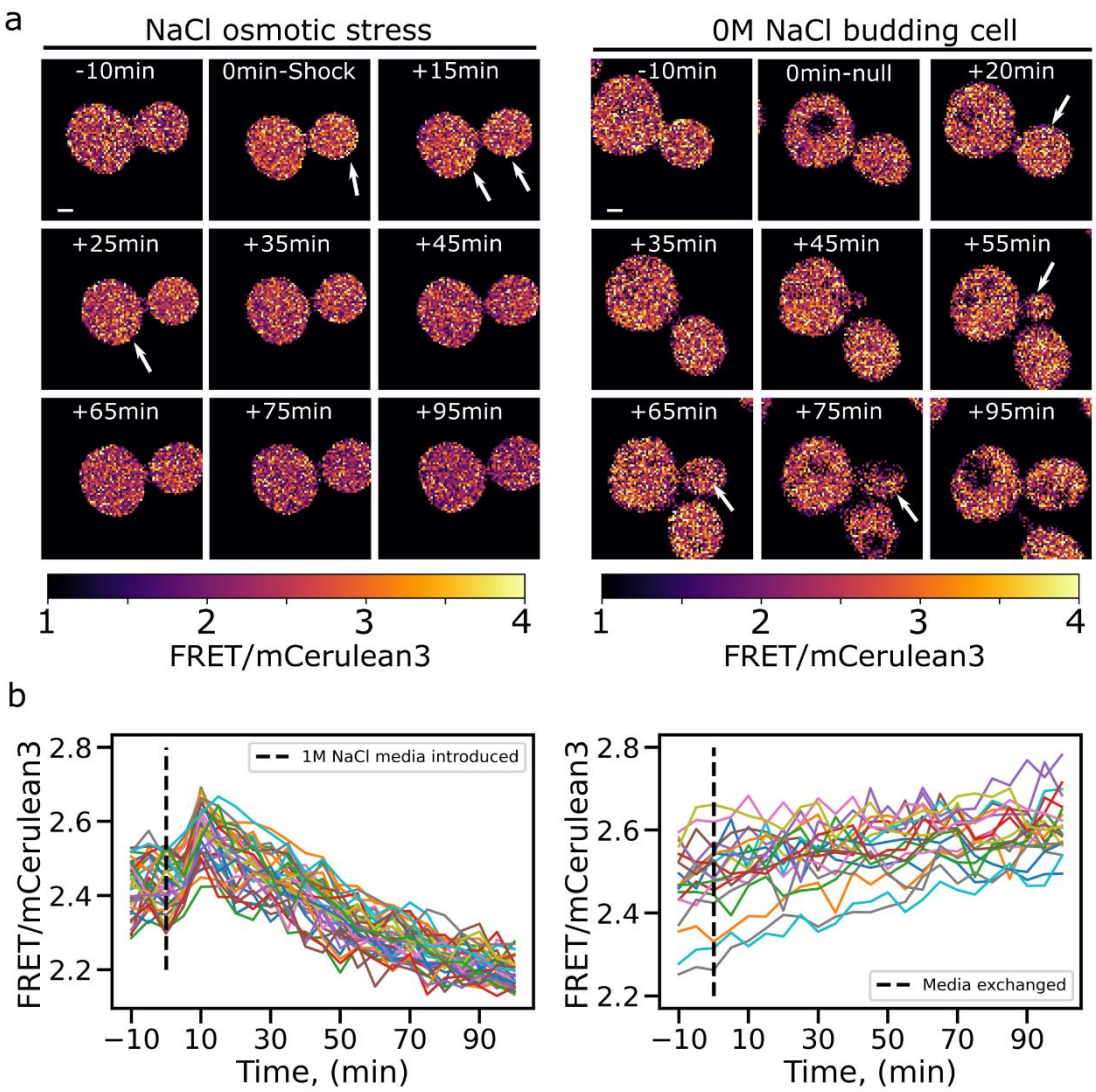

Figure 4-4: Mapping molecular crowding in single cells.

(a) Heatmap of the ratio FRET from confocal images acquired during a time-lapse experiment over 90 minutes. The panel on the left shows cells experiencing osmotic shock with 1 M NaCl after 20 min and imaged during recovery. On the right panel, micrographs show cells left to grow for 90 min in non-stress media where a budding event can be observed on the right panel (white arrow). Scale bars: 1 µm. (b) Ratiometric plot through time for each cell revealing the crowding homogeneous behaviour across the cell population.

3. Tracking the CrGE Sensor – Single-molecule copy number analysis.

Next, I aimed to observe and characterise the sensor at the single molecule level in the cytoplasmic volume. Figure 4-5 shows the results for single molecule analysis of representative yeast acquisitions. Trajectories in Figure 4-5.a were determined with bespoke single-molecule tracking software (Llorente-Garcia et al., 2014; Miller et al., 2015) adapted for two-colour imaging (Shepherd, Lecinski, et al., 2021) are overlaid on the average cell intensity over the acquisition. Surprisingly CrGE tracks are uniformly short demonstrating either that the CrGE acceptor fluorophores are prone to photoblinking, that they diffuse out of the field of view, or that trajectories collide and therefore are terminated by the software. Most likely it is a combination of the three possibilities. No tracks are seen entering the excluded volume vacuole region, as expected, and as there is a ring of fluorescence without tracks at the extreme edges of the cells it appears also that tracks do not enter the cell membrane as hypothesized. The *Isingle* value, the characteristic average brightness of a single dye molecule within the cellular environment (Shepherd, Lecinski, et al., 2021) averaged across all spatial locations of cellular trajectories, was estimated and it was found that the mean copy number of CrGE visible during Slimfield microscopy was approximately 99,000 molecules per cell, matching the number of fluorophores chosen for fluorescence simulations to mimic the appearance of the confocal images. This was done prior to single molecule analysis, and the closeness of the values indicates that this order of magnitude was reasonable. This analysis was possible with the acceptor channel detecting mCitrine signals, however, in the donor channel detecting mCerulean3 signals the single-molecule signal was below the background noise detection threshold. Even though the mCerulean3 fluorophore has improved photophysical properties compared to standard cyan fluorescent protein CFP, its absolute brightness is still lower than higher emission wavelength fluorescent proteins such as mCitrine (Markwardt et al., 2011).

Figure 4-7.b and c show the relative and absolute copy number estimation found by dividing the cell intensities by the total intensity of the field of view and multiplying by the number of cells and the mean number of CrGE per cell. Both the acceptor intensity estimation and conservation of energy method give qualitatively similar results when

comparing the relative stoichiometry, and when comparing the absolute values estimated they remain qualitatively very alike.

The CrGE sensor in all cases can be shown to be non-uniformly distributed inside the cell, while in Figure 4-3 we see that the FRET/mCerulean3 value is largely flat across the cell interior after correcting for autofluorescent noise. This importantly leads to the conclusion that the ratiometric FRET values seen are not simply proportional to the local sensor copy number, as expected for a non-perturbative probe.

Figure 4-5 shows the heatmap of this effect – within the cell, it is clear that there is a range of FRET: copy number ratio values. It is unclear why the CrGE copy number varies widely from cell to cell, but possible explanations for testing could be related to cell temporal or replicative age or stage in the replication cycle.

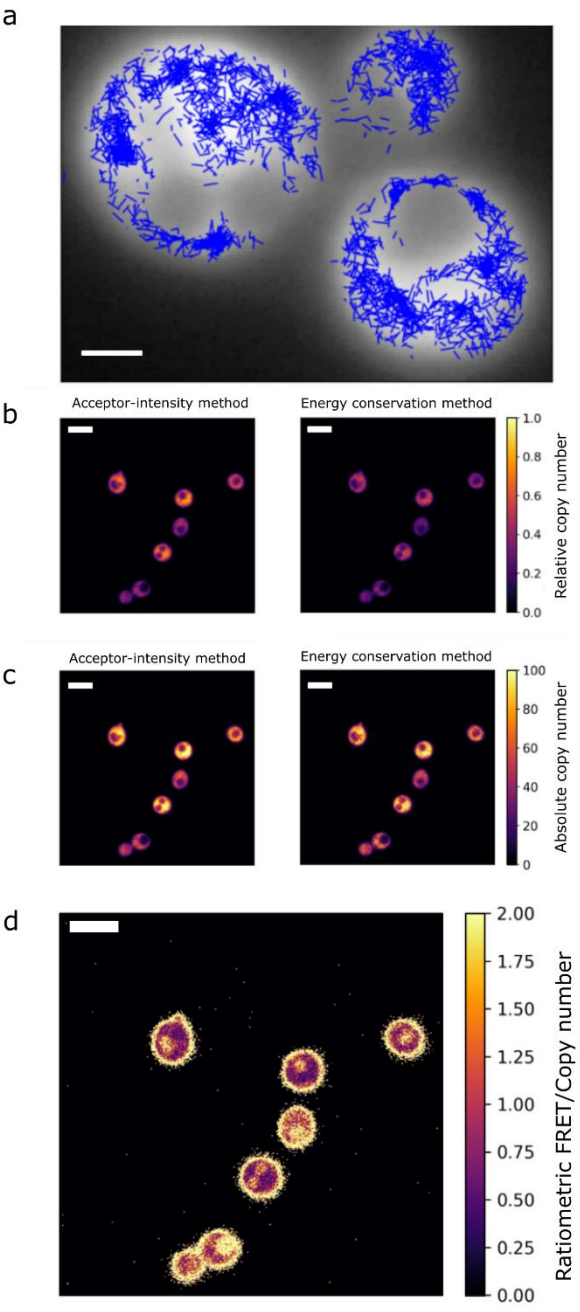

Figure 4-5: Tracking CrGE sensor

(a) Single-molecule trajectories (blue) identified by ADEMSCode, overlaid on frame average Slimfield fluorescence images (grey). Trajectories are uniformly short due to the number of molecules identified and their trajectories colliding. As expected, no tracks enter the excluded vacuole region. Scale bar: 1 µm.

(b) Estimates of relative copy number found through the acceptor intensity method (left) and conservation of energy (right). Scale bars: 5 µm.

(c) Estimated absolute copy number found by assuming each cell has the mean number of fluorophores present. Left: acceptor-intensity method; right: conservation of energy. Scale bars: 5 µm.

(d) Heatmap of the ratio given by dividing the ratiometric FRET by the relative copy number found in panel b. Scale bar: 5 µm.

Finally, the successful observation of CrGE tracks motivated further experimentation to achieve single molecule FRET efficiency readout. We used a new version of the sensor, the CrGE2.3 FRET sensor, made with mEGFP and mScarlet-I, respectively the donor and the acceptor. These fluorophores have more robust optical properties (Mouton et al., 2020) and therefore are more suitable for single-molecule detection and tracking.

Similar to the CrGE sensor, the CrGE.2.3 sensor is endogenously expressed in the budding yeast. As mentioned the two sensors are identical except for the fluorescent proteins used, with CrGE2.3 making use of mEGFP and mScarlet-I offering greater single-protein intensities compared to mCerulean3 and mCitrine (Mouton et al., 2020),

Here we used PySTACHIO (Shepherd, Higgins, et al., 2021) single molecule tracking code which performs two-channel tracking as well as colocalisation analysis using overlap integrals alongside straightforward distance cut-offs (methods described in Chapter 2.3.8.2). The localisation was used to calculate the normalised NFRET value which is possible for this FRET pair due to low spectral overlap and cross-excitation. Detected foci and FRET localisations are shown in Figure 4-6.a.

Figure 4-6.b and c shows the histogram and box plot of single-molecule FRET values taken from yeast cells in both 0 M and 1 M NaCl conditions. smFRET values distributions between the two conditions are highly similar with means 0.17 and 0.16 respectively, in contrast to our whole-cell measurements which clearly show a high shift in FRET under osmotic stress. This can be explained by the photophysics of the system. However, given that FRET pairs bleach asymmetrically we ensure that we are tracking a functional FRET pair by colocalising the donor and acceptor channels. However, as FRET increases, more energy is transferred to the acceptor from the donor and the donor intensity decreases in that image channel. In general, we can localise foci with intensity above *ca.* 0.7 GFP molecules (Miller et al., 2015). With FRET increasing, this limit will quickly be reached, and the donor intensity will drop, reducing the SNR and making localisation of the donor fluorophore impossible. In effect, we are therefore only sampling the low FRET pairs, not the full distribution. This is potentially the cause of semi-anomalous results, though we also note that in general, Slimfield image acquisitions take several minutes and therefore some of the yeast cells may have begun to recover.

In Figure 4-6.c we can also notice this explanation of the NFRET similarity is supported by the higher number of high FRET outliers in the 1 M NaCl data with greater sampling we may observe a greater difference between conditions.

Here we used an exposure of 5 ms and found FRET colocalisation for only *ca.* 1% of the localised foci. We could not, therefore, increase exposure significantly in this highly diffusive regime of cytosolic CrGE2.3 sensors. However, an increase to e.g., 40 ms would

result in a better sampling of the system as well as brighter foci for improved tracking and signal-to-noise ratios. Similarly, using the even brighter CRONOS sensor (Miyagi et al., 2021) and another version which uses mNeonGreen in place of mEGFP would improve sampling efficiency.

These preliminary results are therefore the first attempt toward optimising conditions for single molecule detection and FRET efficiency readout. Several leads are possible to explore, one path worth exploring, for future work, is performing single-molecule imaging only on sensors tagged to known (semi-)static structures or organelles so that the exposure time can be increased, and to make use of microfluidics so that cells are imaged only immediately after the stress conditions are introduced.

In anticipation and expectation to test this hypothesis, I purified *in vitro* the CrGE2.3 sensor, as well as key fluorophores (mNeonGreen, mScarlet-I), see methods Chapter 2.2.3. and initiated a cloning strategy to locally attached the CrGE2.3 sensor at the plasma membrane. See Figure 6-6 for more detail on this original idea and implementation strategy.

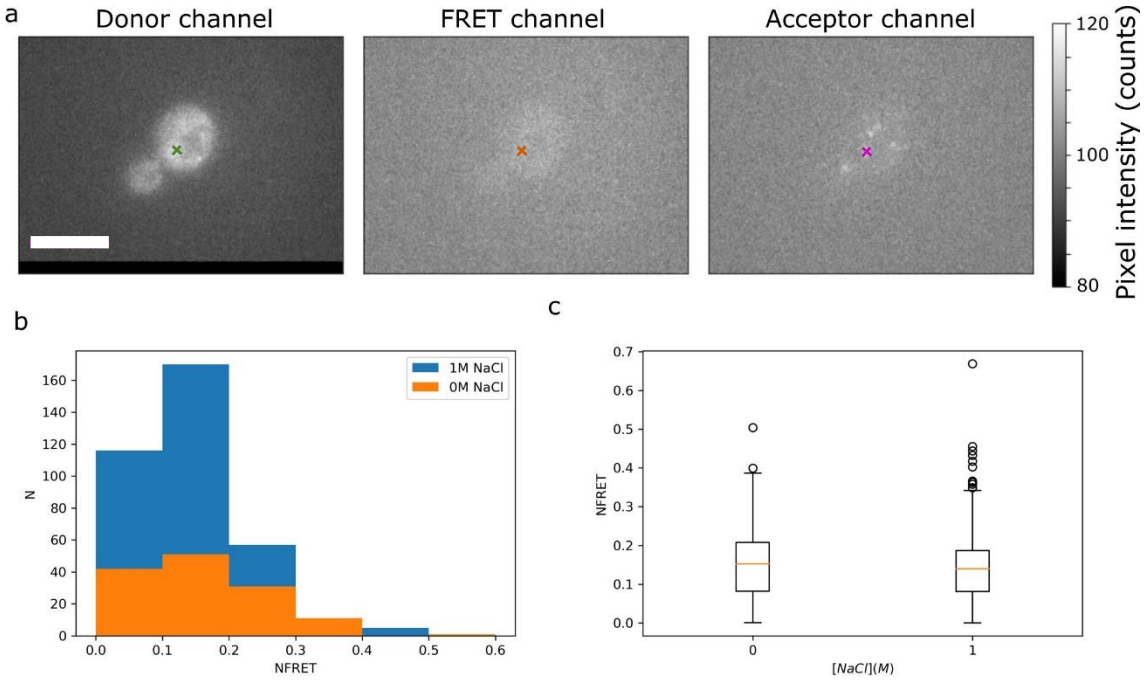

Figure 4-6: *In vivo* CrGE2.3 single molecule detection

(a) Representative colocalised data from our Slimfield experiments in the three channels post-registration. In the donor channel, the localised focus is shown with a green cross, an orange cross is used in the FRET channel to show the average position of the donor and acceptor which is used to measure FRET intensity, and in the acceptor channel, the magenta cross shows the localised position of the acceptor. (b) Histogram of the NFRET data for *S. cerevisiae* in 0 and 1 M NaCl. (c) Boxplot of the same data. Scale bar: 5 µm.

4. A three-colour experiment: combined CrGE and FM4-64 labelling.

Finally, I kept looking at crowding dynamics and directed my effort towards developing a three-colour experiment where the initial CrGE sensor is expressed in cells labelled with FM4-64. I optimised imaging settings so that the FRET signal is captured first using the FRET emission filter and associated excitation conditions (see imaging conditions Chapter 2.3.8.1) I then performed an immediate acquisition of FM4-64 excited by a 561 nm wavelength argon laser (see imaging conditions Chapter 2.3.8.1). Fluorescence micrographs and excitation/emission spectrum for these experiments are shown in Figure 4-7.a and b. I tested this set-up for cells exposed to strong osmotic stress to confirm we have not impaired the crowding sensing quality of our CrGE sensor. The analysis showed we maintained a statistically significant increase of FRET efficiency between the two conditions, reflecting the typical crowding response occurring upon osmotic stress (Figure 4-7.c).

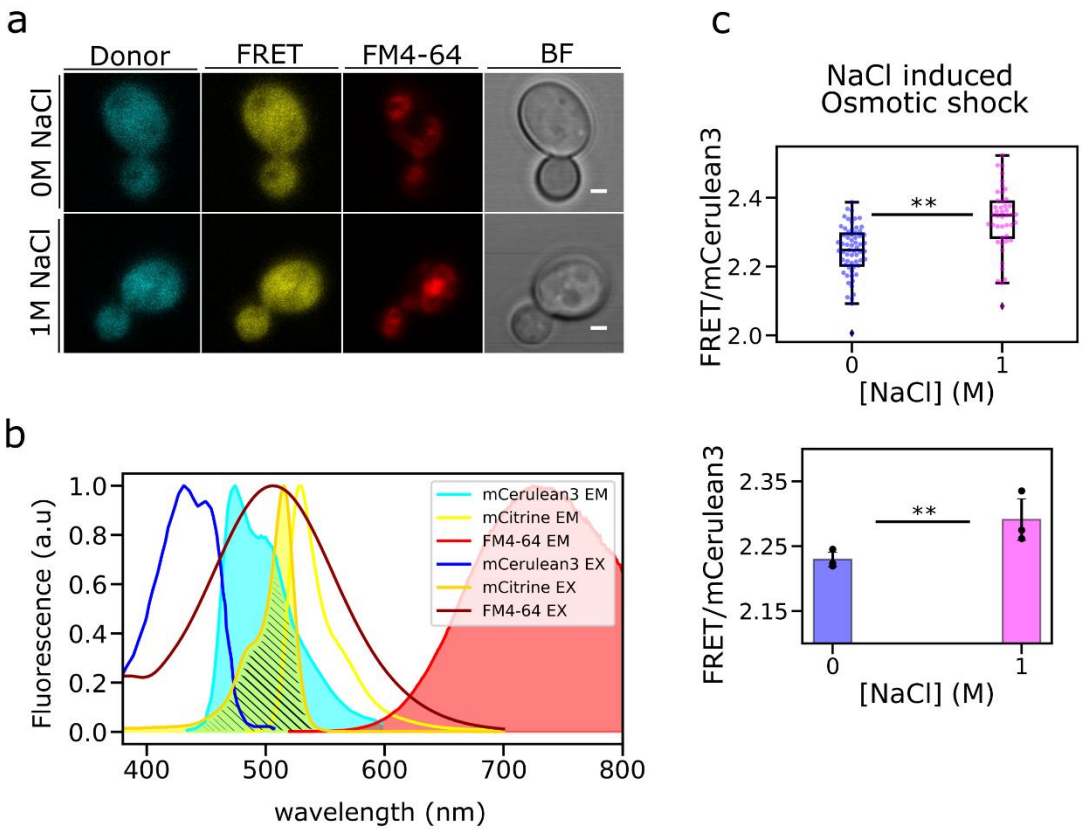

Figure 4-7: Simultaneous crowding sensing and vacuole visualisation

(a) Micrographs of three-colour imaging for 0 M NaCl and 1 M NaCl. Scale bar: 1 µm. (b) Excitation and emission spectra for mCerulean3, mCitrine and FM4-64. The excitation laser for FM4-64 is 561 nm which is above the excitation spectra of mCerulean3 (dark blue) and mCitrine (golden yellow). However, the acquisition is set so that the FRET signal is acquired before the vacuole marker to minimize the impact on the other fluorophore. (c) Quantified crowding for *S. cerevisiae* grown in 2% glucose expressing CrGE and labelled with FM4-64, imaged with 0 or 1 M NaCl. Inset jitter plot shows a representative crowding dataset for these conditions. Below: box plot of three biological replicates with standard deviation error bars. Double asterisk represents non-parametric Brunner-Munzel test (Brunner & Munzel, 2000) with $p<0.05$.

5. Conclusion

Understanding intracellular crowding dynamics is highly challenging with crowding playing a role in a wide range of biomolecular processes. It is therefore difficult to isolate local dynamics in the cell. In this chapter, I targeted the local region of the bud neck and found a difference in ratiometric FRET with enhanced molecular crowding between the mother and daughter cells forming a gradient at the immediate region bordering the bud neck, where the mother cells have a lower crowding readout than the daughter cells (Figure 4-2.b). This result suggests a local crowding polarity between the mother cell and the daughter cell at the bud neck, which is potentially caused by content packaging in the daughter cell combined with its small volume in expansion. The bud neck ring shape structure was visualised using the fluorescent reporter sfGFP-Hof1, and its dimensions were quantified (0.57 µm in thickness along the mother-daughter axis and 0.89 µm diameter) (Figure 4-1.b). This information was used to better target the area delimiting the mother and daughter cells while measuring ratiometric FRET.

This local crowding gradient at the bud neck region represents a stable and active marker of the mother/daughter polarity. Supposedly, the role of this gradient is to help effectively limit the diffusion of freely diffusing material from the mother cell to the daughter cell, for example limiting the free diffusion of protein aggregates, and other ageing by-products. This is in opposition to metabolically transported complexes such as the vacuole, inherited from the mother cell to the daughter cell with acute organisation and control, mainly via polarised cytoskeleton dependant transport processes involving molecular motors.

Furthermore, to test crowding recovery under osmotic stress we salt-shocked yeast and investigated the local crowding dynamics with a time-lapse FRET readout through cell division. We analysed on a whole-cell level, using deep learning based segmentation to identify cell outlines and performed semi-quantitative subcellular visualisation through pixel-by-pixel heatmap generation. With this method, crowding readouts show a non-uniform distribution throughout the cytosol, but have a range of distribution values visible, with the presence of local hotspots and dynamic evolution with time and along

cell division (Figure 4-3 and Figure 4-4). Complementary whole-cell analysis verified that the population-level dynamics were largely homogeneous (Figure 4-4.b).

I presented a range of complementary characterisations performed using the CrGE and CrGE2.3 sensors. This included successful copy numbers and single molecule track characterisations for the CrGE sensor (Figure 4-5) and a promising first attempt to read CrGE2.3 FRET efficiency for single molecules identified *in vivo* (Figure 4-6).

As part of my overarching aim to correlate molecular crowding and organelle trafficking events during cell division, we have also presented here our latest methodological progress to reading out macromolecular crowding while simultaneously visualising the vacuole, demonstrating compatibility for a three-colour imaging experiment where the CrGE sensor (the cyan mCerulean3 donor and the yellow mCitrine acceptor) conserves its sensing properties while the vacuole was labelled with red dye FM4-64 (Figure 4-7).

6. Discussion

Overall, this chapter shows an intracellular dynamic exists and is detectable. It is however challenging to attribute the observed results to a specific mechanism. One can however hypothesise a greater role for this observed crowding difference and gradient, such as being an effective diffusion barrier during cell division, ensuring that only actively transported cargoes reach the growing bud (Figure 4-2).

The presence of various cellular components and organelles that are progressively trafficked and accumulating in the daughter cell volume is considered a possible driving force for the crowding gradient observed. The link between subcellular crowding dynamics and the physical properties of organelles (such as their density or composition) is not clearly identified in the field. The results presented in this chapter lead to considering the occupancy rate and physical presence of macromolecules involved with cell division close to the bud neck and in other parts of the cell. The diffusion dynamics of molecules and elements in various areas are key to understanding the influence of local crowding in the cytoplasm, and maybe identifying factors responsible for the presence of a diffusion barrier between mother and daughter cells (Figure 4-2).

Chapter 5. Aggregation dynamics in yeast

1. Introduction

In eukaryotic cells, the abnormal accumulation of proteins in insoluble structures also called aggregates commonly occurs in response to ageing and environmental stress episodes. These aggregates ultimately accumulate in the cell and escape existing degradation and clearance processes, becoming harmful components for metabolic functions. Using budding yeast, I developed a cellular model that produced fluorescently tagged cytoplasmic aggregate reporters. I then used Slimfield microscopy on this cellular model to observe and determine the influence of osmotic stress on stoichiometry and the diffusion of pre-formed aggregates in the cytoplasm. Finally, I have characterised the localisation of these aggregates during cell division and investigated the vacuole compartment dynamic simultaneously with the presence of aggregates. This chapter contains unpublished data reporting the development of a fluorescent reporter for protein aggregates in the cytoplasm of yeast cells. It presents the single molecule characterisation for stoichiometry and diffusion of this system under the influence of salt and sorbitol, typically inducing a crowding upshift. The section describing vacuolar inheritance visualisation was extracted from our published paper (Lecinski et al., 2021). At last, this section includes bio-image analysis methods developed to segment and characterised fluorescent aggregates.

2. Research contextualisation

Cellular stress (e.g., starvation, osmotic pressure) triggers drastic metabolic responses, such as modulation of protein levels and physiological changes such as cell volume and diffusivity (Fulda et al., 2010; Hohmann et al., 2007). The regulation of these changes is essential to ensure cell survival. The formation, spreading, clearance, and localisation of stress-generated compounds are widely studied for insights into age-related pathologies (Kourtis & Tavernarakis, 2011). Indeed the intracellular formation and

spreading of aggregates are often associated with ageing and neurodegenerative diseases caused by a particular type of aggregate called amyloid (Chiti & Dobson, 2006). Amyloid aggregation is characterised by the formation of organised insoluble fibres resistant to degradation (Campioni et al., 2020; Chiti & Dobson, 2006). But other types of aggregates exist, such as amorphous aggregates forming globular and compact insoluble structures (Housmans et al., 2023; Sethuraman & Belfort, 2005; Weids et al., 2016).

Protein aggregation has also been identified as a protective mechanism to counteract the effects of chronic stress (Arrasate et al., 2004; Tyedmers et al., 2010), reducing metabolic function with a reversible effect when the cell reaches stable homeostasis. However, generally, the presence of stress-induced aggregates is reported to interfere with normal biochemical processes (Olzscha et al., 2011). They have been observed in the cytoplasm, but also in compartments such as the nucleus (Gutekunst et al., 1999), mitochondria (Beal, 2005; Engel, 1964), and the endoplasmic reticulum (Scheper & Hoozemans, 2009).

In the cytoplasm, recent studies have reported the sequestration of misfolded proteins into well-defined structures, such as the aggresome (Johnston et al., 1998; Kopito, 2000; Wang et al., 2009). Observed both in bacteria and eukaryotic cells (Tyedmers et al., 2010), these structures are suspected of limiting harmful intracellular effects and minimising spreading through cell division (Rujano et al., 2006; Tyedmers et al., 2010). Indeed, in yeast, the accumulation of damaged proteins and the formation of aggregates shows an asymmetrical distribution between the mother cell and daughter cell (Liu et al., 2010; Steinkraus et al., 2008; Zhou et al., 2011). Retention in the mother cell prevents the accumulation of damaged products in the daughter cell and therefore is suspected to be responsible for resetting the replicative potential for the newly formed cell (Steinkraus et al., 2008). There are two opposing explanations for mechanisms driving this polarity and diffusion barrier between two dividing cells (Liu et al., 2010; Spokoini et al., 2012; Zhou et al., 2011). The first one involves metabolic responses with active and factor-dependent transport, such as retrograde transport along actin cables (Liu et al., 2010). The second model assumes a stochastic and factor-independent diffusion

process, with the sequestration of aggregates in the mother cell attributed to the diffusive properties of the aggregates in their environment (Spokoini et al., 2012; Zhou et al., 2011; Zhou et al., 2014). It also considers the constraining geometry of yeast budding (Zhou et al., 2011). Misfolded proteins and aggregates can be found in two compartments (Kaganovich et al., 2008): first, the juxtanuclear quality-control compartment (JUNQ) (Sontag et al., 2017), close to the nucleus and composed of recruited ubiquitinated proteins and secondly, the insoluble protein deposit (IPOD) in peri-vacuolar regions (Rothe et al., 2018). They are “aggresome-like” structures regrouping inactive proteins and other protein complexes (Bagola & Sommer, 2008; Kaganovich et al., 2008). The nature of their structure and dynamics remains poorly understood (Kaganovich et al., 2008).

Various biological parameters have been identified to trigger aggregation, such as the intrinsic physical properties of the protein (e.g., hydrophobicity, viscosity), the physical properties of the surrounding environment (e.g., pH, water content) and crowding (see Chapter 1.2.2). Unfolded or misfolded proteins with an exposed portion of hydrophobic sequence are more likely to form aggregates, this is typically observed *in vivo* in cells exposed to thermal stress which destabilised the 3D conformation of the protein (Vabulas et al., 2010).

Mutant proteins prone to aggregation have been developed specifically to study protein aggregation. The Ubc9ts mutant protein for example is a thermosensitive variant of the SUMO-conjugating enzyme Ubc9 (Spence et al., 1995) which cannot properly fold in yeast cells fold in yeast (McClellan et al., 2005). It helped identify JUNK deposits in yeast (Escusa-Toret et al., 2013; Kaganovich et al., 2008; McClellan et al., 2005).

The chaperone protein Hsp104 (Sanchez et al., 1992) is also a key protein used to identify and track damaged proteins during cell division. This molecular chaperone is indeed recruited at the site to promote their clearance (Grimminger-Marquardt & Lashuel, 2010; Saarikangas & Barral, 2015; Zhou et al., 2011) and is crucial for the survival of *Saccharomyces cerevisiae* exposed to various stress (Sanchez et al., 1992). Hsp104 promotes survival up to 1000 fold under extreme thermos-stress (Sanchez & Lindquist, 1990) or high concentrations of ethanol (Ding et al., 2009; Sanchez et al.,

1992). The development of the fluorescence Hsp104-GFP became an efficient reporter to detect the presence of aggregates and misfold proteins (Erjavec et al., 2007; Schneider et al., 2022; Spokoini et al., 2012). A recent study showed that hyper-osmotic shock induced by salts such as lithium or sodium chloride promotes the formation of Hsp104 foci, revealing the presence of salt stress-induced aggregates (Reith et al., 2022).

More relevant to this study, another system to track aggregates has been used in yeast derived from the vacuolar protease carboxypeptidase Y or CPY (Stevens et al., 1982). The trafficking and modification of the native enzyme became a classical model to study ER export, Golgi transit and vacuolar protein sorting mechanisms (Bryant & Stevens, 1998; Stevens et al., 1982; Van Den Hazel et al., 1996; Wolf & Fink, 1975). Soon a mutant version prone to form aggregate CPY* (Finger et al., 1993; Hiller et al., 1996) was developed and allowed to study stress management in the ER (Haynes et al., 2004; Liu & Chang, 2008; Merksamer et al., 2008). Later, with the development of the cytoplasmic ΔssCPY* protein, aggregates clearance dynamics in the cytoplasm were investigated (Park et al., 2007; Park et al., 2013) – see next section.

Moreover, ΔssCPY* is the protein that forms the aggregates observed. This can be useful to study the formation, growth and spreading dynamics of aggregates, as opposed to the recruited Hsp104, at the site of endogenous pre-formed aggregates.

Finally, a recent study (Hanzén et al., 2016) demonstrated Hsp104 was not recruited at the site of ΔssCPY*-GFP aggregates in Tsa1-deficient H2O2 stressed yeast cells (oxidative stress sensitive cells) (Hanzén et al., 2016). This shows some insoluble structures can bypass the recognition pathway through Hsp104 chaperon proteins.

Therefore, a synthetic circuit to induce the expression of trackable aggregates can be valuable to help understand their formation and evolution *in vivo*. To this end, I constructed and optimised a cellular model producing trackable aggregates to study protein aggregate dynamics in *S. cerevisiae*, using ΔssCPY*-mGFP protein fusion.

3. Construction cellular model

3.1. Cytoplasmic aggregates, CPY

To visualise aggregates, ΔssCPY* the Agg protein needs to be associated with a delectable tag, such as a fluorescent protein. The cloning strategy adopted here was to first tag the protein with fluorescent probes (mNeonGreen, mGFP or mScarlet-I) and control the expression with a copper inducible promotor (PCUP1) (Macreadie et al., 1991) (Figure 5-4 and Table 2-1). Secondly, non-fluorescent aggregates were also developed to be co-expressed with the FRET sensor under a two-colour experiment regime (see Chapter 6.4). As a model for cytoplasmic aggregates, a mutant version of the carboxypeptidase Y (CPY) was chosen. This mutant is indeed able to form aggregates in the cytosol and derives from the carboxypeptidase Y (Stevens et al., 1982).

The native carboxypeptidase Y (CPY) is coded by the gene *PCR1* on the 13 chromosomes (Bowman et al., 1997; Valls et al., 1987) and localised in the vacuole lumen where it hydrolyses protein peptides for their degradation (Jung et al., 1999). This hydrolase is first synthesised as a precursor protein before being addressed to the vacuole. Post-translational modifications through the ER, form the p1-CPY precursor, the Golgi forms then the p2-CPY precursor. These are necessary to build the mature active protein. After complete maturation, the active CPY is a protein with a molecular weight of 61 kDa (Jung et al., 1999). CPY mutants with defective vacuolar protein sorting became powerful tools to screen for many factors involved in trafficking events (Bankaitis et al., 1986; Robinson et al., 1988; Rothman, 1989; Rothman & Stevens, 1986). Later, a mutant version termed ΔssCPY* was used as a cytoplasmic protein aggregate model (Eisele, 2011; Öling et al., 2014; Paxman et al., 2022; Schnitzer et al., 2022). ΔssCPY* carries a single amino acid mutation with a glycine substituted by an arginine at position 255 (G255R) (Stolz & Wolf, 2012) responsible for its misfolding (termed CPY*) (see Figure 5-1.a and b).

ΔssCPY* also has an N-terminal truncation to cleave the signal peptide (Δss), in consequence, the protein does not enter the ER and instead accumulates misfolded in

the cytosol, ultimately forming aggregates (Stolz & Wolf, 2012). ΔssCPY* has been shown to localise in both, JUNQ and IPOD (Hill et al., 2017). The mutation responsible for the protein misfolding is the mutation responsible for the aggregative behaviour observed. A prolonged over-expression of CPY*-GFP and ΔssCPY*-GFP leads to the formation of strongly fluorescent aggregates (Clay, Caudron, Denoth-Lippuner, Boettcher, Buvelot Frei, et al., 2014).

Little is known regarding the structure of these mutants. However, the mutation site responsible for the aggregative behaviour, Glycine 255 (G225) is situated in the middle of a beta-sheet in the native protein (See Figure 5-1) very close to the active Serine (257) of this protease (Finger et al., 1993). This study reports substituting a neutral Glycine with a positively charged Arginine, destabilises the protein. The G255R mutant (CPY*), was reported misfolded as rapidly degraded in the cell compared to the native protein and displaying different resistance to proteases *in vitro* (Finger et al., 1993; Hiller et al., 1996; Wolf & Schäfer, 2005).

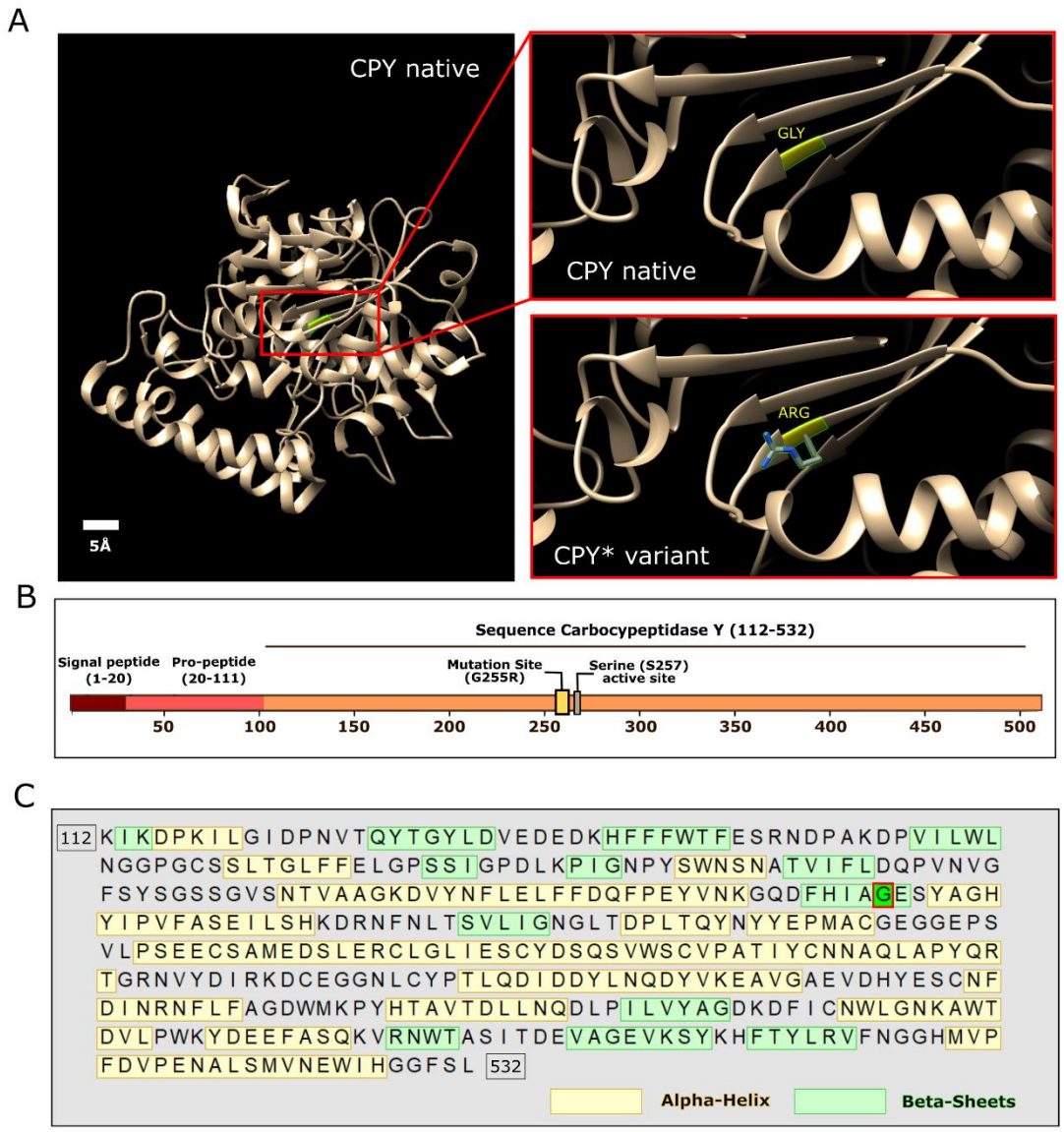

Figure 5-1: CPY* variant prone to aggregation

A) Structural model of native CPY (left) with the zoomed area of the Glycine mutation site at residue 255. In yellow the glycine to arginine substitution of CPY* is indicated (right). Structures were generated in Chimera using a pdb file from the RCBS databank (protein ID:1wpx) and resolved by x.ray diffraction at a resolution of 2.70 angstroms. B) Schematic representation of the carboxypeptidase Y sequence showing CPY* mutation site and active Serine. C) Sequence carboxypeptidase Y with highlighted regions involved in the formation of alpha-Helix (in yellow) or beta-sheets (in green). The glycine mutation site at residue 255 is indicated by a red rectangle.

I further modified the ΔssCPY* to create C-terminal fusions with newer bright fluorescent proteins (mNG and mScarlet-I) to allow the visualisation of aggregates using confocal microscopy or super-resolution Slimfield microscopy.

I then aimed to control the expression of ΔssCPY* independently of its endogenous promoter (PRC1), which is metabolically regulated (i.e., it is upregulated under certain stress conditions, like nutrient limitations (Bradley et al., 2009; Segal et al., 2003)) which might bring confusion to the interpretation of ΔssCPY* aggregates dynamics in response to stress.

Therefore, we modified the 5' sequence to remove the metabolically regulated endogenous promoter (Ichikawa et al., 1993; Van Den Hazel et al., 1996; Wolf & Fink, 1975) and inserted an inducible and titratable copper responsive promoter (*CUP1*) (Macreadie et al., 1991) (Figure 5-2). We found no effects of fluorescence quenching using copper in the media in cells expressing the methionine permease Mup1 under the control of its endogenous promoter (Isnard et al., 1996), even at 200 µM $CuSO_4$, and never experimentally used more than 100 µM for expression of ΔssCPY* (Figure 5-3.a). We also found expression levels ΔssCPY* could be rapidly induced, with robust increase after 1-hour copper, and levels saturated after approximately 4 hours (Figure 5-3.b).

I selected a standard 2h copper incubation time to express ΔssCPY*. Cells were transferred to 37^{o}C on the second hour to promote the formation of trackable fluorescent foci, the aggregates (Figure 5-4.b and c). To maximise downstream applications of our inducible aggregate ΔssCPY* reporter, in addition to creating red and green fluorescent versions, we also switched the auxotrophic marker genes for plasmid selection (from *URA3* to *LEU2* selection). This was achieved by generating the *LEU2* gene from the integration plasmid pRS305, including ~300bp of plasmid common to the ΔssCPY* reporter expression plasmid to facilitate recombination (based on pRS316). The PCR product was transformed into wild-type yeast alongside the *URA3* expression plasmid allowing the marker to be converted to *LEU2* by homologous recombination (Figure 5-4.b).

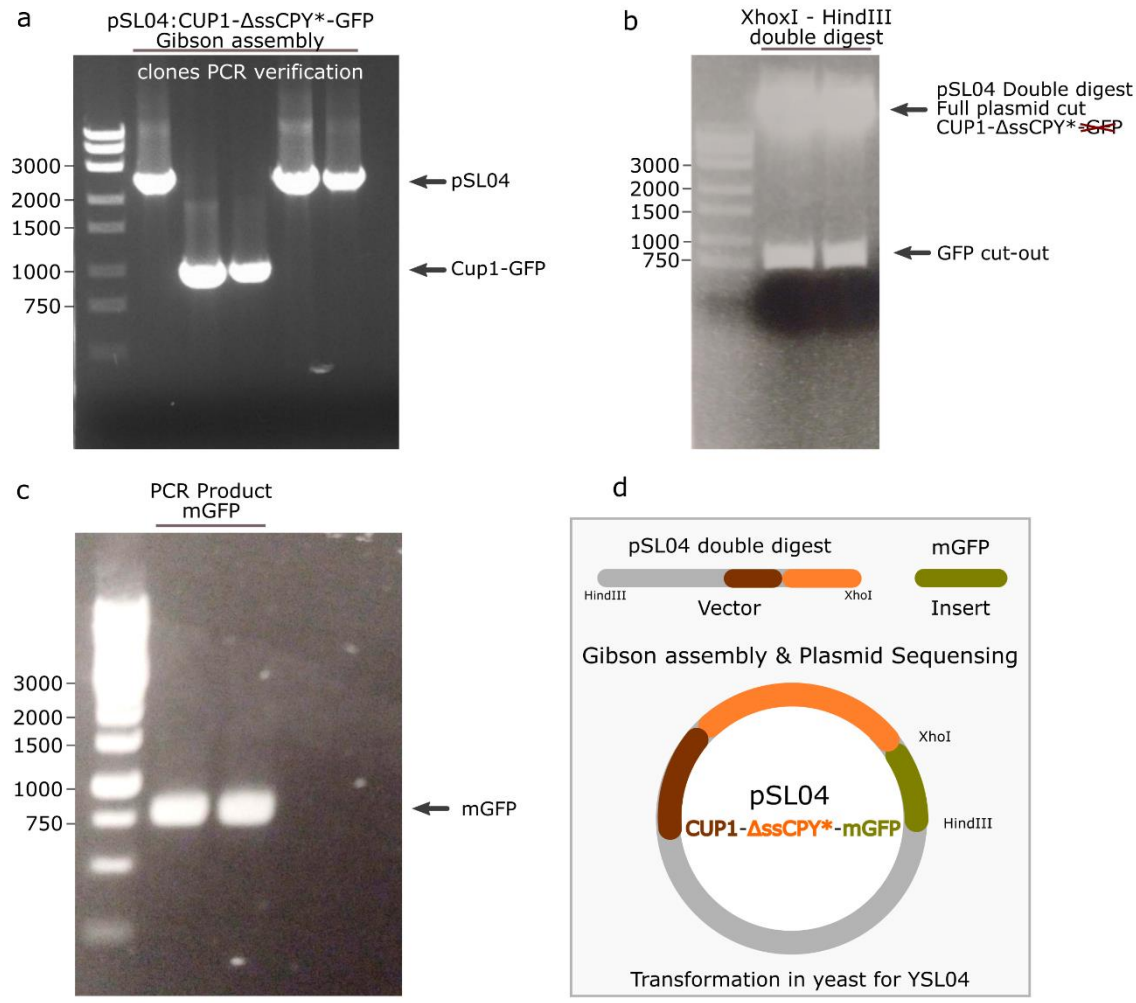

Figure 5-2: Cloning of *CUP1*-ΔssCPY*-mGFP (pSL04).

(a) Gel electrophoresis for visualisation integration of ΔssCPY* in using oligo s5 and cm195 (Table 2-6) to backbone plasmid p695 and generating the pSL04 plasmid, successful clone where sequenced. The first line displays a 1KB ladder. (b) visualisation of successful double digestion of pSL04 with XhoI and HindIII restriction endonuclease, this cloning step allows the removal of the unwanted GFP to be replaced by mGFP. The remaining linearise vector was extracted from the gel (see method Chapter 2.2.1.7) and used as the Gibson assembly vector. (c) Visualisation of mGFP insert generated by PCR using primers s8 and s9 (Table 2-6). (d) schematic visualisation of pSL04 (*CUP1*-ΔssCPY*-mGFP).

a

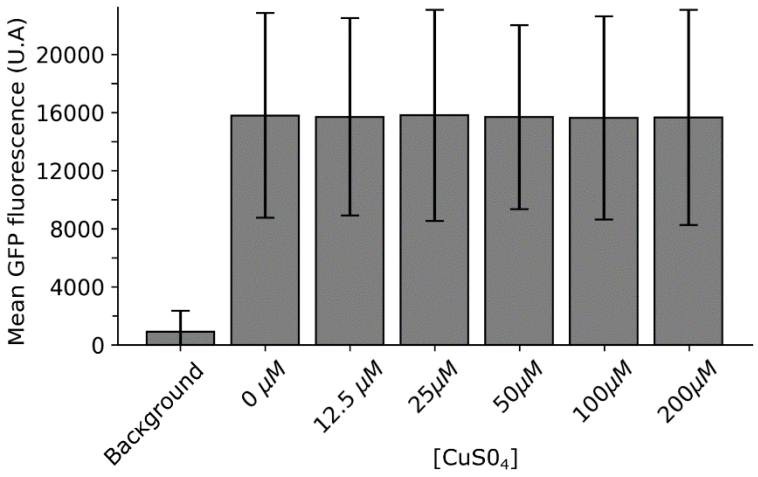

b

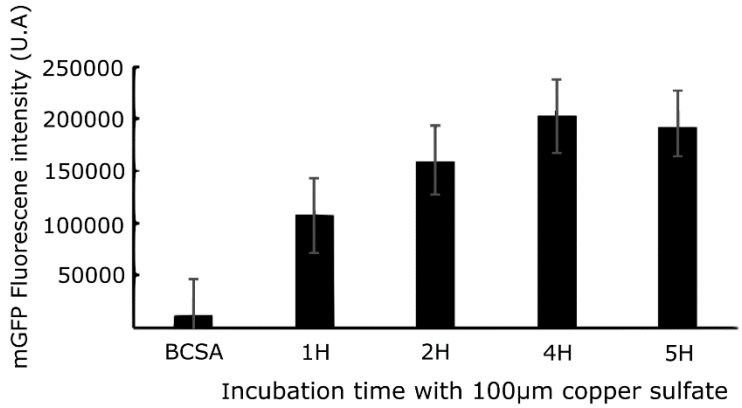

Figure 5-3: Characterisation of the inducible system

(a) Flow cytometry characterisation of the influence of copper sulphate on GFP brightness, from stably expressed Mup1-GFP in BY4742 cells. Each data set, n = >10^4 cells. Error bars show SEM. See also classic scatter plot representation for cytometry data as supplement material (b) Fluorescence intensity *CUP1*-ΔssCPY*-mGFP induced by copper sulphate.

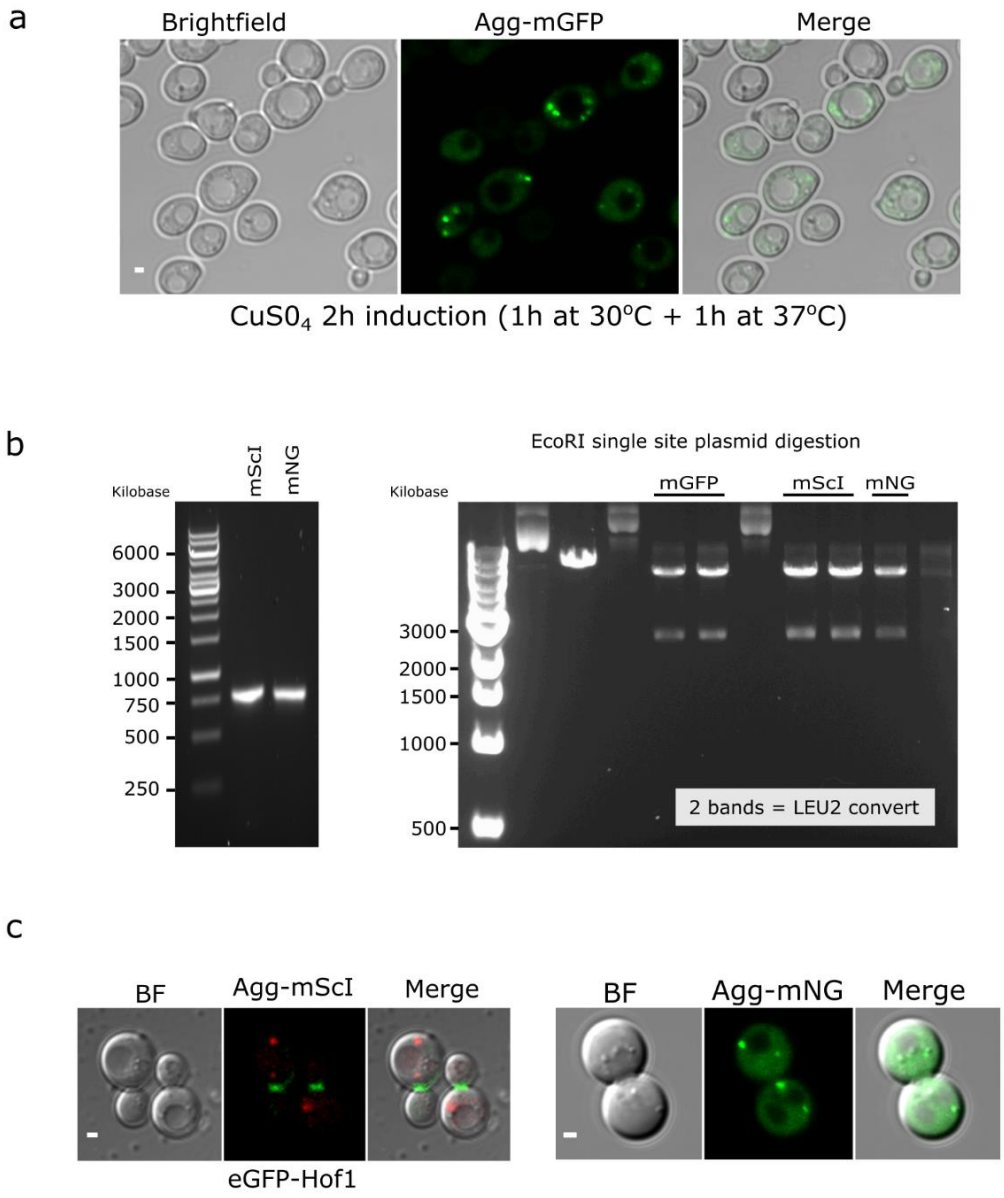

Figure 5-4: Visualisation ΔssCPY* aggregate

(a) Micrographs representing selected conditions to induce visible protein aggregates under confocal microscopy imaging. (b) Electrophoresis gels for the construction of fluorescently tagged ΔssCPY* aggregate with either mScarlet-I or mNeonGreen. On the Left: colony PCR verifying fluorophore exchanged after Gibson assembly, mGFP tag sequence being replaced by either mScarlet-I or mNeonGreen (mNG). On the right: Single digest plasmid with EcoRI to verify plasmid Leu conversion, for mGFP, mScarlet-I and mNeonGreen. Plasmid holding the URA selection only cut once and displaying one band. Plasmid holding the LEU selection will instead display two bands. (c) Micrographs

mNeonGreen and mScarlet-I version of the ΔssCPY* aggregate reporter. Left: Agg-mScarlet-I expressed in EGFP-HOF1 strain. Right: Agg-mNeonGreen expressed in BY4742 WT strain.

3.2. Single-molecule for aggregate stoichiometry and diffusion

To characterise aggregates dynamic under crowding "pressure", newly constructed strains for ΔssCPY* aggregates were imaged using Slimfield microscopy (Figure 5-5) for stoichiometry and diffusion information. Aggregates were produced following the established standard condition, and cells grown to log phase were induced for protein expressing with 100 µM copper for 2 h including 1 h heat shock at 37°C. (See section 0.1 above and Figure 5-4). Osmotic stress with 1 M NaCl and 1.5 M Sorbitol was applied and compared to the control condition with cells in 50 mM NaPi (sodium phosphate buffer). See Figure 5-6.

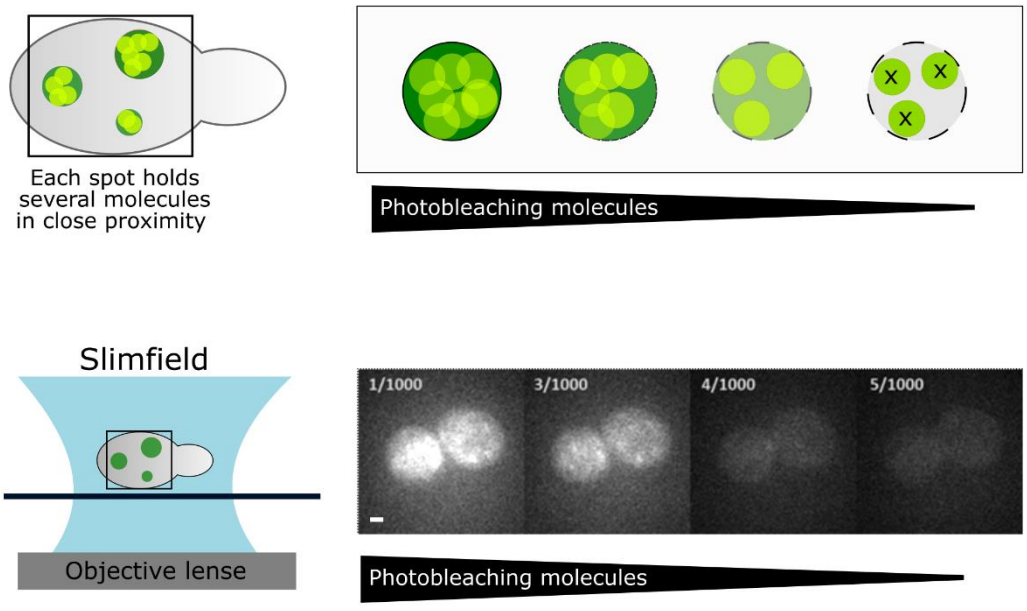

Figure 5-5: Simple schematic Slimfield principle

(a) Right: schematic representation aggregate foci in budding yeast. Left: Schematic for photobleaching process, excitation laser exposure progressively bleaching molecule revealing single molecule, for stoichiometry count, tracking. Process more extensively describes super-resolution section and methods. (b) Right: simple representation of

Slimfield microscopy epifluorescence illumination. Left: micrographs matching the top left schematic and showing a budding yeast in photobleached to reveal single molecules.

In Figure 5-6 we observe an increase in stoichiometry for both stress conditions applied, from 156.67 (+/-24.9) for a non-stress condition with cell in NaPi buffer to 290 (+/-28.28) for 1 M NaCl corresponding to an 85.1% increase. The stoichiometry measured for 1.5 M sorbitol is 216.67 (+/-16.99) a 38.2% increase compared to the control condition (boxplot in Figure 5-6.a). Correlation with the measured coefficient of diffusion from tracked spot showed an associated reduction of aggregate mobilities in a strongly crowded environment. The control condition shows a diffusion coefficient of 0.99 (+/- 0.15) $\mu m^2/s$ compared to 0.47 (+/- 0.04) for 1 M NaCl and 0.36 (+/- 0.057) $\mu m^2/s$ for 1.5 M Sorbitol corresponding respectively at 47.5% and 36.3% mobility decrease (boxplot in Figure 5-6.b). We note the effect of molecular crowding on aggregates stoichiometry and diffusion is of greater extent when induced by 1 M NaCl salt exposure than for 1 M Sorbitol. The respective density plot intensity seems to revels a greater distribution of stoichiometry for spots detected in the 1 M stress condition compared to the two other conditions tested (Figure 5-6.a and b).

Results are consistent with the physical reality of crowding upshift after osmotic shock and display the expected behaviour for aggregates oligomerisation dynamics in a high crowding environment.

The presence of Sorbitol as an inert crowding agent might indirectly influence forces of interaction or oligomerisation between molecules in the confined crowded volume, compared against the more direct effect of dissolved NaCl in the media. However, the difference between Sorbitol and NaCl shock in Figure 5-6 could be explained by an osmolarity difference; indeed, the osmolarity of 1 M NaCl is 2 osmol/L as NaCl dissociates into two species in solution, while the osmolarity of 1 M sorbitol is 1 osmol/L and does not dissolve into smaller pieces. There is, therefore, a difference between the two conditions. 1.5 M sorbitol has a lower osmolarity (1.5 osmols) compared to 1 M NaCl (2 osmols). This difference could explain the greater shift observed for stoichiometry and diffusion with the concentration of NaCl applied compared to the one

of sorbitol. Adjusting the conditions to apply the same osmotic pressure for both sorbitol and NaCl would be a sensible improvement to the experimental setup. This can help elucidate if the nature of the agent responsible for the osmotic shock affects the stoichiometry and/or diffusion of aggregates in the cells.

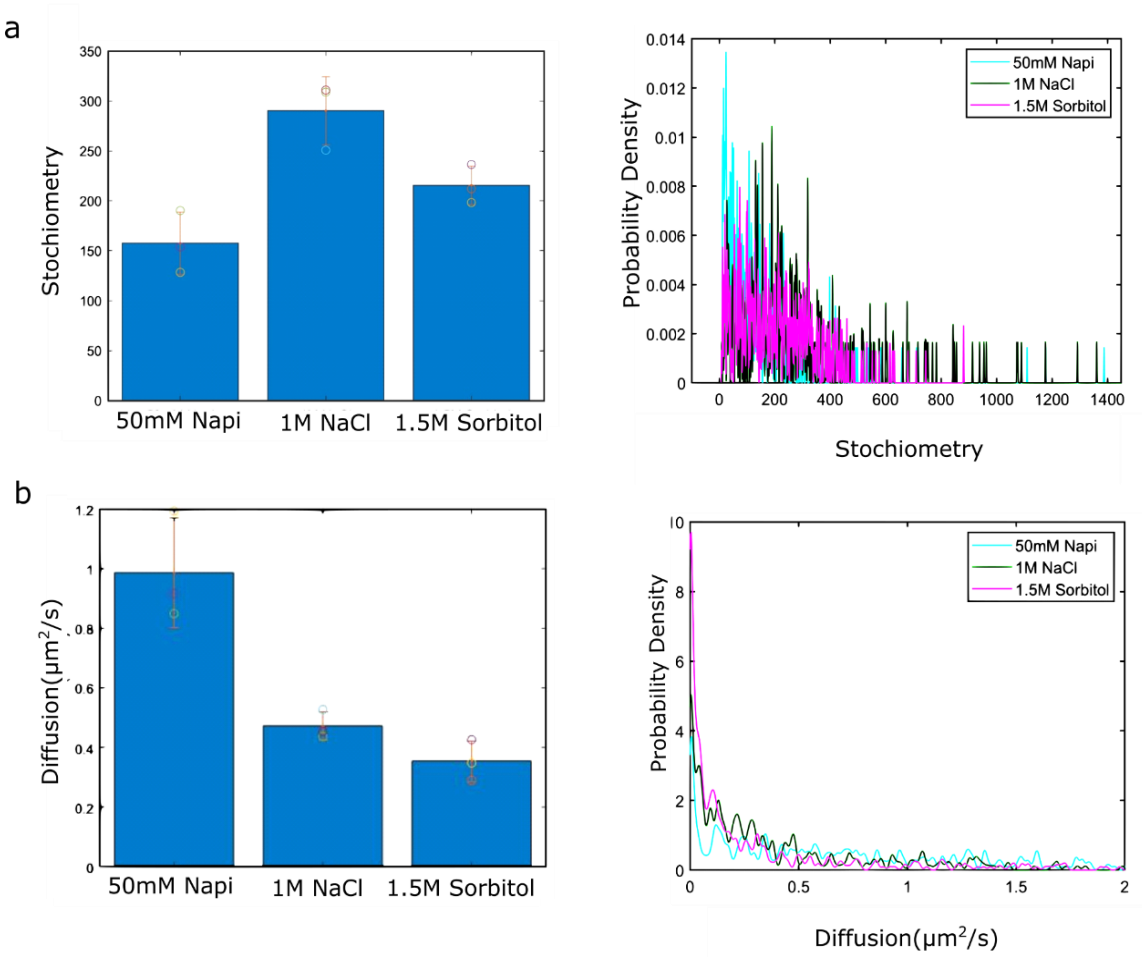

Figure 5-6: Slimfield microscopy for aggregates stoichiometry and diffusion

(a) Boxplot for the three replicates stress condition tested on copper-induced Agg-mGFP strain. The error bar represents the standard deviation between conditions. (b) Equivalent histogram KDE plots showing the distribution of values measured for detected spots.

4. Development analysis tools- spot count with ImageJ

To detect and analyse fluorescent aggregates from confocal images, an ImageJ-based spot count macro/plugin was developed and coded under the Java-based ImageJ-Macro language (see Figure 5-7). On a microscopy image loaded in ImageJ(Fiji), the macro can segment fluorescent foci within a targeted area (e.g., the cell volume) and extract information such as intensity and area. The macro requires overlays for each segmented cell on the initial/input image saved either in ROI-manager or as overlays in the image metadata. These overlays are generally generated using the cell magic wand tool (Walker, 2016) or the ImageJ selection tool. Detected by the macro, these outlines serve to identify the area to specifically run the ImageJ in-built “particle detection” program (Figure 5-7.a). This analysis is performed on a binary image generated beforehand using thresholding options available in ImageJ, including Otsu, Huang, minimum or the ImageJ default one. The type of thresholding is chosen by the user in a dedicated GUI programmed to pop up at the start of the analysis run (Figure 5-7.b). An "object size range" option is available to narrow the spot detection to the user's expectations for object size. The unit is expressed in pixels if the image is not set for scale or in the unit attributed to the image by the metadata, if this information is present (Figure 5-7.a – left). The position of spots newly identified on the binary image is used as a reference to identify the position of objects on the conserved original data and extract their intensity and area. The output is displayed in a result table, which can be saved as a csv text document (Figure 5-7.c). Additionally, the code generates a second table for “spot count” indicating the number of spots detected per cell (Figure 5-7.c).

a

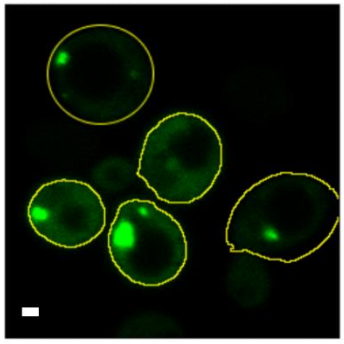

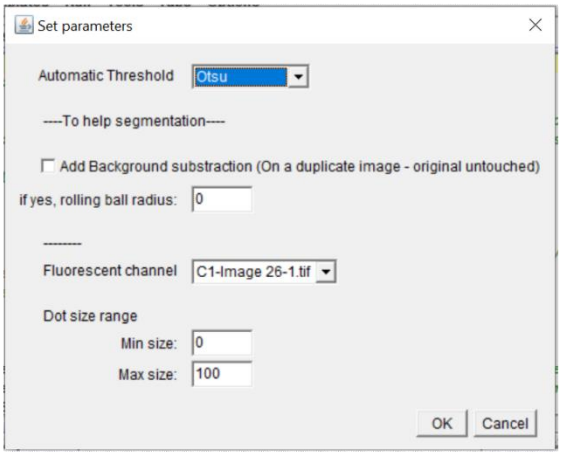

b

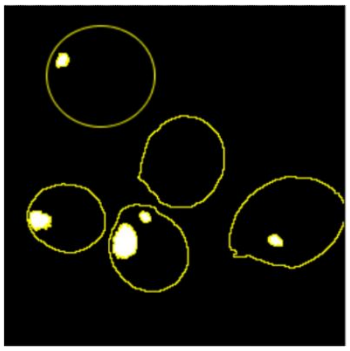

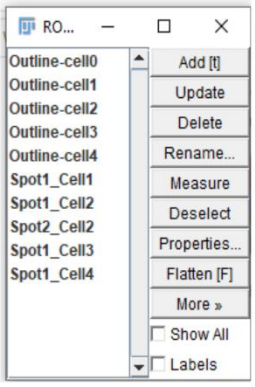

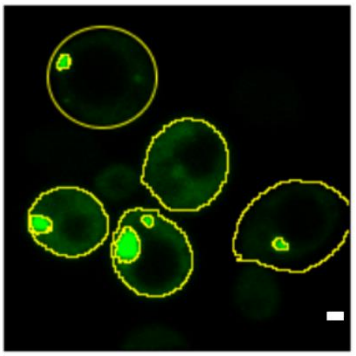

c

Results2.csv

File Edit Font

	Label	Area	Mean	IntDen	RawIntDen
1	Outline-cell0	23.613	9730.590	229771.411	29921563
2	Outline-cell1	16.456	15432.354	253960.438	33071535
3	Outline-cell2	20.995	15696.550	329544.779	42914368
4	Outline-cell3	31.461	3817.199	120094.313	15639063
5	Outline-cell4	34.356	4261.272	146401.965	19064929
6	Spot1_Cell1	0.906	55012.593	49848.930	6491486
7	Spot1_Cell2	0.223	48577.276	10817.898	1408741
8	Spot2_Cell2	2.181	57101.338	124530.674	16216780
9	Spot1_Cell3	0.292	46473.026	13561.142	1765975
10	Spot1_Cell4	0.392	50732.373	19868.591	2587351

Spot count table

File Edit Font

Cell-Number	Spot-count
0	0
1	1
2	2
3	1
4	1

Figure 5-7: ImageJ Macro-plugin development for spot count

(a) Right: input image with cell outlines stored as an overlay or added to ROI manager in ImageJ. Left: GUI displayed to select threshold, segmentation option, and image channel to analyse (b) Left: Intermediate state, a duplicate image is generated and used to create a binary mask following selected thresholding conditions. On this binary mask, as soon

as the "analyse particle" inbuilt utility is launched, it loops through each cell to generate an outline for each spot (cells detected from the initial cell outlines required prior to running the code). Outlines are stored in the ROI-manager table (middle) and transferred to the original image for measurement. (c) The output result table displays the quantified intensities and area measured for each selection on the image. Selections are typically labelled to identify each cell and the associated spot detected within its volume. An additional table is created by plugging, displaying the spot count per cell in the image. See code in Appendix ap.0-9.

5. Time-lapse experiment, vacuole and aggregates

With the library of strains I had generated, I was able to follow inheritance events as cells divided. This section reports the inheritance dynamic of the vacuole during cell division simultaneously with relevant fluorescence markers, including the aggregates model presented above.

Figure 5-8 and the first paragraph below are adapted from (Lecinski et al., 2021). Figure 5-9 and the description completing this section are unpublished data.

The vacuole is conveniently a large organelle that is inherited early in the budding process (Li et al., 2021), I used dual-colour time-lapse microscopy to follow the inheritance of the vacuole and explored organelle inheritance. Using a mNeonGreen tagged version of the uracil permease Fur4, which localises to the plasma membrane and also the vacuolar lumen (Paine et al., 2021), we could track inheritance over time. We also labelled the vacuole by performing a pulse-chase with media containing the red-fluorescent dye FM4-64 (Vida & Emr, 1995) see Methods Chapter 2.3.4.1. This dye does not diffuse freely through the plasma membrane but instead gets internalised by endocytosis and stains the yeast vacuolar membranes (Fischer-Parton et al., 2000; Petranovic et al., 2010). By tracking the inheritance of FM4-64 labelled vacuoles over time in cells co-expressing either the polarised v-SNARE protein Snc1 or the bud neck marked sfGFP-Hof1 strain, we observe vacuole inheritance events (Figure 5-8). The

process observed can be decoupled in three steps. First, the initial vacuole deformation forms an apparent protrusion that migrates toward the bud neck region. Secondly, this is followed by a crossing event, where the vacuole starts occupying the bud neck region and crosses the bud neck cell with progressive transport and relaxation toward the daughter cell cytoplasm. Finally, the scission event occurs almost instantly at the bud neck site. We also noticed some rare events of maternal vacuole retraction at the earlier stage of the crossing phase and thus a failure of efficient vacuolar inheritance during these experiments. Stable and timely occupancy of the near bud neck region appears therefore critical to undergo vacuolar migration; this suggests the existence of an adaptive transition before organelles engage crossing.

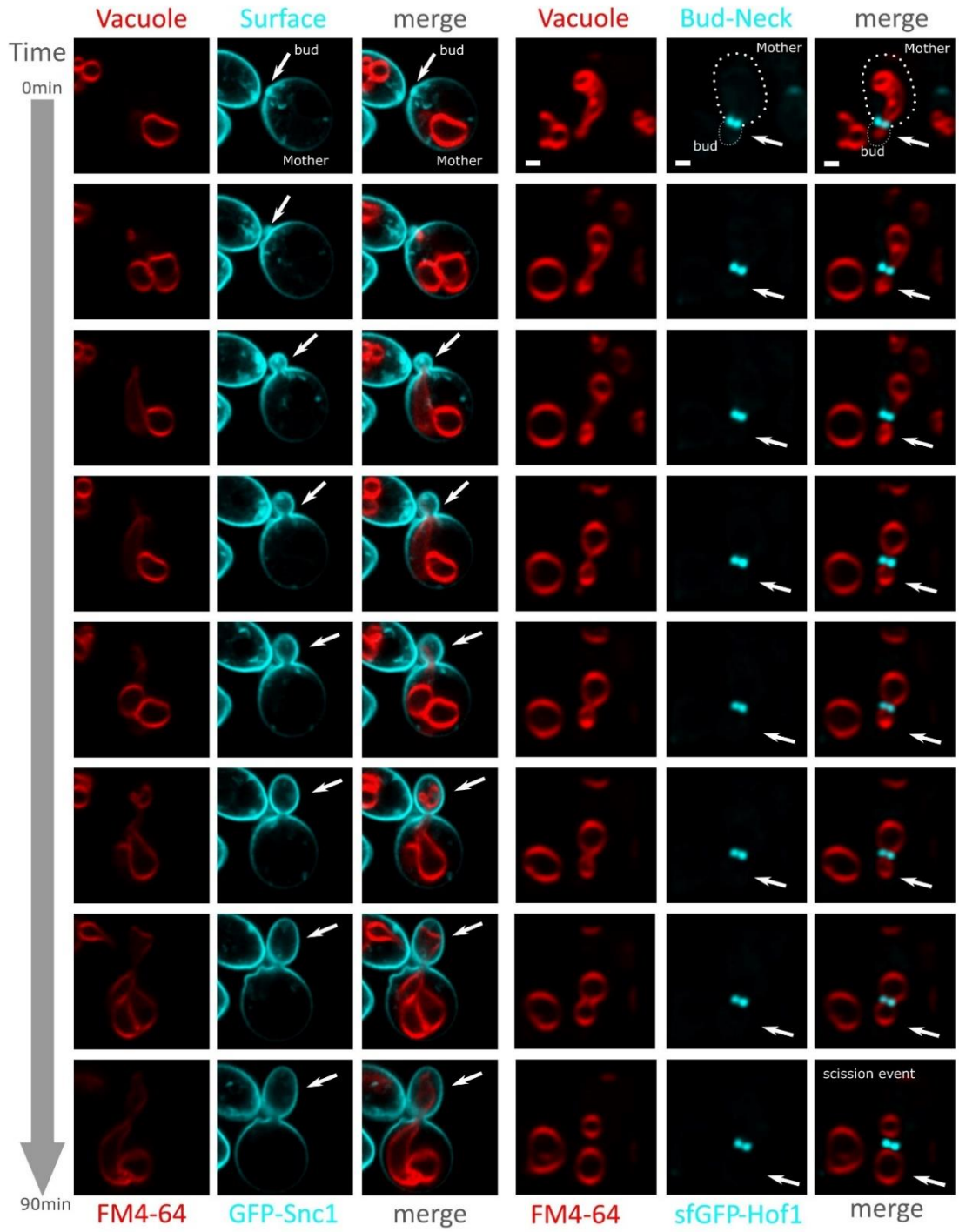

Figure 5-8: Vacuole inheritance

Strain expressing either GFP-Snc1 bud polarized plasma membrane protein and sfGFP-Hof1 bud neck specific protein, combined with pulse and chase staining with FM4-64 to image the vacuole. Micrographs show each channel for the vacuole in red (FM4-64) and the local marker in cyan (GFP & sfGFP), as well as the merge. White arrows to indicate bud/daughter cell position. Scale bar: 1 µm.

Additionally, to assess the spatio-temporal dynamics of aggregates during cell division, I tracked through time the inheritance of the vacuole and the diffusion of aggregates using the mGFP tagged version of the ΔssCPY* aggregate reporter. And similarly stained the strain vacuole with the red fluorescent dye FM4-64 (Vida & Emr, 1995).

Aggregates were induced with copper under the same standard conditions mentioned in the precedent section. The vacuole was labelled following the pulse-chase methods described above (see also Methods Chapter 2.3.4.1). Dual-colour imaging shows the aggregates observed in the mother cell to be retained through cell division, confirming spatial retention of aggregates in the mother cell as previously reported in the literature (Higuchi-Sanabria et al., 2014; Hill et al., 2016; Lindner et al., 2008; Rujano et al., 2006; Spokoini et al., 2012), now preliminary verified with this experiment for our model for cytoplasmic aggregates (Figure 5-9).

Importantly, the cell dividing presented in Figure 5-9 shows the presence of two foci aggregating together (see white arrow in the figure). From this observation, I have hypothesised that such a fusion event occurs at the late stage of division. This event was interesting to observe, revealing that not only free molecules diffusing in the cytoplasm nucleate together to form aggregates but that new aggregates can emerge from the nucleation or fusion of two smaller pre-formed aggregates. We hypothesise also that such an event could play a role in stress responses as a coping mechanism when exogenous and potentially cytotoxic molecules accumulate in the cytoplasm.

Furthermore, we notice aggregates localising close to the vacuole during cell division without being led to the daughter cell when a fraction of the vacuole gets inherited. On the contrary, it appears to be retained in the mother cell. This observation shows that our aggregates model may display the same behaviour as IPOD bodies, describing the localised accumulation of insoluble structures adjacent to the vacuole; and potentially actively involved in the retention of aggregates in the mother cell during cellular growth.

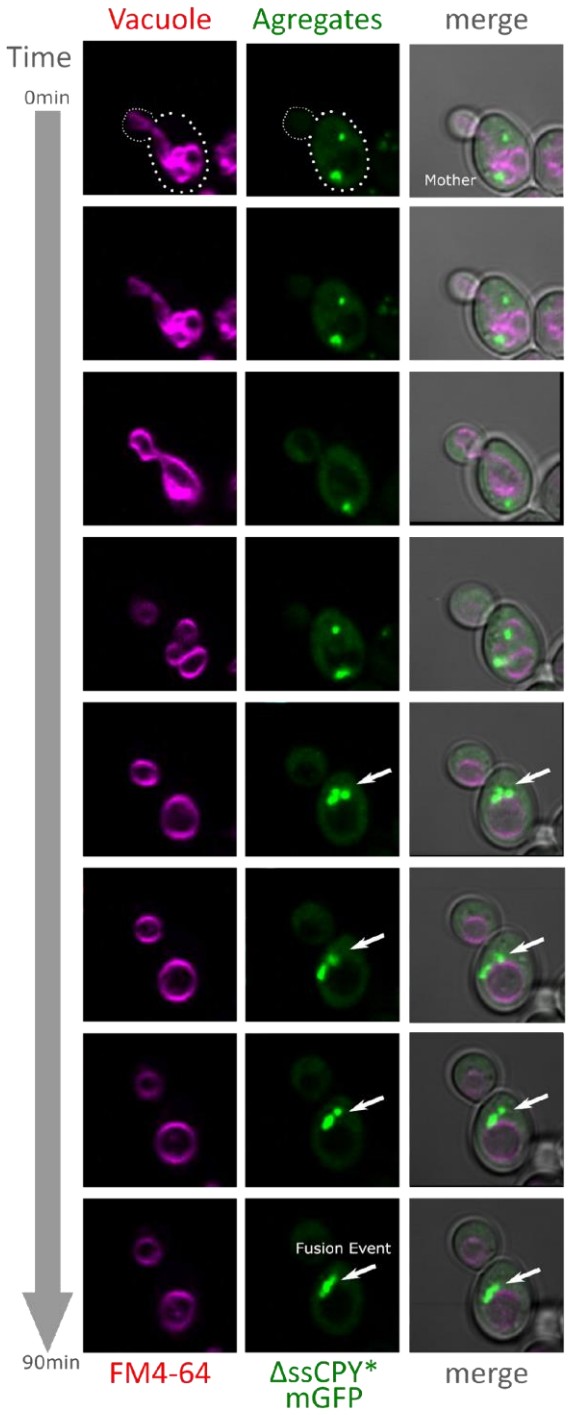

Figure 5-9: Aggregate localisation and fusion event during cell division

Strain expressing cytoplasmic ΔssCPY*-mGFP aggregates combined with pulse and chase staining with FM4-64 to image the vacuole. Micrographs show each channel for the vacuole in red (FM4-64) and in green the Agg (ΔssCPY*) protein, and lastly the merge. White arrows indicate the aggregate fusion event. Scale bar: 1 µm.

6. Conclusion

In this chapter, I presented the cloning strategy adopted for trackable cytoplasmic aggregates expressed in the cytoplasm of yeast cells. For this, I used a mutant version of the vacuole carboxypeptidase, ΔssCPY* and generated several versions fused with various fluorophores (mGFP, mNeonGreen or mScarlet-I). The expression of aggregates is controlled by a copper inducible promoter and versions of the expression vector under different autotrophic markers (Uracil or Leucine selection) (Figure 5-2). I characterised this construct as able to produce cytoplasmic aggregates and reported optimised expression conditions to standardise the production of aggregates in yeast for experimentation (Figure 5-3 and Figure 5-4).

I then proceeded to perform Slimfield imaging of the Agg-mGFP strain for single molecule detection and access to stoichiometry and diffusion information. I specifically assessed the effect of osmotic stress-induced with either 1 M NaCl or 1.5 M Sorbitol. Data analysis demonstrated that exposure to 1 M NaCl and 1.5 M Sorbitol greatly increased aggregate stoichiometry while decreasing the diffusion coefficient compared to the control condition. This reflects lower mobility for aggregates under the high crowding regime induced in the cells shocked by osmotic pressure (Figure 5-6).

I also reported in this chapter the development of a spot count macro tool to characterise bio-images displaying fluorescent foci in cells, to identify and count them in each cell, as well as to extract intensity and area information (Figure 5-7).

Finally, I reported a dual-colour imaging set-up optimised to evaluate both the vacuole and aggregate distribution and polarisation during cell division. Results showed the vacuole synchronised inheritance events and offered new clues for tracking ΔssCPY*-mGFP aggregates in the mother cells and their localisation dynamics in the cytoplasm in comparison to the identification of other compartments in the cell, such as the vacuole, the plasma membrane, or the bud-neck (Figure 5-8 and Figure 5-9).

7. Discussion

I present in this chapter a novel and innovative method to investigate aggregation in the cytoplasm of eukaryotic cells. This combines different technologies: cloning to develop a fluorescent aggregate reporter, super-resolution microscopy to access cutting-edge level system characterisation, and tools and methods to analyse the microscopic data.

This chapter shows all the preliminary data from the engineered yeast strains. The production of cytoplasmic aggregates is controlled by a copper-inducible promoter, CUP1 (Macreadie et al., 1991). Fluorescent tags on the protein prone to form aggregates (ΔssCPY*) ensure the trackability of aggregates *in vivo* by fluorescence microscopy. This system of expression improves the reproducibility of experiments and opens up possibilities for following the growth and spread of cytoplasmic aggregates. We note for future directions that a reachable improvement of this new construct can be reached by the genomic integration of the expression system to allow acute control of the copy number and expression level of the protein of interest.

The combination of this model with various techniques of investigation, such as confocal microscopy and super-resolution microscopy opens research opportunities for cellular behaviour characterisation across different biological scales, from the cell population phenotypic trait to single molecules dynamic information with the access of physical parameters such as stoichiometry and diffusion.

The data presented shows how osmotic shock affects the stoichiometry and diffusion of aggregates. Indeed, they are shown to diffuse significantly slower, while the stoichiometry of foci detected increases. This effect can be the result of high molecular crowding and density in the cell, typically occurring after osmotic stress (see Chapter 3), thus directly affecting the mobility of aggregates and increasing their formation. Various studies also suggest active mechanisms for clearance, including the spatial protein quality control system that can be responsible for mobility changes (Hill et al., 2017; Lindner et al., 2008; Schnitzer et al., 2022; Sunchu & Cabernard, 2020).

Finally, the analysis spot-count tool developed is a proposed solution to perform fast and robust analysis on fluorescent images, identify fluorescent objects, and extract quantifiable information, such as the area and intensities. This programme has the

potential to help perform image analysis for a wide range of bio-imaging projects and therefore support research and discoveries in any field of study relying on image analysis.

The advancements presented in this chapter are perhaps the ones with the greatest potential to inspire future research. Our new system was designed to facilitate the investigation of aggregate dynamics, including the methodology presented for the strategic use of technologies available (e.g., microscopes, analysis tools).

Chapter 6. Additional research experiments

1. Introduction

This chapter presents various experimental leads explored during my PhD with varying degrees of success. The section below is therefore a selection of these side experiments and trials that I found relevant to mention in my thesis and representative of the scientific “test and try” journey.

2. Crowding and lithium chloride induced osmotic stress.

In this section, I present the work resulting from my collaboration with Patrick Reith from Prof Marija Cvijovic and Prof Stefan Hohmann's research groups established in Gothenburg, Sweden (Chalmers University of Technology) and partners in the Syncrop network established by our common funding body (Marie Skłodowska-Curie Actions). Their work notably focuses on metabolic pathways associated with osmotic stress and stress recovery. The presented article focuses on the effect of lithium chloride osmotic stress on yeast cell physiology. I helped bring extra information regarding crowding modulation dynamics under lithium chloride and NaCl osmotic stress by using analysis tools previously developed. (Figure 6-1.d).

The following section and associated Figure 6-1 are extracted and adapted from the published work associated with this collaboration (Reith et al., 2022).

Reith, P., Braam, S., Welkenhuysen, N., Lecinski, S., Shepherd, J., MacDonald, C., ... & Cvijovic, M. (2022). The effect of lithium on the budding yeast *Saccharomyces cerevisiae* upon stress adaptation. Microorganisms, 10(3), 590.

For context, the whole figure (Figure 6-1) presents a complete characterisation of the salt induced osmotic stress response and associated recovery process. First showing the Hog1 phosphorylation profile is dependent on the strength of the osmotic upshift (Figure 6-1). Proteins part of the HOG (High Osmolarity Glycerol) MAP-Kinase signalling pathway indeed regulate glycerol accumulation in yeast cells (Hohmann, 2002). Secondly, it shows the effect of the stress on cell size (Figure 6-1.b) and the heat shock protein Hsp104-GFP used to report aggregation profile during stress conditions (Figure 6-1.c). Finally, my figure on panel d brings extra information on the crowding dynamics for the same stress condition.

To investigate how crowding levels, change upon hyperosmotic stress correlatively to cell volume changes, we used yeast cells expressing a FRET-based sensor, termed CrGE, allowing for acute macromolecular crowding quantification (Boersma et al., 2015). We observed a clear increase in crowding immediately upon stress exposure for all conditions tested (Figure 6-1.d). These observations are consistent with the immediate salt-induced cell volume reduction. In the control condition, where no salt stress was applied, we observed a slight progressive increase in ratiometric FRET values measured between 0 and 90 min.

Upon immediate exposure to 1 M NaCl, the FRET ratio increased by approximately 0.2. 250 mM NaCl and 200 mM LiCl showed a smaller increase in FRET efficiency, a shift coherent with the equivalent osmolality effect. This correlates with the strength of the cell size reduction observed with a high concentration of salt as water flows out of the cells under the strongly associated hypertonic condition (Figure 6-1.b and d).

90 min after stress exposure, as the cells progressively recovered to their initial volume, macromolecular crowding decreased. Ratiometric FRET for all stresses tested reached lower levels than prior to stress application, thus reflecting a lower crowding environment than initially measured. Equally, this progressive crowding reduction was observed to a greater extent after 1 M NaCl exposure compared to the two other conditions. 250 mM NaCl and 200 mM LiCl displayed similar behaviour in the first 40 minutes after shock with macromolecular crowding still being reduced over time.

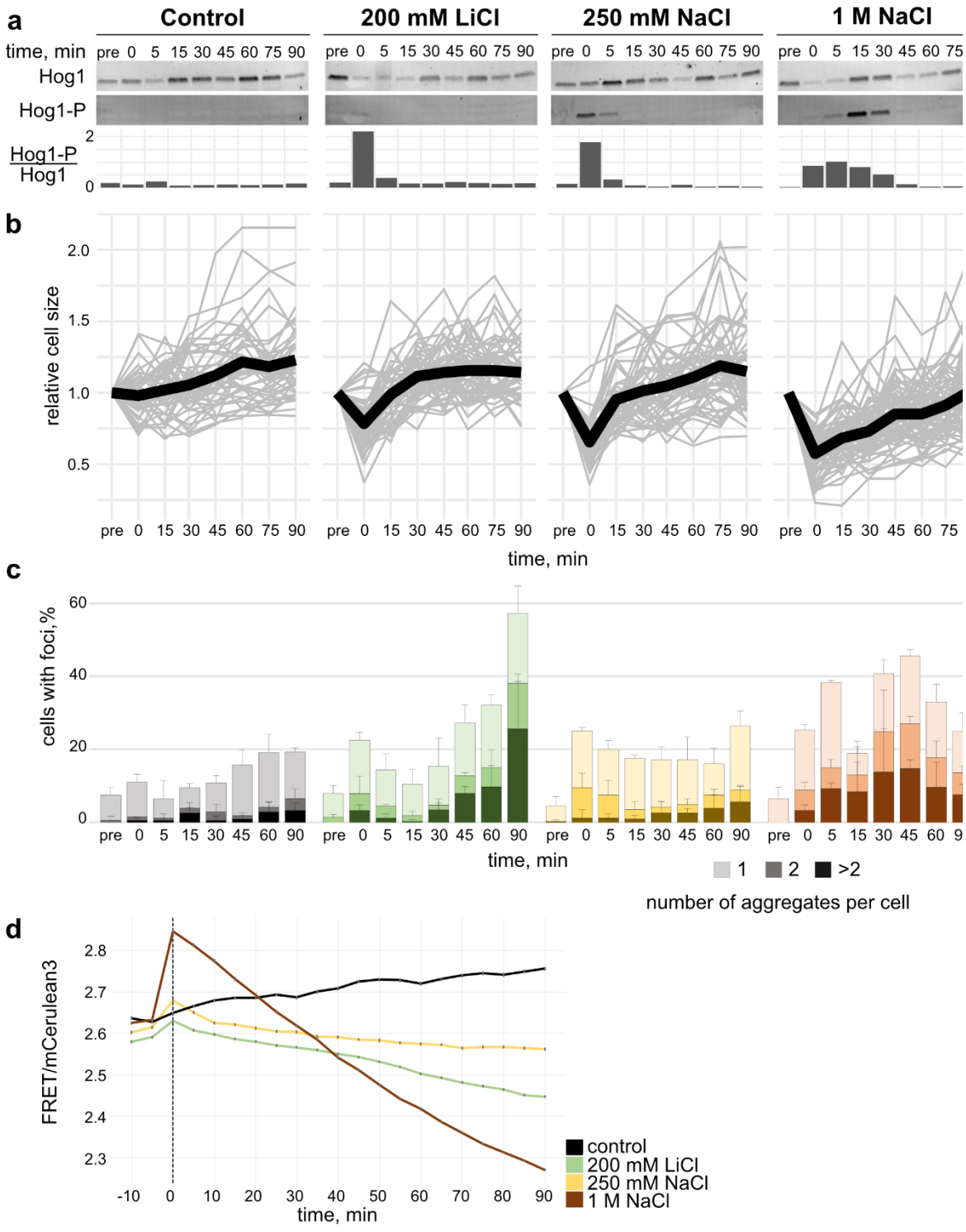

Figure 6-1: Assessment of the impact of salt stress on yeast cells

(a): Activation of the HOG pathway upon salt stress. Western blot of Hog1 phosphorylation in *S. cerevisiae* before and up to 90 min after the addition of salt stress. Hog1-P/Hog1 is the ratio of the Hog1 phosphorylation signal divided by the signal for the total Hog1. (b): Cell volume recovery upon osmotic stress. Single-cell trajectories (grey) and the average (black) are shown. (c): Salt stress-induced aggregation in yeast

cells. Percentage of cells with Hsp104-GFP foci before and after application of salt stress. The colour shades represent the number of aggregates per cell; for each condition, at least 100 cells were assessed per timepoint. Error bars indicate SD (d): NaCl and LiCl stress recovery and crowding. FRET/mCerulean3 ratiometric plot before and after salt upshift (vertical line). Cells were imaged every 5 min for 10 min prior to shock, and 90 min after the media exchange to the standard SDM (grey), 1 M NaCl (red), 250 mM NaCl (yellow) and 200 mM LiCl (green). One out of three representative experiments is shown. Error bars indicate SEM.

Additionally, I developed a small program in Python to complete the main pipeline analysis. It can identify outliers and dead cells to be removed from the analysis using the interquartile range (IQR) method. (Figure 6-2 and Appendix ap.0-7).

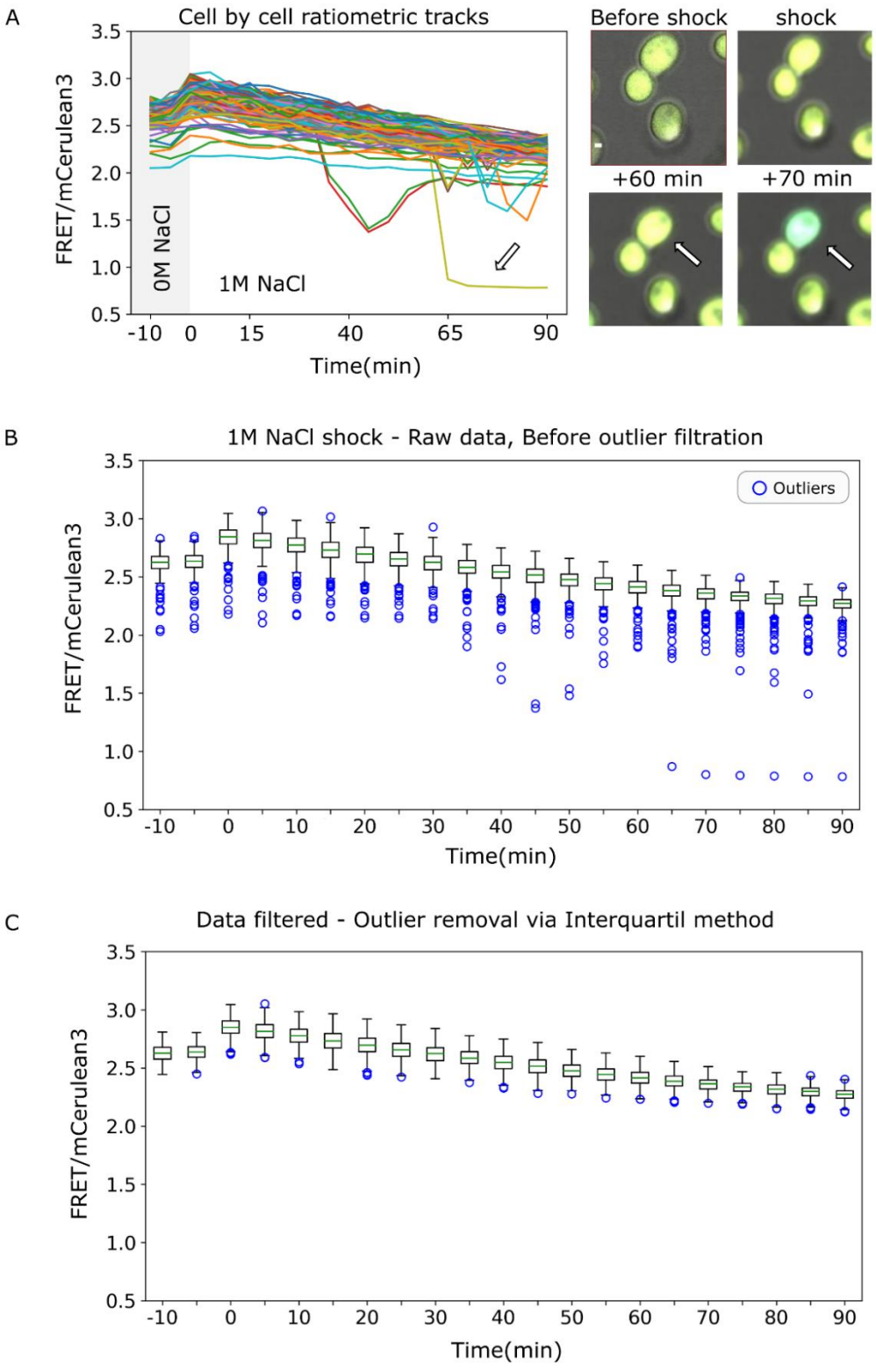

Figure 6-2: Outlier filtration

(a) FRET/mCerulean3 ratiometric plot through time for each cell tracked using our Python-based bespoke analysis pipeline, revealing the presence of outliers and dead cells in the analysis. On the right: fluorescence micrographs to visualise a cell dying after

60 minutes of exposure to 1 M NaCl, a merge of the brightfield, FRET and mCerulean3 channel. Scale bar: 1 µm. The arrow represents the identified dying cell, in the cell-by-cell track plot and the image. (b) Boxplot of the same data, output from our Python3 bespoke utility. Boxes show the interquartile range (IQR), with bars extending 1.5*IQR from the upper and lower quartile. Blue circles for values are considered outliers.
(c) Boxplot for filtered data, using a Python-based bespoke code, values above 1.5*IQR were removed from the analysis.

As a side note regarding crowding dynamics using the CrGE or CrGE2.3: fluorophores are sensitive to pH (e.g., GFP with its pKa of 6). This sensitivity can impact crowding efficiency.

If comparing the readout for the same population of strains is still reasonable to highlight behavioural differences within the same grown cellular population. For future work, a complete characterisation of intracellular pH under selected osmotic stresses will be valuable to better comprehend the data acquired. The same type of experiments will be extremely valuable to understand both intracellular dynamics during stress and to help further characterise this type of sensor. Interestingly, new versions of the sensor may come out soon with enhanced capability, for example using the pH-resistant Gamillus green fluorophore (pKa 3.4) instead of EGFP.

3. Development of a gravity-fed flowcell media exchange system

This gravity-fed flowcell system was specifically constructed for implementation in our epifluorescence Slimfield microscopy to permit single molecule imaging the closest to the instant of the switch.

The device has the advantage of using common lab materials and being washable and reusable. This system is theoretically exportable to work within any lab facility.

An air-tight tunnel on the slide was constructed with a similar process to the one used to produce a standard tunnel slide; however, instead of using double-face tape, a custom silicon sealant was made. Media entry and exit are achieved through previously drilled holes on the slide (an inverted slide with entry and exit points on opposite sides of the coverslip). The great advantage of this system is that it allows following cell-by-cell stress dynamics in a controlled environment, especially when performing Slimfield super-resolution microscopy, where the field of view is reduced to contain only one to two cells. (Figure 6-3). A 3-way Luer lock system was constructed to select between the two 50 ml reservoir syringes which media flow through the channel. Silicon tubes of the same diameter as the drilled holes in the slide (1 mm) were used to connect each slide to the media reservoirs. (Figure 6-3). The flow rate of the system using a syringe holder at approximately 20 ml from the level of the slide is approximately 1 ml per minute.
A homemade holder with a microscope metal rod attached to a purification column holder was made to keep the system in place.

The system is functioning, however, it has proven to be a little tedious to implement for experiments in the restricted space around the microscope. After each usage, the material was cleaned with ethanol. A schematic of the system is presented.

Working together with Dr Jack Shepherd, we finalised a working prototype. This system has the potential to become an entry-level solution to implement easy-flow media

exchange as opposed to more complex microfluidics systems existing in the market that are slower to implement and require advanced skills and training.

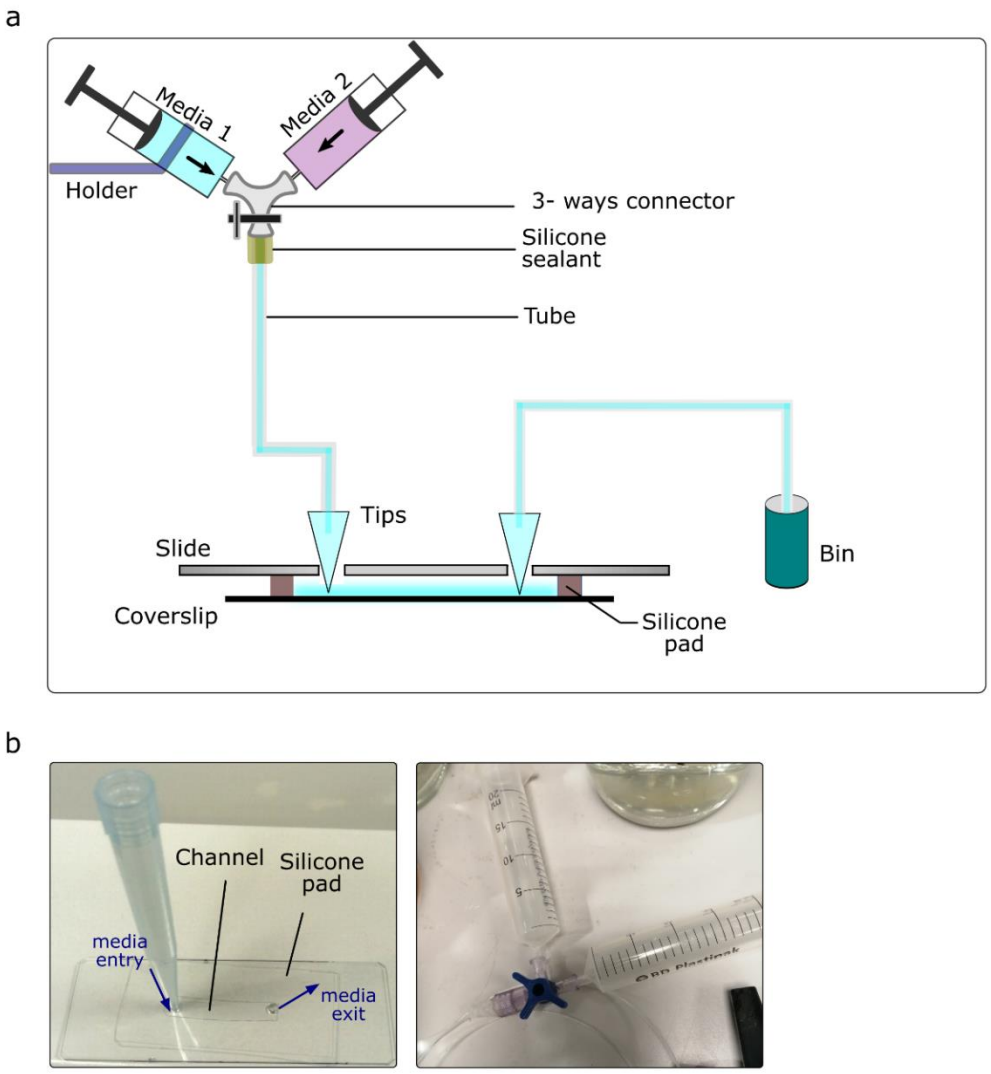

Figure 6-3: Gravity-fed flowcell prototype

(a) Gravity-fed flowcell device, schematic representation. (b) Left: photograph showing the hermetically sealed microscopy slide of the system. The blue arrow shows the point of entry and exit where the gravity media flow is applied. Right: photograph showing the 3-way controlled system for media exchange between two 50 ml syringes and the flow conducting tube.

4. Non-fluorescent 3xHA tagged aggregates

This strain was developed to express non-fluorescent aggregates. Essentially, ΔssCPY* instead of being tagged by a fluorophore protein, was tagged in the C-terminal by a non-fluorescent marker, the 3xHA tag (epitope tag) (Field et al., 1988), consisting of three repetitions of the Human influenza hemagglutinin a small protein with the following amino acid sequence: YPYDVPDYA (1.08 kDa). This protein can be detected by immunostaining (Knop et al., 1996; Russell et al., 1999; Schneider et al., 1995). The following figure shows the western blot results for clones developed by Gibson assembly (see Chapter 2.2.1.1) for CUP1-ΔssCPY*-3xHA expressed in WT BY4742 yeast cells.

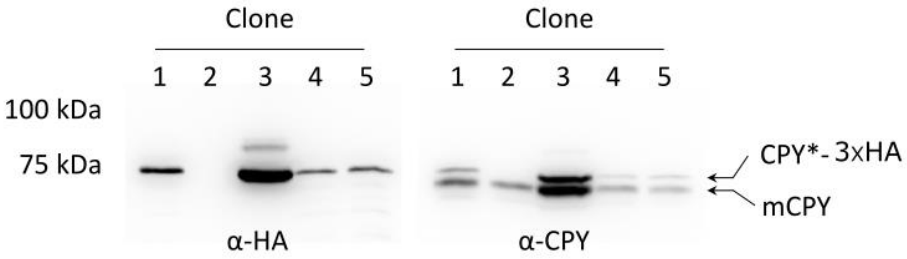

Figure 6-4: Western blot P*CUP1*-Agg-3xHA

Cells were grown for 3 h with 100 µM $CuSO_4$ and revealed using anti-HA or anti-CPY antibodies confirming the presence of *CUP1*-ΔssCPY*-3xHA in clones 1, 3, 4 and 5.

Strains expressing non-fluorescent aggregates can be combined with the FRET sensor or any dual-colour strain of interest. In doing so, the effect of the presence of aggregates can be assessed with fluorescent-based technology, keeping possible experiments on a two-colour regime.

5. Yeast cell growth synchronisation

This section shows the preliminary results for cell synchronisation an extremely valuable technique to homogenise the cell population and assess metabolic effects related to cellular growth and the correlation of various parameters (e.g., crowding) with different stages in the cell cycle. The figure and description are adapted from (Lecinski et al., 2021).

Cell division synchronisation was optimised for wild-type MATa cells to focus on cell division events during crowding analyses. Cell cycle arrest at the G1 phase was performed by incubating cells in 10 µM α-factor for two hours (Robles et al., 2017; Udden & Finkelstein, 1978), leading to the formation of so-called shmoos (Merlini et al., 2013) (Figure 6-5.a). After exchanging the buffer for one not containing the α-factor, we observed a return to cell division. After eight hours of growth we confirmed that all cells were back to a budding elliptical shape while conserving cell cycle synchronicity across the population (Figure 6-5.b). Four hours after α-factor release, some cells were still dividing from a shmoo-like phenotype, forming an unwanted subpopulation of cells that were dividing but not forming a regular bud neck. After 8 hours, all cells display the budding round phenotype, and all cells in the field of view budding at a similar rate (Figure 6-5).

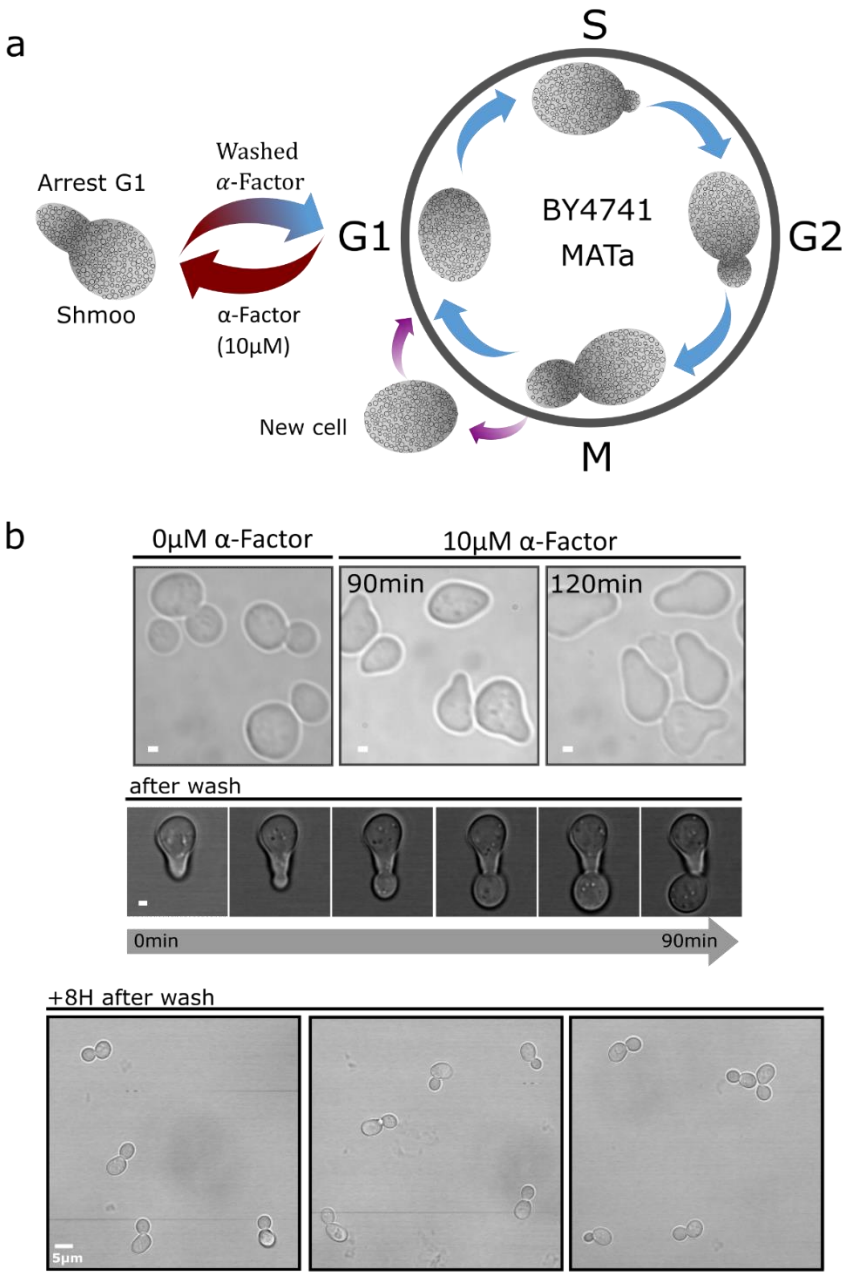

Figure 6-5: Cell cycle synchronization

(a) Schematic representing the cell cycle with its 4 phases (S, G1, M, G2) highlighting arrest of the cycle at the G1 phase when MATa yeast cells are exposed to 10 µM α-factor. Cells stopped dividing and adopted the shmoo phenotype. (b) Brightfield images of shmoos formed after 90 minutes and 120 minutes of incubations with 10 µM α-factor (scale bar: 1 µm). Micrograph below shows a shmoo entering cell division immediately after the removal of α-factor from the media (scale bar: 1 µm), and a micrograph 8 hours after removal showing synchronised budding of yeast cells (scale bar: 5 µm).

6. Marking CrGE FRET sensor fusion at the plasma membrane

Finally, this section will present the early stages of a cloning strategy to attach the CrGE2.3 sensor to the plasma membrane, to target crowding dynamics in proximity to this highly dynamic interface. Secondly, as mentioned in Chapter 4.4 a semi-static structure will be acquired by the sensor tethered to the membrane and therefore not diffuse freely in the 3D volume of the cytoplasm. The potential advantages of this design are to stabilise the FRET efficiency readout as more permissive to higher exposure times when carrying out single-molecule Slimfield imaging.

I selected three protein candidates: Can1 (Ahmad & Bussey, 1986), Sur7 (Sivadon et al., 1997) and Ste3 (Hagen et al., 1986), all proteins expressed at the plasma membrane, for their stability of expression and for being encoded by non-essential genes.

I designed primers that follow the cloning strategy which is to tag the CrGE2.3 sensor, donor fluorophore sequence mEGFP to the C-terminal of the candidate protein (e.g., CAN1, SUR7, STE3) separated by a flexible hydrophilic glycine-serine linker (Van Rosmalen et al., 2017). I selected two different lengths to test: 5 aa or 15 aa. The optimisation of the linker length is often critical to ensure the stability of the fusion protein. The genomic construct finally comprises a his5-pombe loxP (Gueldener et al., 2002) behind the mScarlet-I sequence for autotrophy selection. The figure below (Figure 6-6) is a schematic to summarise the strategy and is followed by a table (Table 6-1) with the list of primers designed for genomic integration.

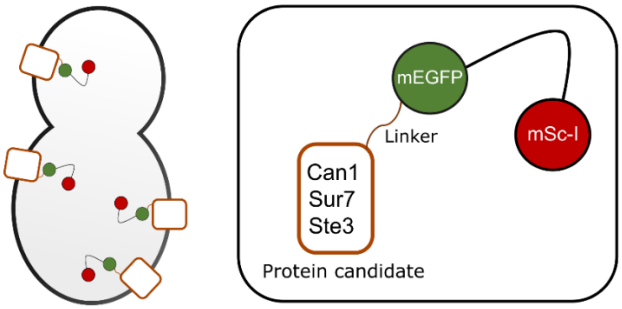

Figure 6-6: Schematic CrGE2.3 at the plasma membrane

Name	5’-3’ sequence	Description
s36	AAGATCATGAACCAAAGACTTTTTGGGACAAATTTTGGAATGTTGTAGCAGGTGGTGGTGGTTCTatgagccatcaccatcaccacc	CAN1-5aaLinker-CrGE2.3 (Forward primer)
s37	AAGATCATGAACCAAAGACTTTTTGGGACAAATTTTGGAATGTTGTAGCAGGCGGTGGGGGATCTGGTGGTGGCGGGTCCGGCGGTGGCGGATCAATGAGCCATCACCATCACCACC	CAN1-15aaLinker-CrGE2.3 (Forward primer)
s38	CGAAGTTATATTAAGGGTTGTCGACCTGCAGCGTACGAAGCTTCAGCTGGCGTTATTTGTACAGCTCATCCATACC	HIS5pombe_Crge2.3 (Reverse primer)
S39	CGAAAGATCTGAAGGTAGACATTCTACTGGTGGTATGGATGAGCTGTACAAATAACGCCAGCTGAAGCTTCGTACGC	CrGE2.3_HIS5 pombe (Forward primer)
S40	CAAGTTGATTAAAATGTGACAAAAATTATGATTAAATGCTACTTCAACAGGAGCATAGGCCACTAGTGGATCTG	HIS5pombe-pUG27vector (Reverse primer)

Table 6-1: List of primers for CrGE2.3 at the plasma membrane

Chapter 7. Thesis discussion and conclusion

1. General summary

This thesis summarises the research work I conducted during my PhD for my project, which focuses on using optical microscopy methods to study cellular stress responses in *S. cerevisiae*. This work gravitates mainly around two axes: the characterisation of macromolecular crowding dynamics and the development of a cellular model to investigate aggregation dynamics.

In the first two chapters of the result section (Chapters 3 and 4) I report my research advancements in assessing macromolecular crowding dynamics at a subcellular level in the budding yeast. To quantify crowding, I used recently developed FRET base sensors, called CrGE and CrGE2.3 (Boersma et al., 2015; Liu et al., 2017), extremely valuable tools in the context of hyper-osmotic stress, translating physical changes due to confinement effects into a quantifiable fluorescence signal. A suspected bet-hedging behaviour for cell population grown at high glucose concentration (Figure 3-4) has raised our interest to investigate crowding dynamics at the single-cell level to access disparities between individual cells constituting the same group and even at the subcellular level in growing cells. I first compared the mother cell and daughter cell FRET readouts for crowding information, which confirmed the relative stability of crowding in the entire volume for both populations (Figure 3-6). This result is coherent with previously published data comparing aged cells with newly formed cells (Mouton et al., 2020). Next, helped by a Python analysis utility I highlighted the presence of a local crowding gradient between mother and daughter cells in proximity to the bud neck (Figure 4-2).

I hypothesise this gradient plays the role of a diffusion barrier between the mother cell and daughter cell and contributes to describing asymmetrical cell division observed in the budding yeast where cytotoxic molecules and ageing markers/by-products have been reported polarised in the mother cell. On the contrary, the vacuole can be inherited by active metabolic mechanisms and bypass this crowding diffusion barrier. I also report in this thesis (Chapter 4) that macromolecular crowding can be sensed in a

three-colour imaging experiment, using sequentially CrGE for FRET readout followed by the near infra-red compatible FM4-64 dye, marking the vacuole (Figure 4-7). This result shows that the mCerulean3-mCitrine FRET pair is compatible with near-IR and by extension infrared probe for three-colour imaging which can be generally valuable for a wide range of studies involving the required visualisation of any compartment of interest while measuring physical parameters such as crowding with the CrGE sensor. This is valid with any other sensors holding the appropriate compatible probes (mCerulean3-mCitrine).

To try to highlight more of the local heterogeneity I also tracked single cells and mapped macromolecular crowding through time in each cell (during growth or osmotic stress). This experiment leads to the detection of local crowding hotspots (Figure 4-4). These hotspots display however a high signal-to-noise ratio in the intracellular environment. We suspect local crowding dynamics to be below this interval, on the millisecond timescale as for other metabolic events and our time-lapse experiments (5 min intervals) with an acquisition time of 1.56 seconds to contribute to increasing the noise surrounding the identified hotspots. The SNR of the hotspots however is close in magnitude to the SNR threshold used for tracking single molecules *in vivo* imaged with the Slimfield technique. This result is therefore encouraging preliminary support for the presence of intracellular local crowding dynamics alongside cellular stress, stress recovery, and during cellular growth. Therefore local crowding dynamics may play a role in various metabolic activities, by influencing molecules diffusion, interactions, and localisation.

Finally, I presented single molecule level characterisation of the CrGE sensor and CrGE2.3 (Figure 4-5 and Figure 4-6). And successfully reported the detection of single molecules by Slimfield microscopy, to extract copy number information and tracks. However, measuring FRET efficiency for individual sensor molecules detected was a challenging task which raised questions about how to optimise the system. One idea would be to image with increased exposure time a semi-static system (e.g., the sensor attached to the plasma membrane) to improve the identification of single molecules and ratioFRET signal. Various parameters, whether technical on the microscope or biological

on the cellular model, can influence the readout and thus complicate the work to find optimal conditions.

For the second part of my PhD project (from chapter 5) I developed a cellular model reporter of aggregation via the production of a fluorescent mutant protein prone to aggregation in the cytoplasm: ΔssCPY*, a mutant version of the vacuolar carboxypeptidase Y. I generated different versions of this copper inducible reporter, expressing different fluorophores such as mNeonGreen and mScarlet-I, the initial construct expressing mGFP tagged ΔssCPY* (Figure 5-3 and Figure 5-4). I first characterised the aggregates with Slimfield super-resolution microscopy and showed how the stoichiometry increase is associated with reduced mobility in cells with aggregates (using copper induction system) exposed to osmotic stress with associated crowding upshift using a high concentration of sodium chloride (1 M) or sorbitol (1.5 M) (Figure 5-6). This copper inducible construct successfully produces fluorescent aggregates and provides preliminary insights into aggregates' dynamics under osmotic stress. The model is opening endless opportunities for studies in various domains, including cellular stress but also ageing and cell polarity.

Through my PhD I have coded several ImageJ macros to automate analysis tasks of my data, this includes the presented macro for ratiometric FRET macro or the presented spot count macro to detect aggregates in cells. Allowing from segmentation mask of the cell to extract all information I require from the image for my analysis (e.g., fluorescence intensities, areas, counts). These are simple tools but very efficient to perform large-scale characterisation of fluorescent images and therefore could be valuable tools to the scientific community.

Finally, the last chapter, chapter 6 presents a non-exhaustive list of valuable side experiments, collaboration results and trials with research new directions and aspirations, such as the gravity-fed flowcell system or the premises of a new cloning strategy to attach locally the CrGE2.3 sensor at the plasma membrane.

This chapter overall represents well the scientific adventure that was my PhD, with many scientific questions and hypotheses identified (nourished by countless debates and

discussions). These hypotheses and new ideas were tested and resulting experimental outcomes progressively shaped my work to the present reported research project.

2. Research impact

2.1. Academic impact

The research's academic impact is evaluated by its contribution to understanding and advancing knowledge in the field investigated and by the dissemination of scientific methods, results, and applications in the discipline(s) concerned. This project was designed to address the above and target key biological-biophysical questions to understand living system dynamics.

The work presented and methodology developed focused on understanding cells' responses to environmental stress and investigating macromolecular crowding and associated spatiotemporal events to ensure cell survival, such as the intracellular distribution of stress-induced aggregates. Investigating the biological mechanisms behind stress survival can lead to a better comprehension of the fundamental rules governing living systems, which are complex and currently poorly understood. In this regard, the project was set-up to answer crucial pending questions that, if answered, will benefit the scientific community and push our biological knowledge further.

The initial focus was on macromolecular crowding dynamics in the cell during cellular stress (osmotic stress, glucose availability) or cell division. Indeed, the intracellular environment is crowded, and the density of molecules at a given time can influence the entire proteostasis and intracellular pathways. It can alter the diffusion and localisation of molecules, the folding and kinetics of proteins, and their interactions (see in more detail in the literature review Chapter 1). To be able to quantify crowding in living cells, Dr. Arnold Boersma and Prof. Bert Poolman have developed bio-compatible sensors

utilising FRET technology (CrGE and CrGE2.3 – see Chapter 3) which we used in this project to measure macromolecular crowding changes in living cells in various conditions and to assess local crowding information.

Therefore, this work directly continues previous research advancements in the field. Importantly, new methodologies were developed to fully utilise the potential of the sensor technology and maximise the information that could be extracted from the data. The development of pixel-by-pixel maps for ratiometric FRET was the first step to accessing molecular crowding information at a subcellular level and opens a new research path regarding the role of crowding at local points in the cells. The experimentation was pushed down to access single-molecule information with biophysical instrumentation such as Slimfiled super-resolution, a bespoke microscope developed in the lab, giving access to dynamics at the millisecond time scales of tracked fluorescent molecules.

Overall, we addressed questions at different biological scales, considering cell populations as a unit but also the disparities in individual cells' behaviour, especially with age differences between cells, for example, heterogeneous and subgroups such as mother cells and daughter cells exist. This includes synthetic biology and genomics to develop a novel fluorescent reporter for aggregation, but also microscopy techniques. This approach is connected with several current research challenges, especially those regarding cellular polarity during cell division and stress responses.

In this project, techniques and tools for acquiring and analysing image data that could benefit the rest of the scientific community were developed and shared through peer-reviewed published articles. This outcome greatly promoted collaborative discussions and new research developments with other research groups. The entire project was highly collaborative, such as our collaboration with Prof. Marija Cvijovic's lab, whose work focuses on the mathematical modelling of biological processes related to ageing (e.g., asymmetrical distribution of aggregates, osmotic stress response pathways).

Finally, the dissemination of the research through articles, seminars, and talks has inspired valuable ideas in this direction for future work and connections between

academics working on similar topics. The interdisciplinary nature of the project also greatly helped the development of a network of scientists and collaborators, as mentioned above, which helped the project's progression and its potential to inspire new research developments in the future.

2.2. Economic and societal impact

This research project was funded by Marie Skłodowska-Curie Actions under the SynCrop consortium (Synthetic Circuits for Robust Orthogonal Production). The project targeted the understanding of key fundamental biological processes (responses to environmental stress, ageing, and crowding) to ultimately answer critical questions for industrial and biotechnology purposes. Specifically, it aimed to anticipate synthetic circuit behaviours introduced in living cells for the production of pharmaceuticals or food additives. The introduction of synthetic components indeed reprograms metabolic pathways in the host organism to achieve the biosynthesis of a desired product. The homeostasis of the cells is disturbed by the accumulation of the exogenic compound, which ultimately induces premature cellular stress and threatens cell integrity. It can impact cell survival and therefore compromise production yields for the compound of interest. In the industry, it became important to develop new approaches to understand and monitor the performance of synthetic circuits and their interaction with core metabolic processes in the cell. Doing so will help model and predict the performance of existing and newly designed synthetic circuits and ultimately permit the optimisation of practices for high-yield production.

This major scientific goal was targeted through the development of a new cellular model in the budding yeast. This organism is commonly used in the industry to produce vitamins (Kessi-Pérez et al., 2022; Lanen et al., 1942; Mata-Gómez et al., 2014) and key pharmaceutical drugs such as the insulin precursor treating diabetes (Kjeldsen, 2000) or hepatitis surface antigens required for to make hepatitis vaccines (Bitter et al., 1988; Madhavan et al., 2021; Nielsen, 2013). The cellular model developed and presented in this thesis has a controllable synthetic circuit for the production of cytoplasmic protein

aggregates attached to a fluorescent reporter (ΔssCPY*-mGFP mutant proteins), which accumulate in the cell and are visible by optical microscopy methods. Importantly, we developed new image analysis tools for their rapid spatiotemporal quantification to monitor and analyse the distribution dynamics of such compounds in stressed cells, especially during osmotic stress for which we got insights into crowding dynamics. We indeed investigated crowding as it is a key physical parameter to maintain cellular homeostasis and cell integrity. Experimental results have helped us better understand how cells manage environmental stress and stress imposed by synthetic gene circuits.

In brief, the work presented found that yeast cells grown with high and low glucose concentrations display low and high intracellular molecular crowding in the population, showing the key relation between nutrient availability and crowding as a physical property of the cytoplasm (see Chapter 3). Using our new analysis pipeline enabled dynamic pixel-by-pixel quantification of macromolecular crowding and showed how osmotic stress and cell growth induce heterogeneous crowding, with potential subcellular hotspots of crowding identified after stress events. We discuss in Chapter 4 the technical challenge of observing these hotspots dynamically, the novelty of this technology, and its potential as a launching ramp for the future development of robust methods for local crowding dynamics with for example improved spatial and temporal resolution. At proximity to the cell bud neck during division, local stable crowding differences were measurable and suspected to influence the cell polarity and diffusion barrier between the mother cell and daughter cell (see Chapter 4). Finally, our project showed how osmotic pressure drives the nucleation of protein aggregates while reducing their intracellular diffusion (see Chapter 5).

These new insights can help develop future strategies to better mediate cellular stress responses and improve expression output from synthetic gene circuits in host organisms. This aims to improve performance, reduce costs, and eventually increase the accessibility of bio-products and pharmaceuticals to the general population.

Finally, the therapeutic and biomedical impact of this research comes from the choice of the cellular model *S. cerevisiae.* This single cell eukaryotic microorganism exhibits

biological properties comparable to those of mammalian cells (Botstein et al., 1997; Gershon et al., 2000; Mager & Winderickx, 2005), with similar intracellular compartmentalisation (e.g., nucleus, ER, mitochondria), protein homeostasis, and fundamental metabolic functions such as cell division and response to cellular stress (Duina et al., 2014; Gershon & Gershon, 2000). Life systems are therefore at equilibrium, and understanding how this is adjusted and maintained over time will meaningfully contribute to understanding stress regulation and ageing processes with great biomedical potential.

Yeast as a cellular model becomes doubly interesting with protein aggregates typically associated with cellular stress, ageing and responsible in humans for pathologies such as neurodegenerative diseases (Miller-Fleming et al., 2008; Piper, 2006; Tenreiro et al., 2013). It is therefore an entry-level model to understand processes of aggregation such as those observed in various pathological conditions (e.g., cataracts, Parkinson and Alzheimer diseases) (Bharadwaj et al., 2010; Bharadwaj et al., 2008; Braun et al., 2015; Mcdonald et al., 2020; Morishita, 2022; Satoh et al., 2021). With the longer life expectancy of our societies, age-related pathologies from diabetes (type 2) (Suastika et al., 2012), cancers (De Magalhães, 2013; Smetana et al., 2016) to neurodegenerative disease (Hou et al., 2019) have progressed to become a current public health problem that needs to be addressed (Niccoli & Partridge, 2012; Prince et al., 2015; Suastika et al., 2012). Our research was therefore designed to address biomedical challenges with high societal impact.

2.3. Conclusion

To conclude, the research's impact, especially in terms of economic and societal influence, can be a challenge to evaluate. To ensure the greatest possible outcome and application of this research, the project was designed to promote communication between the industries and academics, to develop new methods to perform high-throughput characterisation on production systems, and target to find answers to biological questions that will benefit both parties. The project shows the outcome of our effort to quantify and map macromolecular crowding at the intracellular level (pixel-by-

pixel maps from read-outs of biomolecular sensors), identifying key areas with differential local crowding (the bud neck). A parameter directly linked to the regulation of cellular stress and influencing the spatiotemporal dynamics of molecules and metabolic functions. Its understanding is therefore critical to elucidate for both industrial and biomedical purposes. Finally, we also designed a cellular model for controlling protein aggregation that not only mimics the yeast expression system for the production of commercial biomolecules but also permits investigations into the fundamental processes of protein aggregation relevant to the biomedical field. For this purpose, novel methods of imaging were used (Slimfield microscopy), allowing access to dynamic information down to the single-molecule localisation precision and millisecond time resolution. Overall, this work has the potential to inspire a variety of new research developments, both beneficial for the progress of our fundamental understanding of living systems and for the development of applied scientific methodologies with economic and societal benefits.

References

Abbe, E. (1873). Beiträge zur Theorie des Mikroskops und der mikroskopischen Wahrnehmung. *Archiv für mikroskopische Anatomie*, *9*(1), 413-468.

Agozzino, L., Balázsi, G., Wang, J., & Dill, K. A. (2020). How do cells adapt? Stories told in landscapes. *Annual review of chemical and biomolecular engineering*, *11*, 155.

Ahmad, M., & Bussey, H. (1986). Yeast arginine permease: nucleotide sequence of the CAN1 gene. *Current genetics*, *10*, 587-592.

Ahmadpour, D., Geijer, C., Tamas, M. J., Lindkvist-Petersson, K., & Hohmann, S. (2014). Yeast reveals unexpected roles and regulatory features of aquaporins and aquaglyceroporins. *Biochimica et Biophysica Acta (BBA)-General Subjects*, *1840*(5), 1482-1491.

Albers, E., Larsson, C., Andlid, T., Walsh, M. C., & Gustafsson, L. (2007). Effect of nutrient starvation on the cellular composition and metabolic capacity of Saccharomyces cerevisiae. *Applied and Environmental Microbiology*, *73*(15), 4839-4848.

Albertyn, J., Hohmann, S., Thevelein, J. M., & Prior, B. A. (1994). GPD1, which encodes glycerol-3-phosphate dehydrogenase, is essential for growth under osmotic stress in Saccharomyces cerevisiae, and its expression is regulated by the high-osmolarity glycerol response pathway. *Molecular and cellular biology*, *14*(6), 4135-4144.

Albrecht, C. (2008). Joseph R. Lakowicz: Principles of fluorescence spectroscopy. *Analytical and Bioanalytical Chemistry*, *390*(5), 1223-1224.

Alfieri, R. R., & Petronini, P. G. (2007). Hyperosmotic stress response: comparison with other cellular stresses. *Pflügers Archiv-European Journal of Physiology*, *454*(2), 173-185.

Altenbach, H. (2020). Stokes, George Gabriel. *Encyclopedia of Continuum Mechanics*, 2328-2330.

Ando, T., & Skolnick, J. (2010). Crowding and hydrodynamic interactions likely dominate in vivo macromolecular motion. *Proceedings of the National Academy of Sciences*, *107*(43), 18457-18462.

André, A. A., & Spruijt, E. (2020). Liquid–liquid phase separation in crowded environments. *International Journal of Molecular Sciences*, *21*(16), 5908.

Andrews, D. L., & Lipson, R. H. (2021). Molecular fluorescence. In *Molecular Photophysics and Spectroscopy (Second Edition)*. IOP Publishing.

Aravind, L., Walker, D. R., & Koonin, E. V. (1999). Conserved domains in DNA repair proteins and evolution of repair systems. *Nucleic acids research*, *27*(5), 1223-1242.

Arrasate, M., Mitra, S., Schweitzer, E. S., Segal, M. R., & Finkbeiner, S. (2004). Inclusion body formation reduces levels of mutant huntingtin and the risk of neuronal death. *Nature*, *431*(7010), 805-810.

Asarian, L., Gloy, V., & Geary, N. (2012). Homeostasis. InEncyclopedia of Human Behavior, ; Ramachandran, VS, Ed. In: Academic Press: San Diego, CA, USA.

Atkins, P., & De Paula, J. (2014). Atkins' Physical Chemistry. Oxford University Press, 2009.–1008 p.

Babazadeh, R., Lahtvee, P.-J., Adiels, C. B., Goksör, M., Nielsen, J. B., & Hohmann, S. (2017). The yeast osmostress response is carbon source dependent. *Scientific reports*, *7*(1), 1-11.

Badrinarayanan, A., Reyes-Lamothe, R., Uphoff, S., Leake, M. C., & Sherratt, D. J. (2012). In vivo architecture and action of bacterial structural maintenance of chromosome proteins. *Science*, *338*(6106), 528-531.

Bagamery, L. E., Justman, Q. A., Garner, E. C., & Murray, A. W. (2020). A putative bet-hedging strategy buffers budding yeast against environmental instability. *Current biology*, *30*(23), 4563-4578. e4564.

Bagola, K., & Sommer, T. (2008). Protein quality control: on IPODs and other JUNQ. *Current biology*, *18*(21), R1019-R1021.

Baker Brachmann, C., Davies, A., Cost, G. J., Caputo, E., Li, J., Hieter, P., & Boeke, J. D. (1998). Designer deletion strains derived from Saccharomyces cerevisiae S288C: a useful set of strains and plasmids for PCR-mediated gene disruption and other applications. *Yeast*, *14*(2), 115-132.

Bankaitis, V. A., Johnson, L. M., & Emr, S. D. (1986). Isolation of yeast mutants defective in protein targeting to the vacuole. *Proceedings of the National Academy of Sciences*, *83*(23), 9075-9079.

Beal, M. F. (2005). Mitochondria take center stage in aging and neurodegeneration. *Annals of Neurology: Official Journal of the American Neurological Association and the Child Neurology Society*, *58*(4), 495-505.

Bellí, G., Garí, E., Aldea, M., & Herrero, E. (2001). Osmotic stress causes a G1 cell cycle delay and downregulation of Cln3/Cdc28 activity in Saccharomyces cerevisiae. *Molecular Microbiology*, *39*(4), 1022-1035.

Bermejo, C., Haerizadeh, F., Takanaga, H., Chermak, D., & Frommer, W. B. (2011). Optical sensors for measuring dynamic changes of cytosolic metabolite levels in yeast. *Nature protocols*, *6*(11), 1806-1817.

Bertani, G. (1951). Studies on lysogenesis I: the mode of phage liberation by lysogenic Escherichia coli. *Journal of bacteriology*, *62*(3), 293-300.

Betzig, E., Patterson, G. H., Sougrat, R., Lindwasser, O. W., Olenych, S., Bonifacino, J. S., Davidson, M. W., Lippincott-Schwartz, J., & Hess, H. F. (2006). Imaging intracellular fluorescent proteins at nanometer resolution. *Science*, *313*(5793), 1642-1645.

Bevis, B. J., & Glick, B. S. (2002). Rapidly maturing variants of the Discosoma red fluorescent protein (DsRed). *Nature biotechnology*, *20*(1), 83-87.

Bharadwaj, P., Martins, R., & Macreadie, I. (2010). Yeast as a model for studying Alzheimer's disease. *FEMS yeast research*, *10*(8), 961-969.

Bharadwaj, P., Waddington, L., Varghese, J., & Macreadie, I. G. (2008). A new method to measure cellular toxicity of non-fibrillar and fibrillar Alzheimer's Aβ using yeast. *Journal of Alzheimer's Disease*, *13*(2), 147-150.

Bi, E., & Park, H.-O. (2012). Cell polarization and cytokinesis in budding yeast. *Genetics*, *191*(2), 347-387.

Bindels, D. S., Haarbosch, L., Van Weeren, L., Postma, M., Wiese, K. E., Mastop, M., Aumonier, S., Gotthard, G., Royant, A., & Hink, M. A. (2017). mScarlet: a bright monomeric red fluorescent protein for cellular imaging. *Nature Methods*, *14*(1), 53-56.

Bitter, G. A., Egan, K. M., Burnette, W. N., Samal, B., Fieschko, J. C., Peterson, D. L., Downing, M. R., Wypych, J., & Langley, K. E. (1988). Hepatitis B vaccine produced in yeast. *Journal of medical virology*, *25*(2), 123-140.

Bleoanca, I., & Bahrim, G. (2013). Overview on brewing yeast stress factors. *Romanian Biotechnological Letters*, *18*(5), 8559-8572.

Blom, H., & Widengren, J. (2017). Stimulated emission depletion microscopy. *Chemical reviews*, *117*(11), 7377-7427.

Boersma, A. J., Zuhorn, I. S., & Poolman, B. (2015). A sensor for quantification of macromolecular crowding in living cells. *Nature Methods*, *12*(3), 227-229.

Botstein, D., Chervitz, S. A., & Cherry, M. (1997). Yeast as a model organism. *Science*, *277*(5330), 1259-1260.

Bowman, S., Churcher, C., Badcock, K., Brown, D., Chillingworth, T., Connor, R., Dedman, K., Devlin, K., Gentles, S., Hamlin, N., Hunt, S., Jagels, K., Lye, G., Moule, S., Odell, C., Pearson, D., Rajandream, M., Rice, P., Skelton, J., . . . Barrell, B. (1997). The nucleotide sequence of Saccharomyces cerevisiae chromosome XIII. *Nature*, *387*(6632 Suppl), 90-93.

Bowman, S. M., & Free, S. J. (2006). The structure and synthesis of the fungal cell wall. *Bioessays*, *28*(8), 799-808.

Bradley, P. H., Brauer, M. J., Rabinowitz, J. D., & Troyanskaya, O. G. (2009). Coordinated concentration changes of transcripts and metabolites in Saccharomyces cerevisiae. *PLoS computational biology*, *5*(1), e1000270.

Bradski, G. (2000). The openCV library. *Dr. Dobb's Journal: Software Tools for the Professional Programmer*, *25*(11), 120-123.

Braun, R. J., Sommer, C., Leibiger, C., Gentier, R. J., Dumit, V. I., Paduch, K., Eisenberg, T., Habernig, L., Trausinger, G., & Magnes, C. (2015). Modeling non-hereditary mechanisms of Alzheimer disease during apoptosis in yeast. *Microbial Cell*, *2*(4), 136.

Brewster, J. L., & Gustin, M. C. (1994). Positioning of cell growth and division after osmotic stress requires a MAP kinase pathway. *Yeast*, *10*(4), 425-439.

Broach, J. R. (2012). Nutritional control of growth and development in yeast. *Genetics*, *192*(1), 73-105.

Brunner, E., & Munzel, U. (2000). The nonparametric Behrens-Fisher problem: asymptotic theory and a small-sample approximation. *Biometrical Journal: Journal of Mathematical Methods in Biosciences*, *42*(1), 17-25.

Bryant, N. J., & Stevens, T. H. (1998). Vacuole biogenesis in Saccharomyces cerevisiae: protein transport pathways to the yeast vacuole. *Microbiology and molecular biology reviews*, *62*(1), 230-247.

Bubnová, M., Zemančíková, J., & Sychrová, H. (2014). Osmotolerant yeast species differ in basic physiological parameters and in tolerance of non-osmotic stresses. *Yeast*, *31*(8), 309-321.

Bulthuis, E. P., Dieteren, C. E., Bergmans, J., Berkhout, J., Wagenaars, J. A., van de Westerlo, E. M., Podhumljak, E., Hink, M. A., Hesp, L. F., & Rosa, H. S. (2023). Stress-dependent macromolecular crowding in the mitochondrial matrix. *The EMBO Journal*, e108533.

Burri, L., & Lithgow, T. (2004). A complete set of SNAREs in yeast. *Traffic*, *5*(1), 45-52.

Byers, B., & Goetsch, L. (1976). A highly ordered ring of membrane-associated filaments in budding yeast. *The Journal of cell biology*, *69*(3), 717-721.

Cadet, J., Sage, E., & Douki, T. (2005). Ultraviolet radiation-mediated damage to cellular DNA. *Mutation Research/Fundamental and Molecular Mechanisms of Mutagenesis*, *571*(1-2), 3-17.

Cai, N., Lai, A. C.-K., Liao, K., Corridon, P. R., Graves, D. J., & Chan, V. (2022). Recent advances in fluorescence recovery after Photobleaching for decoupling transport and kinetics of biomacromolecules in cellular physiology. *Polymers*, *14*(9), 1913.

Campioni, S., Bagnani, M., Pinotsi, D., Lecinski, S., Rodighiero, S., Adamcik, J., & Mezzenga, R. (2020). Interfaces Determine the Fate of Seeded α-Synuclein Aggregation. *Advanced Materials Interfaces*, *7*(11), 2000446.

Černý, J., & Hobza, P. (2007). Non-covalent interactions in biomacromolecules. *Physical Chemistry Chemical Physics*, *9*(39), 5291-5303.

Champion, L., Linder, M. I., & Kutay, U. (2017). Cellular reorganization during mitotic entry. *Trends in cell biology*, *27*(1), 26-41.

Chant, J., & Pringle, J. R. (1995). Patterns of bud-site selection in the yeast Saccharomyces cerevisiae. *The Journal of cell biology*, *129*(3), 751-765.

Chen, H., Ding, F., Zhou, Z., He, X., & Shen, J. (2020). FRET-based sensor for visualizing pH variation with colorimetric/ratiometric strategy and application for bioimaging in living cells, bacteria and zebrafish. *Analyst*, *145*(12), 4283-4294.

Chen, H., Howell, A. S., Robeson, A., & Lew, D. J. (2011). Dynamics of septin ring and collar formation in Saccharomyces cerevisiae.

Chen, L., & Davis, N. G. (2000). Recycling of the yeast a-factor receptor. *The Journal of cell biology*, *151*(3), 731-738.

Chen, Y., Wang, Y., Zhang, J., Deng, Y., Jiang, L., Song, E., Wu, X. S., Hammer, J. A., Xu, T., & Lippincott-Schwartz, J. (2012). Rab10 and myosin-Va mediate insulin-stimulated GLUT4 storage vesicle translocation in adipocytes. *Journal of Cell Biology*, *198*(4), 545-560.

Chenevert, J. M. (1993). *Establishment of cell polarity during mating in yeast*. (Doctoral Dissertation, UCSF).

Cheung, M. S., & Thirumalai, D. (2007). Effects of crowding and confinement on the structures of the transition state ensemble in proteins. *The Journal of Physical Chemistry B*, *111*(28), 8250-8257.

Chiou, J.-g., Balasubramanian, M. K., & Lew, D. J. (2017). Cell polarity in yeast. *Annual review of cell and developmental biology*, *33*, 77.

Chiti, F., & Dobson, C. M. (2006). Protein misfolding, functional amyloid, and human disease. *Annu. Rev. Biochem.*, *75*, 333-366.

Chiti, F., & Dobson, C. M. (2017). Protein misfolding, amyloid formation, and human disease: a summary of progress over the last decade. *Annu. Rev. Biochem*, *86*(1), 27-68.

Chowdhury, S., Smith, K. W., & Gustin, M. C. (1992). Osmotic stress and the yeast cytoskeleton: phenotype-specific suppression of an actin mutation. *The Journal of cell biology*, *118*(3), 561-571.

Chozinski, T. J., Gagnon, L. A., & Vaughan, J. C. (2014). Twinkle, twinkle little star: Photoswitchable fluorophores for super-resolution imaging. *FEBS Letters*, *588*(19), 3603-3612.

Christiansen, A., Wang, Q., Cheung, M. S., & Wittung-Stafshede, P. (2013). Effects of macromolecular crowding agents on protein folding in vitro and in silico. *Biophysical reviews*, *5*, 137-145.

Clark, A. (2015). Pillow (pil fork) documentation. *Python Imaging Library.readthedocs*.

Clay, L., Caudron, F., Denoth-Lippuner, A., Boettcher, B., Buvelot Frei, S., Snapp, E. L., & Barral, Y. (2014). A sphingolipid-dependent diffusion barrier confines ER stress to the yeast mother cell. *eLife*, *3*, e01883.

Clay, L., Caudron, F., Denoth-Lippuner, A., Boettcher, B., Frei, S. B., Snapp, E. L., & Barral, Y. (2014). A sphingolipid-dependent diffusion barrier confines ER stress to the yeast mother cell. *eLife*, *3*, e01883.

Comings, D. E. (1972). The structure and function of chromatin. *Advances in human genetics*, 237-431.

Cooper, G. M., & Hausman, R. (2000). A molecular approach. *The Cell. 2nd ed. Sunderland, MA: Sinauer Associates*.

Cormack, B. P., Valdivia, R. H., & Falkow, S. (1996). FACS-optimized mutants of the green fluorescent protein (GFP). *Gene*, *173*(1), 33-38.

Cosgrove, J., Novkovic, M., Albrecht, S., Pikor, N. B., Zhou, Z., Onder, L., Mörbe, U., Cupovic, J., Miller, H., & Alden, K. (2020). B cell zone reticular cell microenvironments shape CXCL13 gradient formation. *Nature communications*, *11*(1), 1-15.

Cost, G. J., & Boeke, J. D. (1996). A useful colony colour phenotype associated with the yeast selectable/counter-selectable marker MET15. *Yeast*, *12*(10), 939-941.

Dahiya, R., Mohammad, T., Alajmi, M. F., Rehman, M. T., Hasan, G. M., Hussain, A., & Hassan, M. I. (2020). Insights into the conserved regulatory mechanisms of human and yeast aging. *Biomolecules*, *10*(6), 882.

De Magalhães, J. P. (2013). How ageing processes influence cancer. *Nature Reviews Cancer*, *13*(5), 357-365.

De Virgilio, C. (2012). The essence of yeast quiescence. *FEMS microbiology reviews*, *36*(2), 306-339.

Demas, J. N., & Demas, S. E. (2003). Luminescence. In R. A. Meyers (Ed.), *Encyclopedia of Physical Science and Technology (Third Edition)* (pp. 799-823). Academic Press.

Desfougères, Y., Neumann, H., & Mayer, A. (2016). Organelle size control–increasing vacuole content activates SNAREs to augment organelle volume through homotypic fusion. *Journal of cell science*, *129*(14), 2817-2828.

Devirgiliis, C., Murgia, C., Danscher, G., & Perozzi, G. (2004). Exchangeable zinc ions transiently accumulate in a vesicular compartment in the yeast Saccharomyces cerevisiae. *Biochemical and Biophysical Research Communications*, *323*(1), 58-64.

Dey, D., Marciano, S., Nunes-Alves, A., Kiss, V., Wade, R. C., & Schreiber, G. (2021). Line-FRAP, a versatile method to measure diffusion rates in vitro and in vivo. *Journal of molecular biology*, *433*(9), 166898.

Ding, J., Huang, X., Zhang, L., Zhao, N., Yang, D., & Zhang, K. (2009). Tolerance and stress response to ethanol in the yeast Saccharomyces cerevisiae. *Applied microbiology and biotechnology*, *85*, 253-263.

Dix, J. A., & Verkman, A. (2008). Crowding effects on diffusion in solutions and cells. *Annu. Rev. Biophys.*, *37*, 247-263.

Dong, H., Qin, S., & Zhou, H.-X. (2010). Effects of macromolecular crowding on protein conformational changes. *PLoS computational biology*, *6*(7), e1000833.

Dong, X., Qin, L.-Y., Gong, Z., Qin, S., Zhou, H.-X., & Tang, C. (2022). Preferential Interactions of a Crowder Protein with the Specific Binding Site of a Native Protein Complex. *The Journal of Physical Chemistry Letters*, *13*(3), 792-800.

Dreier, K. (2017). *What are Fluorescence and Phosphorescence?* Chemistryviews.

Duina, A. A., Miller, M. E., & Keeney, J. B. (2014). Budding yeast for budding geneticists: a primer on the Saccharomyces cerevisiae model system. *Genetics*, *197*(1), 33-48.

Dujon, B. (1996). The yeast genome project: what did we learn? *Trends in Genetics*, *12*(7), 263-270.

Dumetz, A. C., Chockla, A. M., Kaler, E. W., & Lenhoff, A. M. (2008). Effects of pH on protein–protein interactions and implications for protein phase behavior. *Biochimica et Biophysica Acta (BBA)-Proteins and Proteomics*, *1784*(4), 600-610.

Dunn, O. J. (1961). Multiple comparisons among means. *Journal of the American statistical association*, *56*(293), 52-64.

Edelhoch, H. (1967). Spectroscopic determination of tryptophan and tyrosine in proteins. *Biochemistry*, *6*(7), 1948-1954.

Edwards, G., Breckenridge, A., Adjepon-Yamoah, K., Orme, M., & Ward, S. (1981). The effect of variations in urinary pH on the pharmacokinetics of diethylcarbamazine. *British journal of clinical pharmacology*, *12*(6), 807-812.

Einstein, A. (1905). Über die von der molekularkinetischen Theorie der Wärme geforderte Bewegung von in ruhenden Flüssigkeiten suspendierten Teilchen. *Annalen der physik*, *4*.

Eisele, F. (2011). Components and mechanisms of cytoplasmic protein quality control and elimination of regulatory enzymes.

Elliott, A. D. (2020). Confocal microscopy: principles and modern practices. *Current protocols in cytometry*, *92*(1), e68.

Ellis, R. J. (2007). Protein misassembly. *Molecular aspects of the stress response: Chaperones, membranes and networks*, 1-13.

Elsliger, M.-A., Wachter, R. M., Hanson, G. T., Kallio, K., & Remington, S. J. (1999). Structural and spectral response of green fluorescent protein variants to changes in pH. *Biochemistry*, *38*(17), 5296-5301.

Engel, S. R., Dietrich, F. S., Fisk, D. G., Binkley, G., Balakrishnan, R., Costanzo, M. C., Dwight, S. S., Hitz, B. C., Karra, K., & Nash, R. S. (2014). The reference genome sequence of Saccharomyces cerevisiae: then and now. *G3: Genes, Genomes, Genetics*, *4*(3), 389-398.

Engel, W. K. (1964). Mitochondrial aggregates in muscle disease. *Journal of Histochemistry & Cytochemistry*, *12*(1), 46-48.

Erjavec, N., Larsson, L., Grantham, J., & Nyström, T. (2007). Accelerated aging and failure to segregate damaged proteins in Sir2 mutants can be suppressed by overproducing the protein aggregation-remodeling factor Hsp104p. *Genes & development*, *21*(19), 2410-2421.

Escusa-Toret, S., Vonk, W. I., & Frydman, J. (2013). Spatial sequestration of misfolded proteins by a dynamic chaperone pathway enhances cellular fitness during stress. *Nature cell biology*, *15*(10), 1231-1243.

Eskes, E., Deprez, M.-A., Wilms, T., & Winderickx, J. (2018). pH homeostasis in yeast; the phosphate perspective. *Current genetics*, *64*(1), 155-161.

Faty, M., Fink, M., & Barral, Y. (2002). Septins: a ring to part mother and daughter. *Current genetics*, *41*(3), 123-131.

Field, J., Nikawa, J.-l., Broek, D., MacDonald, B., Rodgers, L., Wilson, I., Lerner, R., & Wigler, M. (1988). Purification of a RAS-responsive adenylyl cyclase complex from Saccharomyces cerevisiae by use of an epitope addition method. *Molecular and cellular biology*, *8*(5), 2159-2165.

Finger, A., Knop, M., & Wolf, D. H. (1993). Analysis of two mutated vacuolar proteins reveals a degradation pathway in the endoplasmic reticulum or a related compartment of yeast. *European Journal of Biochemistry*, *218*(2), 565-574.

Fiorini, E., Börner, R., & Sigel, R. K. (2015). Mimicking the in vivo environment–The effect of crowding on RNA and biomacromolecular folding and activity. *Chimia*, *69*(4), 207-207.

Fischer-Parton, S., Parton, R., Hickey, P., Dijksterhuis, J., Atkinson, H., & Read, N. (2000). Confocal microscopy of FM4-64 as a tool for analysing endocytosis and vesicle trafficking in living fungal hyphae. *Journal of microscopy*, *198*(3), 246-259.

Fish, K. N. (2009). Total internal reflection fluorescence (TIRF) microscopy. *Current protocols in cytometry*, *50*(1), 12.18. 11-12.18. 13.

Fogel, S., & Welch, J. W. (1982). Tandem gene amplification mediates copper resistance in yeast. *Proceedings of the National Academy of Sciences*, *79*(17), 5342-5346.

Förster, T. (1948). Intermolecular energy transfer and fluorescence. *Ann. Phys. Leipzig.*, *2*, 55-75.

Franzmann, T. M., & Alberti, S. (2019). Protein phase separation as a stress survival strategy. *Cold Spring Harbor perspectives in biology*, *11*(6), a034058.

Franzmann, T. M., Jahnel, M., Pozniakovsky, A., Mahamid, J., Holehouse, A. S., Nüske, E., Richter, D., Baumeister, W., Grill, S. W., & Pappu, R. V. (2018). Phase separation of a yeast prion protein promotes cellular fitness. *Science*, *359*(6371), eaao5654.

Friedman, J. R., & Nunnari, J. (2014). Mitochondrial form and function. *Nature*, *505*(7483), 335-343.

Frohlich, V. C. (2008). Phase contrast and differential interference contrast (DIC) microscopy. *JoVE (Journal of Visualized Experiments)*(18), e844.

Fulda, S., Gorman, A. M., Hori, O., & Samali, A. (2010). Cellular stress responses: cell survival and cell death. *International journal of cell biology*, *2010*.

Fulton, A. B. (1982). How crowded is the cytoplasm? *Cell*, *30*(2), 345-347.

Garcia-Rubio, R., de Oliveira, H. C., Rivera, J., & Trevijano-Contador, N. (2020). The fungal cell wall: Candida, Cryptococcus, and Aspergillus species. *Frontiers in microbiology*, *10*, 2993.

Garner, M. M., & Burg, M. B. (1994). Macromolecular crowding and confinement in cells exposed to hypertonicity. *American Journal of Physiology-Cell Physiology*, *266*(4), C877-C892.

Gershon, H., & Gershon, D. (2000). The budding yeast, Saccharomyces cerevisiae, as a model for aging research: a critical review. *Mechanisms of ageing and development*, *120*(1-3), 1-22.

Gershon, H., Gershon, D., & (2000). The budding yeast, Saccharomyces cerevisiae, as a model for aging research: A critical review. In (Vol. 120, pp. 1-22): Elsevier.

Ghaemmaghami, S., Huh, W.-K., Bower, K., Howson, R. W., Belle, A., Dephoure, N., O'Shea, E. K., & Weissman, J. S. (2003). Global analysis of protein expression in yeast. *Nature*, *425*(6959), 737-741.

Gibson, B. R., Lawrence, S. J., Leclaire, J. P., Powell, C. D., & Smart, K. A. (2007). Yeast responses to stresses associated with industrial brewery handling. *FEMS microbiology reviews*, *31*(5), 535-569.

Gilliland, R. (1971). Yeast classification. *Journal of the Institute of Brewing*, *77*(3), 276-284.

Gilson, M. K., & Zhou, H.-X. (2007). Calculation of protein-ligand binding affinities. *Annu. Rev. Biophys. Biomol. Struct.*, *36*, 21-42.

Gladfelter, A. S., Pringle, J. R., & Lew, D. J. (2001). The septin cortex at the yeast mother–bud neck. *Current opinion in microbiology*, *4*(6), 681-689.

Goffeau, A., Barrell, B. G., Bussey, H., Davis, R. W., Dujon, B., Feldmann, H., Galibert, F., Hoheisel, J. D., Jacq, C., & Johnston, M. (1996). Life with 6000 genes. *Science*, *274*(5287), 546-567.

Gohlke, C. (2020). *Point Spread Function calculations for fluorescence microscopy*.

Gonçalves, P., & Planta, R. J. (1998). Starting up yeast glycolysis. *Trends in Microbiology*, *6*(8), 314-319.

Grimminger-Marquardt, V., & Lashuel, H. A. (2010). Structure and function of the molecular chaperone Hsp104 from yeast. *Biopolymers: Original Research on Biomolecules*, *93*(3), 252-276.

Gueldener, U., Heinisch, J., Koehler, G., Voss, D., & Hegemann, J. (2002). A second set of loxP marker cassettes for Cre-mediated multiple gene knockouts in budding yeast. *Nucleic acids research*, *30*(6), e23-e23.

Guo, M., Pegoraro, A. F., Mao, A., Zhou, E. H., Arany, P. R., Han, Y., Burnette, D. T., Jensen, M. H., Kasza, K. E., & Moore, J. R. (2017). Cell volume change through water efflux impacts cell stiffness and stem cell fate. *Proceedings of the National Academy of Sciences*, *114*(41), E8618-E8627.

Gustafsson, M. G. (2000). Surpassing the lateral resolution limit by a factor of two using structured illumination microscopy. *Journal of microscopy*, *198*(2), 82-87.

Gutekunst, C.-A., Li, S.-H., Yi, H., Mulroy, J. S., Kuemmerle, S., Jones, R., Rye, D., Ferrante, R. J., Hersch, S. M., & Li, X.-J. (1999). Nuclear and neuropil aggregates in Huntington's disease: relationship to neuropathology. *Journal of Neuroscience*, *19*(7), 2522-2534.

Hagen, D. C., McCaffrey, G., & Sprague Jr, G. F. (1986). Evidence the yeast STE3 gene encodes a receptor for the peptide pheromone a factor: gene sequence and implications for the structure of the presumed receptor. *Proceedings of the National Academy of Sciences*, *83*(5), 1418-1422.

Han, J., & Burgess, K. (2010). Fluorescent indicators for intracellular pH. *Chemical reviews*, *110*(5), 2709-2728.

Hancock, R. (2014). Structures and functions in the crowded nucleus: new biophysical insights. *Frontiers in Physics*, *2*, 53.

Hansen, M., Thrane, C., Olsson, S., & Sørensen, J. (2000). Confocal imaging of living fungal hyphae challenged with the fungal antagonist viscosinamide. *Mycologia*, *92*(2), 216-221.

Hanzén, S., Vielfort, K., Yang, J., Roger, F., Andersson, V., Zamarbide-Forés, S., Andersson, R., Malm, L., Palais, G., & Biteau, B. (2016). Lifespan control by redox-dependent recruitment of chaperones to misfolded proteins. *Cell*, *166*(1), 140-151.

Haynes, C. M., Titus, E. A., & Cooper, A. A. (2004). Degradation of misfolded proteins prevents ER-derived oxidative stress and cell death. *Molecular cell*, *15*(5), 767-776.

Heim, R., Prasher, D. C., & Tsien, R. Y. (1994). Wavelength mutations and posttranslational autoxidation of green fluorescent protein. *Proceedings of the National Academy of Sciences*, *91*(26), 12501-12504.

Heintzmann, R., & Huser, T. (2017). Super-resolution structured illumination microscopy. *Chemical reviews*, *117*(23), 13890-13908.

Hell, S. W., & Wichmann, J. (1994). Breaking the diffraction resolution limit by stimulated emission: stimulated-emission-depletion fluorescence microscopy. *Optics letters*, *19*(11), 780-782.

Herschel, J. F. W. (1845). IV. ’Αμόρφωϒa, no. I.— on a case of superficial colour presented by a homogeneous liquid internally colourless. *Philosophical Transactions of the Royal Society of London*, *135*(0), 143-145.

Hettema, N., & Laan, L. (2023). A minimal in vitro system for cell polarization. *Bulletin of the American Physical Society*.

Hieronymus, H., & Silver, P. A. (2004). A systems view of mRNP biology. *Genes & development*, *18*(23), 2845-2860.

Higuchi-Sanabria, R., Pernice, W. M., Vevea, J. D., Alessi Wolken, D. M., Boldogh, I. R., & Pon, L. A. (2014). Role of asymmetric cell division in lifespan control in Saccharomyces cerevisiae. *FEMS yeast research*, *14*(8), 1133-1146.

Hill, S. M., Hanzén, S., & Nyström, T. (2017). Restricted access: spatial sequestration of damaged proteins during stress and aging. *EMBO reports*, *18*(3), 377-391.

Hill, S. M., Hao, X., Grönvall, J., Spikings-Nordby, S., Widlund, P. O., Amen, T., Jörhov, A., Josefson, R., Kaganovich, D., Liu, B., & Nyström, T. (2016). Asymmetric Inheritance of Aggregated Proteins and Age Reset in Yeast Are Regulated by Vac17-Dependent Vacuolar Functions. *Cell Rep*, *16*(3), 826-838.

Hiller, M. M., Finger, A., Schweiger, M., & Wolf, D. H. (1996). ER degradation of a misfolded luminal protein by the cytosolic ubiquitin-proteasome pathway. *Science*, *273*(5282), 1725-1728.

Ho, S. N. (2006). Intracellular water homeostasis and the mammalian cellular osmotic stress response. *Journal of cellular physiology*, *206*(1), 9-15.

Hohmann, S. (2002). Osmotic stress signaling and osmoadaptation in yeasts. *Microbiology and molecular biology reviews*, *66*(2), 300-372.

Hohmann, S. (2009). Control of high osmolarity signalling in the yeast Saccharomyces cerevisiae. *FEBS Letters*, *583*(24), 4025-4029.

Hohmann, S. (2015a). An integrated view on a eukaryotic osmoregulation system. *Current genetics*, *61*(3), 373-382.

Hohmann, S. (2015b). An integrated view on a eukaryotic osmoregulation system. *Current genetics*, *61*, 373-382.

Hohmann, S., Krantz, M., & Nordlander, B. (2007). Yeast osmoregulation. *Methods in enzymology*, *428*, 29-45.

Hohmann, S., & Mager, W. H. (2007). *Yeast stress responses* (Vol. 1). Springer Science & Business Media.

Hou, Y., Dan, X., Babbar, M., Wei, Y., Hasselbalch, S. G., Croteau, D. L., & Bohr, V. A. (2019). Ageing as a risk factor for neurodegenerative disease. *Nature Reviews Neurology*, *15*(10), 565-581.

Housmans, J. A., Wu, G., Schymkowitz, J., & Rousseau, F. (2023). A guide to studying protein aggregation. *The FEBS Journal*, *290*(3), 554-583.

Hsu, H.-E., Liu, T.-N., Yeh, C.-S., Chang, T.-H., Lo, Y.-C., & Kao, C.-F. (2015). Feedback control of Snf1 protein and its phosphorylation is necessary for adaptation to environmental stress. *Journal of biological chemistry*, *290*(27), 16786-16796.

Hu, Z., Jiang, J., & Rajagopalan, R. (2007). Effects of Macromolecular Crowding on Biochemical Reaction Equilibria: A Molecular Thermodynamic Perspective. *Biophysical Journal*, *93*(5), 1464-1473.

Huff, J. (2015). The Airyscan detector from ZEISS: confocal imaging with improved signal-to-noise ratio and super-resolution. *Nature Methods*, *12*(12), i-ii.

Hunter, J. D. (2007). Matplotlib: A 2D graphics environment. *Computing in science & engineering*, *9*(03), 90-95.

Ichikawa, K., Shiba, Y., Jigami, Y., & Serizawa, N. (1993). Secretion and overproduction of carboxypeptidase Y by a Saccharomyces cerevisiae ssl1 mutant strain. *Bioscience, biotechnology, and biochemistry*, *57*(10), 1686-1690.

Isnard, A.-D., Thomas, D., & Surdin-Kerjan, Y. (1996). The study of methionine uptake inSaccharomyces cerevisiaeReveals a new family of amino acid permeases. *Journal of molecular biology*, *262*(4), 473-484.

Jackson, S. P., & Bartek, J. (2009). The DNA-damage response in human biology and disease. *Nature*, *461*(7267), 1071-1078.

Jacobs, K. C., & Lew, D. J. (2022). Pheromone guidance of polarity site movement in yeast. *Biomolecules*, *12*(4), 502.

Jacobson, K., Derzko, Z., Wu, E. S., Hou, Y., & Poste, G. (1976). Measurement of the lateral mobility of cell surface components in single living cells by fluorescence recovery after photobleaching. *Journal of supramolecular structure*, *5*(4), 565-576.

Janapala, Y., Preiss, T., & Shirokikh, N. E. (2019). Control of translation at the initiation phase during glucose starvation in yeast. *International Journal of Molecular Sciences*, *20*(16), 4043.

Janmey, P., & Kinnunen, P. K. (2006). Biophysical properties of lipids and dynamic membranes. *Trends in cell biology*, *16*(10), 538-546.

Jennison, M. H., & Morgan, A. (1950). Fluorescence microscopy. *Tubercle*, *31*(4), 84-87.

Jeon, J.-H., Tejedor, V., Burov, S., Barkai, E., Selhuber-Unkel, C., Berg-Sørensen, K., Oddershede, L., & Metzler, R. (2011). In vivo anomalous diffusion and weak ergodicity breaking of lipid granules. *Physical review letters*, *106*(4), 048103.

Jin, X., Lee, J.-E., Schaefer, C., Luo, X., Wollman, A. J., Payne-Dwyer, A. L., Tian, T., Zhang, X., Chen, X., & Li, Y. (2021). Membraneless organelles formed by liquid-liquid phase separation increase bacterial fitness. *Science Advances*, *7*(43), eabh2929.

Jing, W., Qin, Y., & Tong, J. (2020). Effects of macromolecular crowding on the folding and aggregation of glycosylated MUC5AC. *Biochemical and Biophysical Research Communications*, *529*(4), 984-990.

Johnston, G., Pringle, J., & Hartwell, L. H. (1977). Coordination of growth with cell division in the yeast Saccharomyces cerevisiae. *Experimental cell research*, *105*(1), 79-98.

Johnston, J. A., Ward, C. L., & Kopito, R. R. (1998). Aggresomes: a cellular response to misfolded proteins. *The Journal of cell biology*, *143*(7), 1883-1898.

Jones, E., Webb, G., & Hiller, M. (1997). Molecular biology of the yeast Saccharomyces cerevisiae vol. III. In: Cold Spring Harbor Laboratory Press, Cold Spring Harbor, NY.

Jones, M. C., Marron, J. S., & Sheather, S. J. (1996). A brief survey of bandwidth selection for density estimation. *Journal of the American statistical association*, *91*(433), 401-407.

Joyner, R. P., Tang, J. H., Helenius, J., Dultz, E., Brune, C., Holt, L. J., Huet, S., Müller, D. J., & Weis, K. (2016). A glucose-starvation response regulates the diffusion of macromolecules. *eLife*, *5*, e09376.

Juanes, M. A., & Piatti, S. (2016). The final cut: cell polarity meets cytokinesis at the bud neck in S. cerevisiae. *Cellular and Molecular Life Sciences*, *73*(16), 3115-3136.

Jung, G., Ueno, H., & Hayashi, R. (1999). Carboxypeptidase Y: structural basis for protein sorting and catalytic triad. *The Journal of Biochemistry*, *126*(1), 1-6.

Jung, G., Wiehler, J., & Zumbusch, A. (2005). The photophysics of green fluorescent protein: influence of the key amino acids at positions 65, 203, and 222. *Biophysical Journal*, *88*(3), 1932-1947.

Kaganovich, D., Kopito, R., & Frydman, J. (2008). Misfolded proteins partition between two distinct quality control compartments. *Nature*, *454*(7208), 1088-1095.

Kalpic, D., Hlupic, N., & Lovric, M. (2011). Student's t-Tests. In (pp. 1559–1563). International Encyclopedia of Statistical Science: Springer

Kapuscinski, J. (1995). DAPI: a DNA-specific fluorescent probe. *Biotechnic & histochemistry*, *70*(5), 220-233.

Kessi-Pérez, E. I., González, A., Palacios, J. L., & Martínez, C. (2022). Yeast as a biological platform for vitamin D production: A promising alternative to help reduce vitamin D deficiency in humans. *Yeast*, *39*(9), 482-492.

Khmelinskii, A., Keller, P. J., Bartosik, A., Meurer, M., Barry, J. D., Mardin, B. R., Kaufmann, A., Trautmann, S., Wachsmuth, M., & Pereira, G. (2012). Tandem fluorescent protein timers for in vivo analysis of protein dynamics. *Nature biotechnology*, *30*(7), 708-714.

Kiehl, T. R., Shen, D., Khattak, S. F., Jian Li, Z., & Sharfstein, S. T. (2011). Observations of cell size dynamics under osmotic stress. *Cytometry Part A*, *79*(7), 560-569.

Kirschner, M. W., Honig, L. S., & Williams, R. C. (1975). Quantitative electron microscopy of microtubule assembly in vitro. *Journal of molecular biology*, *99*(2), 263-276.

Kjeldsen, T. (2000). Yeast secretory expression of insulin precursors. *Applied microbiology and biotechnology*, *54*, 277-286.

Kneen, M., Farinas, J., Li, Y., & Verkman, A. (1998). Green fluorescent protein as a noninvasive intracellular pH indicator. *Biophysical Journal*, *74*(3), 1591-1599.

Knoblach, B., & Rachubinski, R. A. (2015). Sharing the cell's bounty–organelle inheritance in yeast. *Journal of cell science*, *128*(4), 621-630.

Knop, M., Finger, A., Braun, T., Hellmuth, K., & Wolf, D. (1996). Der1, a novel protein specifically required for endoplasmic reticulum degradation in yeast. *The EMBO Journal*, *15*(4), 753-763.

König, I., Soranno, A., Nettels, D., & Schuler, B. (2021). Impact of in-cell and in-vitro crowding on the conformations and dynamics of an intrinsically disordered protein. *Angewandte Chemie*, *133*(19), 10819-10824.

Kopito, R. R. (2000). Aggresomes, inclusion bodies and protein aggregation. *Trends in cell biology*, *10*(12), 524-530.

Kourtis, N., & Tavernarakis, N. (2011). Cellular stress response pathways and ageing: intricate molecular relationships. *The EMBO Journal*, *30*(13), 2520-2531.

Kurat, C. F., Natter, K., Petschnigg, J., Wolinski, H., Scheuringer, K., Scholz, H., Zimmermann, R., Leber, R., Zechner, R., & Kohlwein, S. D. (2006). Obese yeast: triglyceride lipolysis is functionally conserved from mammals to yeast. *Journal of biological chemistry*, *281*(1), 491-500.

Kuznetsova, I. M., Turoverov, K. K., & Uversky, V. N. (2014). What macromolecular crowding can do to a protein. *International Journal of Molecular Sciences*, *15*(12), 23090-23140.

Laidlaw, Bisinski, D. D., Shashkova, S., Paine, K. M., Veillon, M. A., Leake, M. C., & MacDonald, C. (2021). A glucose-starvation response governs endocytic trafficking and eisosomal retention of surface cargoes in budding yeast. *Journal of cell science*, *134*(2), jcs257733.

Lakowicz, J. R. (2006). *Principles of fluorescence spectroscopy* (Vol. 3rd ed). Springer.

Lanen, J. V., Broquist, H., Johnson, M. J., Baldwin, I., & Peterson, W. (1942). Synthesis of Vitamin B1 by Yeast. *Industrial & Engineering Chemistry*, *34*(10), 1244-1247.

Lang, F., Lepple-Wienhues, A., Paulmichl, M., Szabo, I., Siemen, D., & Gulbins, E. (1998). Ion channels, cell volume, and apoptotic cell death. *Cellular Physiology and Biochemistry*, *8*(6), 285-292.

Leake, M. (2014). Analytical tools for single-molecule fluorescence imaging in cellulo. *Physical Chemistry Chemical Physics*, *16*(25), 12635-12647.

Leake, M. C. (2013). The physics of life: one molecule at a time. In (Vol. 368, pp. 20120248): The Royal Society.

Leake, M. C., Chandler, J. H., Wadhams, G. H., Bai, F., Berry, R. M., & Armitage, J. P. (2006). Stoichiometry and turnover in single, functioning membrane protein complexes. *Nature*, *443*(7109), 355-358.

Lecinski, S., Shepherd, J. W., Frame, L., Hayton, I., MacDonald, C., & Leake, M. C. (2021). Investigating molecular crowding during cell division and hyperosmotic stress in budding yeast with FRET. In *Current topics in membranes* (Vol. 88, pp. 75-118). Elsevier.

Lesage, G., & Bussey, H. (2006). Cell wall assembly in Saccharomyces cerevisiae. *Microbiology and molecular biology reviews*, *70*(2), 317-343.

Li, F., Long, T., Lu, Y., Ouyang, Q., & Tang, C. (2004). The yeast cell-cycle network is robustly designed. *Proceedings of the National Academy of Sciences*, *101*(14), 4781-4786.

Li, K. W., Lu, M. S., Iwamoto, Y., Drubin, D. G., & Pedersen, R. T. (2021). A preferred sequence for organelle inheritance during polarized cell growth. *Journal of cell science*, *134*(21), jcs258856.

Li, S. C., & Kane, P. M. (2009). The yeast lysosome-like vacuole: endpoint and crossroads. *Biochimica et Biophysica Acta (BBA)-Molecular Cell Research*, *1793*(4), 650-663.

Li, Y., Varala, K., & Coruzzi, G. M. (2015). From milliseconds to lifetimes: tracking the dynamic behavior of transcription factors in gene networks. *Trends in Genetics*, *31*(9), 509-515.

Lichius, A., & Zeilinger, S. (2019). Application of membrane and cell wall selective fluorescent dyes for live-cell imaging of filamentous fungi. *JoVE (Journal of Visualized Experiments)*(153), e60613.

Lindahl, E., & Sansom, M. S. (2008). Membrane proteins: molecular dynamics simulations. *Current opinion in structural biology*, *18*(4), 425-431.

Lindner, A. B., Madden, R., Demarez, A., Stewart, E. J., & Taddei, F. (2008). Asymmetric segregation of protein aggregates is associated with cellular aging and rejuvenation. *Proceedings of the National Academy of Sciences*, *105*(8), 3076-3081.

Liochev, S. I. (2013). Reactive oxygen species and the free radical theory of aging. *Free Radical Biology and Medicine*, *60*, 1-4.

Lippincott-Schwartz, J., Snapp, E. L., & Phair, R. D. (2018). The development and enhancement of FRAP as a key tool for investigating protein dynamics. *Biophysical Journal*, *115*(7), 1146-1155.

Liu, B., Åberg, C., van Eerden, F. J., Marrink, S. J., Poolman, B., & Boersma, A. J. (2017). Design and properties of genetically encoded probes for sensing macromolecular crowding. *Biophysical Journal*, *112*(9), 1929-1939.

Liu, B., Larsson, L., Caballero, A., Hao, X., Öling, D., Grantham, J., & Nyström, T. (2010). The polarisome is required for segregation and retrograde transport of protein aggregates. *Cell*, *140*(2), 257-267.

Liu, B., Mavrova, S. N., van den Berg, J., Kristensen, S. K., Mantovanelli, L., Veenhoff, L. M., Poolman, B., & Boersma, A. J. (2018). Influence of fluorescent protein maturation on FRET measurements in living cells. *ACS sensors*, *3*(9), 1735-1742.

Liu, S., Weaver, D. L., & Taatjes, D. J. (1997). Three-dimensional reconstruction by confocal laser scanning microscopy in routine pathologic specimens of benign and malignant lesions of the human breast. *Histochemistry and cell biology*, *107*(4), 267-278.

Liu, Y., & Chang, A. (2008). Heat shock response relieves ER stress. *The EMBO Journal*, *27*(7), 1049-1059.

Liu, Y., & Xu, J. (2019). High-resolution microscopy for imaging cancer pathobiology. *Current pathobiology reports*, *7*(3), 85-96.

Llopis, J., McCaffery, J. M., Miyawaki, A., Farquhar, M. G., & Tsien, R. Y. (1998). Measurement of cytosolic, mitochondrial, and Golgi pH in single living cells with green fluorescent proteins. *Proceedings of the National Academy of Sciences*, *95*(12), 6803-6808.

Llorente-Garcia, I., Lenn, T., Erhardt, H., Harriman, O. L., Liu, L.-N., Robson, A., Chiu, S.-W., Matthews, S., Willis, N. J., & Bray, C. D. (2014). Single-molecule in vivo imaging of bacterial respiratory complexes indicates delocalized oxidative phosphorylation. *Biochimica et Biophysica Acta (BBA)-Bioenergetics*, *1837*(6), 811-824.

López-Otín, C., Blasco, M. A., Partridge, L., Serrano, M., & Kroemer, G. (2013). The hallmarks of aging. *Cell*, *153*(6), 1194-1217.

Löwe, M., Kalacheva, M., Boersma, A. J., & Kedrov, A. (2020). The more the merrier: effects of macromolecular crowding on the structure and dynamics of biological membranes. *The FEBS Journal*, *287*(23), 5039-5067.

Lu, A. X., Zarin, T., Hsu, I. S., & Moses, A. M. (2019). YeastSpotter: accurate and parameter-free web segmentation for microscopy images of yeast cells. *Bioinformatics*, *35*(21), 4525-4527.

Luby-Phelps, K. (2013). The physical chemistry of cytoplasm and its influence on cell function: an update. *Molecular biology of the cell*, *24*(17), 2593-2596.

Lumpkin, C. K., McGill, J. R., Riabowol, K. T., Moerman, E., Reis, R. J. S., & Goldstein, S. (1985). Extrachromosomal circular DNA and aging cells. In *Werner's Syndrome and Human Aging* (pp. 479-493). Springer.

Macara, I. G., & Mili, S. (2008). Polarity and differential inheritance—universal attributes of life? *Cell*, *135*(5), 801-812.

MacDonald, C., Stringer, D. K., & Piper, R. C. (2012). Sna 3 Is an Rsp 5 adaptor protein that relies on ubiquitination for its MVB sorting. *Traffic*, *13*(4), 586-598.

Mach, H., Middaugh, C. R., & Lewis, R. V. (1992). Statistical determination of the average values of the extinction coefficients of tryptophan and tyrosine in native proteins. *Analytical biochemistry*, *200*(1), 74-80.

Macreadie, I. G., Horaitis, O., Vaughan, P. R., & Des Clark-Walker, G. (1991). Constitutive expression of the Saccharomyces cerevisiae CUP1 gene in Kluyveromyces lactis. *Yeast*, *7*(2), 127-135.

Madhavan, A., Arun, K., Sindhu, R., Krishnamoorthy, J., Reshmy, R., Sirohi, R., Pugazhendi, A., Awasthi, M. K., Szakacs, G., & Binod, P. (2021). Customized yeast cell factories for biopharmaceuticals: From cell engineering to process scale up. *Microbial cell factories*, *20*(1), 124.

Mager, W. H., & Siderius, M. (2002). Novel insights into the osmotic stress response of yeast. *FEMS yeast research*, *2*(3), 251-257.

Mager, W. H., & Winderickx, J. (2005). Yeast as a model for medical and medicinal research. *Trends in pharmacological sciences*, *26*(5), 265-273.

Mahon, M. J. (2011). pHluorin2: an enhanced, ratiometric, pH-sensitive green florescent protein. *Advances in bioscience and biotechnology (Print)*, *2*(3), 132.

Malley, M. (1994). Thermodynamics and cold light. *Annals of science*, *51*(3), 203-224.

Marini, G., Nüske, E., Leng, W., Alberti, S., & Pigino, G. (2020). Reorganization of budding yeast cytoplasm upon energy depletion. *Molecular biology of the cell*, *31*(12), 1232-1245.

Markwardt, M. L., Kremers, G.-J., Kraft, C. A., Ray, K., Cranfill, P. J., Wilson, K. A., Day, R. N., Wachter, R. M., Davidson, M. W., & Rizzo, M. A. (2011). An improved cerulean fluorescent protein with enhanced brightness and reduced reversible photoswitching. *PloS one*, *6*(3), e17896.

Masters, B. R. (2008). Book Review: Principles of Fluorescence Spectroscopy. In: SPIE.

Mata-Gómez, L. C., Montañez, J. C., Méndez-Zavala, A., & Aguilar, C. N. (2014). Biotechnological production of carotenoids by yeasts: an overview. *Microbial cell factories*, *13*(1), 1-11.

McClellan, A. J., Tam, S., Kaganovich, D., & Frydman, J. (2005). Protein quality control: chaperones culling corrupt conformations. *Nature cell biology*, *7*(8), 736-741.

Mcdonald, J. B., Dhakal, S., & Macreadie, I. G. (2020). Yeast contributions to Alzheimer's Disease. *Journal of Human and Clinical Genetics*, *2*(2).

McManus, M. L., Churchwell, K. B., & Strange, K. (1995). Regulation of cell volume in health and disease. *New England Journal of Medicine*, *333*(19), 1260-1267.

McMurray, M. A., Bertin, A., Garcia III, G., Lam, L., Nogales, E., & Thorner, J. (2011). Septin filament formation is essential in budding yeast. *Developmental cell*, *20*(4), 540-549.

Mechler, B., Hirsch, H., Müller, H., & Wolf, D. (1988). Biogenesis of the yeast lysosome (vacuole): biosynthesis and maturation of proteinase yscB. *The EMBO Journal*, *7*(6), 1705-1710.

Mentré, P. (2012). Water in the orchestration of the cell machinery. Some misunderstandings: a short review. *Journal of biological physics*, *38*(1), 13-26.

Merksamer, P. I., Trusina, A., & Papa, F. R. (2008). Real-time redox measurements during endoplasmic reticulum stress reveal interlinked protein folding functions. *Cell*, *135*(5), 933-947.

Merlini, L., Dudin, O., & Martin, S. G. (2013). Mate and fuse: how yeast cells do it. *Open biology*, *3*(3), 130008.

Michel, J., Nolin, F., Wortham, L., Lalun, N., Tchelidze, P., Banchet, V., Terryn, C., & Ploton, D. (2019). Various Nucleolar Stress Inducers Result in Highly Distinct Changes in Water, Dry Mass and Elemental Content in Cancerous Cell Compartments: Investigation Using a Nano-Analytical Approach. *Nanotheranostics*, *3*(2), 179.

Miesenböck, G., De Angelis, D. A., & Rothman, J. E. (1998). Visualizing secretion and synaptic transmission with pH-sensitive green fluorescent proteins. *Nature*, *394*(6689), 192-195.

Miklos, A. C., Li, C., Sharaf, N. G., & Pielak, G. J. (2010). Volume exclusion and soft interaction effects on protein stability under crowded conditions. *Biochemistry*, *49*(33), 6984-6991.

Milczarek, J., Pawlowska, R., Zurawinski, R., Lukasik, B., Garner, L. E., & Chworos, A. (2017). Fluorescence and confocal imaging of mammalian cells using conjugated oligoelectrolytes with phenylenevinylene core. *Journal of Photochemistry and Photobiology B: Biology*, *170*, 40-48.

Miller-Fleming, L., Giorgini, F., & Outeiro, T. F. (2008). Yeast as a model for studying human neurodegenerative disorders. *Biotechnology Journal: Healthcare Nutrition Technology*, *3*(3), 325-338.

Miller, H., Zhou, Z., Wollman, A. J., & Leake, M. C. (2015). Superresolution imaging of single DNA molecules using stochastic photoblinking of minor groove and intercalating dyes. *Methods*, *88*, 81-88.

Minich, W. B., & Ovchinnikov, L. P. (1992). Role of cytoplasmic mRNP proteins in translation. *Biochimie*, *74*(5), 477-483.

Minsky, M. (1961). Microscopy apparatus US patent 3013467. *USP Office, Ed. US*, *658*.

Minton, A. P. (2001). The influence of macromolecular crowding and macromolecular confinement on biochemical reactions in physiological media. *Journal of biological chemistry*, *276*(14), 10577-10580.

Minton, A. P. (2006). How can biochemical reactions within cells differ from those in test tubes? *Journal of cell science*, *119*(14), 2863-2869.

Miura, T., & Yanagita, T. (1972). Cellular Senescence in Yeast Caused by Carbon-Source Starvation I. Changes in Activities of Respiratory System and Lipid Peroxidation Activity. *The Journal of Biochemistry*, *72*(1), 141-148.

Miyagi, T., Yamanaka, Y., Harada, Y., Narumi, S., Hayamizu, Y., Kuroda, M., & Kanekura, K. (2021). An improved macromolecular crowding sensor CRONOS for detection of crowding changes in membrane-less organelles under stressed conditions. *Biochemical and Biophysical Research Communications*, *583*, 29-34.

Mohammadi, S., Saberidokht, B., Subramaniam, S., & Grama, A. (2015). Scope and limitations of yeast as a model organism for studying human tissue-specific pathways. *BMC systems biology*, *9*(1), 1-22.

Morishita, H. (2022). Role of autophagy in the eye: From physiology to disease. *Current Opinion in Physiology*, 100592.

Morris, G., Winters, L., Coulson, G., & Clarke, K. (1986). Effect of osmotic stress on the ultrastructure and viability of the yeast Saccharomyces cerevisiae. *Microbiology*, *132*(7), 2023-2034.

Mortimer, R. K., & Johnston, J. R. (1959). Life span of individual yeast cells. *Nature*, *183*(4677), 1751-1752.

Moseley, J. B., & Goode, B. L. (2006). The yeast actin cytoskeleton: from cellular function to biochemical mechanism. *Microbiology and molecular biology reviews*, *70*(3), 605-645.

Mourão, M. A., Hakim, J. B., & Schnell, S. (2014). Connecting the dots: the effects of macromolecular crowding on cell physiology. *Biophysical Journal*, *107*(12), 2761-2766.

Mouton, S. N., Thaller, D. J., Crane, M. M., Rempel, I. L., Terpstra, O. T., Steen, A., Kaeberlein, M., Lusk, C. P., Boersma, A. J., & Veenhoff, L. M. (2020). A physicochemical perspective of aging from single-cell analysis of pH, macromolecular and organellar crowding in yeast. *eLife*, *9*, e54707.

Munder, M. C., Midtvedt, D., Franzmann, T., Nuske, E., Otto, O., Herbig, M., Ulbricht, E., Müller, P., Taubenberger, A., & Maharana, S. (2016). A pH-driven transition of the cytoplasm from a fluid-to a solid-like state promotes entry into dormancy. *eLife*, *5*, e09347.

Musgrove, E., Seaman, M., & Hedley, D. (1987). Relationship between cytoplasmic pH and proliferation during exponential growth and cellular quiescence. *Experimental cell research*, *172*(1), 65-75.

Nasmyth, K. (1996). At the heart of the budding yeast cell cycle. *Trends in Genetics*, *12*(10), 405-412.

Nestor-Bergmann, A., Stooke-Vaughan, G. A., Goddard, G. K., Starborg, T., Jensen, O. E., & Woolner, S. (2019). Decoupling the roles of cell shape and mechanical stress in orienting and cueing epithelial mitosis. *Cell reports*, *26*(8), 2088-2100. e2084.

Nettesheim, G., Nabti, I., Murade, C. U., Jaffe, G. R., King, S. J., & Shubeita, G. T. (2020). Macromolecular crowding acts as a physical regulator of intracellular transport. *Nature Physics*, *16*(11), 1144-1151.

Nguemaha, V., Qin, S., & Zhou, H.-X. (2019). Transfer free energies of test proteins Into crowded protein solutions have simple dependence on crowder concentration. *Frontiers in molecular biosciences*, *6*, 39.

Niccoli, T., & Partridge, L. (2012). Ageing as a risk factor for disease. *Current biology*, *22*(17), R741-R752.

Nielsen, J. (2013). Production of biopharmaceutical proteins by yeast: advances through metabolic engineering. *Bioengineered*, *4*(4), 207-211.

Northcote, D., & Horne, R. (1952). The chemical composition and structure of the yeast cell wall. *Biochemical Journal*, *51*(2), 232.

Nüske, E., Marini, G., Richter, D., Leng, W., Bogdanova, A., Franzmann, T. M., Pigino, G., & Alberti, S. (2020). Filament formation by the translation factor eIF2B regulates protein synthesis in starved cells. *Biology open*, *9*(7), bio046391.

Nussinov, R., Tsai, C.-J., & Jang, H. (2021). Signaling in the crowded cell. *Current opinion in structural biology*, *71*, 43-50.

Nyström, T., & Liu, B. (2014). The mystery of aging and rejuvenation—a budding topic. *Current opinion in microbiology*, *18*, 61-67.

O'Brien, E. P., Brooks, B. R., & Thirumalai, D. (2012). Effects of pH on proteins: predictions for ensemble and single-molecule pulling experiments. *Journal of the American Chemical Society*, *134*(2), 979-987.

Ohtsuka, H., Imada, K., Shimasaki, T., & Aiba, H. (2022). Sporulation: A response to starvation in the fission yeast Schizosaccharomyces pombe. *MicrobiologyOpen*, *11*(3), e1303.

Okada, S., Leda, M., Hanna, J., Savage, N. S., Bi, E., & Goryachev, A. B. (2013). Daughter cell identity emerges from the interplay of Cdc42, septins, and exocytosis. *Developmental cell*, *26*(2), 148-161.

Öling, D., Eisele, F., Kvint, K., & Nyström, T. (2014). Opposing roles of U bp3-dependent deubiquitination regulate replicative life span and heat resistance. *The EMBO Journal*, *33*(7), 747-761.

Oliphant, T. E. (2006). *A guide to NumPy* (Vol. 1). Trelgol Publishing USA.

Olzscha, H., Schermann, S. M., Woerner, A. C., Pinkert, S., Hecht, M. H., Tartaglia, G. G., Vendruscolo, M., Hayer-Hartl, M., Hartl, F. U., & Vabulas, R. M. (2011). Amyloid-like aggregates sequester numerous metastable proteins with essential cellular functions. *Cell*, *144*(1), 67-78.

Opazo, F., Punge, A., Bückers, J., Hoopmann, P., Kastrup, L., Hell, S. W., & Rizzoli, S. O. (2010). Limited intermixing of synaptic vesicle components upon vesicle recycling. *Traffic*, *11*(6), 800-812.

Orij, R., Urbanus, M. L., Vizeacoumar, F. J., Giaever, G., Boone, C., Nislow, C., Brul, S., & Smits, G. J. (2012). Genome-wide analysis of intracellular pH reveals quantitative control of cell division rate by pHc in Saccharomyces cerevisiae. *Genome biology*, *13*(9), 1-15.

Ormö, M., Cubitt, A. B., Kallio, K., Gross, L. A., Tsien, R. Y., & Remington, S. J. (1996). Crystal structure of the Aequorea victoria green fluorescent protein. *Science*, *273*(5280), 1392-1395.

Otten, J., Tenhaef, N., Jansen, R. P., Döbber, J., Jungbluth, L., Noack, S., Oldiges, M., Wiechert, W., & Pohl, M. (2019). A FRET-based biosensor for the quantification of glucose in culture supernatants of mL scale microbial cultivations. *Microbial cell factories*, *18*(1), 1-10.

Özcan, S., & Johnston, M. (1999). Function and regulation of yeast hexose transporters. *Microbiology and molecular biology reviews*, *63*(3), 554-569.

Pace, C. N., Vajdos, F., Fee, L., Grimsley, G., & Gray, T. (1995). How to measure and predict the molar absorption coefficient of a protein. *Protein science*, *4*(11), 2411-2423.

Paine, K. M., Ecclestone, G. B., & MacDonald, C. (2021). Fur4-mediated uracil-scavenging to screen for surface protein regulators. *Traffic*, *22*(11), 397-408.

Parapouli, M., Vasileiadis, A., Afendra, A.-S., & Hatziloukas, E. (2020). Saccharomyces cerevisiae and its industrial applications. *AIMS microbiology*, *6*(1), 1.

Park, S.-H., Bolender, N., Eisele, F., Kostova, Z., Takeuchi, J., Coffino, P., & Wolf, D. H. (2007). The cytoplasmic Hsp70 chaperone machinery subjects misfolded and endoplasmic reticulum import-incompetent proteins to degradation via the ubiquitin–proteasome system. *Molecular biology of the cell*, *18*(1), 153-165.

Park, S.-H., Kukushkin, Y., Gupta, R., Chen, T., Konagai, A., Hipp, M. S., Hayer-Hartl, M., & Hartl, F. U. (2013). PolyQ proteins interfere with nuclear degradation of cytosolic proteins by sequestering the Sis1p chaperone. *Cell*, *154*(1), 134-145.

Park, S., Barnes, R., Lin, Y., Jeon, B.-j., Najafi, S., Delaney, K. T., Fredrickson, G. H., Shea, J.-E., Hwang, D. S., & Han, S. (2020). Dehydration entropy drives liquid-liquid phase separation by molecular crowding. *Communications Chemistry*, *3*(1), 1-12.

Parry, B. R., Surovtsev, I. V., Cabeen, M. T., O'Hern, C. S., Dufresne, E. R., & Jacobs-Wagner, C. (2014). The bacterial cytoplasm has glass-like properties and is fluidized by metabolic activity. *Cell*, *156*(1-2), 183-194.

Patterson, G. H., Knobel, S. M., Sharif, W. D., Kain, S. R., & Piston, D. W. (1997). Use of the green fluorescent protein and its mutants in quantitative fluorescence microscopy. *Biophysical Journal*, *73*(5), 2782-2790.

Paxman, J., Zhou, Z., O'Laughlin, R., Liu, Y., Li, Y., Tian, W., Su, H., Jiang, Y., Holness, S. E., & Stasiowski, E. (2022). Age-dependent aggregation of ribosomal RNA-binding proteins links deterioration in chromatin stability with challenges to proteostasis. *eLife*, *11*, e75978.

Pédelacq, J.-D., Cabantous, S., Tran, T., Terwilliger, T. C., & Waldo, G. S. (2006). Engineering and characterization of a superfolder green fluorescent protein. *Nature biotechnology*, *24*(1), 79-88.

Perocchi, F., Mancera, E., & Steinmetz, L. M. (2008). Systematic screens for human disease genes, from yeast to human and back. *Molecular bioSystems*, *4*(1), 18-29.

Perrone, G. G., Tan, S.-X., & Dawes, I. W. (2008). Reactive oxygen species and yeast apoptosis. *Biochimica et Biophysica Acta (BBA)-Molecular Cell Research*, *1783*(7), 1354-1368.

Petelenz-Kurdziel, E., Kuehn, C., Nordlander, B., Klein, D., Hong, K.-K., Jacobson, T., Dahl, P., Schaber, J., Nielsen, J., & Hohmann, S. (2013). Quantitative analysis of glycerol accumulation, glycolysis and growth under hyper osmotic stress. *PLoS computational biology*, *9*(6), e1003084.

Petranovic, D., Tyo, K., Vemuri, G. N., & Nielsen, J. (2010). Prospects of yeast systems biology for human health: integrating lipid, protein and energy metabolism. *FEMS yeast research*, *10*(8), 1046-1059.

Petrovska, I., Nüske, E., Munder, M. C., Kulasegaran, G., Malinovska, L., Kroschwald, S., Richter, D., Fahmy, K., Gibson, K., & Verbavatz, J.-M. (2014). Filament formation by metabolic enzymes is a specific adaptation to an advanced state of cellular starvation. *eLife*, *3*, e02409.

Pettersen, E. F., Goddard, T. D., Huang, C. C., Couch, G. S., Greenblatt, D. M., Meng, E. C., & Ferrin, T. E. (2004). UCSF Chimera—a visualization system for exploratory research and analysis. *Journal of computational chemistry*, *25*(13), 1605-1612.

Phillip, Y., & Schreiber, G. (2013). Formation of protein complexes in crowded environments–from in vitro to in vivo. *FEBS Letters*, *587*(8), 1046-1052.

Piekarska, I., Rytka, J., & Rempola, B. (2010). Regulation of sporulation in the yeast Saccharomyces cerevisiae. *Acta Biochimica Polonica*, *57*(3), 241-250.

Piper, P. W. (2006). Long-lived yeast as a model for ageing research. *Yeast*, *23*(3), 215-226.

Pittman, J. K. (2012). Multiple transport pathways for mediating intracellular pH homeostasis: the contribution of H+/ion exchangers. *Frontiers in plant science*, *3*, 11.

Plank, M., Wadhams, G. H., & Leake, M. C. (2009). Millisecond timescale slimfield imaging and automated quantification of single fluorescent protein molecules for use in probing complex biological processes. *Integrative Biology*, *1*(10), 602-612.

Pluskal, T., Hayashi, T., Saitoh, S., Fujisawa, A., & Yanagida, M. (2011). Specific biomarkers for stochastic division patterns and starvation-induced quiescence under limited glucose levels in fission yeast. *The FEBS Journal*, *278*(8), 1299-1315.

Poland, D. (1992). The effect of excluded volume on aggregation kinetics. *The Journal of chemical physics*, *97*(1), 470-481.

Prince, M. J., Wimo, A., Guerchet, M. M., Ali, G. C., Wu, Y.-T., & Prina, M. (2015). World Alzheimer Report 2015-The Global Impact of Dementia: An analysis of prevalence, incidence, cost and trends.

Proft, M., & Serrano, R. n. (1999). Repressors and upstream repressing sequences of the stress-regulated ENA1 gene in Saccharomyces cerevisiae: bZIP protein Sko1p confers HOG-dependent osmotic regulation. *Molecular and cellular biology*, *19*(1), 537-546.

Prosser, D. C., Whitworth, K., & Wendland, B. (2010). Quantitative analysis of endocytosis with cytoplasmic pHluorin chimeras. *Traffic*, *11*(9), 1141-1150.

Prosser, D. C., Wrasman, K., Woodard, T. K., O'Donnell, A. F., & Wendland, B. (2016). Applications of pHluorin for quantitative, kinetic and high-throughput analysis of endocytosis in budding yeast. *JoVE (Journal of Visualized Experiments)*(116), e54587.

Rabouille, C., & Alberti, S. (2017). Cell adaptation upon stress: the emerging role of membrane-less compartments. *Current opinion in cell biology*, *47*, 34-42.

Rana, P. S., Kurokawa, M., & Model, M. A. (2020). Evidence for macromolecular crowding as a direct apoptotic stimulus. *Journal of cell science*, *133*(9), jcs243931.

Rayleigh, L. (1879). XXXI. Investigations in optics, with special reference to the spectroscope. *The London, Edinburgh, and Dublin Philosophical Magazine and Journal of Science*, *8*(49), 261-274.

Record Jr, M. T., Courtenay, E. S., Cayley, D. S., & Guttman, H. J. (1998). Responses of E. coli to osmotic stress: large changes in amounts of cytoplasmic solutes and water. *Trends in biochemical sciences*, *23*(4), 143-148.

Reith, P., Braam, S., Welkenhuysen, N., Lecinski, S., Shepherd, J., MacDonald, C., Leake, M. C., Hohmann, S., Shashkova, S., & Cvijovic, M. (2022). The effect of lithium on the budding yeast Saccharomyces cerevisiae upon stress adaptation. *Microorganisms*, *10*(3), 590.

Reyes-Lamothe, R., Sherratt, D. J., & Leake, M. C. (2010). Stoichiometry and architecture of active DNA replication machinery in Escherichia coli. *Science*, *328*(5977), 498-501.

Riback, J. A., Katanski, C. D., Kear-Scott, J. L., Pilipenko, E. V., Rojek, A. E., Sosnick, T. R., & Drummond, D. A. (2017). Stress-triggered phase separation is an adaptive, evolutionarily tuned response. *Cell*, *168*(6), 1028-1040. e1019.

Rivas, G., Ferrone, F., & Herzfeld, J. (2004). Life in a crowded world: Workshop on the Biological Implications of Macromolecular Crowding. In: John Wiley & Sons, Ltd Chichester, UK.

Rivas, G., & Minton, A. P. (2016). Macromolecular crowding in vitro, in vivo, and in between. *Trends in biochemical sciences*, *41*(11), 970-981.

Robinson, J. S., Klionsky, D. J., Banta, L. M., & Emr, S. D. (1988). Protein sorting in Saccharomyces cerevisiae: isolation of mutants defective in the delivery and processing of multiple vacuolar hydrolases. *Molecular and cellular biology*, *8*(11), 4936-4948.

Robles, L. M., Millán-Pacheco, C., Pastor, N., & Del Río, G. (2017). Structure-function studies of the alpha pheromone receptor from yeast. *Tip*, *20*(1), 16-26.

Rohwer, J. M., Postma, P. W., Kholodenko, B. N., & Westerhoff, H. V. (1998). Implications of macromolecular crowding for signal transduction and metabolite channeling. *Proceedings of the National Academy of Sciences*, *95*(18), 10547-10552.

Rothe, S., Prakash, A., & Tyedmers, J. (2018). The insoluble protein deposit (IPOD) in yeast. *Frontiers in molecular neuroscience*, 237.

Rothman, J. E. (1989). Polypeptide chain binding proteins: catalysts of protein folding and related processes in cells. *Cell*, *59*(4), 591-601.

Rothman, J. H., & Stevens, T. H. (1986). Protein sorting in yeast: mutants defective in vacuole biogenesis mislocalize vacuolar proteins into the late secretory pathway. *Cell*, *47*(6), 1041-1051.

Rujano, M. A., Bosveld, F., Salomons, F. A., Dijk, F., Van Waarde, M. A., Van Der Want, J. J., De Vos, R. A., Brunt, E. R., Sibon, O. C., & Kampinga, H. H. (2006). Polarised asymmetric inheritance of accumulated protein damage in higher eukaryotes. *PLoS biology*, *4*(12), e417.

Rusinga, F. I., & Weis, D. D. (2017). Soft interactions and volume exclusion by polymeric crowders can stabilize or destabilize transient structure in disordered proteins depending on polymer concentration. *Proteins: Structure, Function, and Bioinformatics*, *85*(8), 1468-1479.

Russell, S. J., Steger, K. A., & Johnston, S. A. (1999). Subcellular localization, stoichiometry, and protein levels of 26 S proteasome subunits in yeast. *Journal of biological chemistry*, *274*(31), 21943-21952.

Rust, M. J., Bates, M., & Zhuang, X. (2006a). Stochastic optical reconstruction microscopy (STORM) provides sub-diffraction-limit image resolution. *Nature Methods*, *3*(10), 793.

Rust, M. J., Bates, M., & Zhuang, X. (2006b). Sub-diffraction-limit imaging by stochastic optical reconstruction microscopy (STORM). *Nature Methods*, *3*(10), 793-796.

Saarikangas, J., & Barral, Y. (2015). Protein aggregates are associated with replicative aging without compromising protein quality control. *eLife*, *4*, e06197.

Sáez, A. G., Lozano, E., & Zaldívar-Riverón, A. (2009). Evolutionary history of Na, K-ATPases and their osmoregulatory role. *Genetica*, *136*, 479-490.

Sagot, I., Pinson, B., Salin, B., & Daignan-Fornier, B. (2006). Actin bodies in yeast quiescent cells: an immediately available actin reserve? *Molecular biology of the cell*, *17*(11), 4645-4655.

Saito, H., & Posas, F. (2012). Response to hyperosmotic stress. *Genetics*, *192*(2), 289-318.

Sanchez, Y., & Lindquist, S. L. (1990). HSP104 required for induced thermotolerance. *Science*, *248*(4959), 1112-1115.

Sanchez, Y., Taulien, J., Borkovich, K., & Lindquist, S. (1992). Hsp104 is required for tolerance to many forms of stress. *The EMBO Journal*, *11*(6), 2357-2364.

Sanderson, M. J. (2000). High-speed digital microscopy. *Methods*, *21*(4), 325-334.

Sanfelice, D., Politou, A., Martin, S. R., De Los Rios, P., Temussi, P., & Pastore, A. (2013). The effect of crowding and confinement: a comparison of Yfh1 stability in different environments. *Physical biology*, *10*(4), 045002.

Sankaranarayanan, S., De Angelis, D., Rothman, J. E., & Ryan, T. A. (2000). The Use of pHluorins for Optical Measurements of Presynaptic Activity. *Biophysical Journal*, *79*(4), 2199-2208.

Sarkar, M., Li, C., & Pielak, G. J. (2013). Soft interactions and crowding. *Biophysical reviews*, *5*(2), 187-194.

Satoh, K., Takemura, Y., Satoh, M., Ozaki, K., & Kubota, S. (2021). Loss of FYCO1 leads to cataract formation. *Scientific reports*, *11*(1), 13771.

Satyanarayana, T., Umbarger, H., & Lindegren, G. (1968). Biosynthesis of branched-chain amino acids in yeast: regulation of leucine biosynthesis in prototrophic and leucine auxotrophic strains. *Journal of bacteriology*, *96*(6), 2018-2024.

Scheper, W., & Hoozemans, J. J. (2009). Endoplasmic reticulum protein quality control in neurodegenerative disease: the good, the bad and the therapy. *Current medicinal chemistry*, *16*(5), 615-626.

Schermelleh, L., Ferrand, A., Huser, T., Eggeling, C., Sauer, M., Biehlmaier, O., & Drummen, G. P. (2019). Super-resolution microscopy demystified. *Nature cell biology*, *21*(1), 72-84.

Schneider, B., Seufert, W., Steiner, B., Yang, Q., & Futcher, A. (1995). Use of polymerase chain reaction epitope tagging for protein tagging in Saccharomyces cerevisiae. *Yeast*, *11*(13), 1265-1274.

Schneider, K. L., Ahmadpour, D., Keuenhof, K. S., Eisele-Bürger, A. M., Berglund, L. L., Eisele, F., Babazadeh, R., Höög, J. L., Nyström, T., & Widlund, P. O. (2022). Using reporters of different misfolded proteins reveals differential strategies in processing protein aggregates. *Journal of biological chemistry*, *298*(11).

Schnitzer, B., Welkenhuysen, N., Leake, M. C., Shashkova, S., & Cvijovic, M. (2022). The effect of stress on biophysical characteristics of misfolded protein aggregates in living Saccharomyces cerevisiae cells. *Experimental gerontology*, 111755.

Scott, D. W., & Terrell, G. R. (1987). Biased and unbiased cross-validation in density estimation. *Journal of the American statistical association*, *82*(400), 1131-1146.

Segal, E., Shapira, M., Regev, A., Pe'er, D., Botstein, D., Koller, D., & Friedman, N. (2003). Module networks: identifying regulatory modules and their condition-specific regulators from gene expression data. *Nature genetics*, *34*(2), 166-176.

Sethuraman, A., & Belfort, G. (2005). Protein structural perturbation and aggregation on homogeneous surfaces. *Biophysical Journal*, *88*(2), 1322-1333.

Shaner, N. C., Campbell, R. E., Steinbach, P. A., Giepmans, B. N., Palmer, A. E., & Tsien, R. Y. (2004). Improved monomeric red, orange and yellow fluorescent proteins derived from Discosoma sp. red fluorescent protein. *Nature biotechnology*, *22*(12), 1567-1572.

Shaner, N. C., Lambert, G. G., Chammas, A., Ni, Y., Cranfill, P. J., Baird, M. A., Sell, B. R., Allen, J. R., Day, R. N., & Israelsson, M. (2013). A bright monomeric green fluorescent protein derived from Branchiostoma lanceolatum. *Nature Methods*, *10*(5), 407-409.

Sharp, K. A. (2015). Analysis of the size dependence of macromolecular crowding shows that smaller is better. *Proceedings of the National Academy of Sciences*, *112*(26), 7990-7995.

Shashkova, S., Andersson, M., Hohmann, S., & Leake, M. C. (2021). Correlating single-molecule characteristics of the yeast aquaglyceroporin Fps1 with environmental perturbations directly in living cells. *Methods*, *193*, 46-53.

Shashkova, S., & Leake, M. C. (2017). Single-molecule fluorescence microscopy review: shedding new light on old problems. *Bioscience reports*, *37*(4).

Shashkova, S., Wollman, A. J., Hohmann, S., & Leake, M. C. (2018). Characterising maturation of GFP and mCherry of genomically integrated fusions in Saccharomyces cerevisiae. *Bio-protocol*, *8*(2), e2710-e2710.

Shcheprova, Z., Baldi, S., Frei, S. B., Gonnet, G., & Barral, Y. (2008). A mechanism for asymmetric segregation of age during yeast budding. *Nature*, *454*(7205), 728-734.

Shepherd, J. W., Higgins, E. J., Wollman, A. J., & Leake, M. C. (2021). PySTACHIO: Python Single-molecule TrAcking stoiCHiometry Intensity and simulatiOn, a flexible, extensible, beginner-friendly and optimized program for analysis of single-molecule microscopy data. *Computational and Structural Biotechnology Journal*, *19*, 4049-4058.

Shepherd, J. W., & Leake, M. C. (2022). Localization microscopy: a review of the progress in methods and applications. *Principles of Light Microscopy: From Basic to Advanced*, 299-324.

Shepherd, J. W., Lecinski, S., Wragg, J., Shashkova, S., Macdonald, C., & Leake, M. C. (2021). Molecular crowding in single eukaryotic cells: Using cell environment biosensing and single-molecule optical microscopy to probe dependence on extracellular ionic strength, local glucose conditions, and sensor copy number. *Methods*, *193*, 54-61.

Shi, H., Westfall, C. S., Kao, J., Odermatt, P. D., Anderson, S. E., Cesar, S., Sievert, M., Moore, J., Gonzalez, C. G., & Zhang, L. (2021). Starvation induces shrinkage of the bacterial cytoplasm. *Proceedings of the National Academy of Sciences*, *118*(24), e2104686118.

Shields, S. B., & Piper, R. C. (2011). How ubiquitin functions with ESCRTs. *Traffic*, *12*(10), 1306-1317.

Shimomura, O. (1979). Structure of the chromophore of Aequorea green fluorescent protein. *FEBS Letters*, *104*(2), 220-222.

Shinoda, H., Ma, Y., Nakashima, R., Sakurai, K., Matsuda, T., & Nagai, T. (2018). Acid-Tolerant Monomeric GFP from Olindias formosa. *Cell Chem Biol*, *25*(3), 330-338.e337.

Sidell, B. D., & Hazel, J. R. (1987). Temperature affects the diffusion of small molecules through cytosol of fish muscle. *Journal of Experimental Biology*, *129*(1), 191-203.

Sikorski, R. S., & Hieter, P. (1989). A system of shuttle vectors and yeast host strains designed for efficient manipulation of DNA in Saccharomyces cerevisiae. *Genetics*, *122*(1), 19-27.

Simm, C., Lahner, B., Salt, D., LeFurgey, A., Ingram, P., Yandell, B., & Eide, D. J. (2007). Saccharomyces cerevisiae vacuole in zinc storage and intracellular zinc distribution. *Eukaryotic cell*, *6*(7), 1166-1177.

Simonin, H., Beney, L., & Gervais, P. (2007). Sequence of occurring damages in yeast plasma membrane during dehydration and rehydration: mechanisms of cell death. *Biochimica et Biophysica Acta (BBA)-Biomembranes*, *1768*(6), 1600-1610.

Sinclair, D., Mills, K., & Guarente, L. (1998). Aging in Saccharomyces cerevisiae. *Annual review of microbiology*, *52*, 533.

Sinclair, D. A., & Guarente, L. (1997). Extrachromosomal rDNA circles—a cause of aging in yeast. *Cell*, *91*(7), 1033-1042.

Singh, S., Fatima, A., Tiwari, S., & Prasad, S. M. (2020). Plant responses to radiation stress and its adaptive mechanisms. In *Plant Life Under Changing Environment* (pp. 105-122). Elsevier.

Siraj, N., El-Zahab, B., Hamdan, S., Karam, T. E., Haber, L. H., Li, M., Fakayode, S. O., Das, S., Valle, B., & Strongin, R. M. (2016). Fluorescence, phosphorescence, and chemiluminescence. *Analytical chemistry*, *88*(1), 170-202.

Sivadon, P., Peypouquet, M.-F., Doignon, F., Aigle, M., & Crouzet, M. (1997). Cloning of the multicopy suppressor gene SUR7: Evidence for a functional relationship between the yeast actin-binding protein Rvs167 and a putative membranous protein. *Yeast*, *13*(8), 747-761.

Skóra, T., Popescu, M. N., & Kondrat, S. (2021). Conformation-changing enzymes and macromolecular crowding. *Physical Chemistry Chemical Physics*, *23*(15), 9065-9069.

Slaninová, I., Šesták, S., Svoboda, A., & Farkaš, V. (2000). Cell wall and cytoskeleton reorganization as the response to hyperosmotic shock in Saccharomyces cerevisiae. *Archives of microbiology*, *173*(4), 245-252.

Smetana, K., Lacina, L., Szabo, P., Dvořánková, B., Brož, P., & Šedo, A. (2016). Ageing as an important risk factor for cancer. *Anticancer research*, *36*(10), 5009-5017.

Smits, G. J., Kapteyn, J. C., van den Ende, H., & Klis, F. M. (1999). Cell wall dynamics in yeast. *Current opinion in microbiology*, *2*(4), 348-352.

Song, J., Yang, Q., Yang, J., Larsson, L., Hao, X., Zhu, X., Malmgren-Hill, S., Cvijovic, M., Fernandez-Rodriguez, J., & Grantham, J. (2014). Essential genetic interactors of SIR2 required for spatial sequestration and asymmetrical inheritance of protein aggregates. *PLoS genetics*, *10*(7), e1004539.

Sontag, E., Chen, J.-H., McDermott, G., Gestaut, D., Larabell, C., & Frydman, J. (2017). Sorting Out the JUNQ: the Spatial Nature of Protein Quality Control. *Microscopy and Microanalysis*, *23*(S1), 994-995.

Spear, E. D., & Ng, D. T. (2003). Stress tolerance of misfolded carboxypeptidase Y requires maintenance of protein trafficking and degradative pathways. *Molecular biology of the cell*, *14*(7), 2756-2767.

Spence, J., Sadis, S., Haas, A. L., & Finley, D. (1995). A ubiquitin mutant with specific defects in DNA repair and multiubiquitination. *Molecular and cellular biology*, *15*(3), 1265-1273.

Spokoini, R., Moldavski, O., Nahmias, Y., England, J. L., Schuldiner, M., & Kaganovich, D. (2012). Confinement to organelle-associated inclusion structures mediates asymmetric inheritance of aggregated protein in budding yeast. *Cell reports*, *2*(4), 738-747.

Stagg, L., Zhang, S.-Q., Cheung, M. S., & Wittung-Stafshede, P. (2007). Molecular crowding enhances native structure and stability of α/β protein flavodoxin. *Proceedings of the National Academy of Sciences*, *104*(48), 18976-18981.

Steinkraus, K., Kaeberlein, M., & Kennedy, B. K. (2008). Replicative aging in yeast: the means to the end. *Annual review of cell and developmental biology*, *24*, 29-54.

Stevens, T., Esmon, B., & Schekman, R. (1982). Early stages in the yeast secretory pathway are required for transport of carboxypeptidase Y to the vacuole. *Cell*, *30*(2), 439-448.

Stigter, D. (1960). Interactions in aqueous solutions. II. Osmotic pressure and osmotic coefficient of sucrose and glucose solutions. *The Journal of Physical Chemistry*, *64*(1), 118-124.

Stokes, G. G. (1852). On the change of refrangibility of light. *Philosophical Transactions of the Royal Society of London*(142), 463-562.

Stolz, A., & Wolf, D. H. (2012). Use of CPY* and its derivatives to study protein quality control in various cell compartments. *Ubiquitin Family Modifiers and the Proteasome: Reviews and Protocols*, 489-504.

Suastika, K., Dwipayana, P., Semadi, M. S., & Kuswardhani, R. T. (2012). Age is an important risk factor for type 2 diabetes mellitus and cardiovascular diseases. *Glucose Tolerance*, *5*, 67-80.

Sugiyama, S., & Tanaka, M. (2019). Distinct segregation patterns of yeast cell-peripheral proteins uncovered by a method for protein segregatome analysis. *Proceedings of the National Academy of Sciences*, *116*(18), 8909-8918.

Sunchu, B., & Cabernard, C. (2020). Principles and mechanisms of asymmetric cell division. *Development*, *147*(13), dev167650.

Suter, B., Wellinger, R.-E., & Thoma, F. (2000). DNA repair in a yeast origin of replication: contributions of photolyase and nucleotide excision repair. *Nucleic acids research*, *28*(10), 2060-2068.

Syeda, A. H., Wollman, A. J., Hargreaves, A. L., Howard, J. A., Brüning, J.-G., McGlynn, P., & Leake, M. C. (2019). Single-molecule live cell imaging of Rep reveals the dynamic interplay between an accessory replicative helicase and the replisome. *Nucleic acids research*, *47*(12), 6287-6298.

Tabaka, M., Kalwarczyk, T., Szymanski, J., Hou, S., & Holyst, R. (2014). The effect of macromolecular crowding on mobility of biomolecules, association kinetics, and gene expression in living cells. *Frontiers in Physics*, *2*, 54.

Takahashi, N., & Schachtele, C. (1990). Effect of pH on the growth and proteolytic activity of Porphyromonas gingivalis and Bacteroides intermedius. *Journal of dental research*, *69*(6), 1266-1269.

Takahashi, T. (1997). Significant role of electrostatic interactions for stabilization of protein assemblies. *Advances in Biophysics*, *34*, 41-54.

Tamás, M. J., Rep, M., Thevelein, J. M., & Hohmann, S. (2000). Stimulation of the yeast high osmolarity glycerol (HOG) pathway: evidence for a signal generated by a change in turgor rather than by water stress. *FEBS Letters*, *472*(1), 159-165.

ten Wolde, P. R., & Mugler, A. (2014). Importance of crowding in signaling, genetic, and metabolic networks. *International Review of Cell and Molecular Biology*, *307*, 419-442.

Tenreiro, S., Munder, M. C., Alberti, S., & Outeiro, T. F. (2013). Harnessing the power of yeast to unravel the molecular basis of neurodegeneration. *Journal of neurochemistry*, *127*(4), 438-452.

Teusink, B., Passarge, J., Reijenga, C. A., Esgalhado, E., Van der Weijden, C. C., Schepper, M., Walsh, M. C., Bakker, B. M., Van Dam, K., & Westerhoff, H. V. (2000). Can yeast glycolysis be understood in terms of in vitro kinetics of the constituent enzymes? Testing biochemistry. *European Journal of Biochemistry*, *267*(17), 5313-5329.

Thévenaz, G. L. P. (2021). *pyStackReg image registration tool, python implementation of the ImageJ/FIJI Plugin TurboReg/StackReg*.

Thorn, K. (2016). A quick guide to light microscopy in cell biology. *Molecular biology of the cell*, *27*(2), 219-222.

Thumm, M. (2000). Structure and function of the yeast vacuole and its role in autophagy. *Microscopy research and technique*, *51*(6), 563-572.

Tokunaga, M., Imamoto, N., & Sakata-Sogawa, K. (2008). Highly inclined thin illumination enables clear single-molecule imaging in cells. *Nature Methods*, *5*(2), 159-161.

Tomlin, G. C., Wixon, J. L., Bolotin-Fukuhara, M., & Oliver, S. G. (2001). A new family of yeast vectors and S288C-derived strains for the systematic analysis of gene function. *Yeast*, *18*(6), 563-575.

Tran, C. S., Rangel, S. M., Almblad, H., Kierbel, A., Givskov, M., Tolker-Nielsen, T., Hauser, A. R., & Engel, J. N. (2014). The Pseudomonas aeruginosa type III translocon is required for biofilm formation at the epithelial barrier. *PLoS pathogens*, *10*(11), e1004479.

Trovato, F., & Tozzini, V. (2014). Diffusion within the cytoplasm: a mesoscale model of interacting macromolecules. *Biophysical Journal*, *107*(11), 2579-2591.

Turner, J. J., Ewald, J. C., & Skotheim, J. M. (2012). Cell size control in yeast. *Current biology*, *22*(9), R350-R359.

Tyedmers, J., Mogk, A., & Bukau, B. (2010). Cellular strategies for controlling protein aggregation. *Nature reviews Molecular cell biology*, *11*(11), 777-788.

Udden, M. M., & Finkelstein, D. B. (1978). Reaction order of Saccharomyces cerevisiae alpha-factor-mediated cell cycle arrest and mating inhibition. *Journal of bacteriology*, *133*(3), 1501-1507.

Vabulas, R. M., Raychaudhuri, S., Hayer-Hartl, M., & Hartl, F. U. (2010). Protein folding in the cytoplasm and the heat shock response. *Cold Spring Harbor perspectives in biology*, *2*(12), a004390.

Valdez-Taubas, J., & Pelham, H. R. (2003). Slow diffusion of proteins in the yeast plasma membrane allows polarity to be maintained by endocytic cycling. *Current biology*, *13*(18), 1636-1640.

Valeur, B. (2011). M. r. N. Berberan-Santos. *J. Chem. Educ*, *88*, 731.

Valls, L. A., Hunter, C. P., Rothman, J. H., & Stevens, T. H. (1987). Protein sorting in yeast: the localization determinant of yeast vacuolar carboxypeptidase Y resides in the propeptide. *Cell*, *48*(5), 887-897.

Van Den Berg, J., Boersma, A. J., & Poolman, B. (2017). Microorganisms maintain crowding homeostasis. *Nature Reviews Microbiology*, *15*(5), 309-318.

Van Den Hazel, H. B., Kielland-Brandt, M. C., & Winther, J. R. (1996). Biosynthesis and function of yeast vacuolar proteases. *Yeast*, *12*(1), 1-16.

Van der Walt, S., Schönberger, J. L., Nunez-Iglesias, J., Boulogne, F., Warner, J. D., Yager, N., Gouillart, E., & Yu, T. (2014). scikit-image: image processing in Python. *PeerJ*, *2*, e453.

van Leeuwen, W., & Rabouille, C. (2019). Cellular stress leads to the formation of membraneless stress assemblies in eukaryotic cells. *Traffic*, *20*(9), 623-638.

Van Rosmalen, M., Krom, M., & Merkx, M. (2017). Tuning the flexibility of glycine-serine linkers to allow rational design of multidomain proteins. *Biochemistry*, *56*(50), 6565-6574.

Vechtomova, Y. L., Telegina, T. A., Buglak, A. A., & Kritsky, M. S. (2021). UV radiation in DNA damage and repair involving DNA-photolyases and cryptochromes. *Biomedicines*, *9*(11), 1564.

Veetil, J. V., Jin, S., & Ye, K. (2010). A glucose sensor protein for continuous glucose monitoring. *Biosensors and Bioelectronics*, *26*(4), 1650-1655.

Vellai, T., & Vida, G. (1999). The origin of eukaryotes: the difference between prokaryotic and eukaryotic cells. *Proceedings of the Royal Society of London. Series B: Biological Sciences*, *266*(1428), 1571-1577.

Verdaasdonk, J. S., Stephens, A. D., Haase, J., & Bloom, K. (2014a). B ending the Rules: Widefield Microscopy and the Abbe Limit of Resolution. *Journal of cellular physiology*, *229*(2), 132-138.

Verdaasdonk, J. S., Stephens, A. D., Haase, J., & Bloom, K. (2014b). Bending the Rules: Widefield Microscopy and the Abbe Limit of Resolution. *Journal of cellular physiology*, *229*(2), 132-138.

Veses, V., Richards, A., & Gow, N. A. (2008). Vacuoles and fungal biology. *Current opinion in microbiology*, *11*(6), 503-510.

Vevea, J. D., Wolken, D. M. A., Swayne, T. C., White, A. B., & Pon, L. A. (2013). Ratiometric biosensors that measure mitochondrial redox state and ATP in living yeast cells. *JoVE (Journal of Visualized Experiments)*(77), e50633.

Vida, T. A., & Emr, S. D. (1995). A new vital stain for visualizing vacuolar membrane dynamics and endocytosis in yeast. *The Journal of cell biology*, *128*(5), 779-792.

Vidal, M., & Gaber, R. F. (1994). Selectable marker replacement in Saccharomyces cerevisiae. *Yeast*, *10*(2), 141-149.

Virtanen, P., Gommers, R., Oliphant, T. E., Haberland, M., Reddy, T., Cournapeau, D., Burovski, E., Peterson, P., Weckesser, W., & Bright, J. (2020). SciPy 1.0: fundamental algorithms for scientific computing in Python. *Nature Methods*, *17*(3), 261-272.

Vrabioiu, A. M., & Mitchison, T. J. (2006). Structural insights into yeast septin organization from polarized fluorescence microscopy. *Nature*, *443*(7110), 466-469.

Walker, J. M. (2005). *The proteomics protocols handbook*. Springer.

Walker, T. (2016). *Cell Magic Wand tool*. github-fitzlab-CellMagicWand

Wang, C., Taki, M., Sato, Y., Tamura, Y., Yaginuma, H., Okada, Y., & Yamaguchi, S. (2019). A photostable fluorescent marker for the superresolution live imaging of the dynamic structure of the mitochondrial cristae. *Proceedings of the National Academy of Sciences*, *116*(32), 15817-15822.

Wang, G., & Fang, N. (2012). Detecting and tracking nonfluorescent nanoparticle probes in live cells. *Methods in enzymology*, *504*, 83-108.

Wang, L., Wang, Y., & Ragauskas, A. J. (2012). Determination of cellulase colocalization on cellulose fiber with quantitative FRET measured by acceptor photobleaching and spectrally unmixing fluorescence microscopy. *Analyst*, *137*(6), 1319-1324.

Wang, Y., Meriin, A. B., Zaarur, N., Romanova, N. V., Chernoff, Y. O., Costello, C. E., & Sherman, M. Y. (2009). Abnormal proteins can form aggresome in yeast: aggresome-targeting signals and components of the machinery. *The FASEB Journal*, *23*(2), 451.

Warren, G., & Wickner, W. (1996). Organelle inheritance. *Cell*, *84*(3), 395-400.

Waskom, M. L. (2021). Seaborn: statistical data visualization. *Journal of Open Source Software*, *6*(60), 3021.

Webb, D. J., & Brown, C. M. (2012). Epi-fluorescence microscopy. In *Cell imaging techniques* (pp. 29-59). Springer.

Weids, A. J., Ibstedt, S., Tamás, M. J., & Grant, C. M. (2016). Distinct stress conditions result in aggregation of proteins with similar properties. *Scientific reports*, *6*(1), 1-12.

Weill, U., Yofe, I., Sass, E., Stynen, B., Davidi, D., Natarajan, J., Ben-Menachem, R., Avihou, Z., Goldman, O., & Harpaz, N. (2018). Genome-wide SWAp-Tag yeast libraries for proteome exploration. *Nature Methods*, *15*(8), 617-622.

Winderickx, J., Holsbeeks, I., Lagatie, O., Giots, F., Thevelein, J., & de Winde, H. (2003). From feast to famine; adaptation to nutrient availability in yeast. In *Yeast stress responses* (pp. 305-386). Springer.

Winston, F., Dollard, C., & Ricupero-Hovasse, S. L. (1995). Construction of a set of convenient Saccharomyces cerevisiae strains that are isogenic to S288C. *Yeast*, *11*(1), 53-55.

Wolf, D., & Schäfer, A. (2005). CPY* and the power of yeast genetics in the elucidation of quality control and associated protein degradation of the endoplasmic reticulum. *Dislocation and Degradation of Proteins from the Endoplasmic Reticulum*, 41-56.

Wolf, D. H., & Fink, G. R. (1975). Proteinase C (carboxypeptidase Y) mutant of yeast. *Journal of bacteriology*, *123*(3), 1150-1156.

Wollman, A. J., & Leake, M. C. (2015). Millisecond single-molecule localization microscopy combined with convolution analysis and automated image segmentation to determine protein concentrations in complexly structured, functional cells, one cell at a time. *Faraday discussions*, *184*, 401-424.

Wollman, A. J., & Leake, M. C. (2016). Single-molecule narrow-field microscopy of protein–DNA binding dynamics in glucose signal transduction of live yeast cells. In *Chromosome Architecture* (pp. 5-15). Springer.

Wollman, A. J., Nudd, R., Hedlund, E. G., & Leake, M. C. (2015). From Animaculum to single molecules: 300 years of the light microscope. *Open biology*, *5*(4), 150019.

Wollman, A. J., Shashkova, S., Hedlund, E. G., Friemann, R., Hohmann, S., & Leake, M. C. (2017). Transcription factor clusters regulate genes in eukaryotic cells. *eLife*, *6*, e27451.

Wood, T. I., Barondeau, D. P., Hitomi, C., Kassmann, C. J., Tainer, J. A., & Getzoff, E. D. (2005). Defining the role of arginine 96 in green fluorescent protein fluorophore biosynthesis. *Biochemistry*, *44*(49), 16211-16220.

Xia, Z., & Liu, Y. (2001). Reliable and global measurement of fluorescence resonance energy transfer using fluorescence microscopes. *Biophysical Journal*, *81*(4), 2395-2402.

Xie, X., & Lipke, P. N. (2010). On the evolution of fungal and yeast cell walls. *Yeast*, *27*(8), 479-488.

Yeong, F. M. (2005). Severing all ties between mother and daughter: cell separation in budding yeast. *Molecular Microbiology*, *55*(5), 1325-1331.

Zacharias, D. A., Violin, J. D., Newton, A. C., & Tsien, R. Y. (2002). Partitioning of lipid-modified monomeric GFPs into membrane microdomains of live cells. *Science*, *296*(5569), 913-916.

Zámborszky, J., Hong, C. I., & Csikász Nagy, A. (2007). Computational analysis of mammalian cell division gated by a circadian clock: quantized cell cycles and cell size control. *Journal of biological rhythms*, *22*(6), 542-553.

Zhang, Q., Bai, Q., Zhu, L., Hou, T., Zhao, J., & Liang, D. (2019). Macromolecular crowding and confinement effect on the growth of DNA nanotubes in dextran and hyaluronic acid media. *ACS Applied Bio Materials*, *3*(1), 412-420.

Zhang, W., Yang, X., Chen, L., Liu, Y.-Y., Venkatarangan, V., Reist, L., Hanson, P., Xu, H., Wang, Y., & Li, M. (2021). A conserved ubiquitin-and ESCRT-dependent pathway internalizes human lysosomal membrane proteins for degradation. *PLoS biology*, *19*(7), e3001361.

Zhao, F.-Q., & Craig, R. (2003). Capturing time-resolved changes in molecular structure by negative staining. *Journal of structural biology*, *141*(1), 43-52.

Zhou, C., Slaughter, B. D., Unruh, J. R., Eldakak, A., Rubinstein, B., & Li, R. (2011). Motility and segregation of Hsp104-associated protein aggregates in budding yeast. *Cell*, *147*(5), 1186-1196.

Zhou, C., Slaughter, B. D., Unruh, J. R., Guo, F., Yu, Z., Mickey, K., Narkar, A., Ross, R. T., McClain, M., & Li, R. (2014). Organelle-based aggregation and retention of damaged proteins in asymmetrically dividing cells. *Cell*, *159*(3), 530-542.

Zhou, H.-X. (2013). Influence of crowded cellular environments on protein folding, binding, and oligomerization: biological consequences and potentials of atomistic modeling. *FEBS Letters*, *587*(8), 1053-1061.

Zhou, H.-X., Rivas, G., & Minton, A. P. (2008). Macromolecular crowding and confinement: biochemical, biophysical, and potential physiological consequences. *Annual review of biophysics*, *37*, 375.

Zimmerman, S. B., & Trach, S. O. (1991). Estimation of macromolecule concentrations and excluded volume effects for the cytoplasm of Escherichia coli. *Journal of molecular biology*, *222*(3), 599-620.

Zimmermann, A., Hofer, S., Pendl, T., Kainz, K., Madeo, F., & Carmona-Gutierrez, D. (2018). Yeast as a tool to identify anti-aging compounds. *FEMS yeast research*, *18*(6), foy020.

Appendices

1. CrGE2.3 gel filtration elution profile

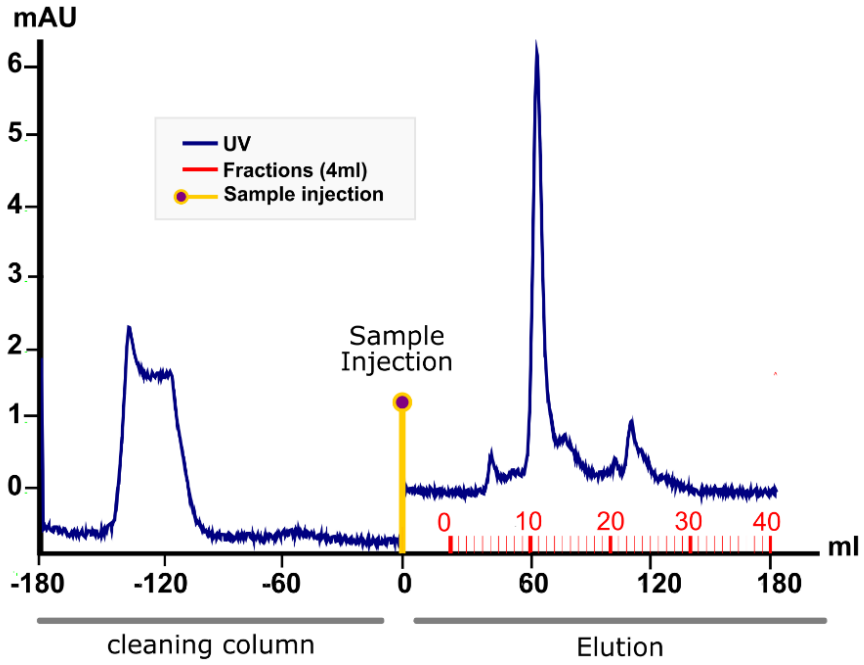

Appendix ap.0-1: CrGE2.3 gel filtration elution profile

U.V Elution profile with legend extracted from the used chromatography system (ÄKTA pure protein purification system, Cytiva). In yellow the sample point of injection, in blue the U.V profile with the characteristic point of injection.

2. Glucose availability and NFRET

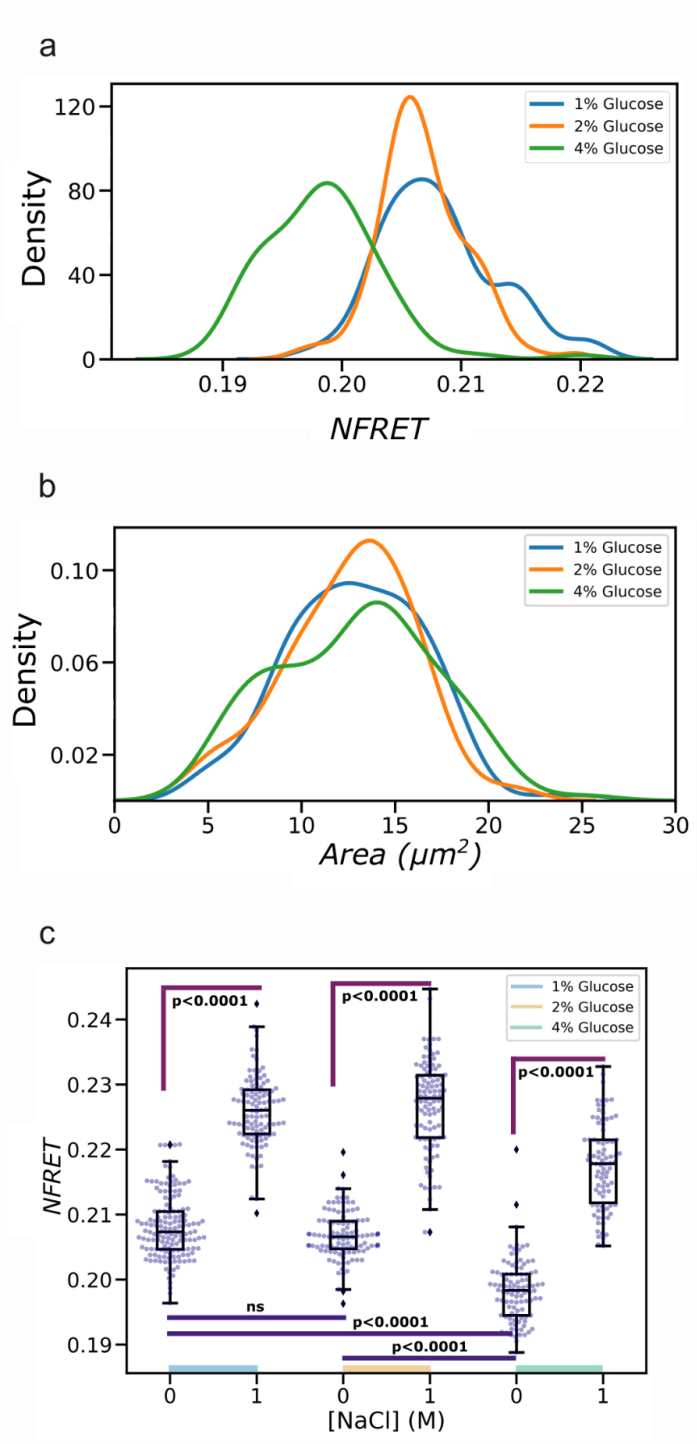

Appendix ap.0-2: Glucose availability and crowding (NFRET)

(a) Kernel density estimates (KDEs) of the NFRET distribution for cells grown in 1%, 2%, and 4% glucose conditions and imaged at 0 M NaCl. For all conditions N>100. (b) KDE of the cell size distribution, with area in μm^2, for cells grown in 1%, 2%, and 4% glucose and imaged at 0 M NaCl. Lines are given by a KDE fit.

(c) Jitter plot showing NFRET at high (1 M) and low (0 M) salt concentration for cells grown at 1%, 2%, and 4% glucose and imaged in 50 mM NaPi. The p-value was corrected with Bonferroni's method.

3. Glucose availability histogram visualisation

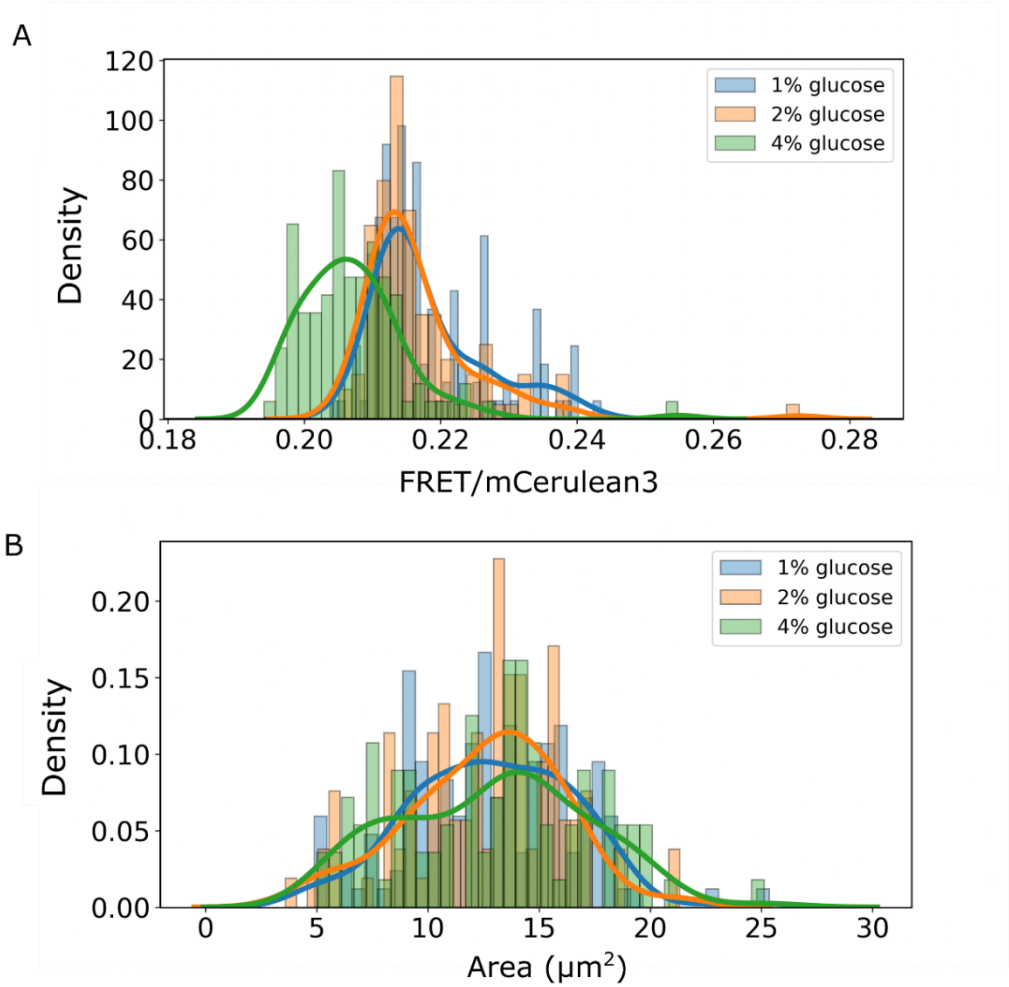

Appendix ap.0-3: Glucose availability, histogram and fit

(A) Histogram and Kernel density estimates (KDEs) of the FRET/Cerulean3 ratio distribution for cells grown in 1%, 2%, and 4% glucose conditions and imaged at 0 M NaCl. Data with only fit in Figure 3-4.a (B) Histogram and KDE of the cell size distribution, with area in µm^2, for cells grown in 1%, 2%, and 4% glucose and imaged at 0 M NaCl. Data with only fit in Figure 3-4.b.

Appendix ap.0-4: Macro code for ratioFRET measurement

```
if (nImages == 0) {
	showMessage("Macro error", "There is no image open");
	exit
}
Dialog.create("Background noise");
Dialog.addNumber("Donor", 180, 2, 5, " ");
Dialog.addNumber("Fret", 370, 2, 5, " ");
Dialog.show();
NoiseDonor = Dialog.getNumber();
NoiseFret = Dialog.getNumber();
imagebatch = getList("image.titles");
Array.sort(imagebatch);
Array.print(imagebatch);
MaskPath = getDir("choose");
MaskPath = MaskPath +File.separator;
//listfile = getFileList(MaskPath);
n = lengthOf(imagebatch) ;
PathOnlyNfretDoc = MaskPath+"ratioFret.csv";
HeadlineDocfret = "RatioFret";
File.append(HeadlineDocfret , PathOnlyNfretDoc);
PathOnlyAreaDoc = MaskPath+"Area.csv";
HeadlineDocarea = "Area ";
File.append(HeadlineDocarea , PathOnlyAreaDoc);

for (i = 0; i < n ; i++) {
	print(i);
	ImInitial = imagebatch[i];
	print(ImInitial);
	selectWindow(ImInitial);
	getDimensions(width, height, channels, slices, frames);
	initialroiCount = roiManager("count");
	selectWindow(ImInitial);
	run("Split Channels");
	wait(20);

	for (j = 0; j < nImages; j++) {
		selectImage(j+1);
		imch = getTitle();
		if (startsWith(imch, "C1")) {
			rename("C1");
		}
		else if (startsWith(imch, "C2")) {
```

```
		rename("C2");
	}
	else if (startsWith(imch, "C3")) {
		run("Close");
		//close();
		print("closed cothers");
	}
	else if (startsWith(imch, "C4")) {
		run("Close");
		//close();
		print("closed cothers");
	}
}

//
ImInitial2 = File.nameWithoutExtension;
maskimg = ImInitial2+"masks.tif";
open(MaskPath+maskimg);
selectWindow(maskimg);
run("Make Binary");
run("Select None");
run("Analyze Particles...", "add");
selectWindow(maskimg);
//close();
//
selectWindow("C1");
roiManager("deselect");
roiManager("measure");
roiManager("draw");
selectWindow("Results");
valuesD = Table.getColumn("Mean");
Area = Table.getColumn("Area");
run("Clear Results");
selectWindow("C2");
roiManager("deselect");
roiManager("measure");
roiManager("draw");
selectWindow("Results");
valuesFret = Table.getColumn("Mean");
run("Clear Results");
for (j = 0; j < lengthOf(valuesD); j++) {
	Donorval = valuesD[j];
	FRETval = valuesFret[j];
	Areaval = Area[j];
	RatioF = (FRETval-NoiseFret)/(Donorval-NoiseDonor);

	File.append(RatioF , PathOnlyNfretDoc);
```

```
            File.append(Areaval , PathOnlyAreaDoc);
            }
        run("Clear Results");
        roiManager("deselect"); //to clear segmentation before next slice
        roiManager("delete");

        selectWindow("C1");
        close();
        selectWindow("C2");
        close();
}
```

5. ImageJ ring shapes macro

Appendix ap.0-5: Macro code for customise ring-shape outline

```
run("Set Measurements...", "area mean min integrated display redirect=None
decimal=3");
if (nImages == 0) {
        showMessage("error", "There is no image open");
        exit
}
else {
        getImageJD();
        initialimagetitle= getTitle();
        StackSlice = nSlices;
}
initialroiCount = roiManager("count");
getImageJD();
initialimagetitle= getTitle();
StackSlice = nSlices;
C0 = "C0-"+initialimagetitle;
C1 = "C1-"+initialimagetitle;
C2 = "C2-"+initialimagetitle;
C3 = "C3-"+initialimagetitle;
C4 = "C4-"+initialimagetitle;
ChoicesChannel = newArray(C1,C2,C3,C4);
n=1;

//Dialogue Box
Dialog.create("Set Values");
Dialog.addNumber("Width (microns):", -0.5);
Dialog.addNumber("iteration", 1);
Dialog.addChoice("Fluorescent Channel:", ChoicesChannel);
```

```
Dialog.addCheckbox("Background correction?", false);
Dialog.addNumber("If yes, Background Mean value:", 0);
Dialog.show();
X = Dialog.getNumber();
nbiteration = Dialog.getNumber();
FluorescentChannel = Dialog.getChoice();
NoiseYes = Dialog.getCheckbox();
BackgroudMean = Dialog.getNumber();

// Overlay

if (Overlay.size != 0){
	run("To ROI Manager");
	initialroiCount = roiManager("count");
}
	else {
		if (initialroiCount == 0) {
		waitForUser("No selection","Create a ROI List and click OK to continue");
		initialroiCount = roiManager("count");
		}
	}

/// Stack
selectWindow(initialimagetitle);
if (StackSlice != 1) {
	run("Split Channels");
	selectWindow(FluorescentChannel);
	ImageAnalysedID = getImageJD();
	}
	else {
		selectWindow(initialimagetitle);
		ImageAnalysedID = getImageJD();
	}

/// Make rings

if (nbiteration == 0) {
	for (i=0; i<initialroiCount; i++) {
		roiManager("select", i);
		if ( i < 10 ) {
			j="0"+i;
		}
			else {
				j=i;
```

```
                }
            roiManager("rename", "cell-"+j+"_00");
        }
}
        else {

for (i=0; i<initialroiCount; i++) {
        roiManager("select", i);
        if ( i < 10 ) {
            j="0"+i;
        }
            else {
                j=i;
            }
            roiManager("rename", "cell-"+j+"_00");
            run("Enlarge...", "enlarge="+X);
            roiManager("Add");
            NewRoiCount = roiManager("count");
            while (n<= nbiteration) {
                roiManager("select", NewRoiCount-1);
                run("Enlarge...", "enlarge="+X);
                roiManager("Add");
                if ( n < 10 ) {
                    m="0"+n;
                }
                    else {
                        m=n;
                    }
                roiManager("rename", "cell-"+j+"_"+m);
                n= n+1 ;
                NewRoiCount = NewRoiCount+1;
                            }
            roiManager("select", NewRoiCount-1);
            roiManager("delete");
            n=1;
}
        }

roiManager("Deselect");
roiManager("Sort");
selectImage(ImageAnalysedID);
roiManager("Show All");
roiManager("measure");
```

```
// Set result table
for (i=0; i<nResults; i++) {
        roiManager("select", i);
        newLabel = getInfo("roi.name");
   setResult("Label", i, newLabel);
   if (NoiseYes == true) {
   MeanCorrected = getResult("Mean", i)-BackgroudMean;
   intDentCorrected = getResult("IntDen", i)-(getResult("Area", i)*BackgroudMean);
   setResult("Mean_NoiseCorrection", i, MeanCorrected);
   setResult("IntDent_NoiseCorrection", i, intDentCorrected);
   }
  }
nDoughnutResult = nResults-2;
k=0;
l = 1;
Doughnutcount= 1;
 for (i = 0; i <= nDoughnutResult ; i++) {
        if (Doughnutcount<=nbiteration) {
        IntDoughnutArea = getResult("IntDen", k)-getResult("IntDen", l);
                if (NoiseYes == true) {
                        IntDoughnutAreaCorr = getResult("IntDent_NoiseCorrection", k)-
getResult("IntDent_NoiseCorrection", l);
                        InitialLabelName = getResultString("Label", i);
                        Compositenumbername = substring(InitialLabelName, 0, 7);
                        setResult("Doughnut", i,
Compositenumbername+"_Donut_"+Doughnutcount);
                        setResult("IntDen-Doughnut", i, IntDoughnutArea);
                        setResult("IntDen-Corrected-Doughnut", i, IntDoughnutAreaCorr);
                        k= k+1;
                        l= l+1;
                        Doughnutcount = Doughnutcount+1;
                 }
                 else {
                        InitialLabelName = getResultString("Label", i);
                        Compositenumbername = substring(InitialLabelName, 0, 7);
                        setResult("Doughnut", i,
Compositenumbername+"_Donut_"+Doughnutcount);
                        setResult("IntDen-Doughnut", i, IntDoughnutArea);
                        k= k+1;
                        l= l+1;
                        Doughnutcount = Doughnutcount+1;
                 }
                }
                else {
```

```
                setResult("Doughnut", i, "--");
                setResult("IntDen-Doughnut", i, "--");
                if (NoiseYes == true) {
                        setResult("IntDen-Corrected-Doughnut", i, "--");
                }
                Doughnutcount = 1 ;
                k= k+1;
                l= l+1;
        }
}
```

6. Growth control bud neck strains

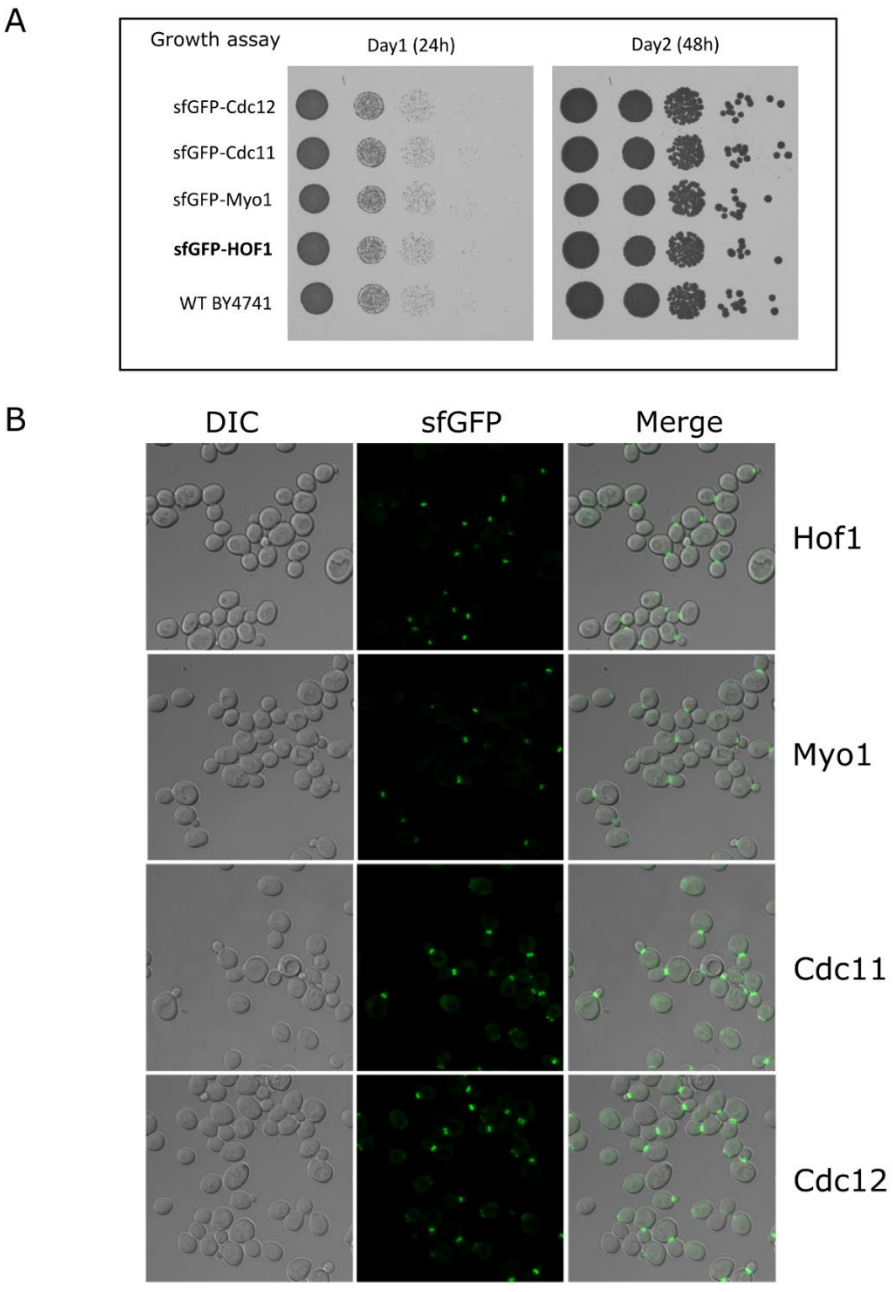

Appendix ap.0-6: Control for yeast growth GFP tagged bud neck reporter

(A) Growth Assay for wild type BY4741 (WT) yeast and a selected range of GFP fluorescent bud neck markers (SWAp-Tag Library - (Weill et al., 2018)) and constitutively expressed under the NOP1 promoter in BY4741 background strain. 10-fold serially diluted plate from a culture grown beforehand to log phase was photographed after 24h and 48h incubation at 30°C. Strains expressing a fluorescent marker (Hof1, Myo1, Cdc11

and Cdc12) grew similar to the WT strain with no growth defect to report for all strains tested (Appendix ap.). (B) Confocal images for each strain tested, with GFP fusion bud neck reporter expressed in budding yeasts. Showing, the DIC grey channel, GFP green fluorescence channel and the merge between the two.

7. Overlay filtration – Python code

Appendix ap.0-7: Python outlier filtration

```
import numpy as np
import matplotlib.pyplot as plt
import csv
import seaborn as sns
import scipy
import statistics as st
import pandas as pd
import math
import matplotlib as mpl
from scipy.stats import sem
from sklearn import preprocessing
import scipy.stats as stats
import glob
import os.path
from itertools import zip_longest

#keep rows with values within 1.5*IQR of Q1 and Q3
#
Dir= r"C:\_DeepLearning\src for Sarah\rep3_boxplot data/"
#dataSaveName = ["ctrl","1M-NaCl","250mM-NaCl","200mM-LiCl"]
dirfiles = glob.glob(Dir+'*')
mydatafiledir =[]
# Working directory
dirfiles = glob.glob(Dir+'*') #os.listdir(Dir) #glob.glob(Dir+"*.xlsx") to get all file
AllData = []
for i in range(len(dirfiles)):
    if dirfiles[i][-1]=="x": #detect excel
        print("excel")
        data = pd.read_excel(dirfiles[i], skiprows=None, index_col=None, header=0) ##
skiprows=None if keeping the header
        #data = data.to_numpy()
```

```
        AllData.append(data)
        mydatafiledir.append(dirfiles[i])
    if dirfiles[i][-1]=="v": # detect csv
        print("csv detected")
        data = pd.read_csv(dirfiles[i], skiprows=None, index_col=None, header=0)
        #data = data.to_numpy()
        AllData.append(data)
        mydatafiledir.append(dirfiles[i])

datalist = AllData

if (len(mydatafiledir)==0):
    print("No files detected")

if (len(mydatafiledir)!=0):
    for i in range(len(datalist)):
        dataOUTLIERclean = pd.DataFrame()
        dataOUTLIERcleanlist = []
        data = datalist[i]
        TheHeader = data.columns

        for j in range (len(data.columns)):
            dataw = data.iloc[:,j]
            dataw = [x for x in dataw if ~np.isnan(x)] # remove NAN
            dataw = pd.DataFrame(dataw)
            a1 = dataw
            ### Interquartil methods
            Q1 = dataw.quantile(q=.25)
            Q3 = dataw.quantile(q=.75)
            IQR = dataw.apply(stats.iqr)
            dataclean = dataw[~((dataw < (Q1-1.5*IQR)) | (dataw > (Q3+1.5*IQR))).any(axis=1)]

            a2 = dataclean
            #a2 = [x for x in a2 if ~np.isnan(x)]
            #datacleanFrame = d.to_frame()
            datacleanlist = dataclean.to_numpy()
            dataOUTLIERcleanlist.append(list(datacleanlist))

          # df = pd.DataFrame.from_records(dataOUTLIERcleanlist)

        df = pd.DataFrame(dataOUTLIERcleanlist).T
        df = df.to_numpy(dtype='float32').T

        #.to_csv(mydatafiledir[i][:-4]+'_Interquartil filtered'+'.csv', header=TheHeader,
index=False)

        with open(mydatafiledir[i][:-4]+'_F'+'.csv', 'w', newline='') as file:
```

```
    wr= csv.writer(file)
    wr.writerow(TheHeader)
    wr.writerows(zip_longest(*df))  # wr.writerows(c) # raw ans not column

file.close()
```

8. Scatter plot: cytometry experiment

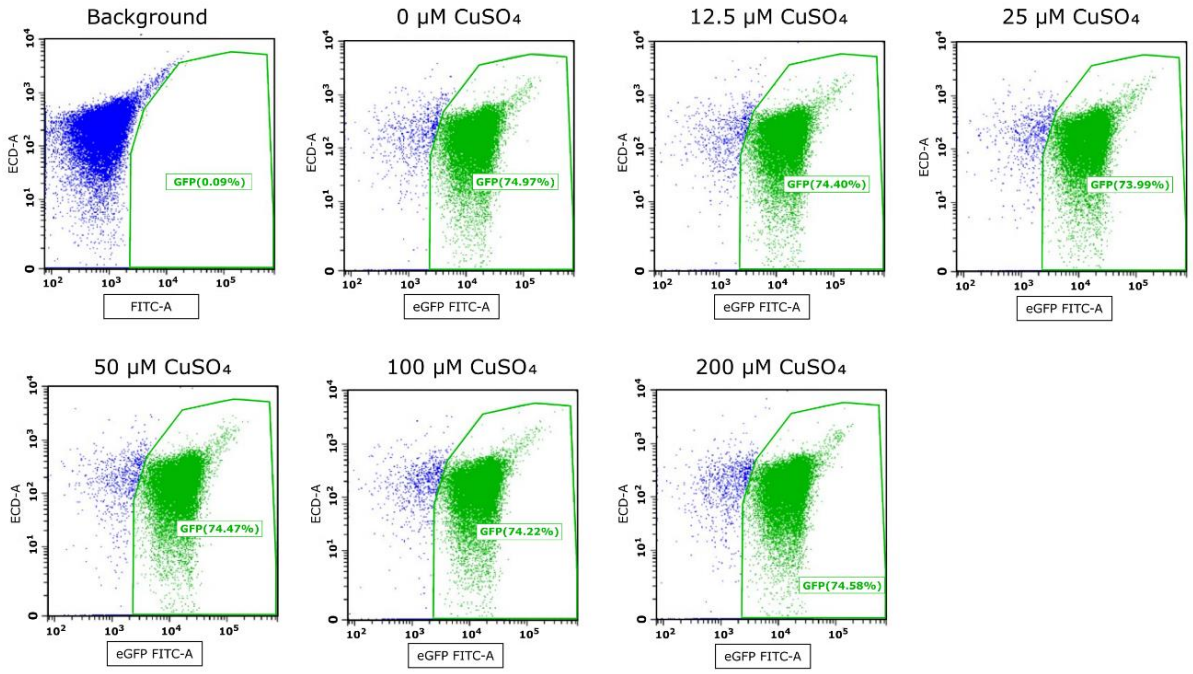

Appendix ap.0-8: GFP positive cells population in presence of copper sulfate

Additional evidence to show that copper levels do not impact the brightness of GFP. Scatter plots obtained by cytometry to identify and measure GFP positive cells, experience performed at various copper sulfate concentrations on BY4742 cells stably expressing Mup1-GFP (the methionine permease).

Appendix ap.0-9: A spot count tool

```
///// initial variable and parameters
if (nImages == 0) {
	showMessage("Macro error", "There is no image open");
	exit
}
else {
	fileName = getInfo("image.filename"); // to save in the name of the file where the image is
	initialimagetitle= getTitle(); // get the name of the image active on ImageJ
	StackSlice = nSlices; // number is 1 if the image is not a stack
	RoiCount = roiManager("count");
}
run("Set Measurements...", "area mean integrated display redirect=None decimal=3");

C1 = "C1-"+initialimagetitle;
C2 = "C2-"+initialimagetitle;
C3 = "C3-"+initialimagetitle;
C4 = "C4-"+initialimagetitle;
ChoicesChannel = newArray(C1,C2,C3,C4);
ChoiceThreshold = newArray("Default","Otsu","Huang","Minimum","Intermodes","MaxEntropy","RenyiEntropy","Yen");

///// Dialogue box //////////

Dialog.create("Set parameters");
Dialog.addChoice("Automatic Threshold ", ChoiceThreshold);
Dialog.addMessage("----To help segmentation----");
Dialog.addCheckbox("Add Background substraction (On a duplicate image - original untouched)", false);
Dialog.addNumber("if yes, rolling ball radius:", 0 );
Dialog.addMessage("--------");
Dialog.addChoice("Fluorescent channel", ChoicesChannel);
Dialog.addMessage("Dot size range");
Dialog.addNumber("Min size:", 0);
```

```
Dialog.addNumber("Max size:", 100);
Dialog.show();
Thresholdop = Dialog.getChoice();
RollingBall = Dialog.getCheckbox();
RBradius = Dialog.getNumber();
FluorescentChannel = Dialog.getChoice();
MinSize = Dialog.getNumber();
MaxSize = Dialog.getNumber();

//// Detect stack and composite image

selectWindow(initialimagetitle);
if (StackSlice != 1) {
	run("Split Channels");
	selectWindow(FluorescentChannel);
	ImageAnalysedID = getImageJD();
	}
	else {
		selectWindow(initialimagetitle);
		ImageAnalysedID = getImageJD();
	}

//// Overlay

if (Overlay.size != 0){
	run("To ROI Manager");
	RoiCount = roiManager("count");
}
	else {
		if (RoiCount == 0) {
			waitForUser("Create ROIs","Create ROI(s) and Click OK to continue \n
if no ROI added, the entire image becomes the ROI");
			RoiCount = roiManager("count");
			if (RoiCount ==0){
				run("Select All");
				roiManager("Add");
				RoiCount = RoiCount+1;
			}
		}
	}
```

```
///// Binary image and spot thresholding
run("Select None");
selectImage(ImageAnalysedID);
run("Duplicate...", "title=---Duplicate");
selectWindow("---Duplicate");
if (RollingBall==true){
	run("Subtract Background...", "rolling="+RBradius);
}
run("Enhance Contrast...", "saturated=0.5 normalize");
run("Gaussian Blur...", "sigma=1");
//setAutoThreshold("Minimum dark no-reset");
setAutoThreshold(Thresholdop+" dark no-reset");
setOption("BlackBackground", true);
run("Convert to Mask");
run("Fill Holes");

////// Spot count table

titleNewTab2 = "[Spot count table]";
run("New... ", "name="+titleNewTab2+" type=Table");
print(titleNewTab2,"\\Headings:Cell-Number \t Spot-count");

for (i=0; i<RoiCount; i++) {
		RoiCountStart = roiManager("count");
		roiManager("select", i);
		selectWindow("---Duplicate");
		run("Analyze Particles...", "size="+MinSize+"-"+MaxSize+" add");
		NewRoicount = roiManager("count");
//		if (NewRoicount != RoiCountStart) {
//			roiManager("Update");
//		}
		//roiManager("Update");
		print(NewRoicount);
		SpotCount = NewRoicount - RoiCountStart;
		print(SpotCount);
		print(titleNewTab2, i +"\t"+SpotCount);
		RoiFirstSpot = NewRoicount - SpotCount;
		j = 1;
			for (k=RoiFirstSpot; k<NewRoicount; k++) {
				roiManager("Select", k);
				roiManager("Rename", "Spot"+j+"_Cell"+i);
```

```
                        j = j+1;
                    }
}

//  Spot measurement on original image
roiManager("Show None");
selectImage(ImageAnalysedID);
roiManager("Show All without labels");
roiManager("Deselect");
roiManager("Measure");

run("Tile");
selectWindow("Results");
selectWindow("Spot count table");
selectWindow("ROI Manager");
roiManager("show all");
```